

UNCLASSIFIED

AD NUMBER

AD875951

LIMITATION CHANGES

TO:

Approved for public release; distribution is unlimited.

FROM:

Distribution authorized to U.S. Gov't. agencies and their contractors; Critical Technology; AUG 1970. Other requests shall be referred to Air Force Rocket Propulsion Laboratory, RPOR-STINFO, Edwards AFB, CA 93523. This document contains export-controlled technical data.

AUTHORITY

AFRPL ltr, 29 Sep 1971

THIS PAGE IS UNCLASSIFIED

6

AD875951

AFRPL-TR-70-82

DEVELOPMENT OF TOTAL AND RADIATIVE  
HEAT FLUX MEASUREMENT SYSTEMS  
FOR ROCKET NOZZLE APPLICATIONS

by

D. L. Baker  
M. R. Wool  
J. W. Schaefer

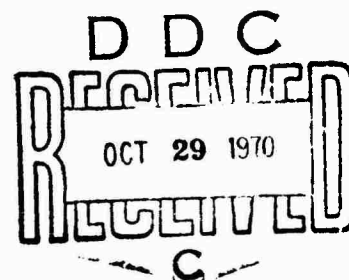
Aerotherm Corporation

Technical Report AFRPL-TR-70-82

Aerotherm Final Report No. 70-11

August 1970

Air Force Rocket Propulsion Laboratory  
Air Force Systems Command  
United States Air Force  
Edwards, California



This document is subject to special export controls and each transmittal to foreign governments or foreign nationals may be made only with prior approval of AFRPL (RPOR-STINFO), Edwards, California 93523

196

ACCESSION NO.	
CPSTI	WHITE SECTION <input type="checkbox"/>
DOC	DIFF SECTION <input checked="" type="checkbox"/>
UNANNOUNCED	<input type="checkbox"/>
JUSTIFICATION	
BY	
DISTRIBUTION/AVAILABILITY CODES	
DIST.	AVAIL. and/or SPECIAL
2	

# NOTICES

When U. S. Government drawings, specifications, or other data are used for any purpose other than a definitely related Government procurement operation, the fact that the Government may have formulated, furnished, or in any way supplied the said drawings, specifications, or other data, is not to be regarded by implication or otherwise, or in any manner licensing the holder or any other person or corporation, or conveying any rights or permission to manufacture, use, or sell any patented invention that may in any way be related thereto.

AFRPL-TR-70-82

DEVELOPMENT OF TOTAL AND RADIATIVE  
HEAT FLUX MEASUREMENT SYSTEMS  
FOR ROCKET NOZZLE APPLICATIONS

D. L. Baker  
M. R. Wool  
J. W. Schaefer

August 1970

This document is subject to special export controls and each transmittal to foreign governments or foreign nationals may be made only with prior approval of AFRPL (RPOR-STINFO), Edwards, California 93523



---

**AEROTHERM CORPORATION**

485 CLYDE AVENUE, MOUNTAIN VIEW, CALIFORNIA 94040  
TELEPHONE (415) 984-3200 • TELEX 34-8355



## FOREWORD

This report was prepared by Aerotherm Corporation under USAF Contract F04611-68-C-0086 and presents the development and demonstration of total heat flux and radiative heat flux measurement systems for use in ablative nozzles. The work was administered under the direction of the Air Force Rocket Propulsion Laboratory with Lt. John R. Ellison and Mr. Harold I. Binder as the Project Officers.

Mr. John W. Schaefer was the Aerotherm Corporation overall program manager and principal investigator in the area of test evaluation. Mr. Duane L. Baker was the principal investigator in the areas of accuracy analysis, measurement systems design, and nozzle design. Mr. Mitchell R. Wool was the principal investigator in the areas of data reduction techniques and analysis of test results. Mr. John J. Reese, Jr. provided support in the test evaluation program.

The authors wish to acknowledge the contribution of Mr. D. Larry Jones, President, Heat Technology Laboratory, Inc., for his support in the design of the radiation heat flux systems and the contribution of the AFRPL test crew who performed the motor firings under this contract.

This technical report has been reviewed and is approved

Charles R. Cooke  
Chief, Solid Rocket Division  
Air Force Rocket Propulsion Laboratory

## ABSTRACT

Total heat flux and radiative heat flux measurement systems were developed for use in ablative solid rocket nozzles. The total heat flux system is a thermocouple instrumented plug of the same material and layup angle as the ablative part in which it is installed. The total heat flux through a firing is determined from an analysis of the measured in-depth temperature histories. The radiative heat flux system is a narrow view angle, Gardon-type radiometer installed in a cavity below the surface of the ablative part. The total radiative heat flux through a firing is determined from a calibration curve relating millivolt output and total radiation flux of a uniform calibration source. The ablative materials considered under the program were MX4926 carbon cloth phenolic and MX2600-96 silica cloth phenolic. Detailed accuracy, design, fabrication, and installation studies were performed to define the system configurations. A preliminary evaluation program was performed in which the measurement systems were installed in two-dimensional nozzles and successfully tested in simulated rocket environments using an arc plasma generator. Final systems evaluation and demonstration was performed through two nozzle firings on the AFRPL 40-inch char motor. A total of six total flux systems and three radiation flux systems were tested in these firings. A high flame temperature aluminized propellant, APG 112D, was used and peak pressures in both firings were approximately 1000 psia with firing durations of approximately 60 seconds. Successful performance of the two measurement systems was demonstrated.

## TABLE OF CONTENTS

Section		Page
1	INTRODUCTION	1-1
2	SUMMARY	2-1
3	MEASUREMENT SYSTEM CONCEPTS	3-1
	3.1 Total Heat Flux System	3-2
	3.2 Radiative Heat Flux System	3-5
4	SYSTEMS STUDY AND DESIGN	4-1
	4.1 Total Heat Flux System	4-1
	4.1.1 Error Analysis	4-1
	4.1.2 Design and Fabrication Analysis	4-30
	4.2 Radiative Heat Flux System	4-39
	4.2.1 Error Analysis	4-40
	4.2.2 Design and Fabrication Analysis	4-52
5	DATA REDUCTION	5-1
	5.1 Total Heat Flux System	5-1
	5.1.1 Definition of Temperature Histories	5-1
	5.1.2 Definition of Total Heat Flux	5-2
	5.1.3 Accuracy of Total Heat Flux	5-8
	5.2 Radiative Heat Flux System	5-11
	5.2.1 Definition of Radiative Heat Flux	5-11
	5.2.2 Accuracy of Radiative Heat Flux	5-16
6	TEST EVALUATION PROGRAM	6-1
	6.1 Phase II Test Evaluation Program	6-1
	6.2 Total Heat Flux System	6-5
	6.2.1 Design and Installation	6-5
	6.2.2 Test Results	6-6
	6.3 Radiative Heat Flux System	6-9
	6.3.1 Design and Installation	6-14
	6.3.2 Test Results	6-14
7	CHAR MOTOR TESTS	7-1
	7.1 Char Motor Nozzles	7-2
	7.1.1 Nozzle Design, Fabrication, and Assembly	7-2
	7.1.2 Char Motor Firing Conditions	7-9
	7.2 Thermal and Ablation Nozzle Response	7-9
	7.3 Total Heat Flux Measurement System	7-23
	7.3.1 System Design and Installation	7-23
	7.3.2 Sensor Response	7-25
	7.3.3 Total Heat Flux System Evaluation	7-28
	7.4 Radiative Heat Flux System	7-50
	7.4.1 Design and Installation	7-52
	7.4.2 Test Results	7-52
	7.4.3 Interpretation of the Radiation Results	7-58
8	CONCLUSIONS AND RECOMMENDATIONS	8-1

## LIST OF TABLES

Number		Page
4-1	Thermal Properties of Tungsten	4-17
4-2	Summary of Thermocouple Depth Uncertainty Analyses	4-28
4-3	Accuracies in Measured Temperatures for a Local Material Temperature of about 2500°R	4-29
4-4	Thermocouple Depths and Types to be Used in Measurement System Plugs	4-34
4-5	Radiometer Accuracy	4-51
4-6	Characteristics of Narrow View Angle Radiometer Located at the Nozzle Throat	4-56
4-7	Characteristics of the Narrow View Angle Radiometer Located at an Expansion Ratio of 3.0	4-56
6-1	Nominal Phase II Test Matrix	6-4
6-2	Summary of Test Conditions and Test Results	6-4
7-1	Elemental Composition of APG 112D Propellant	7-10
7-2	Molecular Composition of APG 112D at Anticipated Chamber Conditions	7-10
7-3	Summary of Char Motor Operating Conditions	7-10
7-4	Summary of Char Motor Nozzle Ablation Response Measurements	7-22
7-5	Details of Total Heat Flux Measurement System Designs	7-24
7-6	Thermocouple Calibration Curve-Fit Constants	7-29
7-7	Results of In-Depth Solutions	7-41
7-8	Summary of Surface Chemical Response Results	7-47
7-9	Optical Depth and Blackbody Emissive Power	7-61

## LIST OF FIGURES

Number		Page
3-1	Characterization of the Solid Propellant Rocket Environment and the Response of a Charring Ablator	3-1
3-2	Schematic of Total Heat Flux Measurement System	3-3
3-3	Schematic of Char Motor Nozzle with Measurement System Installed	3-4
3-4	Schematic of Radiation Heat Flux Measurement System	3-7
3-5	Char Motor Nozzle - Total and Radiative Heat Flux Sensors	3-8
4-1	Temperature Profiles at Nozzle Throat, MX-4926, 60° Wrap	4-5
4-2	Temperature Profiles at Initial Area Ratio of 4.0, MX-2600-96	4-5
4-3	In-Depth Transient Temperature Response	4-6
4-4	Constant Density Specific Heat Which Accounts for In-Depth Charring	4-8
4-5	Constant Density Thermal Conductivity which Accounts for In-Depth Charring	4-9
4-6	Nodal Geometry for MX-4926 ASTHMA Analysis	4-10
4-7	Nodal Geometry for MX-2600-96 ASTHMA Analysis	4-11
4-8	Comparison of Perturbed and Unperturbed Temperature Distributions for MX-4926	4-12
4-9	Comparison of Perturbed and Unperturbed Temperature Distributions for MX-2600-96	4-13
4-10	Temperature Distortion Around Thermocouple Cavity	4-14
4-11	Comparison of Axisymmetric and Flat Plate CMA Solutions at the Nozzle Throat for MX-4926	4-15
4-12	Thermal Model for Thermocouple Response Lag Analysis	4-16
4-13	Thermocouple Lag for MX-4926	4-18
4-14	Comparison of Seebeck and Peltier EMF's for W5Re/W26Re	4-20
4-15	Electrical Circuit for W5Re/W26Re Thermocouple	4-20
4-16	Simplified Thermocouple Electrical Circuit	4-21

# LIST OF FIGURES (continued)

Number		Page
4-17	Deviation of W/W26Re Thermocouple in Direct Contact with Carbon Heater at 3182 <sup>o</sup> F	4-22
4-18	Total Heat Flux Sensor Correctly Positioned in X-Ray Beam	4-24
4-19	Total Heat Flux Sensor Incorrectly Positioned in X-Ray Beam	4-26
4-20	In-Depth Response and Thermocouple Locations for the Throat of the Char Motor Nozzle	4-31
4-21	In-Depth Response and Thermocouple Locations for A/A <sub>*</sub> = 4.0 in the Char Motor Nozzle	4-31
4-22	Thermocouple EMF Outputs	4-33
4-23	Schematic of Thermocouple Lead Wire Connection Scheme	4-36
4-24	Phase II Thermocouple Recording and Calibrating Circuit	4-39
4-25	Constantan Foil Temperature Distribution at Maximum Heat Flux for Various Body Temperatures	4-42
4-26a	Variation of Temperature Difference with Temperature Level and Incident Heat Flux	4-43
4-26b	Variation of Recorded EMF Output with Temperature Difference and Temperature Level	4-43
4-27	Effect of Thermal Conductivity and Thermocouple Output Variations with Temperature on Sensor Output	4-44
4-28	Approximate Radiation Heat Loss from Sensor at Maximum Incident Heat Flux	4-45
4-29	Optical Properties of Lens Materials and Surface Coating	4-46
4-30	Black Body Emissive Power as a Function of Wavelength for Source Temperatures at 3000, 5000, and 7000 <sup>o</sup> R	4-47
4-31	Non-Dimensional Calorimeter Response as a function of Non-Dimensional Time	4-49
4-32	Effect of View Angle on Measured Heat Flux	4-54
4-33	Control Volume for Defining Gas Purge Flow Rate	4-57
4-34	Radiometer Purge Gas Requirements	4-59

# LIST OF FIGURES (continued)

Number		Page
4-35	Narrow Angle Radiometer	4-59
4-36	High Pressure Radiometer	4-60
4-37	Radiation Heat Flux Measurement System Installation in Char Motor Nozzle	4-62
4-38	Installation of High Pressure Radiometer in Nozzle Steel Housing	4-62
5-1	Effect of Measurement Uncertainties on the Determined Surface Temperature	5-9
5-2	Sensitivity of Total Heat Flux to Surface Temperature Uncertainty	5-10
5-3	Schematic of Radiometer Data Reduction Considerations	5-12
5-4	Simplified One-Dimensional Geometry for Development of Radiative Transport Equation	5-12
5-5	Physical Model for Radiative Transport Equation	5-12
6-1	Aerotherm Constrictor Arc, Rocket Simulator Configuration	6-2
6-2	Two-Dimensional Nozzle Test Configuration	6-2
6-3	Measured Thermal Response of an MX-4926 Carbon Phenolic Ablative Plug, Test 1318	6-7
6-4	Comparison Between Measured and Determined Surface Temperature	6-7
6-5	Comparison Between Measured and Determined Surface Temperature	6-8
6-6	Comparison Between Measured and Determined Surface Temperature	6-8
6-7	Comparison Between Measured and Determined Surface Temperature	6-10
6-8	Comparison Between Measured and Determined Surface Temperature	6-10
6-9	Measured Total and Convective Heat Fluxes	6-11
6-10	Measured Total and Convective Heat Fluxes	6-11
6-11	Measured Total and Convective Heat Fluxes	6-12
6-12	Comparison Between Measured and Predicted Convective Heat Transfer Coefficients	6-12
6-13	Comparison Between Measured and Predicted Convective Heat Transfer Coefficients	6-13

# LIST OF FIGURES (continued)

Number		Page
6-14	Test Configuration for APG Radiative Tests	6-15
7-1	Nozzle Design for First Char Motor Firing	7-3
7-2	Nozzle Design for Second Char Motor Firing	7-4
7-3	Char Motor Chamber Pressure History for MX-4926 Nozzle Throat Material (Initial Throat Dia = 2.30 In.)	7-6
7-4	Nitrogen Gas Purge System for the First Char Motor Firing	7-8
7-5	Nitrogen Gas Purge System for the Second Char Motor Firing	7-8
7-6	Measured Chamber Pressure Histories for the Two Char Motor Firings	7-11
7-7	Throat Ablation Response Measurements a. 1st Char Motor Nozzle Test Firing b. 2nd Char Motor Nozzle Test Firing	7-13 7-13
7-8	Pre- and Post-Test Char Motor Nozzle Surface Contours and Char Depth Contour, First Firing a. 0° Section View b. 45° Section View c. 90° Section View d. 135° Section View e. 180° Section View f. 225° Section View g. 270° Section View h. 315° Section View	7-14 7-14 7-15 7-15 7-16 7-16 7-17 7-17
7-9	Pre- and Post-Test Char Motor Nozzle Surface Contours and Char Depth Contour, Second Firing a. 0° Section View b. 45° Section View c. 90° Section View d. 135° Section View e. 180° Section View f. 225° Section View g. 270° Section View h. 315° Section View	7-18 7-18 7-19 7-19 7-20 7-20 7-21 7-21
7-10	Photographs of Nozzle Surfaces Showing Ablative Plug Sensors a. First Char Motor Test Firing b. Second Char Motor Test Firing	7-26 7-26 7-27



# LIST OF FIGURES (continued)

Number		Page
7-11	Measured and Computed In-Depth Temperature and Determined Surface Temperature	
	a. $A/A^* = -2.0$ (Subsonic), 1st Nozzle Firing	7-30
	b. Throat, 1st Nozzle Firing	7-30
	c. $A/A^* = 2.0$ (Supersonic), 1st Nozzle Firing	7-31
	d. $A/A^* = 4.0$ (Supersonic), 1st Nozzle Firing	7-31
	e. Throat, 2nd Firing	7-32
	f. $A/A^* = 3.0$ (Supersonic), 2nd Nozzle Firing	7-32
7-12	Typical Thermocouple Millivolt Outputs Showing Temperature Rise Rate Decrease Near 3000°R	7-33
7-13	Assignment of Thermocouple Measurements to Verify the Temperature Data and the In-Depth Heat Conduction Model	7-36
7-14	Surface Recession Histories of Total Heat Flux Measurement Systems	
	a. 1st Char Motor Nozzle Test Firing	7-37
	b. 2nd Char Motor Nozzle Test Firing	7-37
7-15	Temperature Profiles Utilized to Estimate First Guess Surface Temperature History	7-39
7-16	Schematic of Material Surface Recession Mechanisms	7-42
7-17	Evaluation of $B'_g$ from $T_w$ and $\dot{m}_c/\dot{m}_g$	7-45
7-18	Evaluation of $h_w$ from $T_w$ and $B'_g$	7-45
7-19	Evaluation of $\sum Z_{iw} h_i^w$ from $T_w$ and $B'_g$	7-46
7-20	Evaluation of $\sum K_{ie} h_i^w$ and $\sum Z_{ie}^* h_i^w$ from $T_w$	7-46
7-21	Total Heat Flux Determined from Measurement System Data	
	a. MX-4926 Carbon Phenolic Total Heat Flux Sensors	7-49
	b. MX-2600-96 Silica Phenolic Total Heat Flux Sensor, $A/A^* = 4.0$	7-49
7-22	Comparison of Predicted to Measured Total Incident Heat Flux	7-51
7-23	Radiometer Output and Associated Information for the First Char Motor Firing	7-53
7-24	Measured Radiative Heat Flux at the Nozzle Throat for the First Char Motor Firing	7-55
7-25	Nitrogen Purge Gas System Pressures for the Second Char Motor Firing	7-55
7-26	Measured Copper Heat Sink Temperatures for the Second Char Motor Firing	7-56

LIST OF FIGURES (concluded)

Number		Page
7-27	Transient Chamber Pressure and Nozzle Throat and Exit Cone Radiometer Output for the Second Char Motor Firing	7-56
7-28	Measured Hemispherical Radiative Heat Flux for the Second Char Motor Firing	7-57
7-29	Emissivity of a One-Dimensional Slab of Scattering and Emitting Particles	7-63

# LIST OF SYMBOLS

A	area
B	fraction of radiation scattered backward
B'	dimensionless mass removal rate
B <sub>a</sub>	dimensionless gas phase ablation rate
B <sub>*</sub>	dimensionless condensed phase removal rate
C	specific heat
C <sub>1</sub> , C <sub>2</sub>	radiative constants
C <sub>H</sub>	Stanton number
C <sub>M</sub>	non-dimensional mass transfer coefficient
D	diameter as defined by equation on p. 7-61
e <sub>b</sub>	Planck's blackbody emissive power
E	electromotive force
E <sub>A,B</sub>	Seebeck voltage for metals A and B
G	scattering function
h	enthalpy
h <sub>i</sub>	enthalpy of species i
h <sub>ii</sub>	enthalpy of injectant at inlet to radiometer cavity
h <sub>ie</sub>	enthalpy of injectant at exit of the radiometer cavity
I	radiation intensity or current
K	thermal conductivity
K <sub>i</sub>	concentration of species i
K'	defined by equation on p. 7-61
L	length
Le	Lewis number

# LIST OF SYMBOLS (continued)

$\dot{m}$	mass flux
$M$	$\sigma_a/(\sigma_a + \sigma_s)$
$n$	index of refraction or propellant burning rate exponent
$N_p$	particle density
$P_c$	chamber pressure
$Q$	heating rate
$\dot{q}, q$	heat flux
$\dot{q}_{r_b}$	total hemispherical radiative heat flux from a blackbody source
$\dot{q}_{r_c}$	radiative heat flux absorbed by sensor
$\dot{q}_{r_G}$	radiative heat flux emitted by a slab of combustion products
$Q_t$	extinction efficiency factor
$r$	radius
$r^*$	nozzle throat radius
$r_{pm}$	mean particle radius
$R$	electrical resistance or radius
$S$	thickness
$S_{swell}$	thickness due to char swell
$S_A^*$	entropy transfer coefficient for metal A
$t$	time or thickness
$T$	temperature
$u$	velocity
$W$	solid angle
$x, X$	distance
$y, Y$	distance
$Z_i$	unequal diffusion quantity for species i
$d$	temperature coefficient of thermal conductivity or view angle
$\beta$	extinction coefficient
$\gamma$	scattering coefficient
$\Delta$	temperature difference

# LIST OF SYMBOLS (continued)

$\delta_{TC}$	thermocouple depth
$\epsilon$	emissivity
$\epsilon'$	emissivity of sensor coating
$\epsilon_G$	hemispherical emittance
$\zeta$	twice the motor ignition transient time or blowing rate factor
$\theta$	angle or time
$\kappa$	absorption coefficient
$\lambda$	wavelength or blowing reduction parameter
$\mu$	viscosity or cosine of angle
$\pi_{A,B}$	Peltier coefficient for the combination of metals A and B
$\rho$	density
$\rho u C_H$	convective heat transfer coefficient
$\rho u C_M$	mass transfer coefficient
$\sigma$	Stefan-Boltzman constant
$\sigma_a$	absorption cross section
$\sigma_A$	Thomson coefficient for metal A
$\sigma_s$	scattering cross section
$\sigma_t$	extinction cross section
$\tau$	time constant
$\tau'$	transmissivity
$\tau_c$	char thickness
$\tau_o$	optical thickness
$\theta$	angle
$\omega_n$	uncertainty of the $n^{th}$ variable
SUBSCRIPT	
aw	adiabatic wall
b	blackbody
c	cross section, convective, or char
e	effective or edge

LIST OF SYMBOLS (concluded)

eff	effective
g	gas
o	reference, base state, initial state, or non-blowing condition
r	radiation or recovery
s	sensible
t	total (sensible plus chemical)
w	wall
$\lambda$	monochromatic
*	condensed phase
SUPERSCRIPT	
$T_w$	reference state
*	steady state
.	rate derivative

## SECTION 1

### INTRODUCTION

A knowledge of the convective and radiative heat flux incurred by ablative materials in solid rocket nozzles is important in the design of these nozzles and in the analysis of material response. No practical and effective methods for measuring these heat fluxes have been available, however. The objective of the program described herein was the development of measurement systems for use in ablative nozzle materials. Total and radiation heat flux incident to the material surface are measured by these systems, convective heat flux is defined by difference.

The total heat flux measurement system is a thermocouple instrument plug of the same ablative material and reinforcement tape layup angle as the nozzle part in which it is installed. The primary instrumentation is several fine-wire thermocouples which are installed in the plug to accurately measure the thermal response of the ablative material. The total surface heat flux is defined from an analysis of the in-depth temperature measurements.

The radiation flux measurement system is a narrow view angle Gardon-type radiometer which is installed in a cavity in the ablative nozzle. The radiometer is gas purged and employs a sapphire window to eliminate convective heating and particle deposition. The millivolt output from the narrow view angle radiometer is converted directly to a hemispherical radiative heat flux utilizing a calibration based on measurements of a known uniform radiative energy source. This simplified technique for obtaining the hemispherical radiative heat flux was used because of the difficulty in directly measuring the total hemispherical radiative heat flux in an ablative nozzle and because of cost considerations in making such measurements.

The program was divided into three phases:

- Phase I Study and Design
- Phase II Fabrication, Test, and Evaluation
- Phase III Rocket Nozzle Static Firings

The results from these phases are summarized in Section 2. A more detailed description of the Phase I effort is described in Sections 3, 4 and 5. Section 3 presents both an evaluation of the measurement systems studied and a general description of the total and radiative systems used in the present program. Section 4 presents the results of a detailed systems study and, also, the design which was formulated from this study. The systems study included an error analysis of the primary measurements for both the total and radiative heat flux systems. In addition, this section describes the instrument fabrication and installation procedures, and the accessory recording instrumentation required to make the primary measurement. Section 5 presents the data reduction procedures for both measurement systems. Section 6 presents the Phase II effort which consisted of the test evaluation of the measurement systems in a simulated environment which was generated by the Aerotherm arc plasma generator (APG). The Phase III effort is presented in Section 7. The performance for several measurement systems of both types is presented for two ablative nozzles that were test fired on the AFRPL 40-inch char motor. Finally, conclusions and recommendations are presented in Section 8.



## SECTION 2

### SUMMARY

Total heat flux and radiation heat flux measurement systems were developed for application in the severe environment of a solid rocket nozzle firing. These systems are installed in the ablative components of a nozzle and are designed to perform continuously throughout a firing.

The total heat flux system is a thermocouple instrumented plug of the same material and with the same layup angle as the ablative part in which it is installed. Tungsten 5 percent rhenium/tungsten 26 percent rhenium and Chromel/Alumel thermocouples are employed at five in-depth locations in the plug. The total heat flux is determined by a computer code analysis which considers the measured in-depth temperatures and post-test surface recession to (1) define the surface recession and surface temperature histories and (2) define all the surface heat flux terms such that the total heat flux is the only unknown in the surface energy balance. The total flux system may be used in any material for which the thermal and ablative properties are well characterized. MX4926 carbon cloth phenolic and MX2600-96 silica cloth phenolic were considered in this program.

The radiative heat flux system is a narrow view angle, Gardon-type radiometer. The narrow view angle is required so that the radiometer can be recessed in a cavity below the ablative surface to protect it from the combustion products and to allow for surface recession. The constantan foil sensor is protected by a sapphire lens which is in turn protected by a nitrogen gas purge. The total (hemispherical) radiation heat flux is determined directly from a calibration curve relating the sensor output to the total radiation flux of a uniform source. The radiative flux system may be used in any material or nozzle configuration providing the installation does not result in a high thermal load on the radiometer due to conduction from the material. The radiometers were installed in MX4926 carbon phenolic in this program.

The program encompassed detailed accuracy, design, fabrication, and installation analyses; definition of the data reduction techniques and procedures; preliminary evaluation program in which the measurement systems were tested under simulated rocket environment

conditions in an arc plasma generator; and final evaluation and demonstration program in which the measurement systems were tested in two 40-inch char motor test firings. This program sequence applied to both measurement system types; also each char motor nozzle in the final evaluation and demonstration program incorporated both the total and radiative flux systems.

For the total flux system, the analysis of potential errors considered:

- Accuracy of the indicated temperature
- Accuracy of the thermocouple output
- Accuracy of the thermocouple location

The errors associated with temperature field distortions due to the presence of the thermocouple and the hole that accepts the thermocouple and to the contact resistance between the "flat plate" plug geometry and the axisymmetric geometry of the part in which it is installed were defined. The errors in thermocouple output due to electrical shorting across the conducting char and due to thermocouple calibration uncertainties and possible high temperature calibration shifts were defined. Finally, the uncertainties in the X-ray photography measurement of the thermocouple locations in the plug were defined. The potential uncertainty in the total heat flux which resulted from these accuracy analyses ranged from -11 to 5 percent for the thermocoupled MX4926 plug and from -20 to 13 percent for the thermocoupled MX2600-96 plug. The results of the accuracy analyses were incorporated into the plug design.

The thermocouple locations and thermocouple types are selected based on the anticipated response of the ablative material at the installation location. Bare wire 5 mil thermocouples are used and are fed through a stepped hole along an isothermal plane in the plug such that the bead (thermocouple junction) rests against the step at the plug centerline. The thermocouple wires are fed through beryllia sleeving along each side of the plug to prevent electrical shorting. The thermocouple wire/lead wire connection is made on pins installed in the bottom of the total flux plug. The plug is bonded into the ablative part with epoxy resin.

For the radiative flux system, the accuracy analysis considered:

- Errors due to thermal effects
- Errors due to optical effects
- Calibration uncertainties

The errors associated with a change in the radiometer body temperature and its effect on the sensor calibration and radiation interchange were defined. In addition, the errors due to the wavelength response of the sapphire protective lens and the high emissivity sensor coating as it relates to wavelength differences between the calibration source and the measured source were defined. Finally, the uncertainties in the sensor calibration and in the assumption of a uniform radiation flux in the rocket nozzle were defined. The uncertainty in the measured radiative heat flux resulting from the accuracy analysis varied from -6 to -2 percent which could be reduced to -3 to 2½ percent by making the necessary corrections for the body temperature.

The radiometer employs a heat sink body to maintain an acceptable sensor temperature level without the added complication of water cooling. The unit is nitrogen gas purged to protect the sapphire lens from convective heating and oxide particle contamination. The radiometer is installed in a cavity in the ablative part and is recessed below the exposed surface to protect it from the solid propellant combustion products. The design allows for minimum thermal contact between the radiometer and the high temperature region of the ablative part. The unit is potted in place with epoxy resin or threaded into the nozzle steel shell.

Data reduction for the total heat flux measurement system encompasses:

- Iterative in-depth conduction solutions using the Charring Material Ablation (CMA) computer code; final solution provides a close match of the measured and calculated in-depth temperature histories and defines the surface recession, surface temperature, and some of the surface heat flux terms.
- Definition of the thermochemical surface heat flux terms from the above results and using the Aerotherm Chemical Equilibrium (ACE) computer code.
- Summation of the various terms of the surface energy balance to define total heat flux.

The final result is the total heat flux history at the measurement location throughout the nozzle firing. Data reduction for the radiative heat flux system is accomplished by simply relating the measured millivolt output of the radiometer to the calibration curve of millivolts vs total radiative heat flux. The final result is the total radiative heat flux history at the measurement location throughout the nozzle firing.

In the preliminary evaluation test program, six total flux systems and two radiative flux systems were installed in carbon phenolic and silica phenolic two-dimensional nozzles. These nozzles were test fired in an arc plasma generator under conditions which simulated a rocket nozzle firing and which also allowed an independent measurement of total and radiative heat flux, surface temperature history, and surface recession history. The measurement systems were designed to closely duplicate those used in an actual rocket nozzle. The units performed properly from both functional and measurement standpoints.

In the final evaluation and demonstration program, six total flux systems and three radiative flux systems were installed in two ablative nozzles which were test fired on the AFRPL 40-inch char motor. The sequence of the test firings was such that the second nozzle firing incorporated modifications suggested by the first firing. A summary of system locations and materials in both nozzles is presented below:

Nozzle	System Type	System Location, Area Ratio	Nozzle Ablative Material
1	Total	-2.0	MX4926 Carbon Phenolic
		1.0	
		2.0	
		4.0	
	Radiative	1.0	MX2600-96 Silica Phenolic
2	Total	1.0	MX4926 Carbon Phenolic
		3.0	
		1.0	
		3.0	
	Radiative	1.0	

A highly aluminized propellant, APG 112D, with a flame temperature of 7020°R at 1000 psia was used in both test firings. The maximum chamber pressures were 1080 and 930 psia for the first and second firings, respectively; the chamber pressures were highly regressive due to the surface recession of the ablative throat with final pressures in both firings of about 300 psia. The test firing times were just under one minute for both firings.

The total heat flux measurement systems performed satisfactorily and repeatably in both test firings and provided an accurate definition of the total heat flux histories. In the first firing, a

failure of the nitrogen purge gas to the radiative flux system caused a malfunction of the radiometer early in the firing. Modifications were made to the purge gas system to eliminate this problem in the second firing. The radiometer at an area ratio of 3.0 in the second firing performed satisfactorily throughout the firing and provided an accurate definition of the total radiation heat flux history. The view of the radiometer at an area ratio of 1.0 was apparently partially obstructed through most of the firing and therefore the results at this location are questionable.

The end result of the program was the successful development of total and radiative heat flux measurement systems for use in ablative solid rocket nozzles.

### SECTION 3

#### MEASUREMENT SYSTEM CONCEPTS

The proper selection of total and radiation heat flux measurement systems requires consideration of the response of ablative materials such as the cloth phenolics to solid propellant combustion environments. This material response and the environmental boundary conditions to which the material is exposed are illustrated schematically in Figure 3-1. The surface recedes due to surface thermochemical reactions and/or thermomechanical erosion. The material degrades in depth forming a char through which the gaseous degradation products flow. This response is typically transient, steady state ablation conditions being achieved only late in a rocket firing if at all.

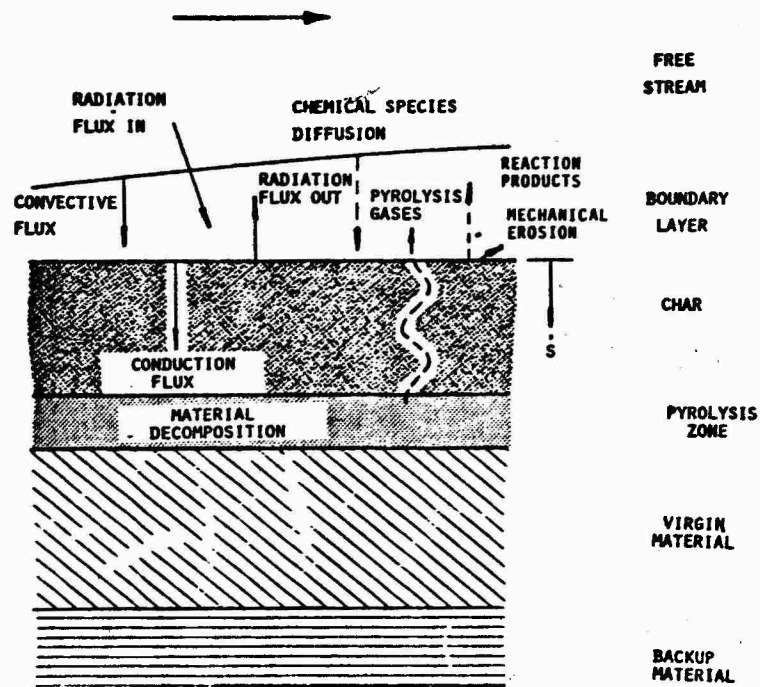


FIGURE 3-1 CHARACTERIZATION OF THE SOLID PROPELLANT ROCKET ENVIRONMENT AND THE RESPONSE OF A CHARRING ABLATOR

As shown by this figure, the heat flux from the combustion products to the nozzle wall is a combination of a convective flux, a chemical species diffusion flux, and a radiative flux. The convective flux represents sensible energy transfer to the wall, and the diffusion flux represents chemical energy transfer to the wall. These two terms are generally combined and referred to as the convective flux. The objective of the instrumentation systems is to measure both the total and radiative heat flux to the nozzle wall. The difference between these two heat fluxes represents the convective flux which is a combination of the sensible and chemical energy transfer. The ground rules for selection, the approaches considered, and the selected approach are presented in Section 3.1 for the total heat flux system and in Section 3.2 for the radiative heat flux system.

### 3.1 TOTAL HEAT FLUX SYSTEM

The surface response of an ablative material is indeed complicated and the events which make up this response are interrelated (Figure 3-1). In order to measure the total heat flux to an ablative material, the measurement system must therefore represent a negligible disturbance to the surface and in-depth response of the material. A system which employs a plug of the ablative material that is instrumented with fine wire thermocouples satisfies this requirement. The in-depth thermal response of the material is measured and the surface response including total heat flux is determined from this measurement. This concept best satisfies the requirement of an accurate measurement of total heat flux to an ablative material and was therefore the concept selected. The system advantages are summarized as follows:

- negligible disturbance to the in-depth and surface response of the material; measured temperature is that of the material
- data are obtained continuously through a firing; total heat flux is defined throughout a firing
- design, fabrication technique, data reduction procedure, and calibration procedure are within the current state-of-the-art
- necessary recording instrumentation and data reduction tools are readily available

The measurement system design is illustrated in Figure 3-2, and its installation in a rocket nozzle is shown schematically in Figure 3-3. The measurement system consists of a plug of the same ablative material and layup angle as that of the part in which it is installed. The plug is instrumented with five thermocouples such that temperature measurements to 5400°F are possible. A

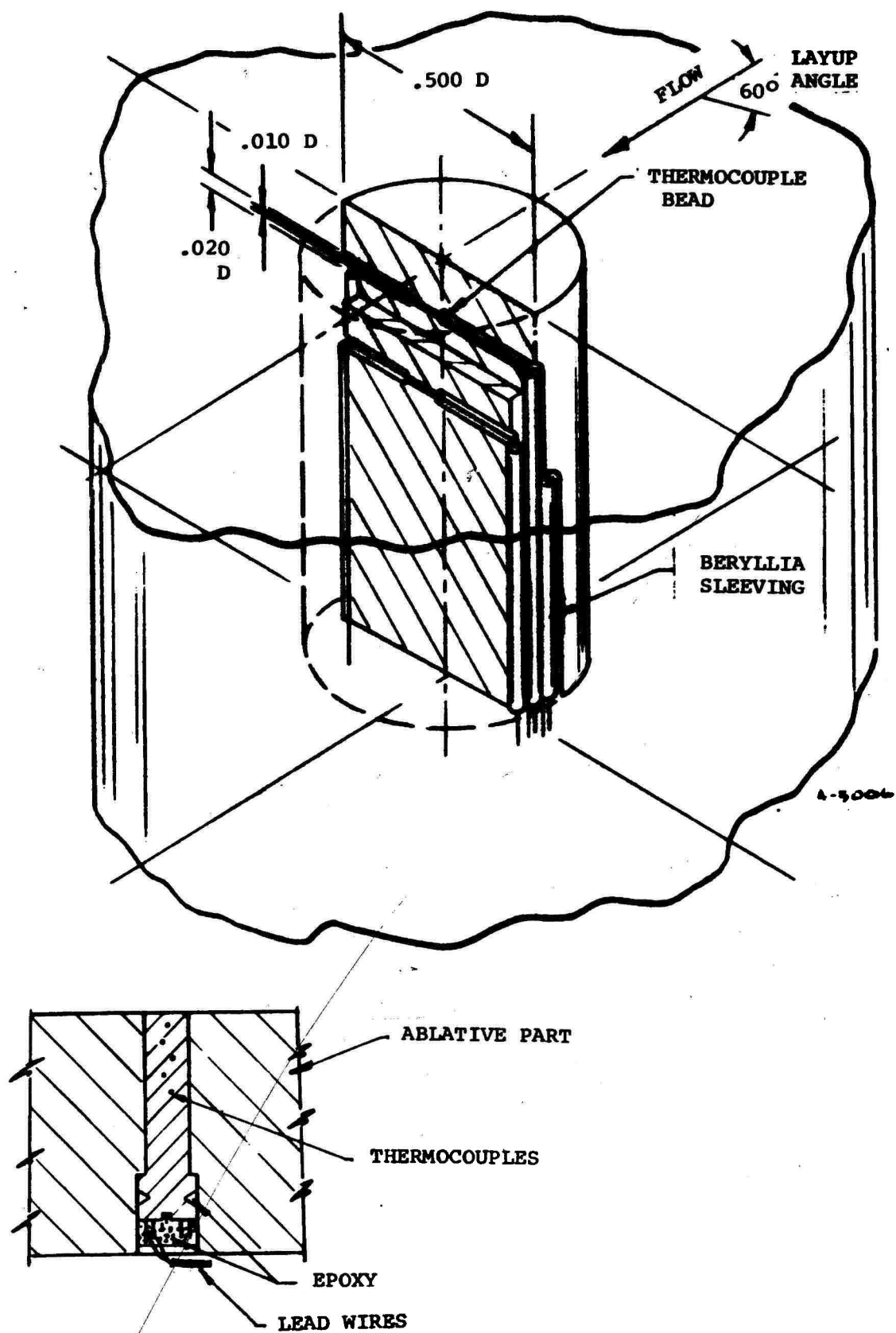


FIGURE 3-2 SCHEMATIC OF TOTAL HEAT FLUX MEASUREMENT SYSTEM



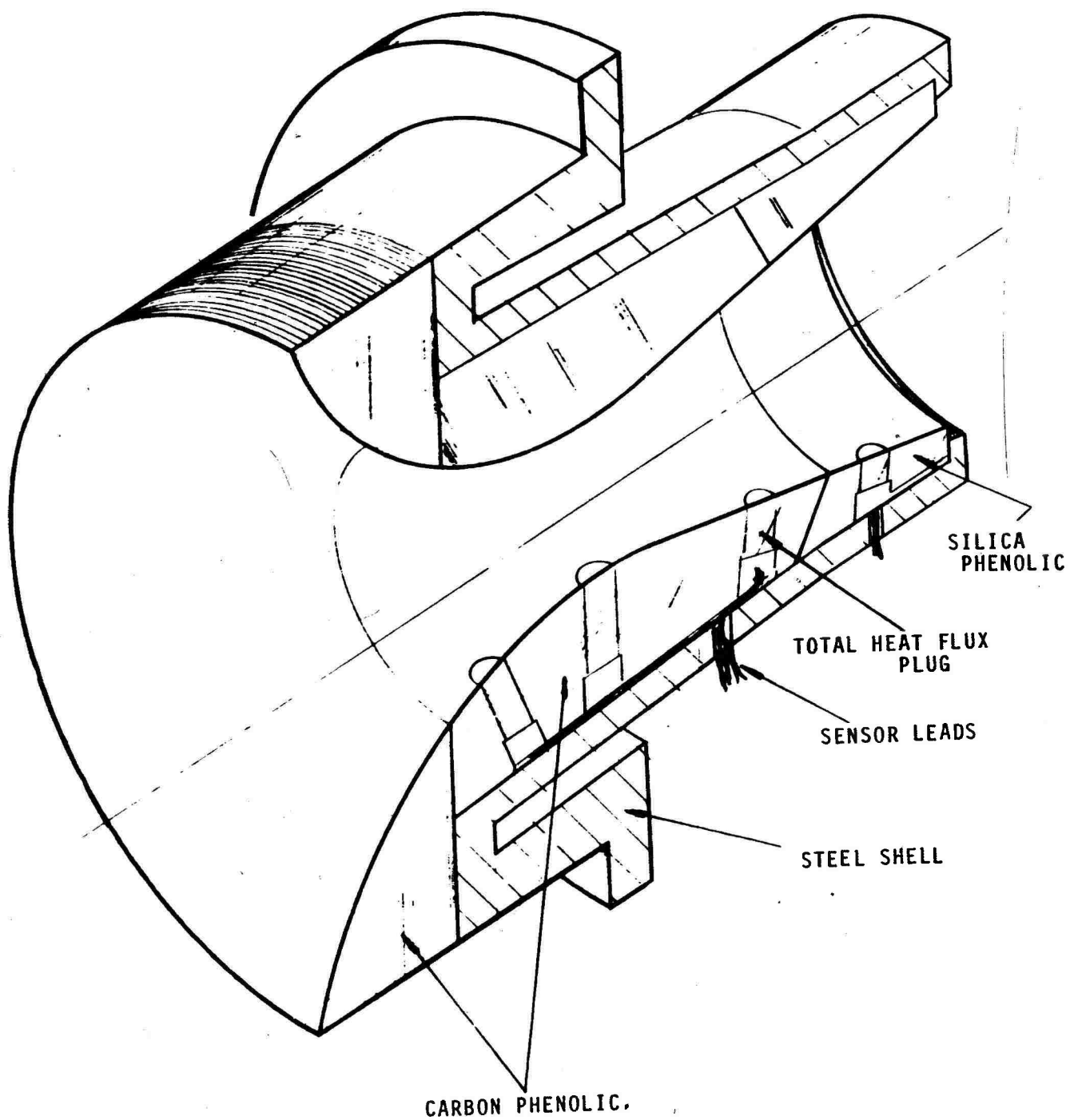


FIGURE 3-3 SCHEMATIC OF CHAR MOTOR NOZZLE WITH MEASUREMENT SYSTEM INSTALLED

A-1267

continuous measurement of the in-depth thermal response of the ablative material is therefore made throughout a firing. An in-depth conduction solution which is based on these measurements and considers the response mechanisms depicted in Figure 3-1 then provides the required total heat flux to the material surface. The two ablative materials selected for measurement system evaluation are MX 4926 carbon phenolic and MX 2600-96 silica phenolic. These materials are representative of those of interest for the measurement system application and also are accurately characterized in terms of their properties and response mechanisms.

Other measurement system concepts were also considered but none was as attractive as that selected. The major drawback of most concepts is the finite size of the sensor and the resultant disturbance of the surface and in-depth response. Measurement techniques in this category include the transient slug calorimeter, the steady-state Gardon-type gauge, and the conduction calorimeter (based on the  $\Delta T$  across a low conductivity wafer). With these techniques, the total heat flux measured is not the heat flux to the ablative material and, because of the complicated interaction between the sensor and the material in which it is installed, the relation between the measured and desired fluxes is very difficult if not impossible to define. Some of the problems in this regard are the discontinuity in the energy and mass boundary layers associated with a dissimilar material in the ablative part, the disturbance to the thermal conduction, pyrolysis gas flow, and thermal decomposition of the ablative material, the dissimilar surface recession of the two materials, and the availability of data at only a discrete time or times. Note that these comments also apply to the use of several sensors of the same type stacked together to form a measurement system plug. Another general approach considered is the direct measurement of surface temperature. Optical techniques are not possible because of the optically thick particle cloud in solid propellant combustion products. The various techniques for measuring surface temperature using a thermocouple approach have proved to be unreliable (Reference 3-1) and therefore are not attractive. The thermocouple instrumented plug of the ablative material avoids the above problem areas and was therefore the logical selection for the measurement system.

### 3.2 RADIATIVE HEAT FLUX SYSTEM

The total radiative heat flux to the surface of an ablative material in a solid rocket nozzle results from the aluminum oxide particles, from various gas phase species, and from the opposite walls. This radiative flux is a function of parameters such as particle density, particle temperature, particle emissivity, and particle optical depth, and, with the exception of particle emissivity, these parameters vary with nozzle axial location. This radiative

intensity is therefore a complicated function of the direction of the line of sight. Because of this complication and because of the variation in the chamber conditions during the motor firing, the following ground rules were established tentatively for the design of the radiative heat flux measurement system.

- a. Continuous measurement through a firing since the chamber pressure will, in general, be changing with time.
- b. Measurement of total radiative heat flux to the nozzle wall (as opposed to spectral and narrow angle flux).
- c. Measurement location(s) at the same area ratio(s) as the ablative plugs.

Unfortunately, (a) and (b) are incompatible in that a total radiation flux sensor must be mounted at the surface for a  $180^\circ$  view but the severe heat flux and the surface recession preclude a continuous measurement capability. An attractive solution is (1) the use of a narrow view angle radiometer which is recessed below the ablative surface for continuous measurement, (2) the use of a wide view angle ( $180^\circ$ ) radiometer which becomes exposed at the surface for an instantaneous measurement before it is subsequently destroyed, and (3) the use of the two measurements at the identical times to calibrate the relationship between the total and narrow angle radiation fluxes. The development of two radiation measurement systems was beyond the scope of the subject program, however, and therefore the continuous measurement system, the narrow view angle radiometer, was selected for development.

The design of the narrow view angle radiometer is shown in Figure 3-4, and the installation within the nozzle is shown schematically in Figure 3-5. From this figure, one notes that the radiometer is placed in a cavity below the initial surface of the nozzle, and, thus, it is never directly exposed to the solid propellant combustion products even though surface recession occurs during the motor firing. The narrow view angle restriction is required to eliminate the possibility of the radiometer viewing the side walls of the cavity.

The basic components of the narrow view angle radiometer shown in Figure 3-4 are

- Gardon-type heat flux gauge
  - blackened constantan sensing disk
  - copper mounting heat sink body
  - copper lead wire connected to constantan disk center
- nitrogen purge gas flow system
- sapphire lens
- copper body
- thermocouple to measure body temperature

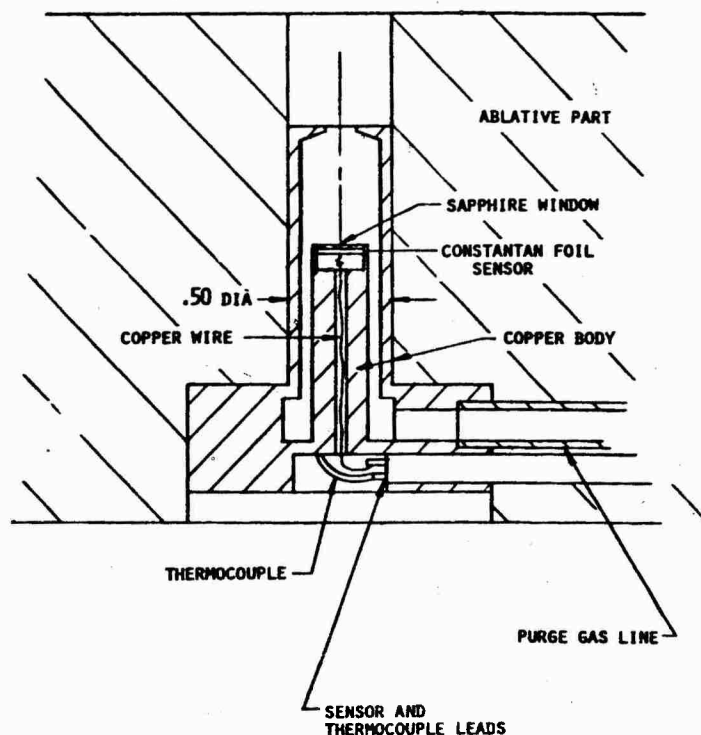


FIGURE 3-4 SCHEMATIC OF RADIATION HEAT FLUX MEASUREMENT SYSTEM

A complete description of the analytical background of a Gardon-type heat flux gauge is given in Reference 3-2. Simply stated, the temperature difference between the center of the constantan foil sensor and the copper heat sink body results in a thermocouple emf which varies linearly with incident heat flux. The nitrogen purge gas provides convective cooling of the sensor body and the lens. The lens shields the foil disk from convective heating (or cooling). In this configuration, the millivolt response of the Gardon-type heat flux gauge represents only the incident radiative heat flux.

In addition to the radiometer technique for radiative flux measurement, a spectral approach was also considered. This technique employed the measurement of the spectral emittance of the sources over a narrow view angle using a reference source and a spectrometer. This approach was rejected because it requires sophisticated and delicate instrumentation and requires a basic knowledge of the various sources of radiation and the directional variation which is currently unavailable.

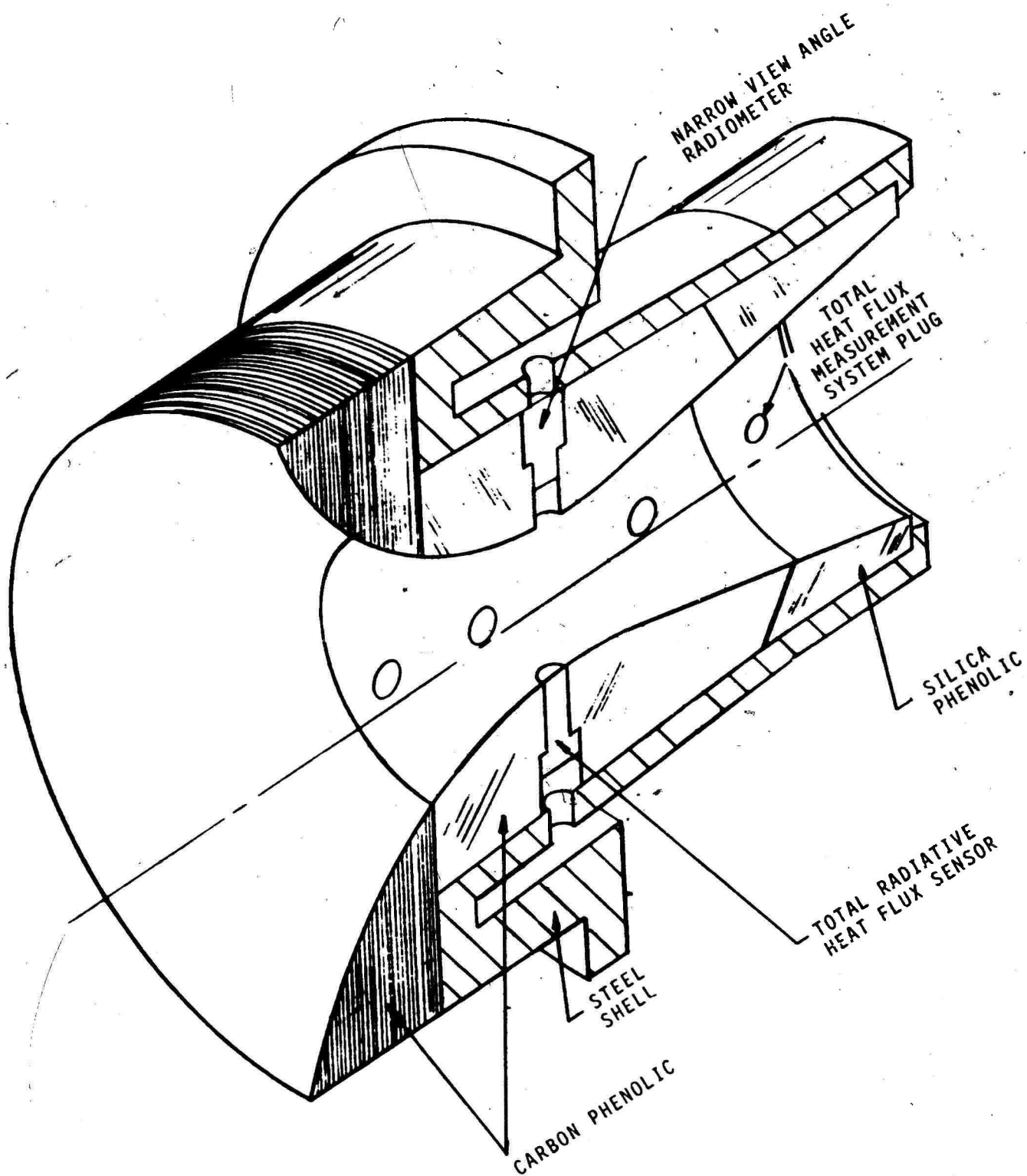


FIGURE 3-5 CHAR MOTOR NOZZLE - TOTAL AND RADIATIVE HEAT FLUX SENSORS

A-1268

#### REFERENCES

- 3-1 Rindal, R.A., Clark, K.J., Moyer, C.B., and Flood, D.T.: Experimental and Theoretical Analyses of Ablative Material Response in a Liquid-Propellant Rocket Engine. NASA-CR-72301 (Aerotherm Report No. 67-15), September 1, 1967.
- 3-2 Gardon, R.: An Instrument for the Direct Measurement of Intense Thermal Radiation. The Review of Scientific Instruments, Vol. 24, No. 5, May 1953.

## SECTION 4

### SYSTEMS STUDY AND DESIGN

The general approach to be used in making the total heat flux and radiation heat flux measurements were defined in Section 3. A systems study of these approaches for the purpose of defining the errors in the primary measurements was performed and a detailed design was formulated which minimized these errors. The results of this study and design are in Section 4.1 for the total heat flux measurement system and in Section 4.2 for the radiative heat flux system.

#### 4.1 TOTAL HEAT FLUX SYSTEM

The total heat flux measurement system is dependent on the accurate measurement of in-depth temperatures using thermocouples. Errors which are associated with the use of thermocouples to measure in-depth temperatures include distortion of the temperature field, thermocouple response lag, thermocouple electrical shorting, thermocouple calibration, and accuracy of thermocouple location. These sources of error are discussed in Section 4.1.1. Once the errors were defined, a design and fabrication analysis was performed which defined an economical measurement system configuration that minimized the measurement error. This analysis is presented in Section 4.1.2 and includes a discussion of thermocouple locations and types, thermocouple installation, system configuration and installation, and peripheral recording instrumentation. Note that even though the error, design, and fabrication analyses are presented separately, these analyses were performed concurrently and several iterations were required before a final design was adopted.

##### 4.1.1 Error Analysis

The primary measurement required in the total heat flux measurement system concept (Section 3.1) is temperature. Its measurement in ablative materials can be the source of significant errors. The problem areas related to temperature measurement with thermocouples are 1) the thermocouple perturbs the temperature distribution which would otherwise exist in the material, 2) the thermocouple junction temperature lags the temperature of the material due to heat conduction and thermal capacity effects, 3) the thermocouple wires, except along an isotherm, must be electrically insulated from each other in order to prevent any discrepancy between the electromotive force (emf) generated at the thermocouple junction and the

measured emf, and 4) the location of the thermocouple must be accurately known. The first three problems were considered in the selection of the measurement system, and two of the more important design objectives were to minimize problems one and two and to eliminate problem three. The design of the thermocouple plug is not directly influenced by the fourth problem, and thus, this problem can be solved after the design of the thermocouple plug has been finalized. The purpose of the error analysis presented in this section is to determine whether or not these design objectives are satisfied and to define the overall accuracy of the primary measurement, temperature, required by the measurement system.

The accuracy of the thermocouple temperature (problems 1 and 2) is established in Section 4.1.1.1 followed in Section 4.1.1.2 by an analysis of the accuracy of the thermocouple emf measurement. In this last section, an analysis is presented for the possible shunting effect across the thermocouple wires (problem 3), and this effect is combined with the guaranteed accuracy of the thermocouple and lead wires. The problem of accurately defining the in-depth thermocouple location is discussed in Section 4.1.1.3. Finally, the errors associated with the individual problems are combined and summarized in Section 4.1.1.4, and an overall temperature measurement accuracy is defined.

#### 4.1.1.1 Accuracy of Indicated Temperature

An ideal thermocouple which is located within a material would generate an emf corresponding to the temperature which would exist at the same location in the absence of the thermocouple. This temperature and corresponding emf will be referred to hereafter as the unperturbed temperature or emf. From a detailed investigation of the thermocouple plug design shown in Figure 3-2, one notes three regions which may cause a difference, assuming no emf error, between the measured and unperturbed temperatures; namely 1) the region incorporating the cylindrical cavities in which the thermocouple is located, 2) the region along the sidewalls of the plug assembly, including the bondline, and 3) the region within the cavity which includes both the thermocouple junction and the thermocouple wires. The first two regions which will cause distortions in the temperature field, and the third region which will cause a response lag in the temperature of the thermocouple junction are analyzed in the following sections. In these sections, only the tungsten 5% rhenium/tungsten 26% rhenium (W5Re/W26Re) thermocouple nearest the surface is analyzed in detail. This thermocouple location was chosen for analysis because it experiences the most rapid temperature response, and, as a result, the errors associated with measuring the in-depth temperature are maximized.



4.1.1.1.1 Distortion of Temperature Field. In order to define the distortion of the temperature field, the unperturbed temperature distribution was first determined. The nozzle configuration used for this analysis was shown schematically in Figure 3-3, and the representative analysis locations of interest were at the nozzle throat and at a supersonic area ratio of four. The material at the nozzle throat is carbon cloth phenolic (MX 4926) at a 60° layup angle with respect to the nozzle centerline. At a supersonic area ratio of four, the material is silica cloth phenolic (MX 2600-96) also at a 60° layup angle with respect to the nozzle centerline. The thermal analysis was performed using the Charring Material Ablation (CMA) and Aerotherm Chemical Equilibrium (ACE) computer programs (References 4-1, 4-2, and 4-3). (The ACE computer program is an expanded version of the Equilibrium Surface Thermochemistry (EST) computer program (Reference 4-4).) The thermal analysis of rocket nozzles using these programs has been documented in References 4-5 and 4-6 and will only be summarized here.

In brief, the ACE computer program was used to generate the required in-depth and surface thermochemical information for input into the CMA computer program. This information was generated assuming the alumina particles do not penetrate the boundary layer. For carbon phenolic, the surface information was generated based on diffusion controlled thermochemistry. For silica phenolic both diffusion controlled thermochemistry and mechanical melt removal were considered in generating this information. The CMA program calculates the transient one-dimensional temperature distributions using the ACE generated information together with 1) virgin material and char thermal properties, 2) virgin material decomposition coefficients assuming three Arrhenius rate equations, 3) incident radiative heat flux, and 4) convective and mass diffusion coefficients. Items 1 and 2 were obtained from References 4-5 and 4-6. Item 3 is satisfied by specifying the emissivity and radiating temperature of the particle laden combustion species, the absorptivity of the wall material, and the view factor. The radiating temperature was assumed to be the local static temperature, and the emissivity of the cloud of alumina particles, using the initial chamber pressure of 740 psia, was defined to be 0.71 at the nozzle throat and 0.24 at a supersonic area ratio of four. The absorptivity (and emissivity) used for both wall materials was 0.85, and the view factor used was 1.0. The convective heat transfer coefficient (Item 4) was evaluated as a function of wall enthalpy using the energy thickness method described in Appendix A of Reference 4-7 to solve the governing turbulent boundary layer equations. Here again, the initial chamber pressure of 740 psia was used. Since previous experience (Reference 4-6) indicates that this method of analysis consistently gives results which cause the surface recession rate to be overpredicted by approximately 25%, they were multiplied by 0.75 before being input to the CMA program. At the nozzle throat location, the CMA program

modifies the initial convective heat transfer coefficient according to the proportionality

$$\rho u C_H \propto \left(\frac{1}{r^*}\right) \frac{1.8-0.2n}{1-n} \quad (4-1)$$

where

$\rho u C_H$  - convective heat transfer coefficient

$r^*$  - nozzle throat radius

$n$  - propellant burning rate exponent (0.625)

Equation (4-1) accounts for the decrease in the convective heat transfer coefficient due to the chamber pressure decay resulting from the nozzle throat erosion. Based on the CMA analysis at the nozzle throat, the convective heat transfer coefficient at the station defined by an initial area ratio of four was evaluated as a function of time, accounting for the variation in chamber pressure and local area ratio caused by the nozzle throat erosion. The mass transfer coefficient (Item 4) for both locations was evaluated by employing the relationship.

$$C_M = C_H Le^{2/3} \quad (4-2)$$

where

$C_M$  - non-dimensional mass transfer coefficient

$C_H$  - Stanton number

$Le$  - Lewis number

Using the method of analysis described above, transient one-dimensional temperature profiles were calculated at the nozzle throat (MX 4926) and in the exit cone at an area ratio of four (MX 2600-96). Representative profiles are shown in Figures 4-1 and 4-2 for times corresponding to motor burnout and to 60 seconds following motor burnout. In addition, the surface recession, excluding the effect of char swell, are tabulated in these figures as a function of motor burn time. Therefore, these figures provide information required for defining the thermocouple locations and the minimum length of the thermocoupled plug. Since the preliminary design of the plug had

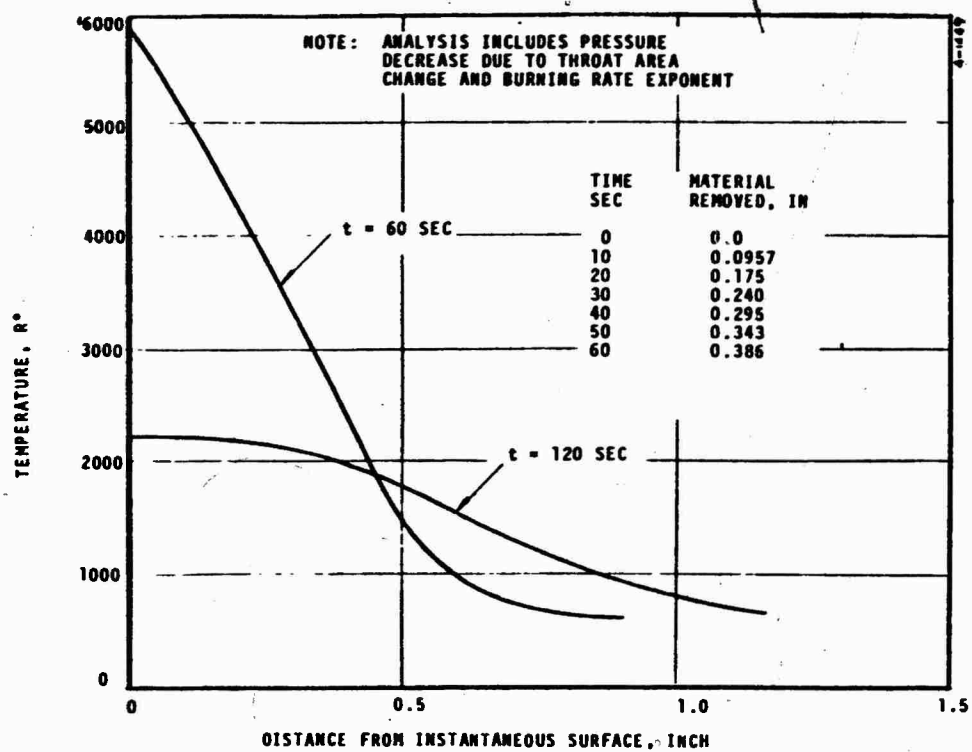


FIGURE 4-1 TEMPERATURE PROFILES AT NOZZLE THROAT  
MX-4926, 60° WRAP

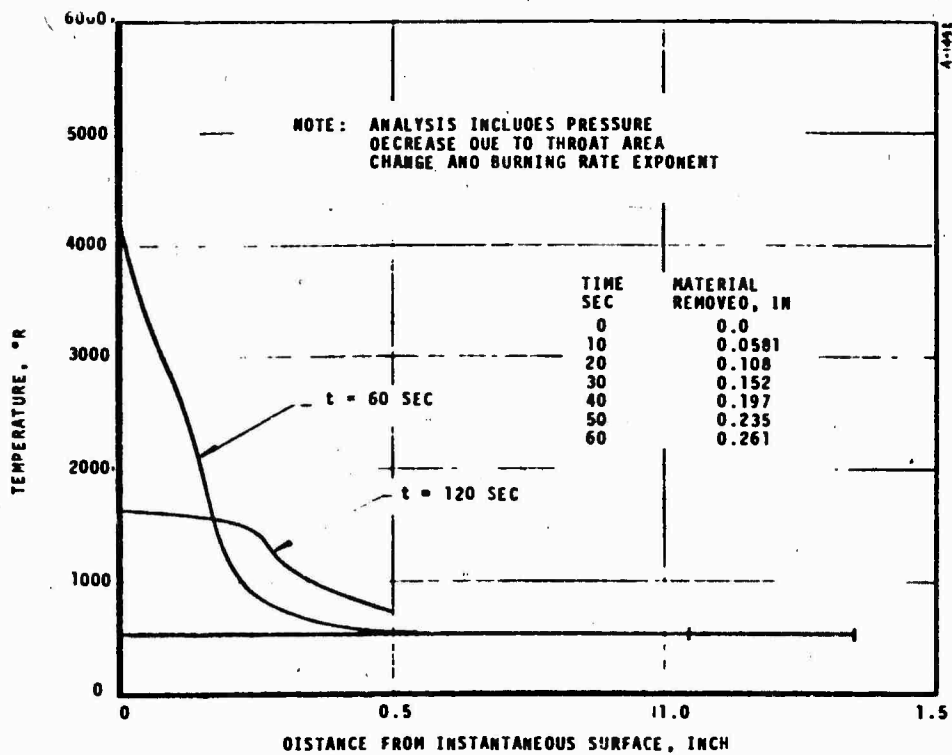


FIGURE 4-2 TEMPERATURE PROFILES AT INITIAL AREA RATIO  
OF 4.0 MX-2600-96

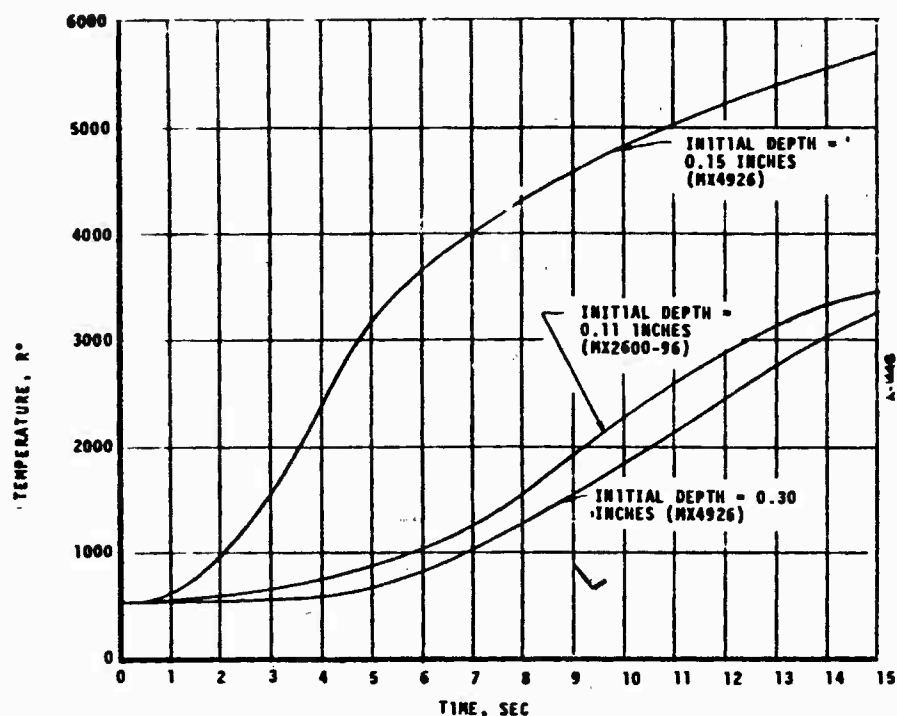


FIGURE 4-3 IN-DEPTH TRANSIENT TEMPERATURE RESPONSE

five thermocouples and since it is desired to have at least three thermocouples recording at all times during the motor firing, the depth of the thermocouple nearest the surface was taken to be approximately the same as the surface recession after 20 seconds of motor firing. Therefore, in the error analysis presented here, the disturbance to the temperature field caused by the presence of the thermocouple is evaluated for the thermocouple nearest the surface being at a depth of 0.15 inches for the MX 4926 material and 0.11 for the MX 2600-96 material. The unperturbed transient temperature at these locations plus at a depth of 0.30 inches for the MX 4926 are shown in Figure 4-3. These temperatures provide the baseline for defining differences between the unperturbed and perturbed temperatures; thus, the errors presented are based on the percent change in the variable of interest between the value calculated from the unperturbed temperature and the value calculated from the perturbed temperature.

Since the presence of the thermocouple perturbs the temperature field as a result of two-dimensional heat conduction effects, a transient two-dimensional heat conduction analysis was performed. The computerized analysis procedure employed for this analysis was the Axi-Symmetric Transient Heating and Material Ablation (ASTHMA) computer program (Reference 4-8). Since the ASTHMA program does not allow for in-depth charring, a set of constant density thermal properties was generated based on the relationship between the CMA and ASTHMA nodal energy balances and on the results from the CMA analysis. These effective thermal properties

are shown in Figures 4-4 and 4-5. Using these thermal properties, the impressed temperature and surface recession defined by the CMA analysis, and assuming no radiative heat transfer across the cavity, ASTHMA was run for the nodal geometries shown in Figures 4-6 and 4-7. The void, designated as the null node (or nodes), simulates one half of the thermocouple hole cavity as the heat conduction is symmetrical about a line which is both perpendicular to the surface and passes through the center of the cylindrical cavity. The y-dimension of the nodal network was made large enough so that any disturbance caused by the null node (or nodes) would not influence the temperature distribution at the left hand face ( $y=L$ ). The disturbance caused by the void is then the difference between the temperature distribution at  $y = 0$  and at  $y = L$ . These distributions are shown in Figures 4-8 and 4-9 for the MX 4926 and MX 2600-96 plugs, respectively. The errors (designated by the solid lines) are plotted as a function of time in Figure 4-10. As noted from this figure, the maximum  $\Delta T$  for the MX 4926 is approximately  $50^{\circ}\text{R}$  which is less than 1% of the local temperature. The maximum error for MX 2600-96 is approximately  $+200^{\circ}\text{R}$  or 8% of the local temperature. The abrupt reversal in the sign of the temperature difference occurs in the temperature range in which the thermal conductivity goes through an abrupt increase (see Figure 4-5). Due to the large error which occurred in the MX 2600-96 material, another look was taken at both the analysis procedure and the results. This reinvestigation showed that, particularly for the MX 2600-96 material, radiative heat transfer across the void was significant. The ASTHMA analysis for the MX 2600-96 material was modified to approximately account for this radiative heat transfer. The error,  $\Delta T$ , resulting from this analysis is also shown in Figure 4-10, and it is significantly less than the one obtained when radiative heat transfer across the void was considered negligible. The maximum error is  $+25^{\circ}\text{R}$  which results in an accuracy of 2.5 percent for local material temperatures of approximately  $1000^{\circ}\text{R}$  and less than -1 percent for local material temperatures above  $2500^{\circ}\text{R}$ .

The only remaining temperature distortion caused by the plug is due to the bondline between the plug and the remainder of the material. To accurately assess the magnitude of this distortion, one would require an exact measurement of the bondline thickness, the charring characteristics of the bonding agent, and a detailed stress analysis which accurately depicts the deformations resulting from pressure and thermal stresses. Since this degree of sophistication is not warranted, an analysis was performed which would yield the maximum possible distortion. This was done by comparing, at the nozzle throat, the temperature profile resulting from an axisymmetric solution to the temperature profile resulting from a flat plate solution. For the flat plate solution to be valid, an infinite thermal contact resistance would have to exist at the thermal bondline. The results of the analysis are shown in Figure 4-11 which shows that the maximum distortion occurs in the temperature range

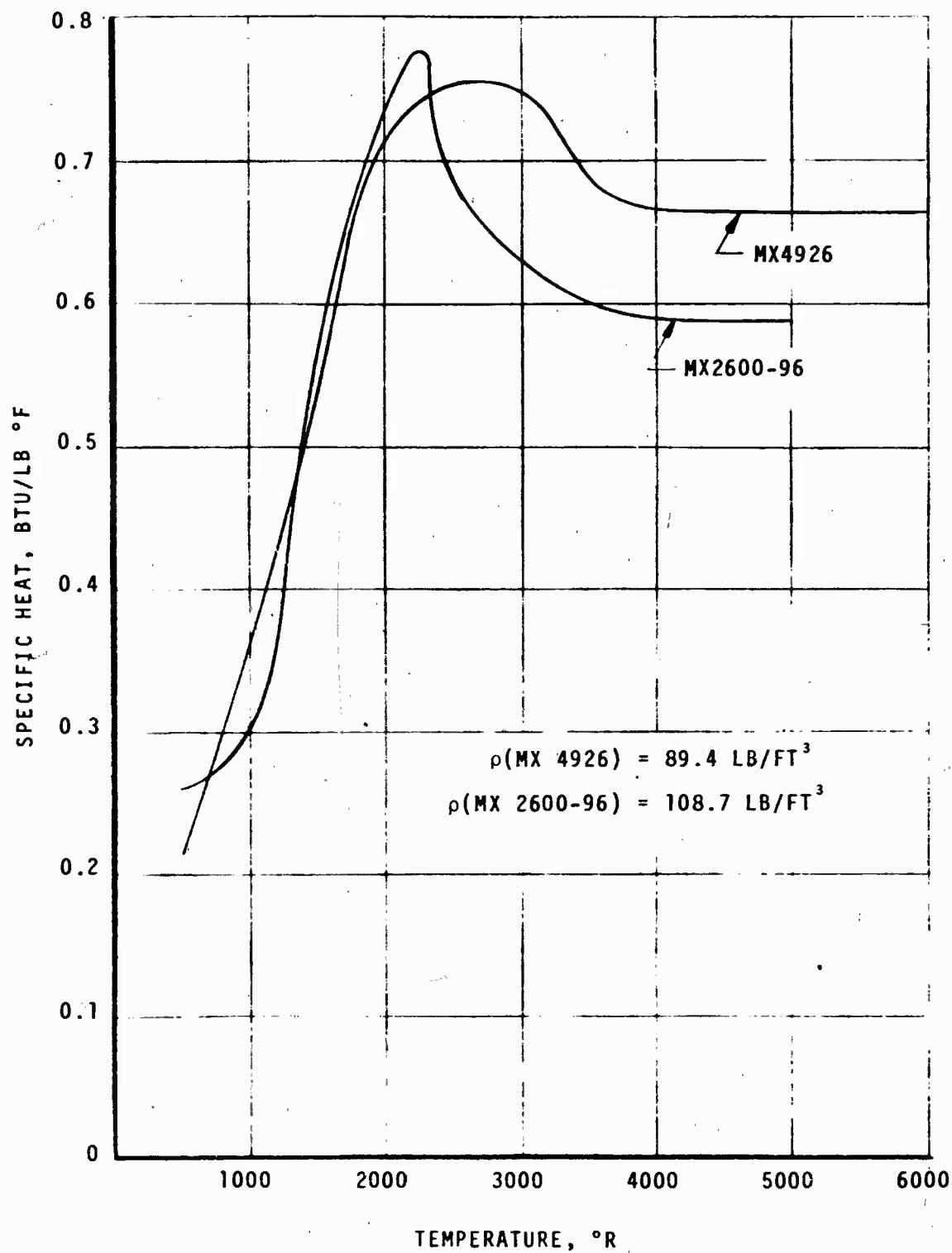


FIGURE 4-4 CONSTANT DENSITY SPECIFIC HEAT WHICH ACCOUNTS FOR IN DEPTH CHARRING

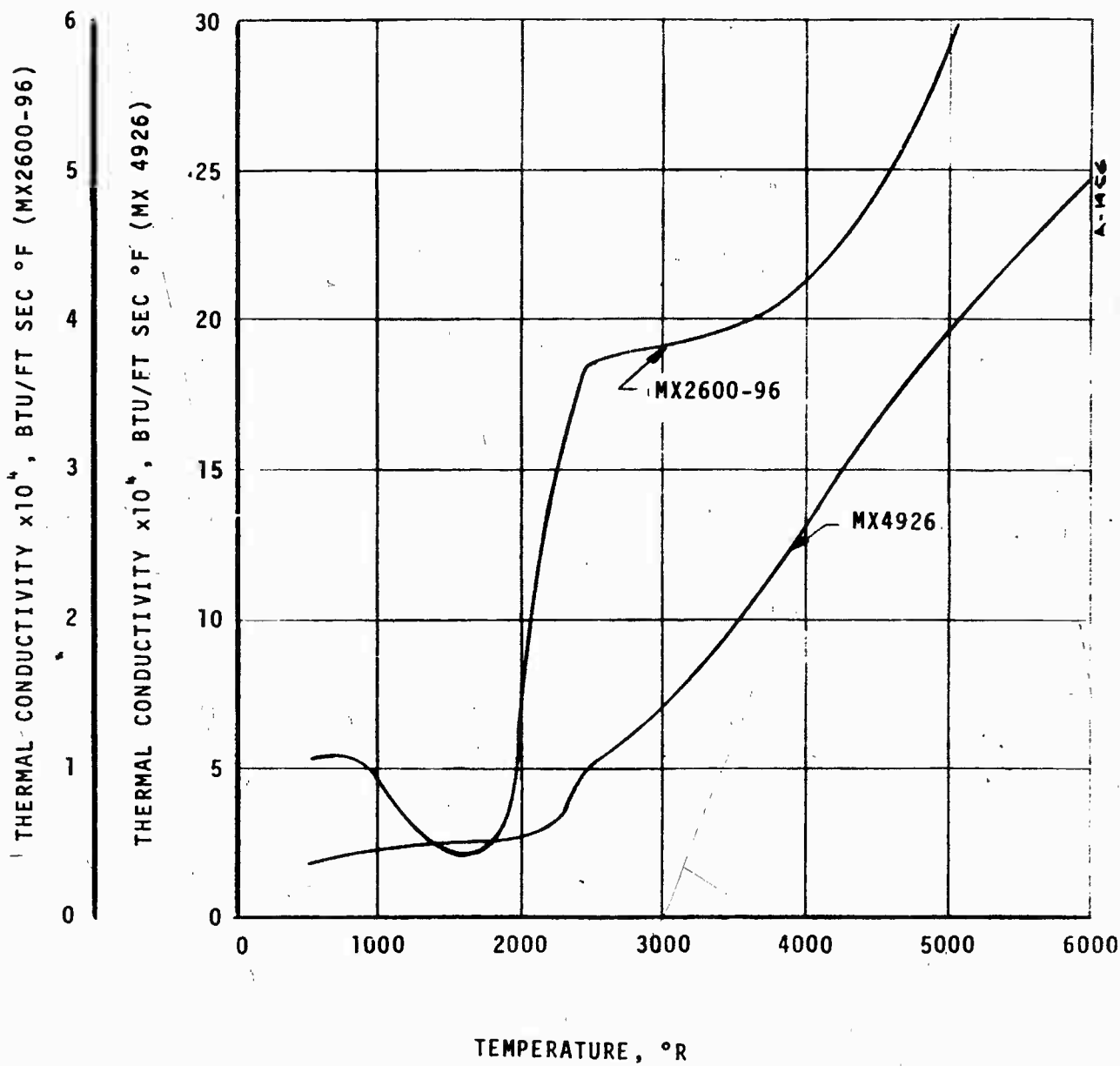
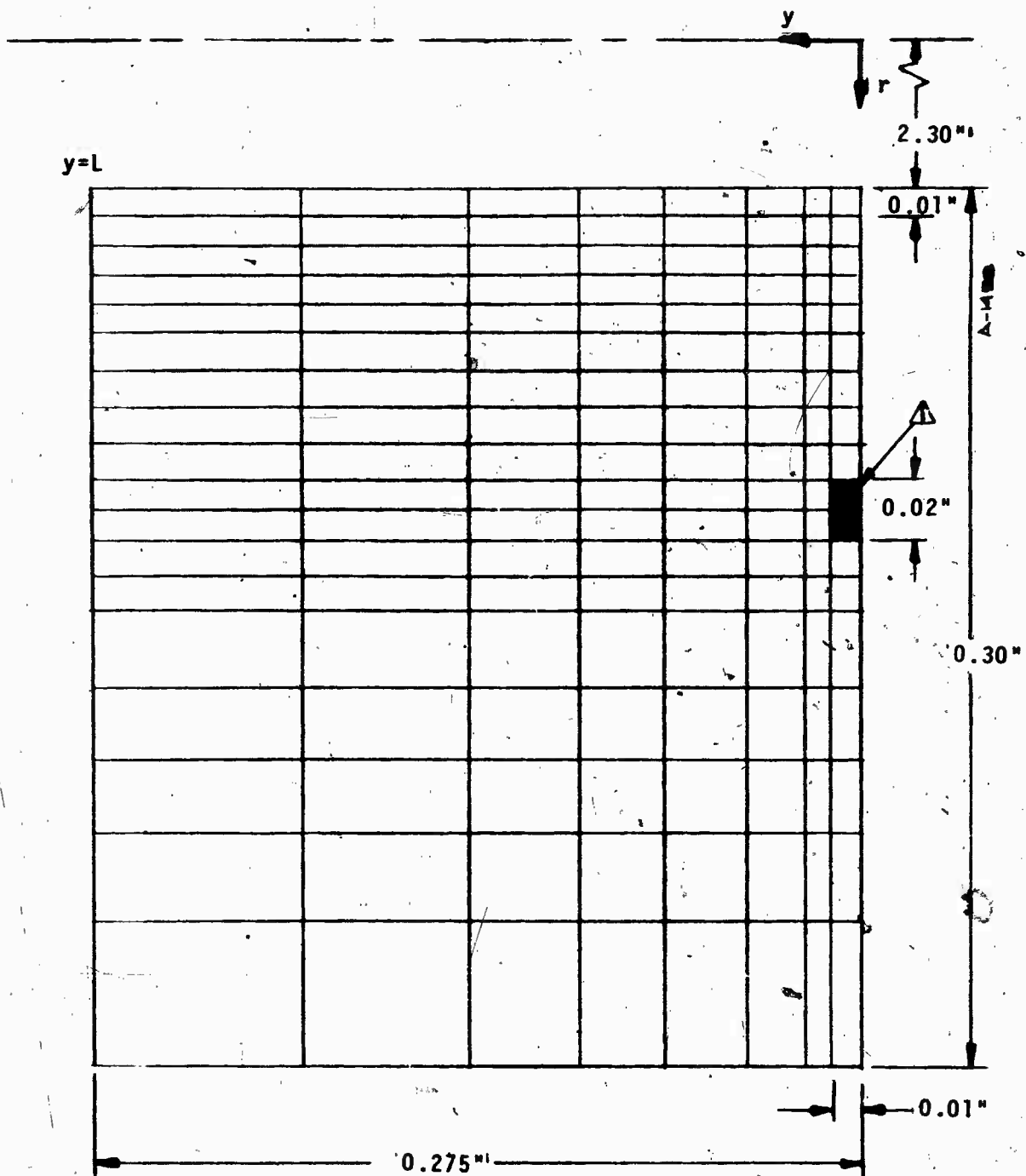


FIGURE 4-5 CONSTANT DENSITY THERMAL CONDUCTIVITY WHICH ACCOUNTS FOR IN-DEPTH CHARRING







△ VOID SIMULATED BY TWO NULL NODES.

FIGURE 4-7 NODAL GEOMETRY FOR  
MX2600-96 ASTHMA ANALYSIS

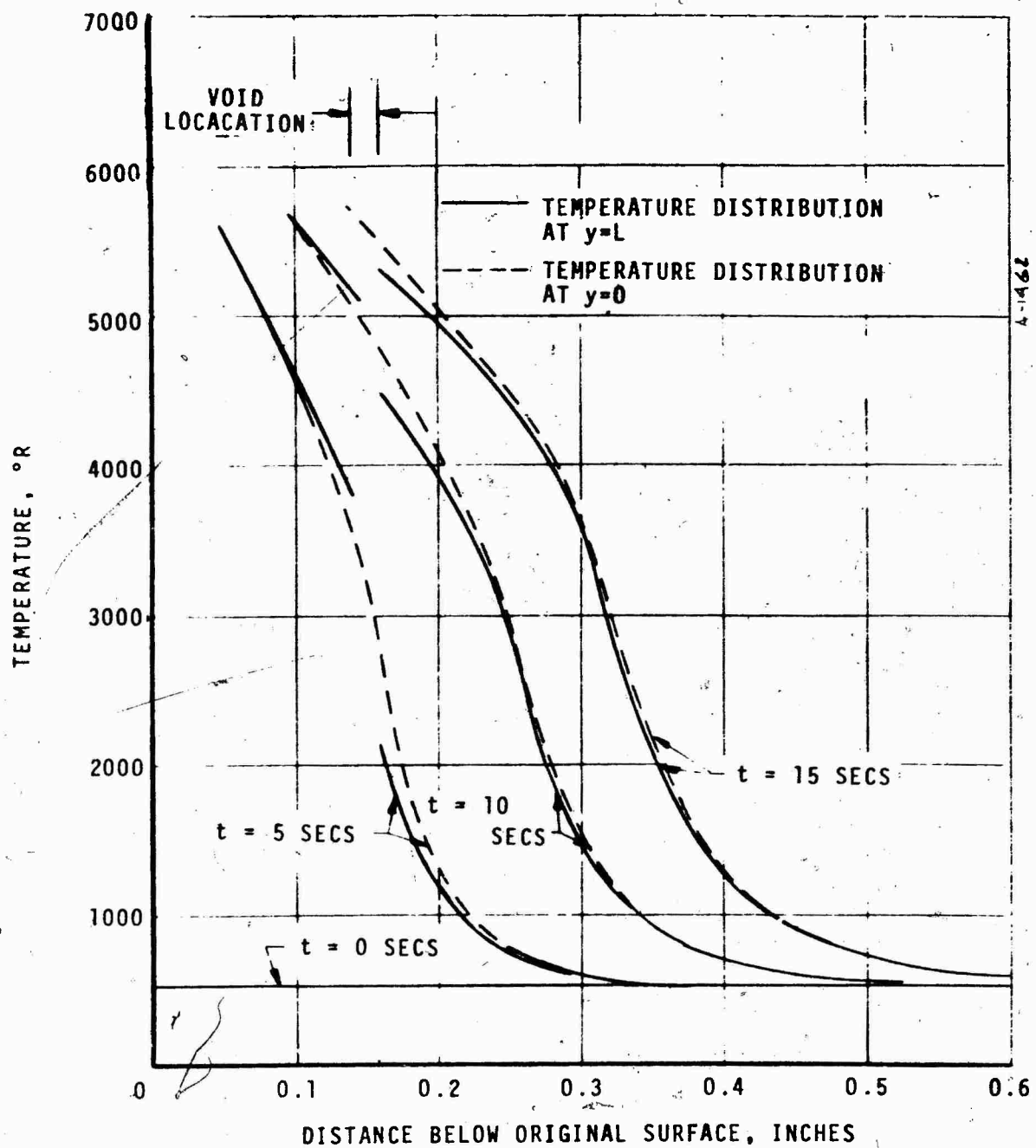


FIGURE 4-8 COMPARISON OF PERTURBED AND UNPERTURBED TEMPERATURE DISTRIBUTIONS FOR MX4926

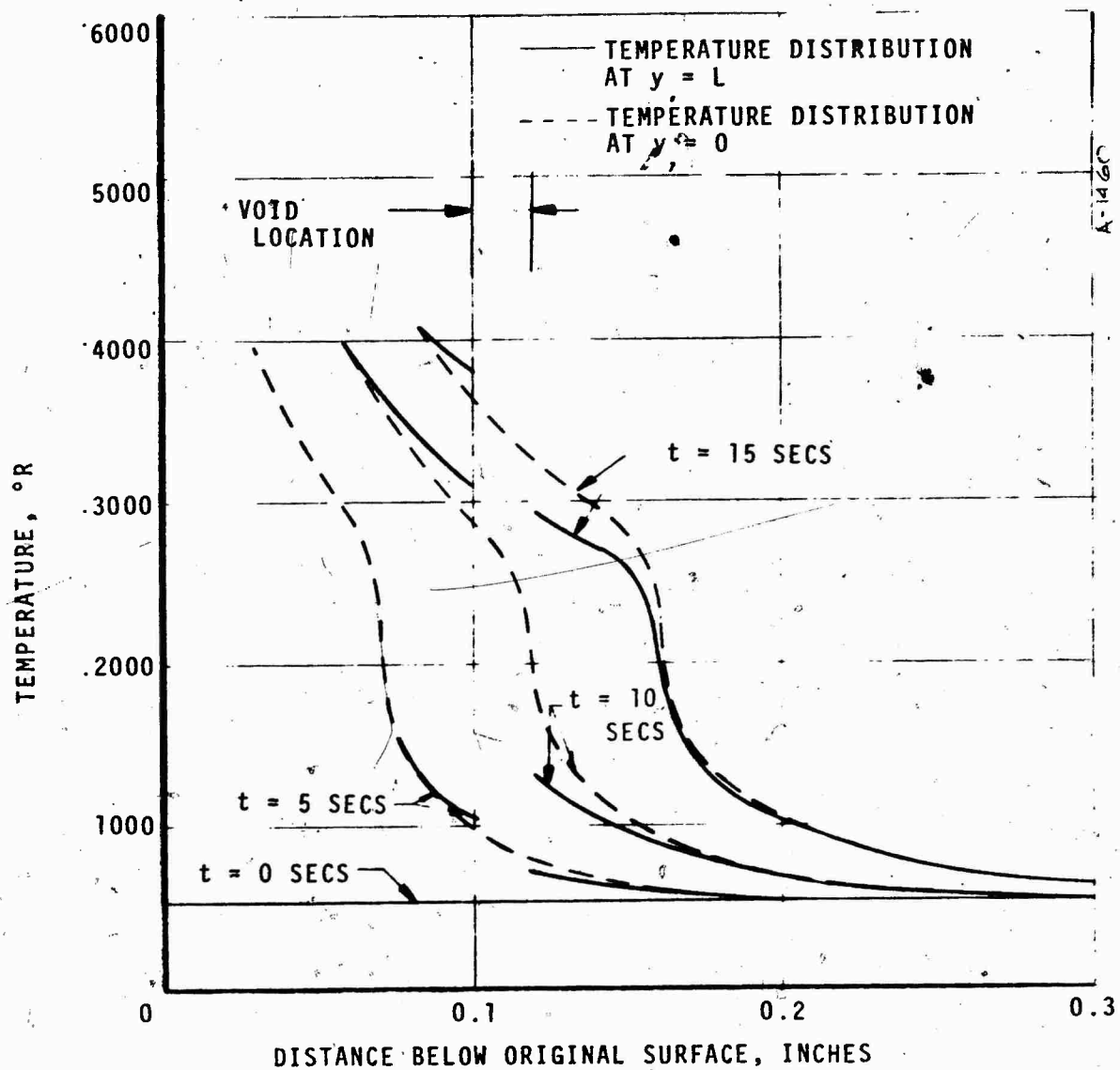


FIGURE 4-9 COMPARISON OF PERTURBED AND UNPERTURBED TEMPERATURE DISTRIBUTIONS FOR MX2600-96

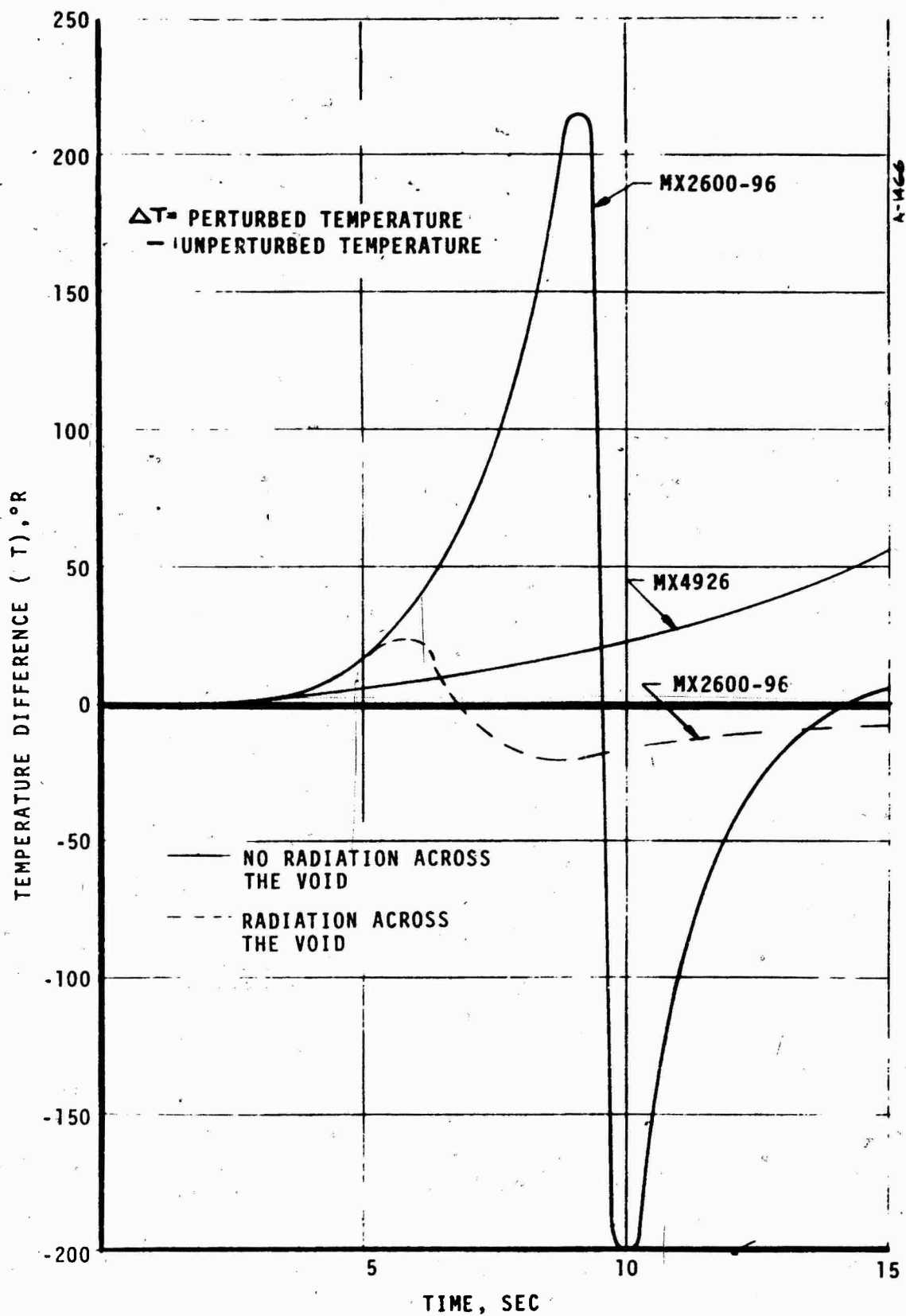


FIGURE 4-10 TEMPERATURE DISTORTION AROUND THERMOCOUPLE CAVITY

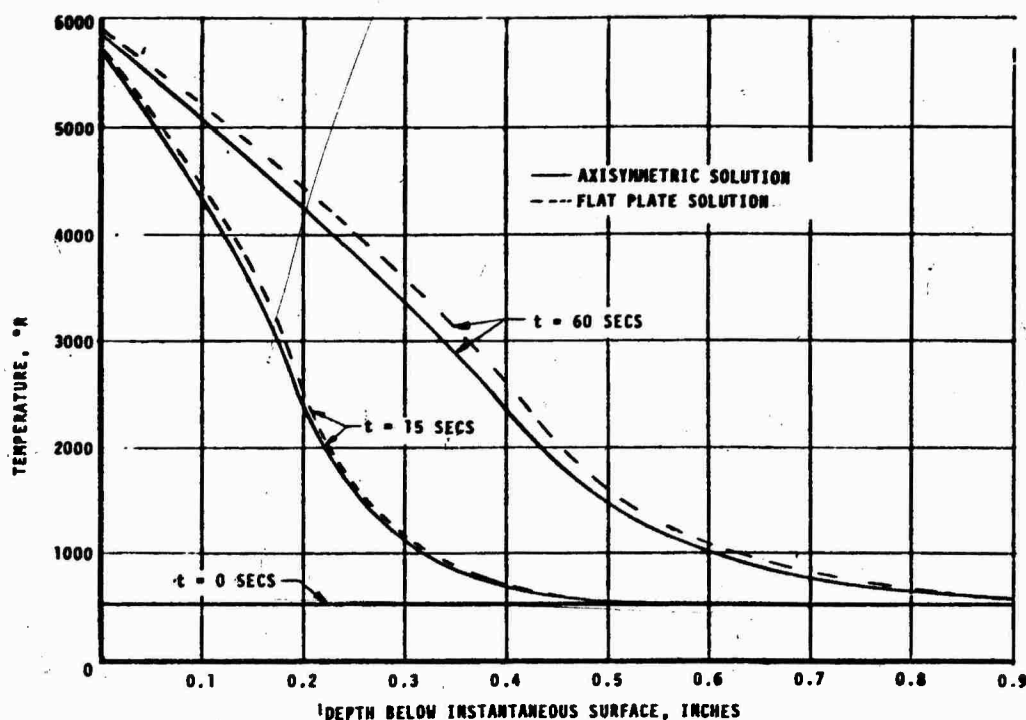


FIGURE 4-11 COMPARISON OF AXISYMMETRIC AND FLAT PLATE CMA SOLUTIONS AT THE NOZZLE THROAT FOR MX4926

from 1000°R to 2000°R at the later firing times. Since an infinite resistance is certainly not realistic and since the thermal conductivity of the phenolic resin and the bonding agent are similar, the temperature distortion would be expected to be less than 1%.

**4.1.1.1.2 Response Lag.** The configuration for the thermocouple wire and junction in the plug assembly is shown in Figure 4-12. The thermal response of the thermocouple junction is governed by the net radiative heat transfer to the wire and by the conductive heat transfer from the material to the junction at the point of contact. The maximum thermal lag of the thermocouple would occur when there is no contact between the junction and the ablative material. This is not the desired configuration but is investigated here to determine whether or not it is tolerable.

The net radiative transfer to the thermocouple wire can be obtained assuming two concentric cylinders and is given by

$$q = \frac{\sigma A_1 (T_2^4 - T_1^4)}{1/\epsilon_1 + A_1/A_2 (1/\epsilon_2 - 1)} \quad (4-3)$$

where

$\sigma$  - Stefan-Boltzmann constant  
 $A$  - cylindrical surface area

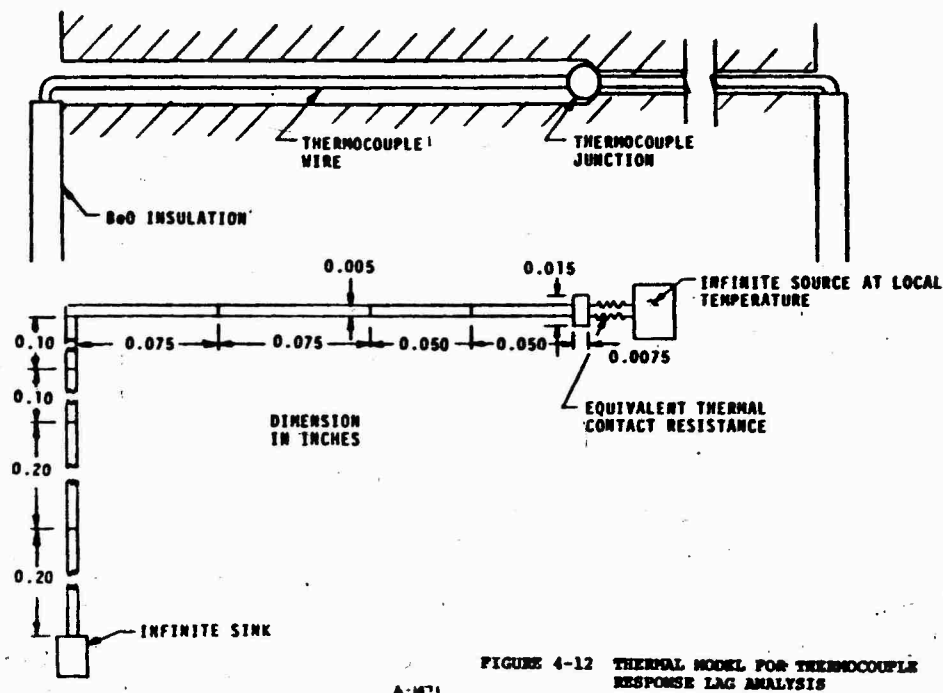


FIGURE 4-12 THERMAL MODEL FOR THERMOCOUPLE RESPONSE LAG ANALYSIS

$\epsilon$  - emissivity

$T$  - temperature

$q$  - net radiative heat flux

and subscripts 1 and 2 correspond to the inner and outer cylinder, respectively. Equation (4-3) can be put in the form

$$q = \sigma A_1 \epsilon_{\text{eff}} (T_1^4 - T_2^4) \quad (4-4a)$$

where

$$\epsilon_{\text{eff}} = \frac{1}{1/\epsilon_1 + A_1/A_2(1/\epsilon_2 - 1)} \quad (4-4b)$$

Employing the assumption that the thermal content of the ablative material adjacent to the thermocouple junction is large compared to the heat flux to the junction, the thermal model for determining the lag of the thermocouple can be put in the form shown in Figure 4-12. The above assumption permits the driving potential for the heat transfer by conduction from the ablation material to the thermocouple junction to be an infinite source at the local material temperature. This temperature is taken to be the unperturbed material temperature as given in Figure 4-1. Also shown in the thermal model is an infinite sink which is held at the initial temperature (approximately room temperature). The effect of this sink is to maximize the conduction losses. The radiative flux is applied along the horizontal portion of the thermocouple wire. Using the thermal

model of Figure 4-12, two solutions were obtained for the thermocouple nearest the surface; namely 1) infinite thermal contact resistance with radiation to the thermocouple wire and 2) both radiative and conductive heating of the thermocouple wire assuming zero contact resistance. The thermal properties used in the analysis are listed in Table 4-1 and the source temperatures at the two different locations are from Figure 4-3. The results of this analysis are given in Figure 4-13. For the case of both conductive and radiative heating, the thermal contact surface area was taken as 17 percent of the surface area of the bead. From the results of Figure 4-13, one concludes that 1) at temperatures below  $3000^{\circ}\text{R}$ , contact must be maintained between the material and the thermocouple junction, and 2) the thermal conduction error, which is less than 2.5 percent at temperatures above  $3000^{\circ}\text{R}$ , is acceptable.

TABLE 4-1

THERMAL PROPERTIES OF TUNGSTEN

Density lb/ft <sup>3</sup>	1185.0
Specific Heat, Btu/lb <sup>o</sup> F	
@ $527^{\circ}\text{R}$	0.33
@ $2290^{\circ}\text{R}$	0.41
@ $4100^{\circ}\text{R}$	0.47
Thermal Conductivity, Btu/hr ft <sup>o</sup> F	
@ $527^{\circ}\text{R}$	96.5
@ $1390^{\circ}\text{R}$	70.0
@ $2290^{\circ}\text{R}$	65.4
@ $4100^{\circ}\text{R}$	60.4

4.1.1.2 Accuracy of Thermocouple Output

The first problem of the measurement system concept was the distortion of the temperature field which was discussed in the previous section (Section 4.1.1.1). The second problem is accurately defining the temperature of the thermocouple junction from the emf output. Factors which could cause errors in the emf measurement are electrical shorting and thermocouple (including lead wire) calibration. The first item is associated with shunting across two points at different electrical potential resulting in secondary electrical circuits within the primary thermocouple electrical circuit. The second item is associated with the guaranteed accuracy of the thermocouple and lead wires and with the tungsten-carbon reaction at high temperatures which can cause a shift in the emf-temperature characteristics of the thermocouple junction for certain environmental conditions. These potential sources of error are considered in the following subsections.

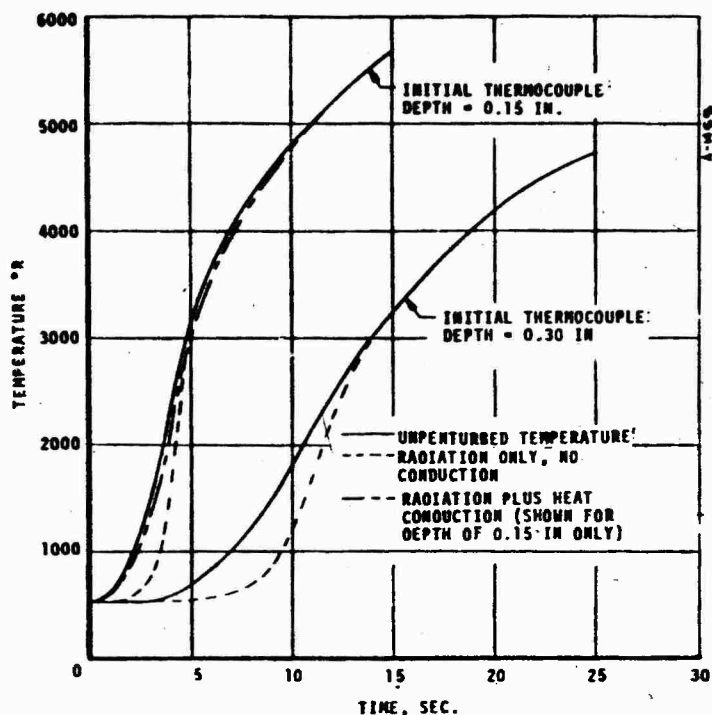


FIGURE 4-13 THERMOCOUPLE LAG  
FOR MX 4926

4.1.1.2.1 Electrical Shorting. The voltage measured in a thermocouple circuit is due to the Seebeck emf which is a combination of the Peltier and Thomson emf's. The Peltier emf is generated at the thermocouple junction and the Thomson emf can be visualized as being generated in the thermal gradient region (References 4-9 and 4-10) of each of the homogeneous wires making up the thermocouple circuit. These thermoelectric emf's are evaluated by using the thermocouple equations in the form (Reference 4-11)

$$\pi_{A,B} = T \frac{dE_{A,B}}{dT} \quad (4-5a)$$

$$\sigma_A - \sigma_B = -T \frac{d^2 E_{A,B}}{dT^2} \quad (4-5b)$$

$$E_{A,B} = \pi_{A,B}(T) - \pi_{A,B}(T_0) + T_0 \int_{T_0}^T (\sigma_A - \sigma_B) dT \quad (4-5c)$$

where

$E_{A,B}$  - Seebeck voltage for metals A and B  
for a temperature difference of  $T - T_0$

$T$  - temperature

$S_A^*, S_B^*$  - entropy transport coefficient for metals  
A and B respectively



$\pi_{A,B}$  - Peltier coefficient for the combination of metals A and B

$\sigma_A, \sigma_B$  - Thomson coefficients for metals A and B respectively

If the relationship between  $E_{A,B}$  and  $T$  is known, then the magnitude of the Peltier and Thomson emf's can be determined. For W5Re/W26Re, this relationship is (Reference 4-12).

$$E = 0.293341 + 9.01521 \times 10^{-3} T + 2.70124 \times 10^{-5} T^2 - 3.15783 \times 10^{-8} T^3 + 1.78838 \times 10^{-11} T^4 - 5.04944 \times 10^{-15} T^5 + 5.52473 \times 10^{-19} T^6 \quad (4-6)$$

The emf's resulting from this equation are shown in Figure 4-14.

An electrical circuit for one W5Re/W26Re thermocouple in the plug assembly is shown in Figure 4-15. The W5Re/W26Re was chosen for analysis because it would be exposed to the most severe temperature and temperature gradient. The Peltier and Thomson emf's are distributed at various distinct locations with only the Peltier emf in series with each shunt resistance as the shunt leg is assumed to be along an isothermal plane. The number of locations is determined by the accuracy desired in the analysis. It is obvious from the circuit that to obtain an accurate measurement of the thermocouple junction emf, shunting across the two legs of the thermocouple wire must be negligible. This means that the electrical resistance in each of the shunt legs must be large compared to the electrical resistance in the remainder of the electrical circuit. The electrical resistance in the shunt leg is made large by encapsulating the lead wire in beryllia (BeO) or alumina (Al<sub>2</sub>O<sub>3</sub>) insulation. Beryllia insulation was chosen because of

- its higher melt temperature than alumina (4600°F compared to 3700°F)
- its compatibility with tungsten rhenium wire at high temperature as compared to thoria, for example, which affects the calibration curve of tungsten-rhenium thermocouples.

With the electrical insulator chosen, all the materials used in the thermocouple electrical circuit have been defined. Before proceeding with the analysis, however, the circuit was simplified by

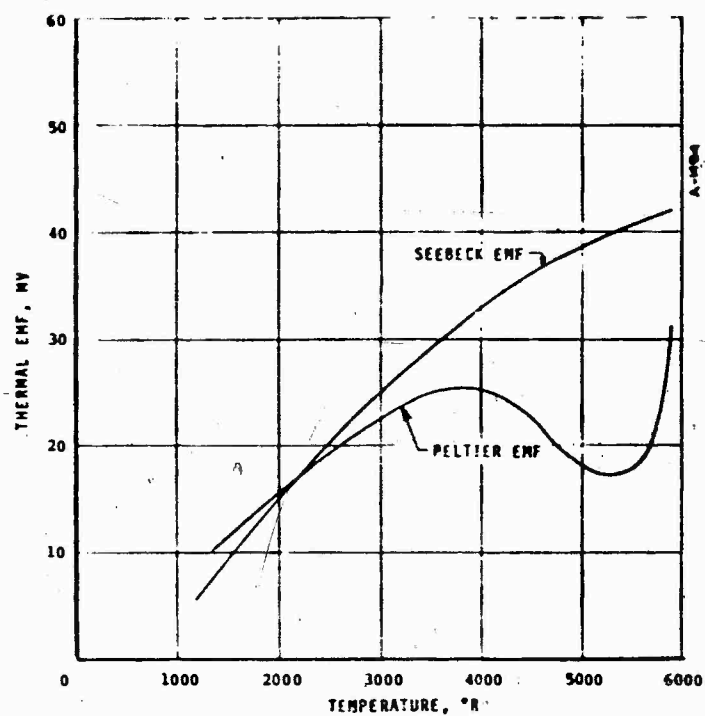


FIGURE 4-14 COMPARISON OF SEEBECK AND PELTIER EMF'S FOR W5Re/W26Re

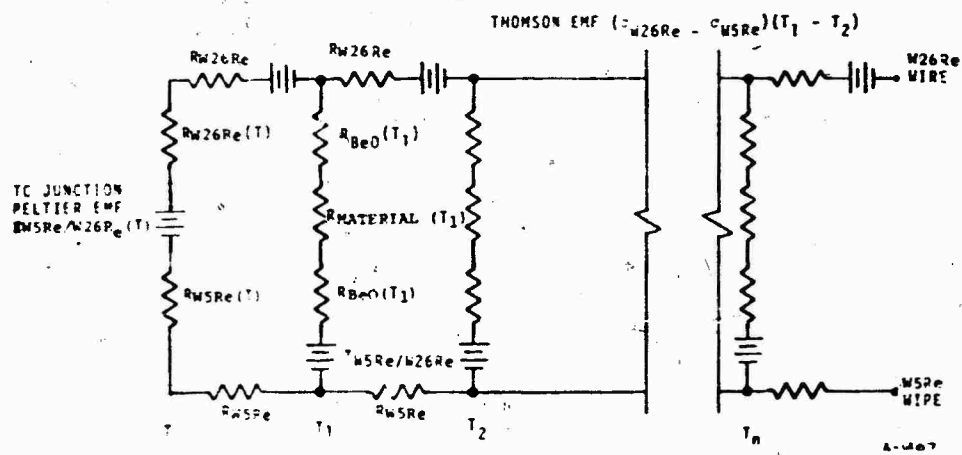


FIGURE 4-15 ELECTRICAL CIRCUIT FOR W5Re/W26Re THERMOPILE

combining the Peltier and Thomson emf's into a distributed Seebeck emf as shown in Figure 4-16. This simplification is conservative in that it will slightly magnify the shunt effect due to the Seebeck emf being larger than the Peltier emf. A representative temperature distribution which was used in the analysis is also shown in this figure.

The equations describing the electrical circuit shown in Figure 4-16 were solved, and this solution is described in considerable detail in Reference 4-11. In summary, it showed that due to the  $R_n^*$  resistances being a factor of  $10^4$  to  $10^5$  larger than the other resistances, the shunting effect is negligible and the measured emf will indeed be the emf generated at the thermocouple junction. At temperatures above the melt temperature of beryllia (greater than  $5000^\circ\text{F}$ ) the shunt resistance would still be expected to be adequate (Reference 4-12) provided the liquid beryllia remains around the thermocouple wire.

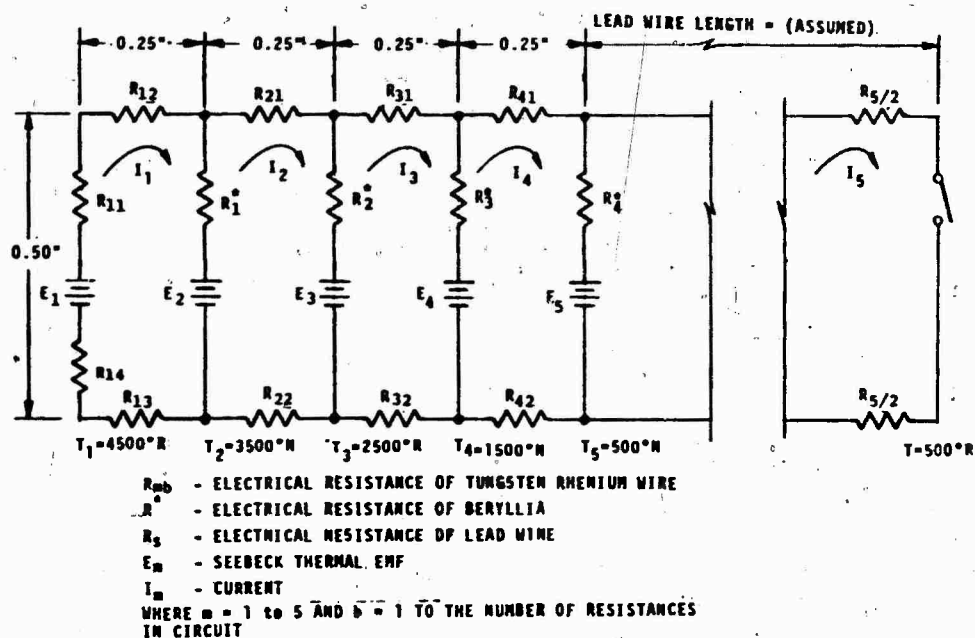


FIGURE 4-16 SIMPLIFIED THERMOCOUPLE ELECTRICAL CIRCUIT

A-1448

**4.1.1.2.2 Thermocouple Calibration.** The remaining inaccuracies in the thermocouple circuit analysis are the possible variation in the emf-temperature relationship due to the tungsten-carbon reaction at high temperatures and the guaranteed calibration accuracy of the thermocouple and lead wire as supplied by the manufacturer.

A literature survey was performed to define whether or not the tungsten-carbon reaction for short durations at high temperature would affect the calibration of the thermocouple. Spooner and Hall (Reference 4-13) performed stability tests for W/W26Re thermocouples in a carbon vapor atmosphere for durations up to 30 hours and found a maximum calibration change of approximately  $+30^{\circ}\text{C}$ . These reported data are for a different environment than the one expected to be encountered in the thermocouple plug assembly, carbon vapor at  $2100^{\circ}\text{C}$  to  $2500^{\circ}\text{C}$  for 30 hours compared to direct carbon contact at temperatures from  $530^{\circ}\text{F}$  to  $5500^{\circ}\text{F}$  within 60 seconds. Further investigation, Reference 4-14, resulted in the data shown in Figure 4-17. These data are for a W/W26Re thermocouple, 0.020" wire diameter, in direct contact with a carbon heater at  $3182^{\circ}\text{F}$ . The deviation is the difference between the readings from a thermocouple and an optical pyrometer.

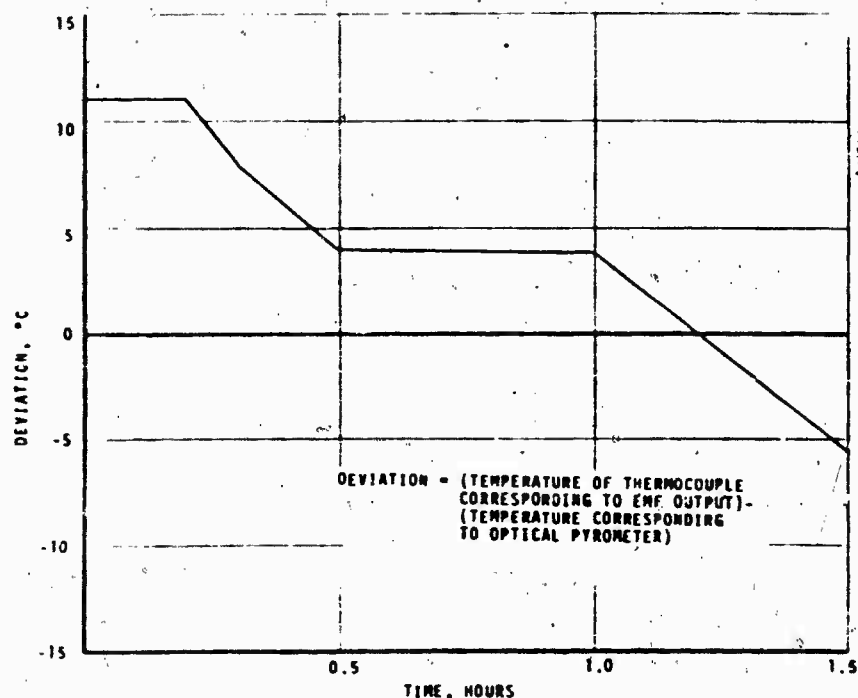


FIGURE 4-17 DEVIATION OF W/W26Re THERMOCOUPLE IN DIRECT CONTACT WITH CARBON HEATER AT  $3182^{\circ}\text{F}$

If the differences in the deviations are attributed to the tungsten-carbon reaction, then the maximum error is  $0^{\circ}\text{C}$  for an exposure of 0.2 hours,  $3^{\circ}\text{C}$  for 0.3 hours, and  $7^{\circ}\text{C}$  for 0.5 hours. Since the deviation is a function of the amount of material affected, the volume of the thermocouple junction would be expected to influence the deviation, the smaller the volume, the larger the deviation. Assuming the difference in deviation is inversely proportional to the diameter squared of the thermocouple wire, then this difference is only  $48^{\circ}\text{C}$  after 0.3 hours (18 minutes). Based on these data, the effect of the tungsten-carbon reaction is negligible for temperatures up to  $3182^{\circ}\text{F}$  ( $3642^{\circ}\text{R}$ ). From Reference 4-15, these data are felt to be representative for temperatures up to  $2500^{\circ}\text{C}$  ( $5000^{\circ}\text{R}$ ), at which temperature carbon and tungsten form a eutectic. However, due to the short exposure times at temperatures above  $5000^{\circ}\text{R}$ , less than 10 seconds; the effect of the carbon-tungsten reaction is expected to be negligible even at these very high temperatures. The guaranteed accuracy (Reference 4-16) of the tungsten rhenium wire and the lead wires are  $\pm 1\%$  and  $\pm 0.5\%$  respectively. Since these are random errors, they can be combined (by root mean square) to give an accuracy of  $\pm 1.23\%$ .

#### 4.1.1.3 Accuracy of Thermocouple Location

The location of the thermocouple bead within the heat flux sensor is an important parameter which must be accurately defined to obtain useful thermal response data. For the plugs fabricated in this program, the position of the thermocouples relative to the pre-installation surface were found by measurement of x-ray photographs. As described in Section 4.1.2.3, the plugs were installed in the nozzle with some excess plug material protruding above the flame surface. This protuberance was machined flush with the surrounding area. The amount machined was measured and subtracted from the x-ray measurements to obtain the pre-fire thermocouple depths below the flame surface. The accuracy analysis presented here considers both the accuracy of the x-ray measurement techniques and the accuracy of measuring the amount removed during the final machining procedure. X-ray measurement uncertainties are discussed first, followed by a brief discussion of the final machining uncertainty. Finally, these uncertainties are combined and then converted to an uncertainty in the measured temperature.

A schematic representation of the heat flux sensor positioned for X-ray exposure is given in Figure 4-18. The top surface of the sensor is defined on the X-ray negative by butting the sensor against a steel slug. The position of each bead in the material relative to the defined surface can therefore be determined. A slight correction for parallax from the plane of the thermocouples to the film plane must be made because the incident X-ray beams are not parallel. For the case where the sensor is placed exactly as shown in Figure 4-18, the thermocouple depths are evaluated as follows:

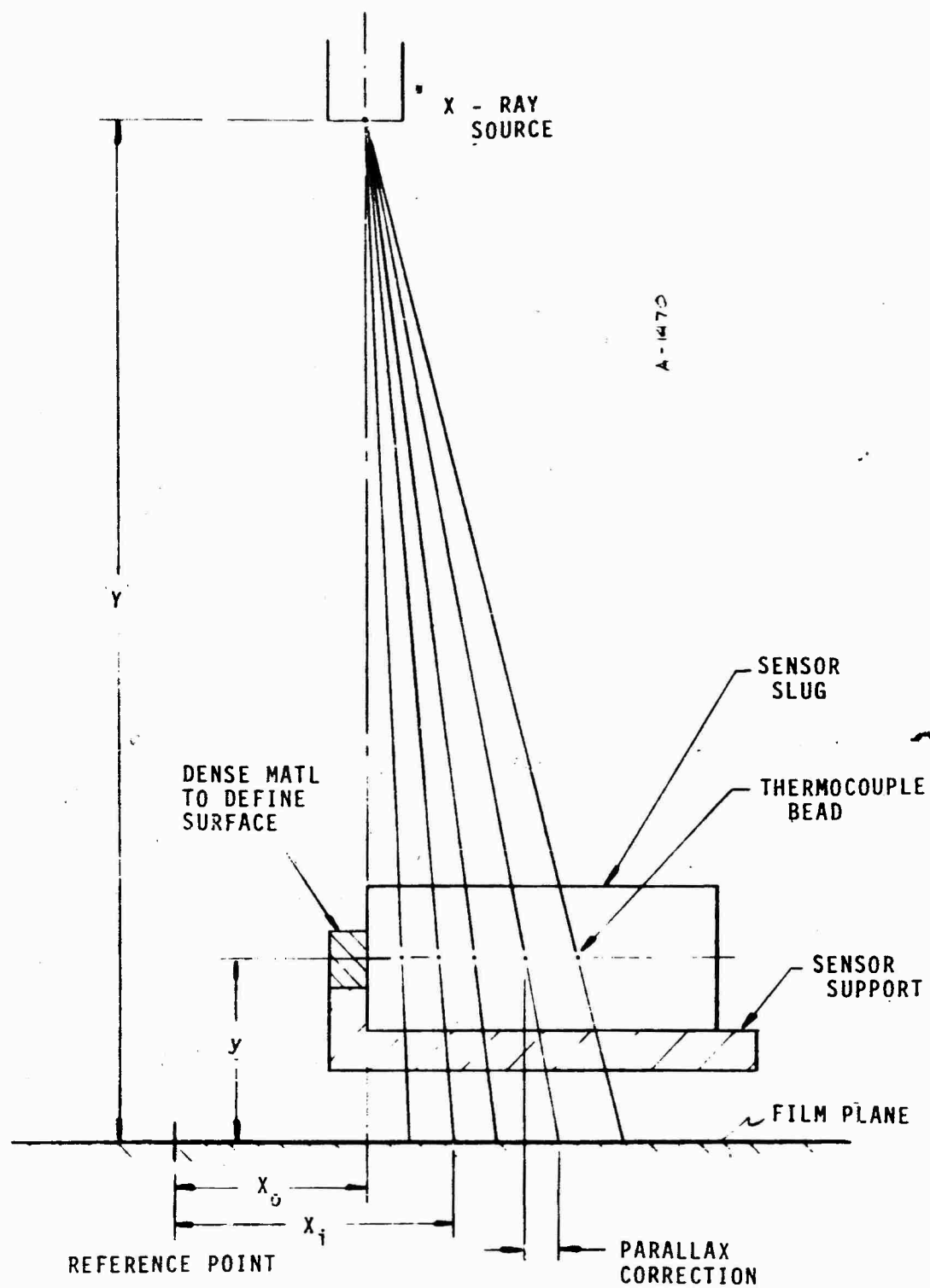


FIGURE 4-18 TOTAL HEAT FLUX SENSOR CORRECTLY POSITIONED IN X-RAY BEAM

$$\delta_{TC} = (x_i - x_o) \left(1 - \frac{Y}{Y}\right) \quad (4-7)$$

In order to evaluate the uncertainty in the calculated thermocouple depths, the method of Reference 4-17 was utilized in this analysis. Briefly, the method considers the mathematical propagation of uncertainties in primary quantities into the uncertainty in the calculated result (the primary quantities being those variables which must be directly or indirectly measured). Two sources of error exist in the X-ray technique:

- uncertainties in the measurements of the bead locations on the X-ray negative
- uncertainties in the positioning of the sensor slug in the X-ray beam

Figure 4-19 gives an exaggerated schematic of a sensor slug incorrectly placed for the X-ray photograph. The primary geometrical quantities which need to be measured to determine the thermocouple depths in such a set up are:

- distance from the X-ray source to the film plane, Y
- distance from the plane of the thermocouples to the film plane, Y
- angular relation of the thermocouple plane to the film plane,  $\phi$
- angular displacement of the sensor surface from the verticle ray,  $\theta$

The equation to evaluate the thermocouple depths from the above quantities was easily derived from geometric considerations

$$\delta_{TC} = \left(1 - \frac{Y}{Y}\right) x_i - x_o + \left[ \frac{w \cos(\phi - \theta)}{2 \left(1 - \frac{Y - w/2}{Y}\right)} \right] \quad (4-8)$$

Notice that Equation (4-7) is the same as Equation (4-8) except for the additional term containing the  $\phi$  and  $\theta$  angles. Since  $\phi$  and  $\theta$  are very close to  $90^\circ$  and  $0^\circ$ , respectively, the last term is generally very close to zero and, for the purpose of calculating  $\delta_{TC}$ , may be ignored. However, to determine the propagation of angular uncertainties to the thermocouple depth result, the term must be considered.

Based on the method of Reference 4-17 and Equation (4-8) the following equation for the uncertainty in the thermocouple position was derived

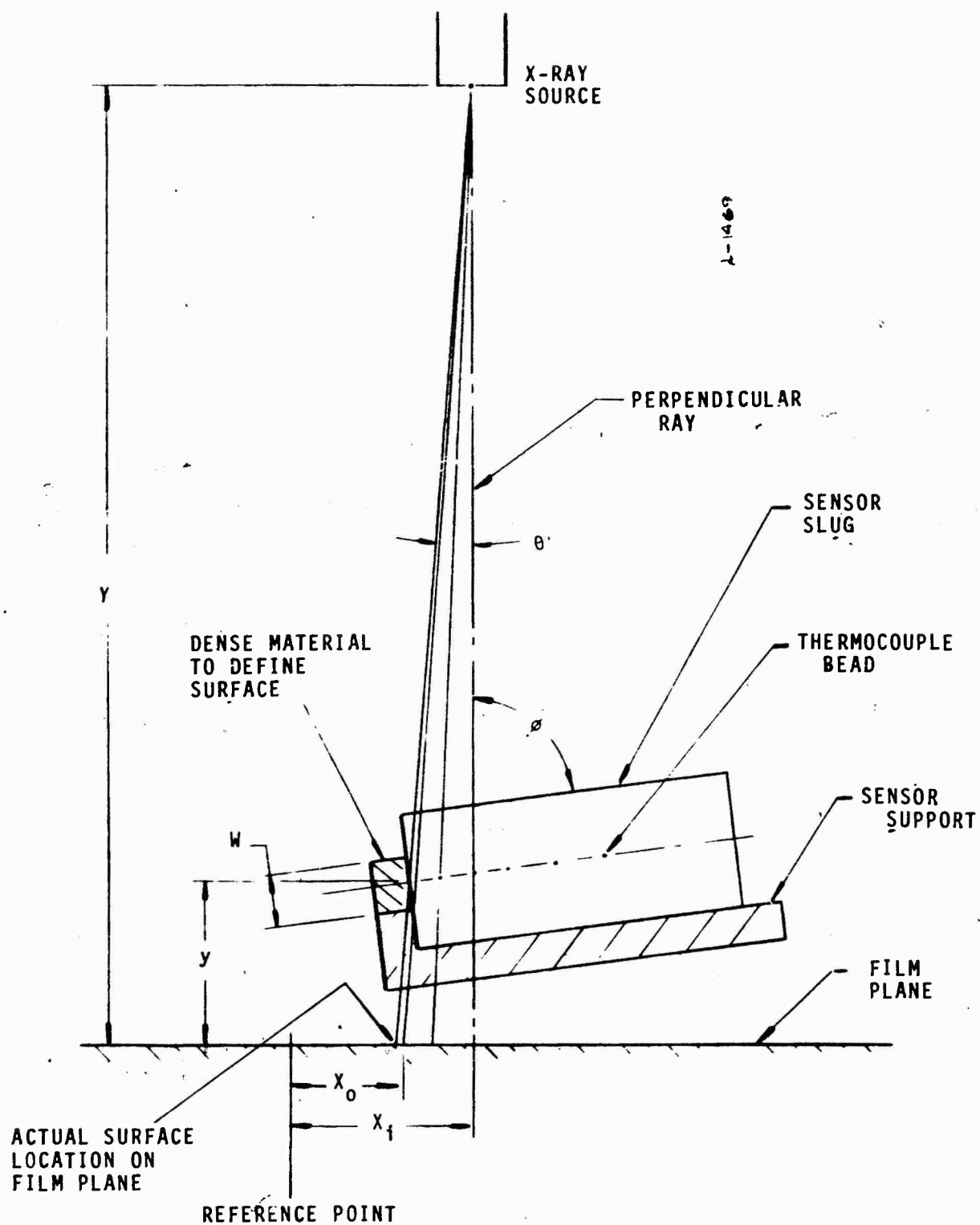


FIGURE 4-19 TOTAL HEAT FLUX SENSOR INCORRECTLY POSITIONED IN X-RAY BEAM



$$\omega_{\delta_{TC}} = \left\{ \left(1 - \frac{Y}{Y}\right)^2 \left[ (\omega_{x_i}^2 + \omega_{x_o}^2) + \left(\frac{w}{2(1 - \frac{Y - w/2}{Y})}\right)^2 (\omega_{\phi}^2 + \omega_{\theta}^2) \right] + \left[ (x_i + x_o) / Y \right]^2 \left[ \left(\frac{Y\omega_Y}{Y}\right)^2 + \omega_Y^2 \right] \right\}^{1/2} \quad (4-9)$$

where  $\omega$  is the uncertainty in the  $n^{\text{th}}$  variable and where  $\phi$  and  $\theta$  have been evaluated at  $90^\circ$  and  $0^\circ$ , respectively.

Table 4-2 presents the results of applying Equation (4-9) to thermocouples at approximately 0.1 and 0.6 inches below the surface. The parameter values and uncertainties given in the table are based on past experience with the X-ray measurement technique. Also shown in Table 4-2 for each primary quantity is the thermocouple location uncertainty which would be calculated if the uncertainties of the other primary quantities were neglected. The resultant uncertainty is the square root of the sum of the squares of the individual uncertainties. Table 4-2 shows that the location uncertainty is quite insensitive to the thermocouple depth below the pre-installation surface ( $\pm 0.0016$  to  $\pm 0.0017$  inch). The most significant sources of error are due to the X-ray negative reading uncertainty. The angular orientation uncertainties also contribute slightly to the overall location uncertainty.

After installation and final potting of the thermocouple plug within the nozzle, the amount of plug protruding from the flame surface is measured either by a vernier calipers or from dial settings during machining. Least indicator accuracy in either case is  $\pm 0.001$  inches. This random uncertainty combines as the square root of the sum of the squares with the X-ray dimensional measurement to give a cumulative location uncertainty of  $\pm 0.002$  inches.

The relation of thermocouple location uncertainty to an equivalent temperature uncertainty is defined by the slope of the temperature profile. For a typical MX 4926 carbon phenolic response such as shown in Figure 4-1, a  $\pm 0.002$  inch location uncertainty would present a  $\pm 30^\circ\text{R}$  temperature uncertainty or about  $\pm 1.2$  percent for local temperatures above  $2500^\circ\text{R}$ . For MX 2600-96, however, the slope of the temperature profile is larger so that a  $\pm 0.002$  inch uncertainty would represent an uncertainty of  $\pm 40^\circ\text{R}$  or  $\pm 1.5$  percent for local temperatures above  $2500^\circ\text{R}$ .

#### 4.1.1.4 Overall Temperature Measurement Accuracy

In Sections 4.1.1.1 through 4.1.1.3, accuracies were defined for those items which would cause the temperature obtained from the measured thermocouple emf and for the measured thermocouple

Table 4-2 SUMMARY OF THERMOCOUPLE DEPTH UNCERTAINTY ANALYSIS

	$x_o$ (in)	$x_i$ (in)	Y (in)	Y (in)	W (in)	$\phi$	$\theta$	$\delta_{TC}$ (in)	$w_{\delta TC}$
<u>Shallow</u>	Measurement	0.	0.104	104.	0.125	$\pi/2$	0.	0.1031	$\pm 0.0016$
	Uncertainty	$\pm 0.001$	$\pm 0.001$	$\pm 0.5$	$\pm 0.01$	$\pm 0.01$	$\pm 0.01$		
	Percentage Uncertainty	-	1.0%	0.5%	8.0%	0.6%	-		1.6%
	Individual Uncertainty <sub>3</sub> in $\delta_{TC}$	1.40	0.05	0.04	0	0.63	0.63		
<u>Deep</u>	Measurement	0.	0.603	104.	0.125	$\pi/2$	0.	0.5980	$\pm 0.0017$
	Uncertainty	$\pm 0.001$	$\pm 0.001$	$\pm 0.5$	$\pm 0.01$	$\pm 0.01$	$\pm 0.01$		
	Percentage Uncertainty	-	0.2%	0.5%	8.0%	0.6%	-		0.4%
	Individual Uncertainty <sub>3</sub> in $\delta_{TC}$	1.40	0.29	0.18	0.	0.63	0.63		

location to be different than the unperturbed temperature which would be obtained from an ideal precisely located thermocouple. In this section, these inaccuracies will be combined to give an overall system accuracy for the in-depth temperature measurements. Since the temperatures above 2500°R are the ones of primary significance in defining the thermal heat conduction into the ablative material, the accuracies presented are limited to this temperature range.

Table 4-3 presents the accuracies defined in Sections 4.1.1.1 through 4.1.1.3 for a local material temperature of approximately 2500°R. If the accuracies preceded by a plus or minus sign (but not both) are considered to result from fixed errors and all others to result from random errors, then the desired overall system accuracy can be obtained from

$$\delta_{\text{system}} = (\sum_i \delta_i) \text{ fixed errors} \pm \sqrt{(\sum_i \delta_i^2) \text{ random errors}} \quad (4-19)$$

Substituting the numbers listed in Table 4-3 into Equation 4-19, the overall accuracy for a local material temperature of about 2500°R is +0.2 percent and -3.2 percent for MX 4926 and -1.6 percent and -5.4 percent for MX 2600-96. For higher material temperatures, the magnitude of all the fixed errors in terms of temperature difference decrease with increasing temperature; thus the accuracies on a percentage basis will be better at the higher material temperatures. Assuming the magnitude of the fixed errors (and the percentage of the random errors) remains the same, the accuracies considering only the effect of the higher material temperature are +0.8 percent and -2.7 percent for MX 4926 and +0.3 percent and 4.1 percent for MX 2600-96, based on a material temperature of 4000°R.

TABLE 4-3  
ACCURACIES IN MEASURED TEMPERATURES  
FOR A LOCAL MATERIAL TEMPERATURE  
OF ABOUT 2500°R

Item	Section	Error (Percent)	
		MX 4926	MX 2600-96
Distortion of Temperature Field	4.1.1.1.1	+1	-1
Response Lag of Thermocouple	4.1.1.1.2	-2.5	-2.5
Guaranteed Accuracy of Thermocouple and Lead Wires	4.1.1.2.2	+1.23	+1.23
Thermocouple Depth	4.1.1.3	+1.2	+1.5
Overall	---	+0.2 -3.2	-1.6 -5.4

The accuracies stated in this section are, with the exception of the thermocouple and lead wires, based on analysis using conservative assumptions. If these assumptions are correct, which there is no reason to doubt at the present time, and if the problems considered are the only significant ones, then the above stated accuracies are realistic and attainable.

#### 4.1.2 Design and Fabrication Analysis

The design of the total heat flux measurement system combines the practical requirements of fabrication and assembly and the accuracy requirements discussed in the previous section. The design and fabrication techniques which satisfied these requirements are discussed in the following sections. Section 4.1.2.1 presents the thermocouple locations, types, and installation scheme. Section 4.1.2.2 presents the overall measurement system configuration and, Section 4.1.2.3 describes its installation. Finally, Section 4.1.2.4 discusses the recording instrumentation required for the system measurements.

##### 4.1.2.1 Thermocouples

The considerations related to the thermocouple installation were the location and number of thermocouples in the measurement system plug, the types of thermocouples required, the configuration of the hole which accepts the thermocouples, and the method of leading the thermocouple wires down the side wall of the plug. The measurement system design in these areas is presented in the following paragraphs.

4.1.2.1.1 Thermocouple Locations and Types. The definition of the location and number of thermocouples in the measurement system plugs was based on the anticipated response of the material in which it is installed. This anticipated response was calculated using the Aerotherm Chemical Equilibrium (ACE) and Charring Material Ablation (CMA) computer programs for the Phase III char motor nozzle, and was estimated based on past experience and calculations for the Phase II evaluation tests. The calculated response of the char motor nozzle at the throat (MX 4926 carbon phenolic) and at  $A/A_* = 4.0$  (MX 2600-96 silica phenolic)\* is presented in Figures 4-20 and 4-21 in terms of the in-depth temperature distributions at three times through the firing. The selected thermocouple locations, based on this anticipated response, are indicated in the figures. The five thermocouples for

---

\*The two other measurement system locations are  $A/A_* = -2.0$  (subsonic) and 2.0, both being MX 4926 carbon phenolic.

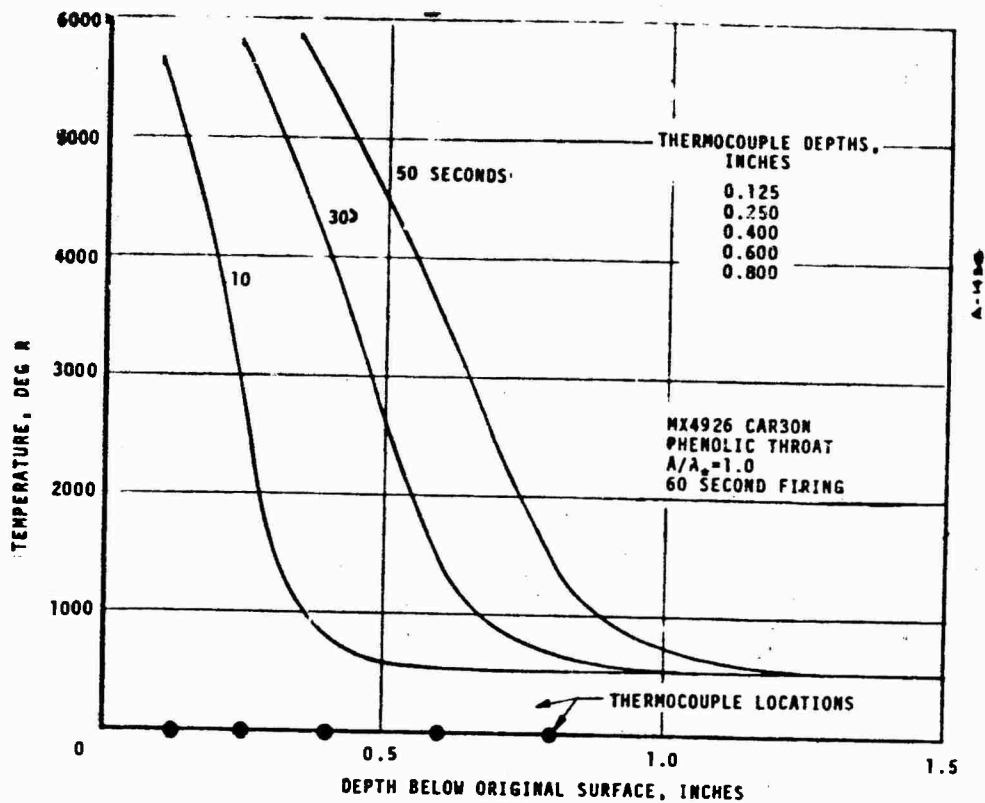


FIGURE 4-20 IN-DEPTH RESPONSE AND THERMOCOUPLE LOCATIONS FOR THE THROAT OF THE CHAR MOTOR NOZZLE

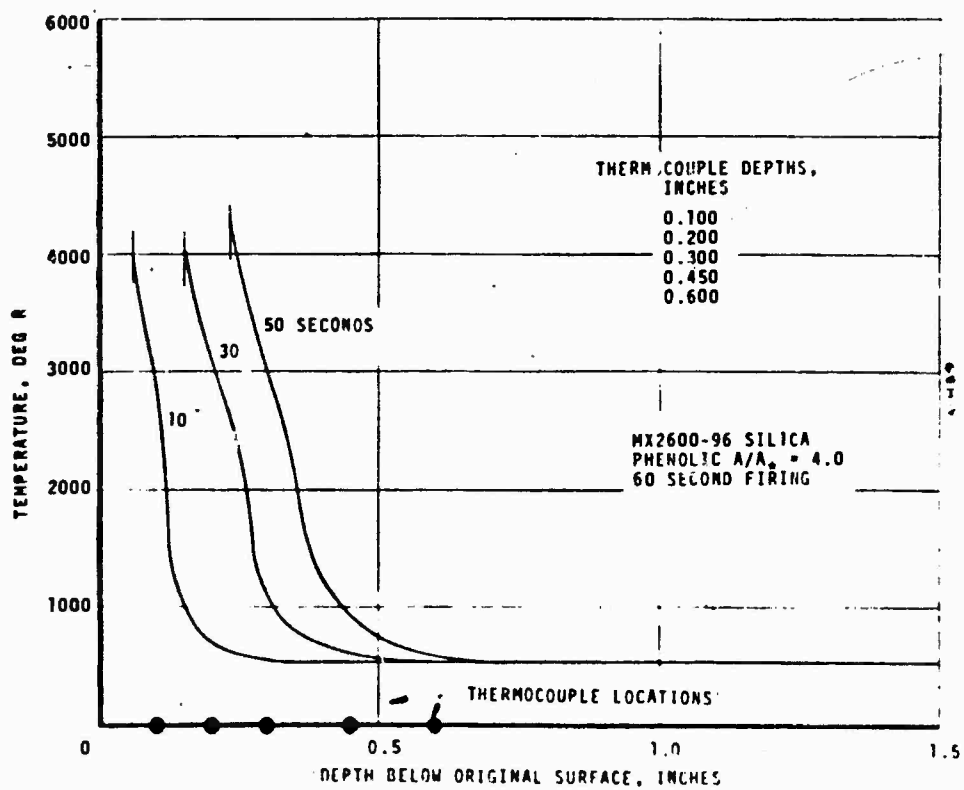


FIGURE 4-21 IN-DEPTH RESPONSE AND THERMOCOUPLE LOCATIONS FOR A/A<sub>0</sub> = 4.0 IN THE CHAR MOTOR NOZZLE

each material and location provide an accurate definition of the in-depth response throughout the 60 second firing. The thermocouple pattern of Figure 4-20 is also proper for the other two measurement system locations, MX 4926 carbon phenolic at  $A/A_* = -2.0$  (subsonic) and 2.0.

The thermocouple pattern for the Phase II evaluation tests is presented in the table below.

Depth Below Surface (in)
0.050
0.125
0.200
0.300
0.400

This pattern was used for both the MX 4926 carbon phenolic and the MX 2600-96 silica phenolic materials, both of which were subjected to similar test conditions. (See Section 6 for the complete outline of this program.) Since the surface recession was somewhat less than that anticipated in the char motor, the thermocouples are closer to the surface.

The types of thermocouples to be used in the plugs were selected based on the maximum expected temperature at the particular thermocouple locations, the thermocouple response characteristics, and the fabrication and handling characteristics of the thermocouples. The tungsten rhenium thermocouple systems provide the highest temperature capability. Standard calibrations are available to 4200°F for both tungsten/tungsten 26% rhenium (W/W26Re) and tungsten 5% rhenium/tungsten 26% rhenium (W5Re/W26Re) as shown in Figure 4-22. Calibration results to higher temperatures are also available; results from Reference 4-12 to 5400°F for W5Re/W26Re are also shown in Figure 4-22. As seen from the figure, W/W26Re has a greater output sensitivity (millivolts per degree) at high temperature and is therefore preferable from this standpoint. Based on Aerotherm experience and the experience of others (e.g. References 4-12 and 4-16), pure tungsten presents problems in handling, however. Pure tungsten is very brittle and the thermocouple junction formed is very delicate. The W5Re/W26Re system reduces these problems considerably although care in handling is required with this system as well. On the basis of the above, W5Re/W26Re was chosen as the thermocouple type for all locations where temperatures above 2500°F are expected.

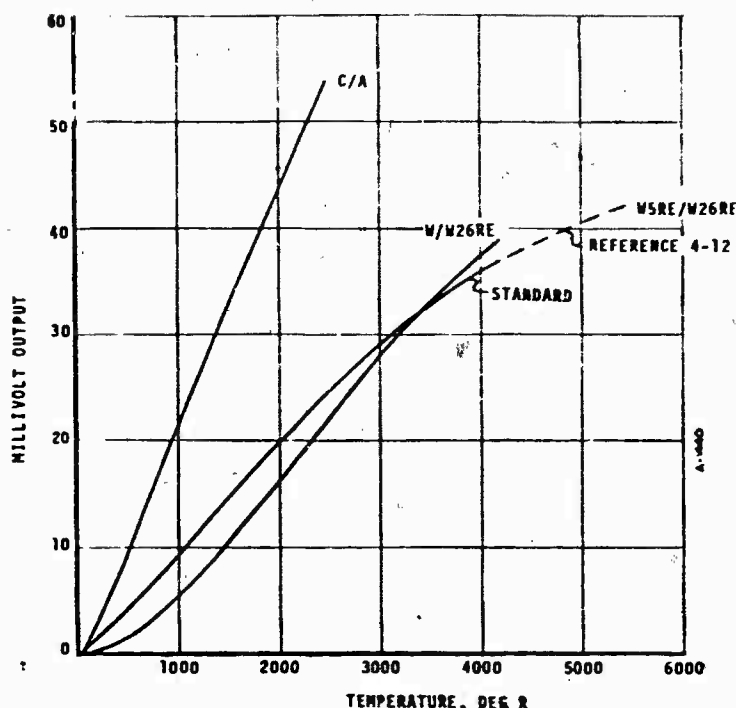


FIGURE 4-22 THERMOCOUPLE EMF OUTPUTS

For temperatures below 2500°F, the Chromel/Alumel (C/A) system was chosen. This thermocouple type combines high output sensitivity (Figure 4-22) and moderately high temperature capability and is also rugged. The other possible candidates for this temperature range are the platinum rhodium systems; however, they exhibit a quite low output sensitivity.

The thermocouple wire to be used in all measurement system plugs was calibrated by the manufacturer (Hoskins Manufacturing Co.), this calibration being directly traceable to the National Bureau of Standards.

Based on the selected thermocouple locations and on the temperature capabilities of the thermocouple types, the locations and corresponding types of thermocouples selected for the Phase III char motor nozzle and the Phase II test sections are presented in Table 4-4. Because of the relatively high surface recession anticipated in the carbon phenolic part of the char motor nozzle, four of the five thermocouples at the three measurement system locations are W5Re/W26Re.

TABLE 4-4. THERMOCOUPLE DEPTHS AND TYPES TO BE USED IN MEASUREMENT SYSTEM PLUGS

Char Motor				Phase II Test Sections	
MX 4926 Carbon Phenolic A/A <sub>o</sub> = -2.0, 1.0, 2.0		MX 2600-96 Silica Phenolic A/A <sub>o</sub> = 4.0		MX 4926 Carbon Phenolic and MX 2600-96 Silica Phenolic A/A <sub>o</sub> = 1.0	
Depth <sup>a</sup> (inch)	Thermocouple Type	Depth (inch)	Thermocouple Type	Depth (inch)	Thermocouple Type
0.125	W5Re/W26Re	0.100	W5Re/W26Re	0.050	W5Re/W26Re
0.250		0.200		0.125	
0.400		0.300		0.200	
0.600		0.450	C/A	0.300	C/A
0.800	C/A	0.600		0.400	

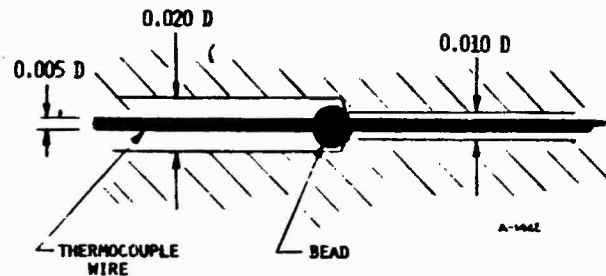
a) Depth below original surface

b) Tungsten 5% rhenium/tungsten 26% rhenium or Chromel/Alumel

In the other cases, it is necessary that only three be W5Re/W26Re. These requirements are apparent for the char motor nozzle from Figures 4-20 and 4-21.

**4.1.2.1.2 Thermocouple Installation.** The configuration of the holes which accept the thermocouples is shown in the sketch below. The stepped-hole scheme provides intimate contact between the thermocouple and material and provides the means of precisely locating the thermocouple bead on the plug centerline. The 0.010-inch diameter hole size was dictated by the type of materials of interest. The cloth phenolics are very hard and also have macroscopic (relative to 0.010 inch) variations in density and structure. This combination represents a significant hazard to small drills both in terms of dulling and breaking. Also, once broken, the removal of a drill is usually impossible. The 0.010-inch hole was therefore found to be the minimum practical size for successful drilling of these materials.





The 0.010-inch hole diameter dictated the selection of 0.005-inch diameter thermocouple wire. This is a standard and readily available size and is also a convenient size to handle and install. The thermocouple bead size which results is about 0.015 inch in diameter; this dictated the 0.020-inch diameter hole size which accepts the bead.

Because the drills tend to follow the ply direction in cloth reinforced materials, drilling at any angle not parallel to the plies greatly increases the chances of drill breakage. All thermocouple holes were therefore parallel to each other in a direction also parallel to the plies as shown in Figure 3-2. In order to keep the thermocouple locations as close to the plug centerline is practical, the three closest-to-the-surface thermocouples are led down the side walls through the insulative sleeving and the two other thermocouples are potted into the groove formed by the two adjacent insulators. The insulative sleeving used is beryllium oxide as discussed in Section 4.1.1. The potting material selected is a boron nitride slurry which cures to a hard, high temperature, non-conducting material. The sleeving diameter selected is  $0.029 \pm .002$  inch because it is a convenient, commercially available size.

#### 4.1.1.2 System Configuration

The overall measurement system plug configuration was presented previously in Figure 3-2. A more detailed description is presented in the following paragraphs.

The basic plug diameter is 1/2 inch. This is a practical upper limit for convenience in thermocouple hole drilling and a practical lower limit in terms of the thermocouple wire conduction loss discussed in Section 4.1.1.1.2. The overall plug length for the char motor nozzle was approximately 1/4 inch less than the thickness of the part in which it was installed. This provides sufficient clearance below the back wall of the part for the lead wire connections and allows adequate potting for plug retention.

The measurement system plugs were fabricated from billets of the two materials, MX 4926 carbon phenolic and MX 2600-96 silica phenolic, such that the layup angles matched those for the locations at which they were installed. The surface and in-depth response of the plug therefore matched that of the surrounding material, as required. The surface contour of the plugs was machined to match the contours at the respective installation locations.

The thermocouple lead wire junctions at the bottom of the plug were formed on pins mounted in the plug as shown in Figure 4-23. This technique eliminated any strain on the thermocouple wires due to handling the lead wires. The pin was a short section of large diameter thermocouple lead wire of the same material as the thermocouple lead itself. This eliminated any errors due to a possible temperature gradient between the thermocouple connection point and the lead wire connection point. The end of the connection pin that was mounted in the plug was dipped in epoxy resin before installation so that it

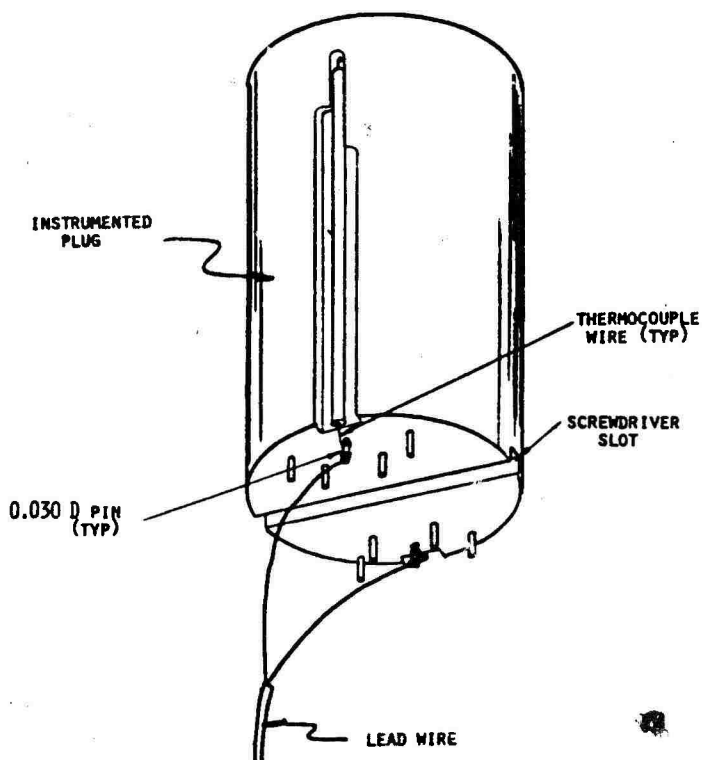


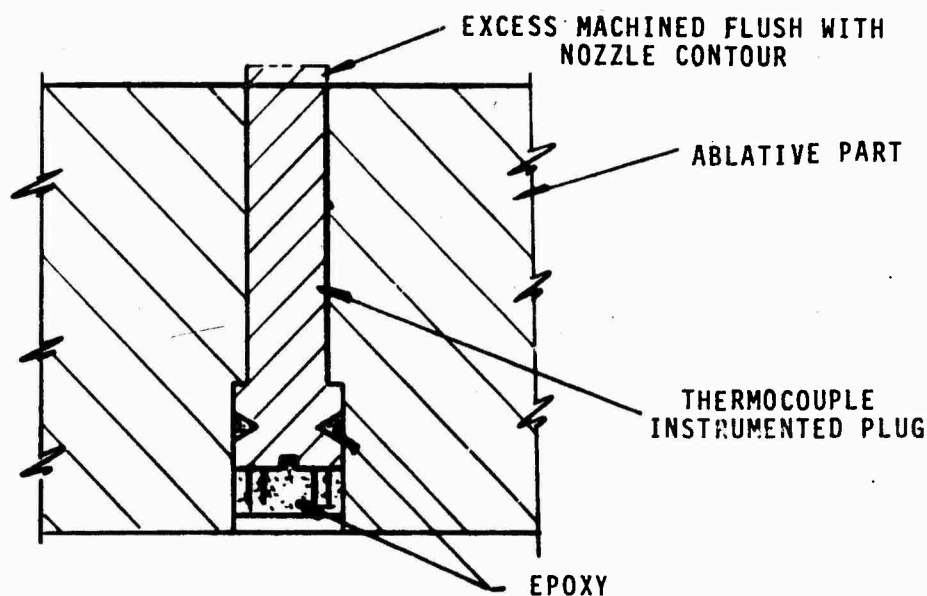
FIGURE 4-23 SCHEMATIC OF THERMOCOUPLE LEAD WIRE CONNECTION SCHEME  
4-144C

was insulated from the plug once installed. The pins were also held in place with epoxy resin. The thermocouple lead and the lead wire were spot welded to the pins.

#### 4.1.2.3 Installation

The measurement system plug was press-fit into its mating hole in the ablative part or test section. The back of the plug was slotted for a screwdriver as shown in Figure 4-23 so that rotational and depth adjustments could be made. The connecting pin pattern provided ample room for a screwdriver without danger to the thermocouple and leads.

The hole in the ablative part and the thermocoupled plug were match machined in order to insure a snug fit. For the Phase III char motor firings, this hole was counter-bored as shown in the sketch below



to a depth which allowed the plug to protrude above the internal surface of the nozzle by approximately 0.050 inch. The amount of the protusion was accurately measured and then machined flush with the nozzle contour.

The plug was bonded to the ablative part using a low viscosity epoxy resin (Epon 815 and DTA). The bond line included the external surface of the plug with the exception of the surface exposed to the internal surface of the nozzle. In addition, the cavity at the backside of the plug is partially filled with epoxy resin. The thickness of this resin is approximately equal to the length of the strain relieving pins, and, thus, it protects the wire connections made at the back of the thermocoupled plug. During the installation of the plug, the thermocouple lead wires are bent and led out in the proper direction for installation of the ablative nozzle into the steel housing.

#### 4.1.2.4 Recording Instrumentation

Standard recording instrumentation was used for the measurement system. In the Phase II evaluation test program, the thermocouple outputs were recorded on an oscillograph continuously through each test. The recording circuit used for all thermocouples is presented schematically in Figure 4-24. A room temperature reference junction was used; the reference temperature was measured with a mercury-in-glass thermometer. The circuit sensitivity, millivolts per inch of galvanometer deflection, was adjusted to yield a maximum of 6 inches of deflection (the usable range of the galvanometer) for the maximum temperature anticipated for each thermocouple. The galvanometers used and the circuit resistance were matched to yield the proper galvanometer damping characteristics.

Each thermocouple circuit was calibrated just prior to test using an external emf source (Figure 4-24). The calibration consists of imposing four or five emf values in steps up to the maximum anticipated in the test and simultaneously recording the galvanometer deflections. The precise calibration emf values are determined with a potentiometer.

In the Phase III char motor firings, the thermocouple outputs were measured with the RPL SEL-600 digital voltmeter system and recorded on magnetic tape. A 150°F oven provided the reference temperature for all thermocouples. No circuit calibration was required since direct voltage measurements were made.

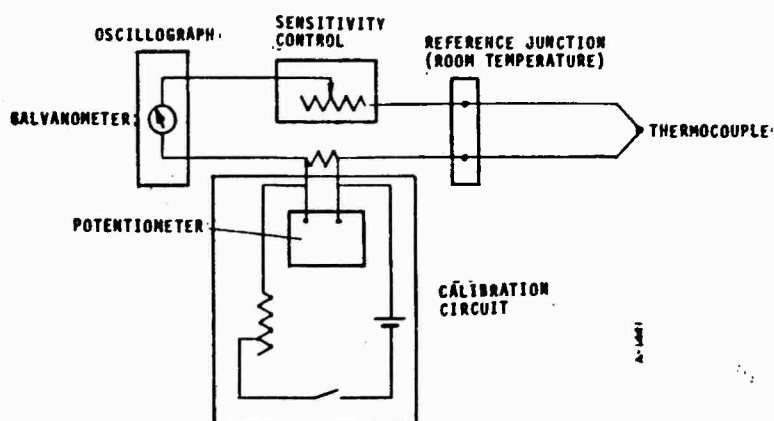


FIGURE 4-24 PHASE II THERMOCOUPLE RECORDING AND CALIBRATING CIRCUIT

## 4.2 RADIATIVE HEAT FLUX SYSTEM

The radiative heat flux measurement system is dependent on measuring the temperature difference from the center to the edge of the constantan foil in the narrow view angle radiometer (Section 3.2, Figure 3-4). This temperature difference is recorded as an emf output which is converted to incident heat flux based on the instrument calibration. In making this conversion, potential sources of error include the wavelength characteristics of the lens and sensor surface coating, the response time of the constantan foil sensor, the procedure used for instrument calibration, and the copper heat sink temperature. These potential errors are discussed in Section 4.2.1. Once the potential sources of error are defined, the instrument design, fabrication, and installation are defined in Section 4.2.2.

As mentioned in Section 1 and described in more detail in Section 7, two 40-inch char motor tests were conducted under this contract. Each firing had a narrow view angle radiometer at the nozzle throat plane. In addition, the second char motor firing had a narrow view angle radiometer of a different configuration at a supersonic area ratio of 3.0. The design of this radiometer was dictated by the requirements of a high chamber pressure motor (Reference 4-18), and these requirements will not be discussed here. Therefore, the error analysis presented in Section 4.2.1 is directed to the radiometer located at the nozzle throat plane. However both radiometers are discussed in Section 4.2.2.

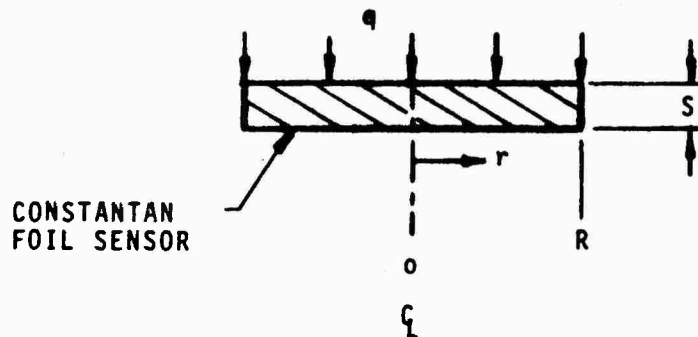
#### 4.2.1 Error Analysis

The errors associated with measuring the narrow view angle radiation flux using the radiometer shown in Figure 3-4 can be categorized as those resulting from thermal effects, optical effects, response time, and method of instrument calibration. The thermal effects include the variation of emf output with the copper sink temperature and the variation of the elemental view factor across the constantan disk, and these effects are defined in Section 4.2.1.1. The optical effects result from the variation of the lens transmissivity and of the sensor surface coatings absorbtivity with wavelength and from the coupling of this variation with the wavelength characteristics of the radiative source. The optical effects are defined in Section 4.2.1.2. The error associated with the time constant of the instrument is dependent on the fluctuations which are expected in the emissive power of the radiative source, and this is discussed in Section 4.2.1.3. The final error associated with measuring the radiative heat flux is the method of instrument calibration, and this is discussed in Section 4.2.1.4. Finally, the errors from the various sources are combined to give the overall system accuracy in Section 4.2.1.5.

##### 4.2.1.1 Thermal Effects

The recorded output of the narrow view angle radiometer is an emf which is dependent on the temperature difference across the constantan disk which is in turn dependent on the incident radiative heat flux. The temperature distribution for the constantan foil sensor shown in the sketch below is given by

$$T - T_{r=R} = \frac{\dot{q}}{4sK} (R^2 - r^2) \quad (4-10)$$



From Equation (4-10), one notes that for a constant heat flux the temperature distribution is independent of the copper sink temperature provided the thermal conductivity of constantan is independent of temperature. Since the thermal conductivity of constantan increases with increasing temperature, the temperature difference across the sensor decreases with increasing copper sink temperature. If the thermal conductivity of constantan is represented by

$$K = K_0 (1 + \alpha T)$$

where  $T$  - is the temperature above the reference temperature.  
(In this analysis  $T = T_{R-R}$  is taken as the reference temperature).

$$\alpha = 1.28 \times 10^{-3} / ^\circ\text{F}$$

$$K_0 = 12.6 \text{ Btu/hr ft}^\circ\text{F @ } 32^\circ\text{F}$$

and if  $q = 10 \text{ Btu/ft}^2\text{sec}$

$$s = 0.0005 \text{ in}$$

$$R = 0.0775 \text{ in}$$

then, the temperature distributions for copper sink temperatures of 100, 200, and 300°F are shown in Figure 4-25. The temperature difference for sink temperatures of 100 and 300°F is shown in Figure 4-26a as a function of heat flux. Due to the variation of the temperature difference ( $T_{R=0} - T_{R=R}$ ) with sink temperature, the recorded emf output also varies. However, one notes from the standard emf charts for copper/constantan that the measured emf for a constant temperature difference is dependent on the temperature level. This dependency is shown in Figure 4-26b. When the results of Figures 4-26a and 4-26b are combined, the effect of sink temperature on the relationship of incident heat flux vs. recorded emf is shown in Figure 4-27. For a sink temperature variation of 200°F, the error in heat flux is -3 percent.

Another source of error which is caused by an increase in the copper sink temperature is due to reradiation from the sensor. As shown previously in Figure 4-24, the maximum sensor temperature increases with increasing sink temperature for a constant incident heat flux. This results in an increase in the effective sensor temperature which is defined by

$$T_e = T_0 + 0.75\Delta T$$

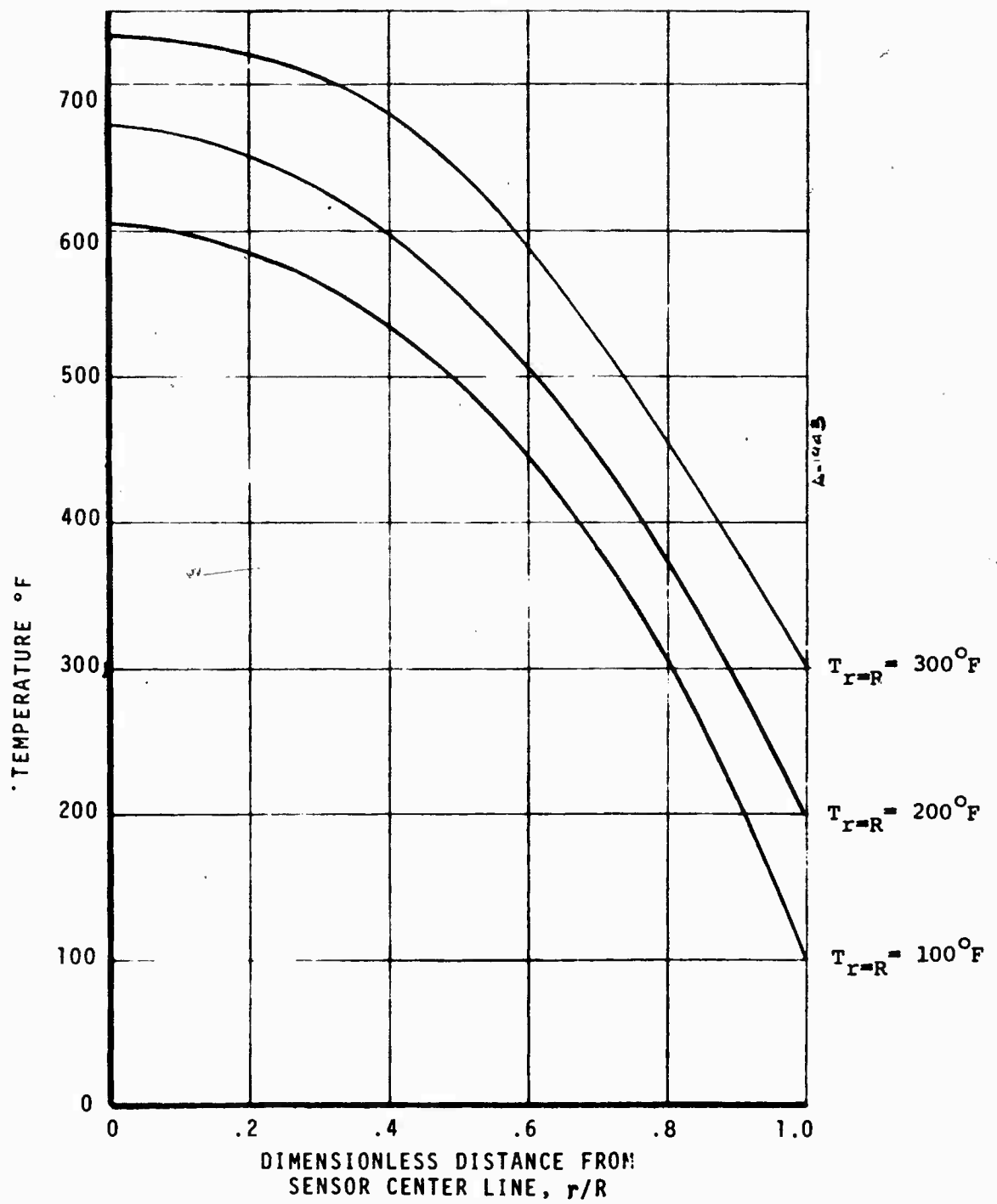


FIGURE 4-25 CONSTANTAN FOIL TEMPERATURE DISTRIBUTION AT MAXIMUM HEAT FLUX FOR VARIOUS BODY TEMPERATURES



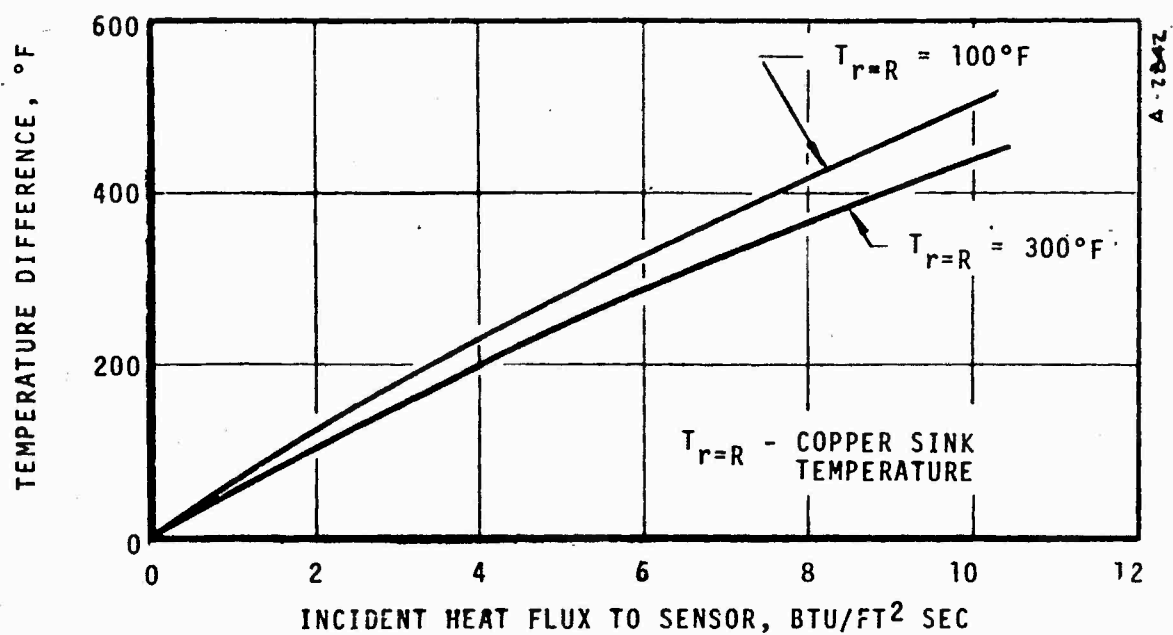


FIGURE 4-26a VARIATION OF TEMPERATURE DIFFERENCE WITH TEMPERATURE LEVEL AND INCIDENT HEAT FLUX

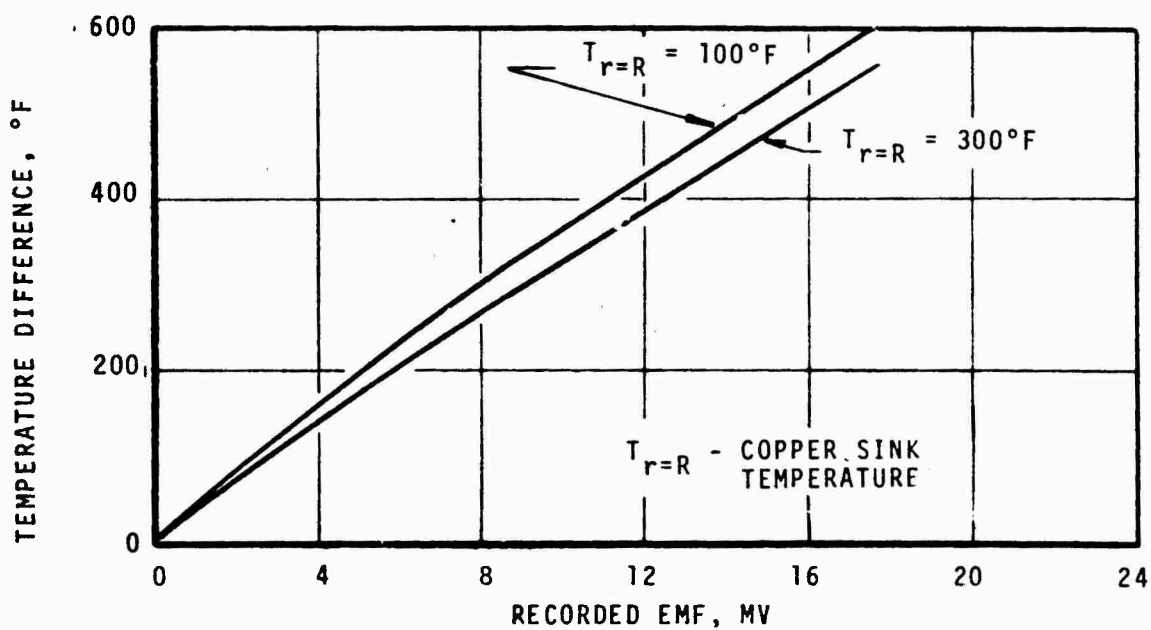


FIGURE 4-26b VARIATION OF RECORDED EMF OUTPUT WITH TEMPERATURE DIFFERENCE AND TEMPERATURE LEVEL

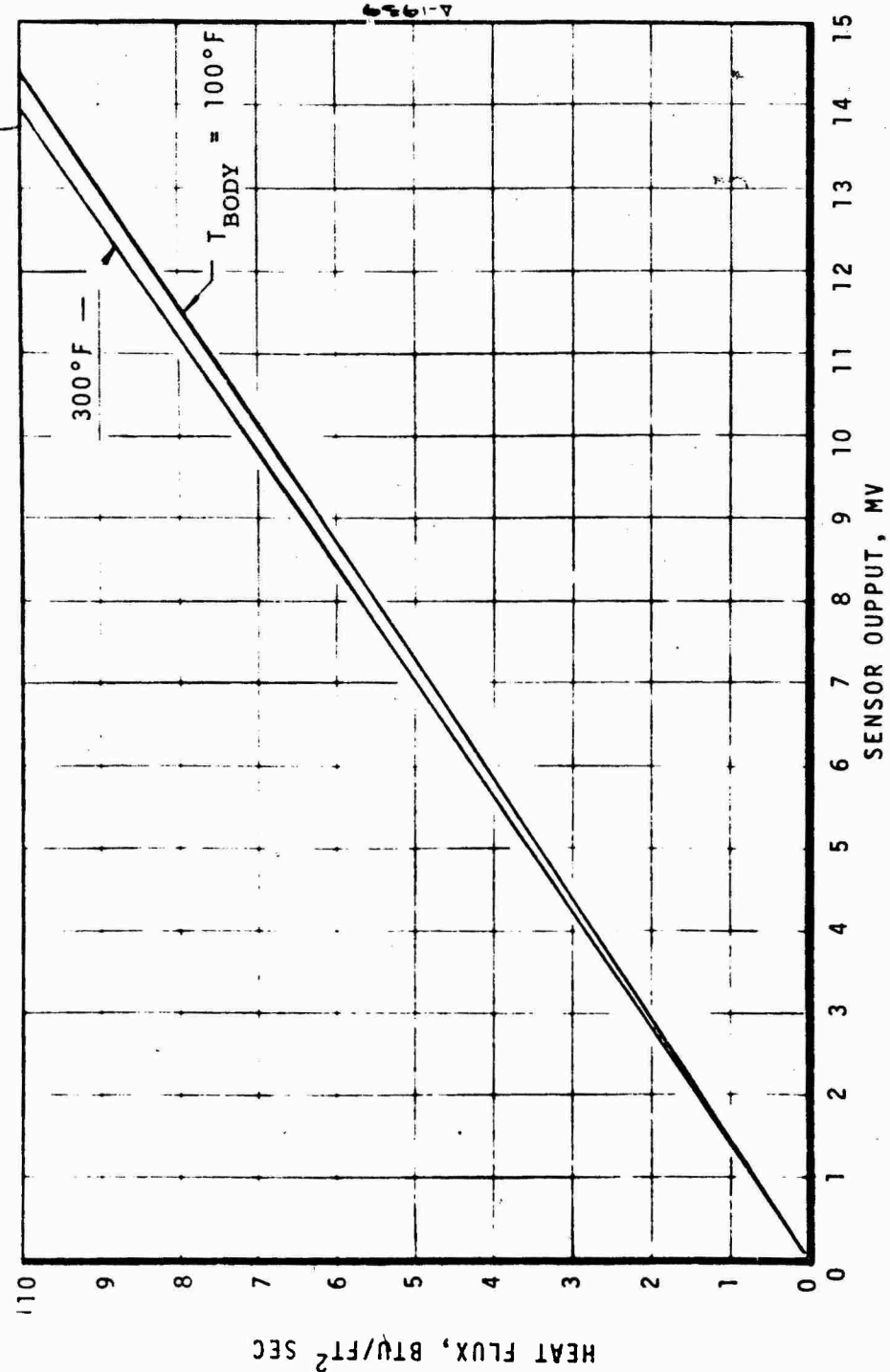


FIGURE 4-27 EFFECT OF THERMAL CONDUCTIVITY AND THERMOCOUPLE OUTPUT VARIATIONS WITH TEMPERATURE ON SENSOR OUTPUT

For the maximum sensor heat flux, the reradiative flux, defined using the effective sensor temperature, is shown in Figure 4-28 as a function of the heat sink temperature. The results shown in this figure are just from the blackened face of the sensor. Due to the small emissivity ( $\epsilon \approx 0.06$ ) of constantan, reradiation from the opposite face of the sensor is negligible. For the situation of the maximum heat flux, an increase in sink temperature from 100 to 300°F causes a -3 percent error in the measured heat flux.

#### 4.2.1.2 Optical Effects

The narrow view angle radiometer has a lens which transmits the radiative heat flux to the sensor while protecting it from any convective heating. In addition, a special coating is put on the sensor so that it acts as much like a black body as possible. However, both the transmissivity of the lens and the absorptivity of the sensor coating exhibit some wavelength dependency, and this dependency is shown in Figure 4-29 for the sapphire lens and coating materials used by Heat Technology Laboratory in their fabrication of narrow view angle radiometers. One notes from this figure that the absorptivity of the sensor coating is approximately 0.90 and increases

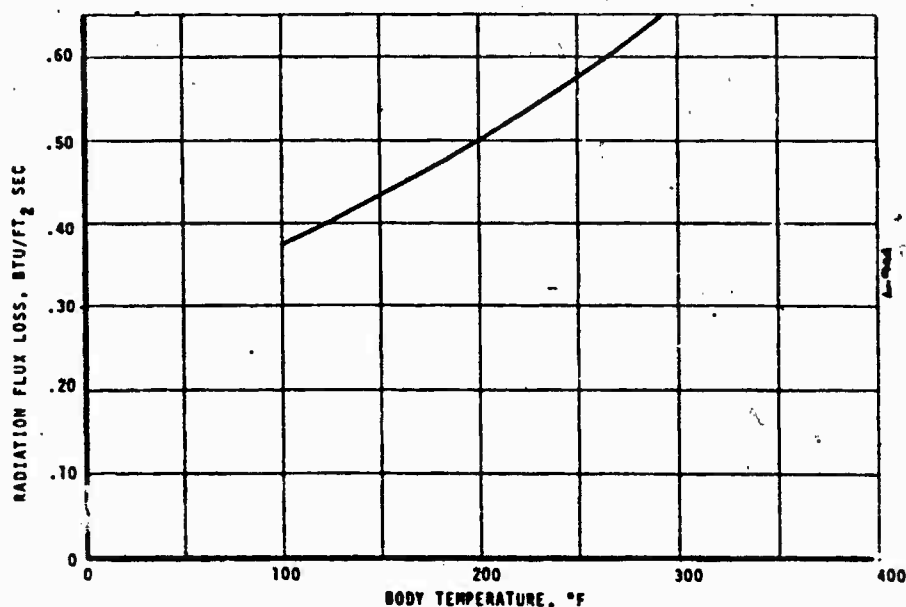


FIGURE 4-28 APPROXIMATE RADIATION HEAT LOSS FROM SENSOR AT MAXIMUM INCIDENT HEAT FLUX

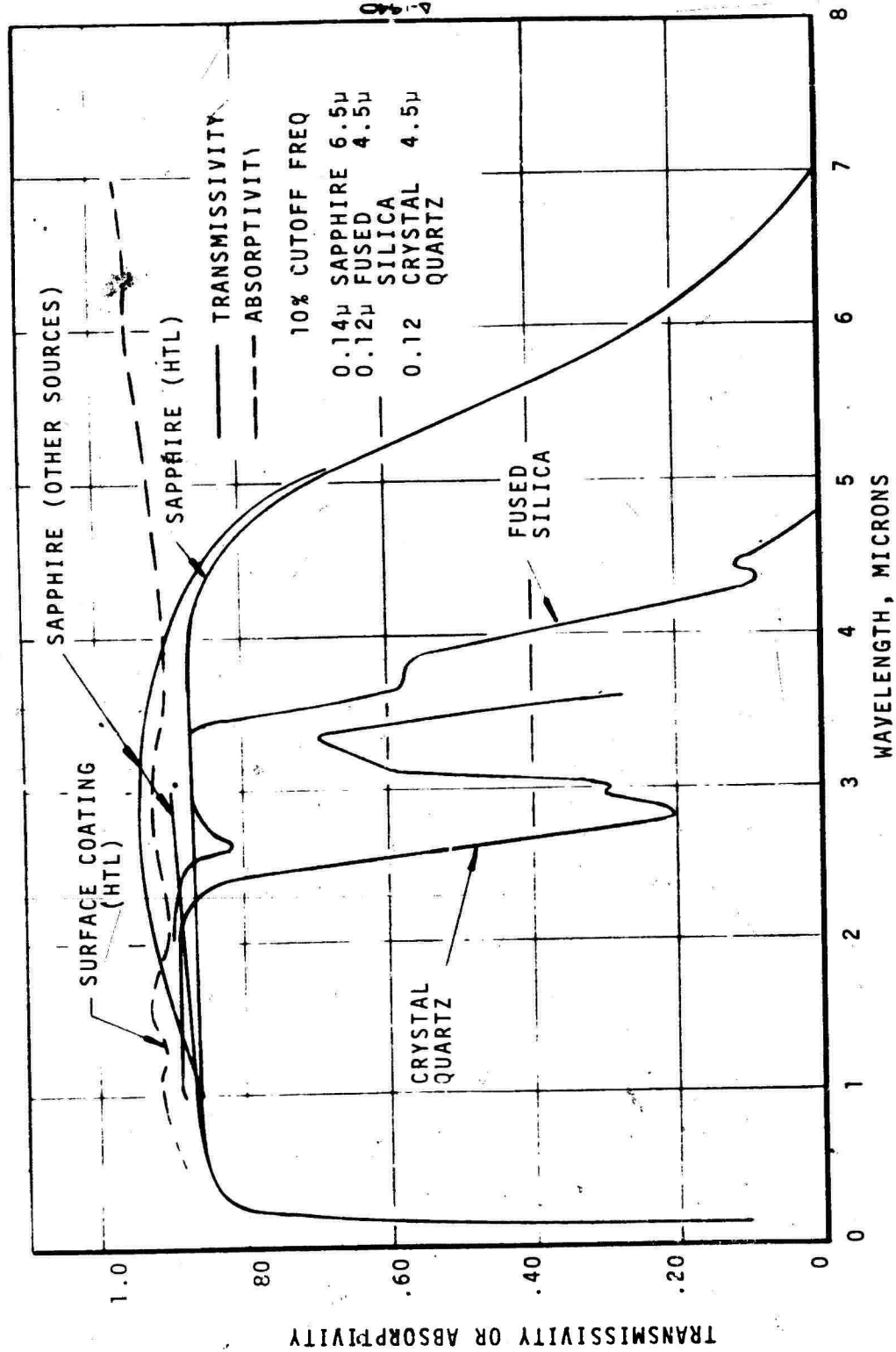


FIGURE 4-29 OPTICAL PROPERTIES OF LENS MATERIALS AND SURFACE COATING

slightly with wavelength while the transmissivity of the sapphire lens is approximately constant between 0.5 and 4.5 microns and decreases for wavelengths outside of this range. The wavelength dependency of the coating and of the sapphire lens can introduce an error into the measurement of the radiative heat flux if the emissive power wavelength characteristics of the source being measured are different than those of the calibration source. The significance of this error must be evaluated for the particular application of interest and is evaluated below for temperatures representative of those encountered in solid rocket motors.

Since the calibration source simulates a blackbody source, its emissive power wavelength characteristics as a function of source temperature are adequately described by the blackbody relationships, and these are shown in Figure 4-30 for source temperatures of 3000, 5000, and 7000°R. One notes that the emissive power is concentrated in the shorter wavelengths as the source temperature increases. The effect on the measured heat flux of the wavelength characteristics of the source combined with the wavelength characteristics of the sapphire lens and sensor coating is best illustrated by an example. In the first case of this example, the heat flux incident on the sapphire lens is from a blackbody source at 4000°R, and, in the second case, the same heat flux is generated by a 6000°R gray body source with an emissivity of 0.135. For these cases, the heat flux absorbed by the sensor is 3% less for the blackbody source than for the gray body source. If a similar example was performed which considered a black body source at 3000°R and a gray body source at 6600°R that emitted the identical heat flux, the difference in the heat flux absorbed by the sensor would be greater than 3%. This is due to the higher attenuation of the black body source by the sapphire lens.

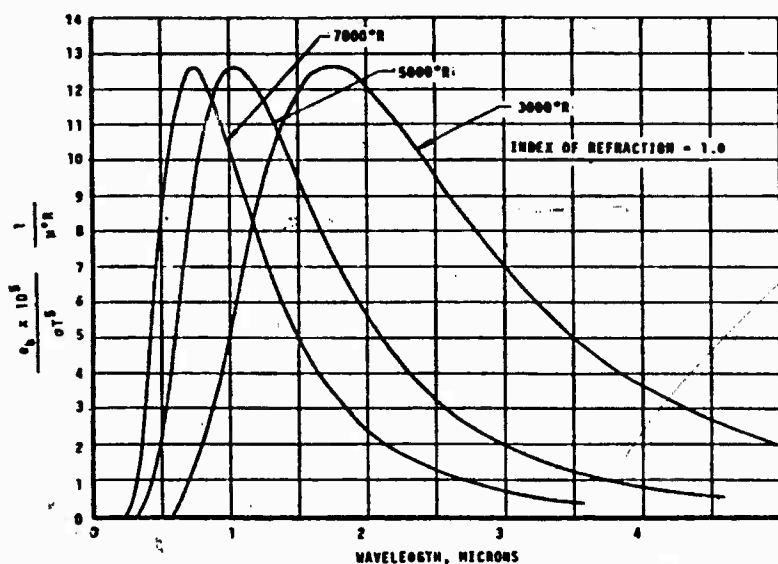


FIGURE 4-30 BLACK BODY EMISSIVE POWER AS A FUNCTION OF WAVELENGTH FOR SOURCE TEMPERATURES AT 3000, 5000, AND 7000°R

#### 4.2.1.3 Response Time

The response time of a Gardon type radiometer is given in Reference 3-2 as

$$\tau = \frac{c\rho R^2}{4K} \quad (4-11)$$

For the application being considered here, the radius of the sensor is approximately 0.0775 inches. Thus, for a constantan foil, this gives a time constant of approximately 0.10 seconds. Whether a time constant of this magnitude is acceptable depends on the characteristics of the heat source which are to be accurately recorded. As described earlier, the source viewed by the narrow view angle radiometer is a combination of gas radiation, particle radiation, and opposite wall radiation. Since start up transient information concerning the radiancy of the opposite wall and the radiancy of the particle laden combustion products would be valuable, it is desirable to have a time constant which is an order of magnitude less than the time period in which these initial start up transients occur. In the following paragraphs, an analysis is performed which shows the response of a Gardon type narrow view angle radiometer to a sinusoidally time varying heat flux input. This shape was chosen for the heat flux input because a quarter cycle is a reasonable approximation for the radiancy of the opposite wall and the alumina particles during the motor start up.

As described in Reference 3-2 the rate of temperature rise of the circular foil sensor can be represented by an exponential law such as

$$T = T^* (1 - e^{-t/\tau}) \quad (4-12)$$

Where  $T^*$  - steady state temperature

Since the temperature of the sensor is approximately linear with heat flux, the above relation also implies that

$$\dot{q}' = \dot{q} (1 - e^{-t/\tau}) \quad (4-13)$$

where  $\dot{q}$  - actual calorimeter absorbed flux

$\dot{q}'$  - heat flux inferred (recorded)

The sinusoidal profile selected for this analysis was

$$\dot{q} = \dot{q}_0 \sin \frac{\pi \theta}{\zeta} \quad (4-14)$$

where

$\dot{q}_0$  - peak heat flux

$\zeta$  - twice the motor ignition transient time

Now the differential equation whose solution is Equation (4-13) is

$$\tau \frac{dq'}{dt} = \dot{q} - \dot{q}' \quad (4-15)$$

By substituting Equation (4-14) into Equation (4-15) and solving the differential equation with the appropriate boundary condition, one obtains the results shown in Figure 4-31. Due to the large free volume of the char motor the ignition transient is on the order of five seconds which, for a time constant of 0.1 seconds, corresponds to a  $\tau/\ell$  ratio of 0.01. For this ratio, one notes from Figure 4-31 that the recorded heat flux is in close agreement with the incident heat flux.

#### 4.2.1.4 Calibration

The narrow view angle radiometer is calibrated by exposing it to a radiation source which is an electrically heated graphite block.

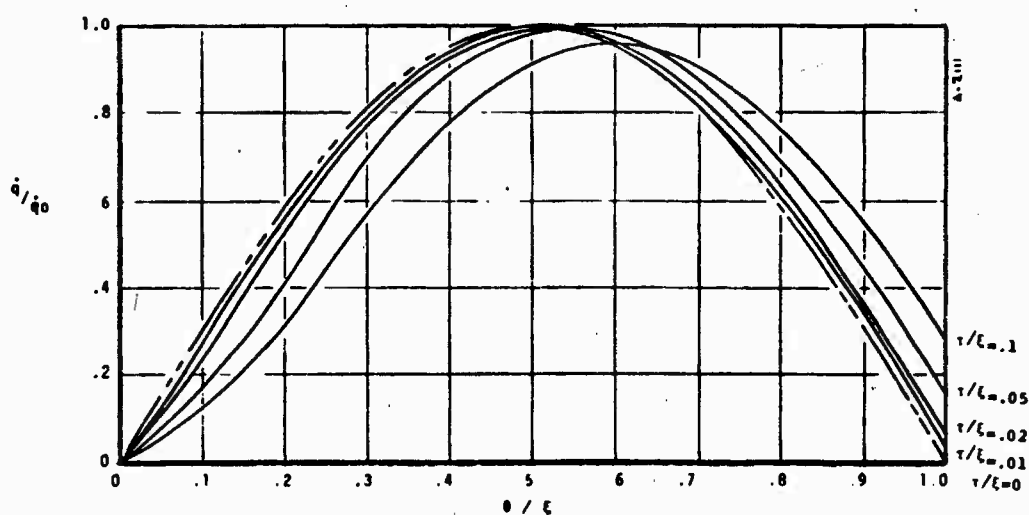


FIGURE 4-31 NON-DIMENSIONAL CALORIMETER RESPONSE AS A FUNCTION OF NON-DIMENSIONAL TIME

The uniformity of the heat flux from the graphite block has been carefully mapped using a standard view angle radiometer. During the calibration procedure, the transducer to be calibrated is held in a water cooled holder, and the aperture of the transducer is facing the graphite block. The distance between the aperture and the graphite block is such that the field of view of the transducer is located within the uniform heat flux region of the graphite block. The standard transducer is located on the opposite side of the uniform temperature block, but it views the same region. The transducer to be calibrated has the lens in place and the sensor coating applied prior to calibration. The upper limit on the calibration heat flux is approximately 250 Btu/ft<sup>2</sup>sec. This means that the calibration curve for transducers whose range is outside this limit must be obtained by extrapolating the available calibration data. For Gardon type radiometers, a straight line extrapolation of the available calibration data is used for the higher (725 Btu/ft<sup>2</sup>sec) heat flux range. This extrapolation is in agreement with that which is predicted by analytical methods. The output from the calibration procedure is a curve which relates incident hemispherical heat flux to recorded emf output. The incident heat flux is defined using the output from the standard transducer.

The important items to note from the above description of the calibration procedure are 1) the transducer is in a water cooled holder and, thus, its sink temperature is approximately ambient temperature, 2) the lens is in place during calibration, 3) the limit on the calibration heat flux is 250 Btu/ft<sup>2</sup>sec and 4) the calibration curve relates total hemispherical heat flux to recorded emf output. The uncertainty in the calibration procedure is stated by the manufacturer to be +2% which includes nonlinearity effects. This uncertainty is in addition to the errors described in the previous sections.

#### 4.2.1.5 Overall Output Accuracy

In Sections 4.2.1.1 through 4.2.1.4, the errors associated with the use of a narrow view angle radiometer to measure the total radiancy at a nozzle throat location were discussed. These errors which are summarized in Columns 1 and 2 of Table 4-5 are uncorrected errors as no effort was made to reduce their magnitude through the use of either analytical techniques or experimental data. The errors shown in Column 1 are the maximum errors and would occur only if the transducer sink temperature became 300°F and if the wavelength characteristics of the source simulate a black body. Since the expected maximum sink temperature for the radiometer being used in rocket nozzle is 200°F, the probable error due to this effect is 1-1/2%. The probable errors resulting from radiation heat loss from the sensor and from differences in the temperature and wavelength characteristics between the calibration and measurement sources



TABLE 4-5  
RADIOMETER ACCURACY

Sources of Error	Uncorrected Maximum Error (Percent)	Uncorrected Probable Error (Percent)	Corrected Error (Percent)
Calibration Shift with Body Temperature	-3	-1.5	-0.5
Radiation Loss from Sensor	-7	-3.5	+0.5/-1
Temperature Differ- ence between Calibration/ Measurement Sources	+3	+1	+0.5
Calibration Uncertainty (Nonlinearity and Error)	+2	+2	+2
Overall Error	-5/-9	-2/-6	+2.5/-3

are also less than the uncorrected maximum errors as shown by a comparison of Columns 1 and 2.

Since the first two errors shown in Table 4-5 result from a temperature rise of the transducer sink temperature, a knowledge of this temperature would permit the user to correct the recorded emf output for these errors, and, thus, they could be essentially eliminated. The required information is obtained from a thermocouple which is attached to the copper sink and the reduced error is shown by Column 3 of the table. Even with this sink temperature, the errors cannot be entirely eliminated because of such items as the possibility of temperature gradients within the copper heat sink, the possibility of the aperture and the copper barrel increasing in temperature and, thus, influencing the heat flux to the sensor, and the possibility of higher heat conduction loss in the thermocouple wire with increasing sensor temperature.

Although the radiancy from the alumina particles in a solid rocket plume as a function of wavelength and temperature is not well understood, the error resulting from the temperature difference between the calibration and measurement sources can be reduced assuming the calibration source is a black body and the measurement source is a gray body. Due to the uncertainties in the characteristics of the measurement source, this reduction in error can be considered only

a first order correction. More knowledge of the measurement source must be available before any further corrections could be made.

The overall radiometer accuracy for the three cases studied (uncorrected maximum error, uncorrected probable error, and corrected error) is determined from the following relationship

$$\text{error} = \Sigma(\text{fixed errors}) + \sqrt{\Sigma(\text{random errors})^2}$$

All the errors are fixed errors except the calibration uncertainty which is a random error. The overall accuracy for the three cases are tabulated on the last line of Table 4-5

#### 4.2.2 Design and Fabrication Analysis

Narrow view angle radiometers have been used extensively to measure the total radiative heat flux, and they are commercially available as off-the-shelf or custom-built instruments. Design or configuration options include size, shape, view angle, gas purge, optical lens, and water cooling. The design considerations which were evaluated in defining the transducer requirements are discussed in Section 4.2.2.1. The incorporation of the transducer requirements, design considerations, and fabrication techniques into an overall system configuration is discussed in Section 4.2.2.2. The installation of the transducer into the rocket nozzle is discussed in Section 4.2.2.3, and, finally, the recording instrumentation and associated hardware required by the transducer are defined in Section 4.2.2.4.

##### 4.2.2.1 Design Considerations

Once the requirements of a narrow view angle radiometer have been defined the radiometer design is formulated based on satisfying certain geometrical constraints and cooling requirements. Most of the transducer requirements have been defined in Section 3.2 but they are briefly summarized below:

- Continuous reading for the duration of the rocket motor firing
- Must not jeopardize the integrity of the nozzle or cause a significant degradation in its performance
- Must be within the current state-of-the-art

In addition to these general transducer requirements, specific requirements are that the recorded millivolt output should be approximately 10 mv for the maximum expected radiative flux, and that the maximum temperature of the constantan sensor should not exceed approximately 700°F. This latter requirement is due primarily to the emf falling off rapidly above this temperature. Based on these requirements, the solution of the geometrical and cooling problems are discussed separately in Section 4.2.2.1.1 and 4.2.2.1.2, respectively.

4.2.2.1.1 Geometrical Constraints. Before a preliminary design of the radiometer can be developed, the geometrical constraints, which include the cavity diameter, depth of the transducer aperture below the original nozzle surface, and the total thickness of the ablative component at the measurement location must be defined. With the exception of the latter item which is fixed by the nozzle design, there is some latitude in defining the remaining two items. In the paragraphs below, the general guidelines in accomplishing the radiometer design are described, and the geometry of the final design is presented. This discussion is based on the measurement system at the throat of the char motor nozzle (Section 7).

From Figure 4-1, one notes that in order to prevent the aperture of the radiometer from reaching the nozzle surface it must be recessed greater than 0.386 inches. This figure also shows that to prevent excessive temperatures of the copper shell due to heat conduction from the carbon phenolic ablative component, the radiometer should be located approximately 0.6 inches below the nozzle surface at motor burnout. In addition, one notes from the description of the char motor nozzle design presented in Section 7.1 that the ablative component has a thickness of 2.7 inches. With these constraints, the radiometer would be approximately 1.7 inches long and its aperture would be approximately one inch below the original nozzle surface.

Design constraints related by the response of the narrow view angle radiometer are dictated by the following relations:

$$\dot{q} = \dot{q}_0 \sin^2(\alpha/2) \quad (4-16)$$

where

$\alpha$  - view angle  
 $\dot{q}_0$  - hemispherical radiation flux emitted by source

$$T - T_2 = \frac{\dot{q}}{4sK} (R^2 - r^2) \quad (4-17)$$

$$E/\dot{q} = 16.7 \frac{R^2}{s} \quad (4-18)$$

$$\tau_{r=0} = \frac{c\rho R^2}{4K} \quad (4-19)$$

Equation (4-16) defines the heat flux incident to the radiometer as a function of the view angle. The ratio of  $q/q_0$  is shown in Figure 4-32 as a function of the view angle for the range of interest here. Also shown in this figure is the variation across the sensor of the incident heat flux. Equation (4-17) defines the temperature rise across a thin circular disk sensor for a specific incident heat flux; Equation (4-18) defines the transducer sensitivity,

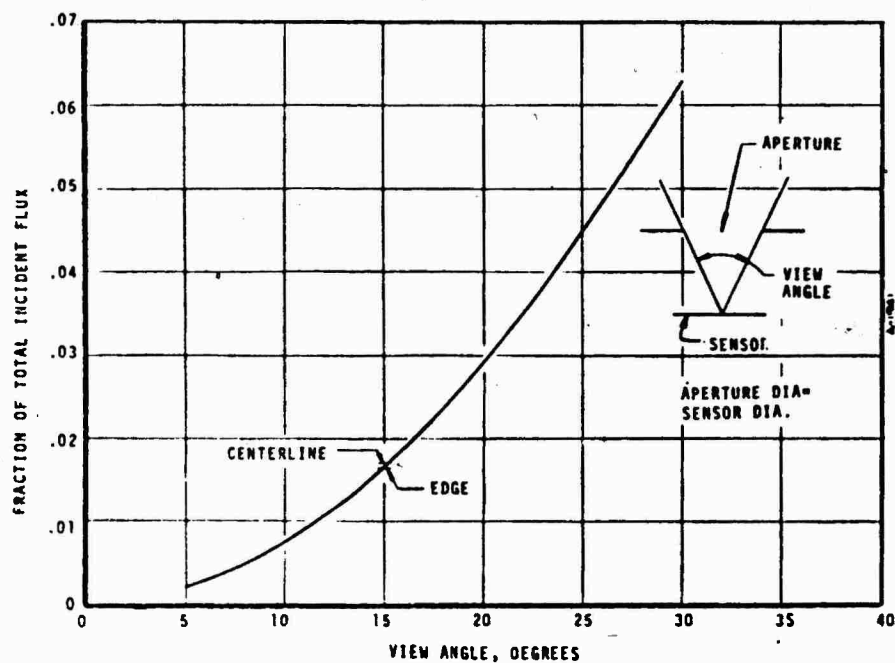
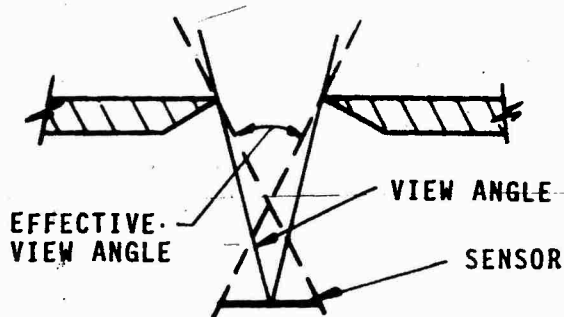


FIGURE 4-32 EFFECT OF VIEW ANGLE ON MEASURED HEAT FLUX

and Equation (4-19) defines the transducer time constant. In addition to the above relationships, two other factors which must be considered are 1) the relationship between the view angle and the effective view angle as shown schematically by the sketch below and 2) the requirement that, if only 10% or less of the total (hemispherical) emitted flux is incident on the sensor, the aperture and sensor diameters must be approximately equal. The first factor is important



in defining the cavity depth below the ablative surface before the sensor sees the cavity walls, and the second is necessary if the elemental view factor at any location on the sensor is to be essentially constant, thus minimizing any nonlinear effect which would have been introduced into the transducer design.

Before considering the transducer design using the above information one should note from Equation (4-18) that the transducer sensitivity is inversely proportional to the sensor thickness. Since it is desirable to maximize the instrument sensitivity, the sensor thickness should be minimized. The practical minimum thickness is 0.0005 inches. This bit of information together with the desire to have an emf output of 10 mv allows one to solve Equations (4-16) (4-17), and (4-18) for  $\dot{q}$ ,  $T$ , and  $R$  as a function of view angle. By iterating using the view angle as the independent variable, a narrow view angle radiometer was defined which satisfactorily met all the requirements. The pertinent characteristics of this radiometer are tabulated in Table 4-6. With the effective view angle shown in this table, the aperture in a 0.5 inch diameter cavity can be recessed no more than 0.725 inches. This is based on a sensor diameter of 0.156 inches. One also notes from the transducer sensitivity that a 10 mv output is obtained for a source radiance of 630 Btu/ft<sup>2</sup>sec which approximates the maximum expected radiance of 570 Btu/ft<sup>2</sup>sec. In addition, as described in Section 4.2.1.3 the time constant is sufficiently small that the transducer can follow the ignition transients.

As described previously, the requirements for the radiometer located at an expansion ratio of 3.0 were dictated by the requirements of a high chamber pressure motor. The characteristics of this radiometer are tabulated in Table 4-7.

TABLE 4-6

CHARACTERISTICS OF NARROW VIEW ANGLE  
RADIOMETER LOCATED AT THE NOZZLE THROAT

View Angle, Degrees	12.1
Effective View Angle, Degrees	26.4
Sensitivity, mv/(Btu/ft <sup>2</sup> sec)	9.0 (at 570 Btu/ft <sup>2</sup> sec)
Time Constant, sec.	0.194

TABLE 4-7

CHARACTERISTICS OF THE NARROW VIEW ANGLE RADIOMETER  
LOCATED AT AN EXPANSION RATIO OF 3.0

View Angle, Degrees	12.2
Effective View Angle, Degrees	24.0
Sensitivity, mv/(Btu/ft <sup>2</sup> sec)	9.0 (at 570 Btu/ft <sup>2</sup> sec)
Time Constant, sec.	0.190

4.2.2.1.2 Cooling Requirements. Once the basic dimensions of the transducer have been defined, the next problem is to define its cooling requirements. Heat is transferred to the transducer by radiation heating of the sensor, aperture, and inner cylindrical walls, by convective heating of the aperture from the hot combustion chamber gases in the cavity, and by conductive heating of the copper housing from the ablative component. The introduction of a gas purge which flows around the sapphire lens and exits through the aperture provides an effective method of eliminating the convective heat transfer from the combustion products. Another advantage of this purge gas is that it prevents any alumina particles or ablative surface material residue from contaminating the lens. This purge gas flow rate was approximately defined by making an energy balance on the control volume shown in Figure 4-33. The equation which describes this energy balance is

$$\dot{m}_i = \frac{\dot{q}_r A_c + \rho_e u_e C_H (h_{aw} - h_c) A_c}{(h_{ie} - h_{ii})}$$

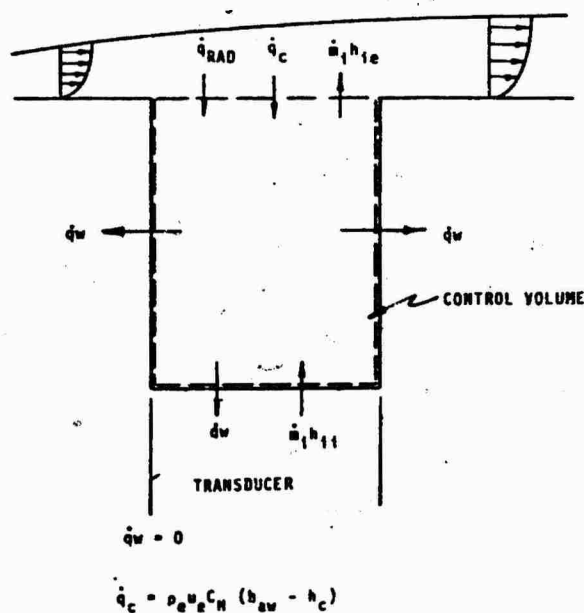


FIGURE 4-33 CONTROL VOLUME FOR DEFINING GAS PURGE FLOW RATE

4-136-1

Solving the above equation for purge flow rate as a function of cavity temperature gives the results shown in Figure 4-34 for both the char motor firing and the arc plasma generator tests. These results show that an average cavity temperature of 1000°R can be maintained for purge gas flow rates on the order of 0.010 lbs/sec. In order to be assured that this flow rate is obtained, the stagnation pressure for the purge system must be approximately twice the nozzle throat static pressure. For the motor being considered here, this means that the purge system stagnation pressure must be on the order of 1500 psia.

The conductive heat transfer from the ablative component to the transducer is a result of heat penetration from the nozzle surface. Previously, it was mentioned that the aperture should be approximately 1.0 inches below the original nozzle surface in order to keep the tip of the transducer below 1000°R. However, geometrical limitations make it impossible to have the transducer recessed this deep. To solve the problems of both the conductive heating and the geometrical limitation, the barrel of the transducer was tapered as shown in Figure 4-35.

With the convective and conductive heat transfer to the transducer minimized, acceptable copper temperatures can be maintained by using a heat sink cooling approach without having to use water cooling. The copper flange shown in Figure 4-17 was sized to prevent the average copper temperature at the end of a 60 second motor firing from exceeding 200°F. Advantages of the heat sink, rather than the water cooling approach, are that it simplifies the radiometer design, simplifies the nozzle assembly and on site supporting hardware, and simplifies the reduction of data.

The external configuration for the high pressure radiometer is shown in Figure 4-36. The components for this configuration are basically the same as those described for the radiometer shown in Figure 3-4. The configuration was dictated primarily by the installation and high purge pressure requirements for the high chamber pressure motors to be fired under Contract F04611-69-C-0065.\*

#### 4.2.2.2 System Configuration

Based on the reasoning described in Section 3.2, a narrow view angle radiometer was selected to measure the radiative heat flux from the opposite wall and the combustion products. These transducers are available as off the shelf items in several basic configurations. However, the configurations described in Section 4.2.2.1 are not standard configurations, and, thus, these transducers had to be fabricated as a specialty item. After Aerotherm had developed the requirements for the

---

\* High Chamber Pressure Nozzle Material Development, United Technology Center, Sunnyvale, California



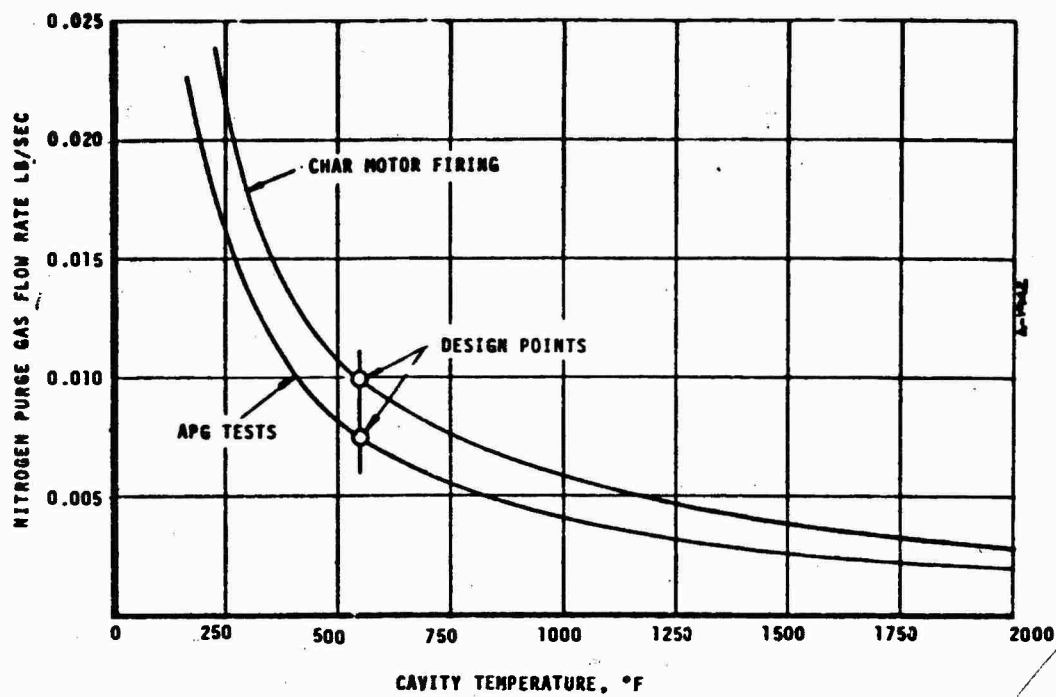


FIGURE 4-34 RADIOMETER PURGE GAS REQUIREMENTS

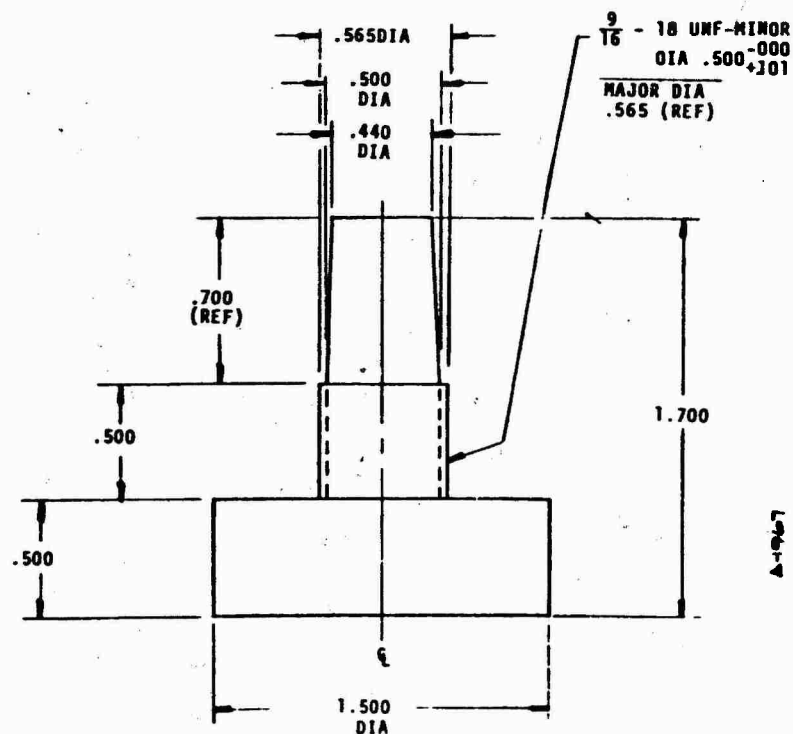


FIGURE 4-35  
NARROW ANGLE RADIOMETER



The housing of the radiometer as well as the heat sink is made from copper primarily because of the high thermal conductivity of this material which insures that the sink is at a uniform temperature. The sensor is composed of a thin blackened constantan disk. This material is particularly attractive because its thermal emf characteristics are known and because its sensitivity is approximately linear over the temperature range of interest. The sensor surface is blackened so that it absorbs all but a small percentage of the incident radiative flux. The gas purge line is a thin walled stainless steel tube which is brazed to the copper housing. This tube must be flexible, and it must be adequately joined with the copper housing so that a moderate amount of bending can be tolerated during the assembly of the radiometer in the steel housing.

The most critical item in assembling the radiometer in the nozzle is making sure that a good seal exists between the radiometer and the mating nozzle component. For the radiometers installed at the nozzle throat plane, the epoxy resin bond acts both as the seal and as the retention system. For the high pressure radiometer in the exit cone, the seal is made using an "O" ring which is compressed when the proper torque is applied to the radiometer. The installation of the radiometers in the nozzle is described in more detail in the following section.

#### 4.2.2.3 Installation

The narrow view angle radiometer at the nozzle throat is located in the MX 4926 ablative component as shown in Figure 4-37. The radiometer was bonded in the ablative component using Epon 828 resin with a Versamid 140 hardener. The primary bondlines are along the threaded portion of the barrel and along the face and sides of the 1.50 inch diameter heat sink. These bonds were cured prior to the installation of the ablative component in the steel shell. During the installation of the ablative component, the purge line, sensor leads, and thermocouple leads were routed through the opening in the steel shell.

The installation of the high pressure narrow view angle radiometer in the steel shell is shown in Figure 4-38. Since this radiometer was sized by the high chamber pressure motor application, considerable modification of the steel shell was required in order to achieve the proper installation. This modification was dictated by the cavity diameter, by the required recessed depth of the transducer, and by the method of transducer attachment. Since it was considered impractical to drill the cavity in the ablative component prior to installing it in the steel shell, then the cavity diameter must not exceed the diameter of the transducer. This dictated that the steel shell be

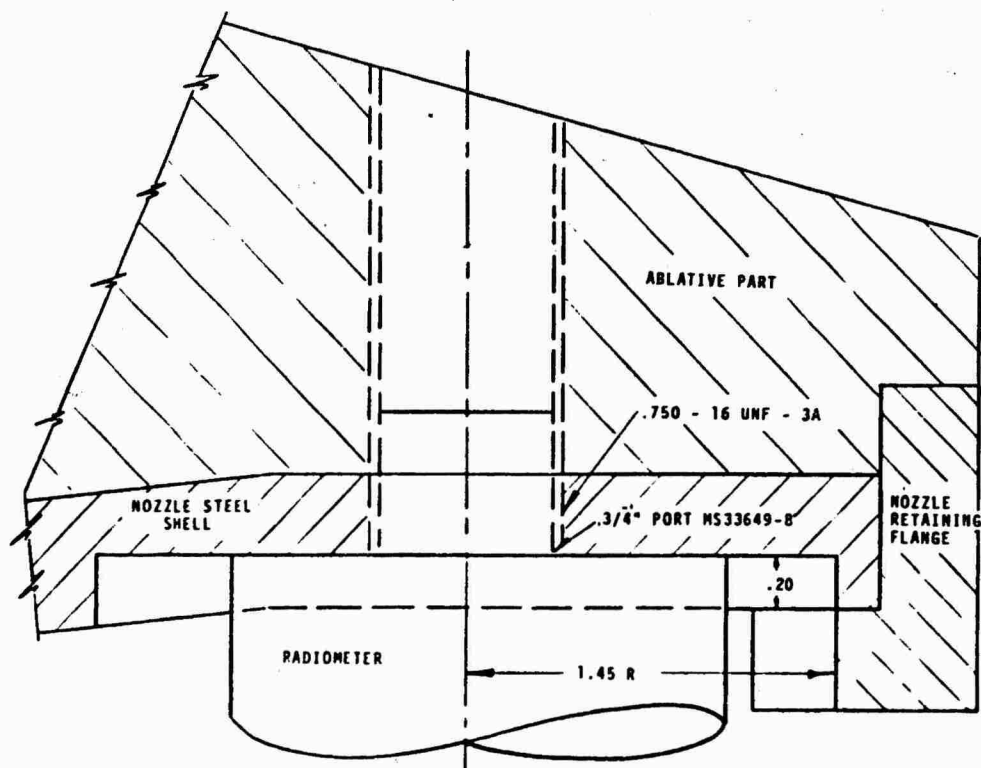
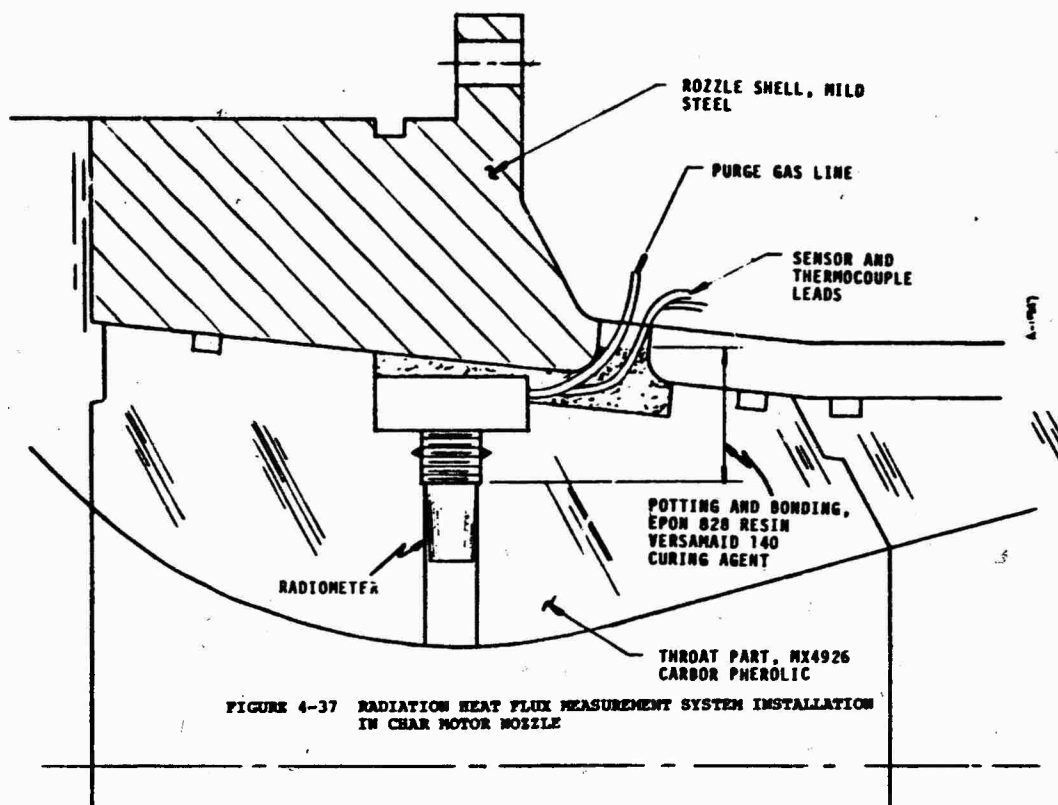


FIGURE 4-38 INSTALLATION OF HIGH PRESSURE RADIOMETER IN NOZZLE STEEL HOUSING

counterbored a maximum of approximately 0.20 inches, and that the upstream edge of the cavity be tapered. After allowing approximately 0.10 inches for the "O" ring groove, this leave 0.20 inches of thread engagement which is sufficient for the maximum expected static pressure at an expansion ratio of 3. The counterbore diameter is 2.90 inches which allows 1/2 inch on the radius for clearance of the gas purge line and thermocouple and sensor leads. The counterbore of the steel shell was machined prior to installing the ablative component. In addition, a small centering hole was machined. However the hole was not made in the steel shell and ablative component until after the nozzle assembly, including curing of the bondlines. After completing the necessary machining the radiometer and the "O" ring were installed using a torque of approximately 10 ft-lbs.

#### 4.2.2.4 Recording Instrumentation

Since the wires leading out of the radiometer are both copper (one being attached to the center of the constantan disk sensor and the other to the copper housing), an emf is measured which corresponds to the temperature drop across the sensor, and, thus, no reference temperature junction is required. This deletion of the reference temperature junction was the only difference between the recording circuit for the radiometer and that described in Section 4.1.2.4 for the thermocouple. The output from the thermocouple which was attached to the copper heat sink was recorded using the instrumentation circuit described in Section 4.1.2.4. Therefore, standard recording instrumentation was used for the radiometer as well as the thermocoupled plug.

#### REFERENCES

- 4-1 Moyer, C. B. and Rindal, R.A.: Finite Difference Solution for the In-Depth Response of Charring Materials Considering Surface Chemical and Energy Balances. Aerother Corporation, Mountain View, Calif., Final Report No. 66-7, Part II, March 14, 1967.
- 4-2 User's Manual, Aerotherm Charring Material Ablation Program, Version 2. Aerotherm Corporation, January 1966.
- 4-3 Kendall, R.M.: A General Approach to the Thermochemical Solution of Mixed Equilibrium-Nonequilibrium, Homogeneous on Heterogeneous Systems. Aerotherm Corporation, Mountain View, Calif., Final Report No. 66-7, Part V.
- 4-4 User's Manual, Aerotherm Equilibrium Surface Thermochemistry Program, Version 2, Aerotherm Corporation, June 1966.
- 4-5 Schaefer, J.W. and Dahm, T.J.: Studies of Nozzle Ablation Material Performance for Large Solid Boosters. NASA CR-72080, Aerotherm Report No. 66-2, December 15, 1966.
- 4-6 Schaefer, J. W., Dahm, T. J., Rodriguez, D. A., Reese, Jr. J. J., and Wool, M. R.: Studies of Ablative Material Performance for Solid Rocket Nozzle Applications. NASA CR-72429, Aerotherm Report No. 68-30, March 1, 1968.
- 4-7 McCuen, P., Schaefer, J., Lundberg, R., and Kendall, R.: A Study of Solid Propellant Rocket Motor Exposed Materials Behavior. Report Number AFRPL-TR-65-33, Vidya Report No. 149, Vidya Division of Itek Corp., February 26, 1965.
- 4-8 Moyer, C.B.: Axi-Symmetric Transient Heating and Material Ablation Program (ASTHMA) Description and User's Manual. Aerotherm Corporation, Final Report No. 68-27, January 15, 1968.
- 4-9 Roeser, Wm. F.: Thermoelectric Thermometry. Temperature, Its Measurement and Control in Science and Control in Science and Industry, Reinhold Publishing Co., 1941.
- 4-10 Brown, E.A., et al: Thermocouple Development for Project Rover. High Temperature Thermometry, Wash. 1067, March 1967.
- 4-11 Zemansky, M.W.: Heat and Thermodynamics. McGraw-Hill, 4th Edition, 1957.
- 4-12 Asamoto, R.R. and Novak, P.E.: Tungsten-Rhenium Thermocouples for Use at High Temperatures. The Review of Scientific Instruments, Volume 38, No. 8, August 1967.

REFERENCES (conc.)

- 4-13 Hall, Jr., B.F. and Spooner, N.F.: Temperature Measurement in a Graphite Environment. ISA Preprint 16.13-3-64, Presented at 19th Annual ISA Conference and Exhibit.
- 4-14 Supporting Data for ISA Preprint 16.13-3-64.
- 4-15 Private Communication with Mr. Norman McClure, Hoskins Manufacturing Co.
- 4-16 Tungsten-Rhenium Thermocouple Alloys, Hoskins Manufacturing Co.
- 4-17 Kline, S.J. and McClintock, F.A.: Describing Uncertainties in Single-Sample Experiments, Mech. Engr., P. 3, January 1953.
- 4-18 Baker, D.L.: Evaluation of Thermochemical Analysis Techniques, Thermochemical Screening, and Thermal Instrumentation Methods for High Pressure Solid Rocket Motors (U), Aerotherm Report 69-52, August 15, 1969, (Confidential).

## SECTION 5

### DATA REDUCTION

The basic data measured by the two heat flux measurement systems described in Section 4 must be properly reduced to define the desired total and radiative fluxes. These procedures are described in this section. Section 5.1 describes the procedure for relating the in-depth thermocouple output from the total heat flux measurement system to a total surface heat flux. Section 5.2 describes the procedure for relating the millivolt output of the narrow angle directional radiometer to a total surface radiative heat flux.

#### 5.1 TOTAL HEAT FLUX SYSTEM

The data reduction procedure for the total heat flux measurement system requires the conversion of data which define the temperature histories at five in-depth locations in the material to total heat flux at the material surface. The details of this procedure are presented in this section. Section 5.1.1 discusses the reduction of the recorded data to temperature histories and Section 5.1.2 discusses the conversion of these temperature histories to total heat flux. Finally, Section 5.1.3 discusses the accuracy of these total heat fluxes as related primarily to uncertainties associated with the data reduction process.

##### 5.1.1 Definition of Temperature Histories

The definition of the temperature histories is straightforward and employs standard data reduction techniques. The continuously recorded thermocouple output, in the form of millivolts or in the form of galvanometer deflection, is converted to temperature through appropriate calibration curves. (In the latter case, an intermediate step to convert galvanometer deflection to millivolts is typically required.) The calibration curve is a fit of the thermocouple temperature - emf characteristic which normally falls within  $\pm 1$  percent of the actual thermocouple calibration. Chromel/Alumel thermocouple wire typically agrees very closely with the NBS standard and therefore a fit of this standard calibration may be used. Tungsten 5 percent rhenium/tungsten 26 percent rhenium has no NBS standard and therefore a fit of the actual calibration for the particular wire used or the manufacturers accepted calibration is employed. The manufacturers actual or accepted calibration



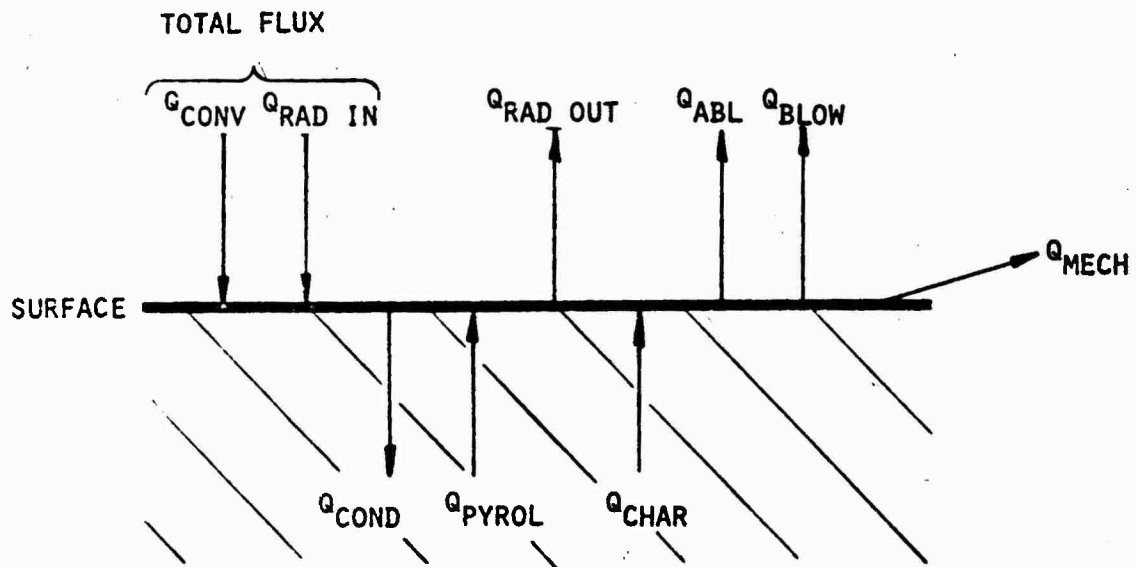
typically goes up to 4200°F only but the fit may be extended to 5400°F based on the results of Reference 4-12.

The recorded thermocouple output and the reduced data are subjected to close scrutiny to relate thermocouple failure to surface recession and to relate the temperature at thermocouple failure to surface temperature. Any anomolous behavior is noted for consideration in the subsequent data reduction process.

#### 5.1.2 Definition of Total Heat Flux

The basic experimental results in the form of in-depth temperature histories discussed in the previous section provide the basis for the conduction solution and definition of total heat flux. The sequence of events in this procedure is 1) the definition of certain energy flux terms, surface recession, and surface temperature, based primarily on the measured temperatures, 2) the definition of other necessary flux terms related primarily to the surface thermochemical response, and then 3) the definition of the desired total heat flux. The background behind this procedure and the mechanics of accomplishing it are presented in the following paragraphs.

The energy balance at the surface of a charring ablator is shown in the sketch below (see also Figure 3-1). These flux terms vary with time due to the transient response of the material and



due to surface recession. The flux terms in the sketch are defined as follows:

- convective heat flux

$$q_{\text{conv}} = \rho u C_{H_2O} (h_r - h_w)_s + \rho u C_{M_0} \sum_i (z_{ie} - z_{iw}) h_i^{T_w} \text{ which reduces to the more familiar } \rho u C_{H_2O} (h_r - h_w)_t \text{ for unity Lewis number and equal diffusion coefficients}$$

- radiation heat flux from the free stream and/or opposite wall

$$q_{\text{rad in}} = \epsilon_{\text{eff}} \sigma T_{\text{eff}}^4 \text{ where this equation is more descriptive than computationally solvable}$$

- heat flux conducted into the material

$$q_{\text{cond}} = - \left( k \frac{\partial T}{\partial x} \right)_w$$

- radiation heat flux from the wall

$$q_{\text{rad out}} = \epsilon_w \sigma T_w^4$$

- energy flux due to pyrolysis gas convection

$$q_{\text{pyrol}} = (\dot{m}_g h_g)_w$$

- energy flux due to char convection

$$q_{\text{char}} = \dot{m}_c h_{c_w} = \dot{m}_c \rho_c h_{c_w}$$

- energy flux due to convection of the ablation products

$$q_{\text{abl}} = (\rho v)_w h_w$$

- convective heat flux decrement due to blowing at the wall

$$q_{\text{blow}} = \left(1 - \frac{\zeta}{e^{\zeta} - 1}\right) q_{\text{conv}} \quad \text{where } q_{\text{conv}} \text{ is defined above, net}$$

convective flux to the wall is  $q_{\text{conv}} - q_{\text{blow}} =$

$$\frac{\zeta}{e^{\zeta} - 1} q_{\text{conv}}$$

- energy flux due to mechanical removal of condensed phase

$$q_{\text{mech}} = \dot{m}_* h_{*w}$$

The sum of the first two terms above,  $q_{\text{conv}} + q_{\text{rad in}}$ , is the desired total heat flux which is given by\*

$$q_{\text{conv}} + q_{\text{rad in}} = q_{\text{cond}} + q_{\text{rad out}} + q_{\text{abl}} + q_{\text{blow}} - q_{\text{pyrol}} - q_{\text{char}} + q_{\text{mech}} \quad (5-1)$$

The data reduction procedure encompasses the evaluation of the terms on the right of Equation (5-1) from the primary measurements of internal temperature.

The first step is an internal conduction calculation using the Charring Material Ablation (CMA) computer program (Reference 4-1) wherein the surface recession and surface temperature histories are specified (Option 2). This calculation is performed iteratively by successive inputs of surface recession and surface temperature histories until good agreement between the measured and calculated in-depth temperature histories is achieved.\*\* The initial inputs are based on the measured in-depth temperature histories and the post-test measured recession. The final inputs for which good agreement between in-depth temperatures is achieved define the actual surface and in-depth response of the material in terms of:

\* The theoretical details of the surface energy balance and the terms therein are presented in References 4-1 and 4-2.

\*\* This same procedure has been used successfully in a reverse fashion wherein the surface boundary conditions were known and the material thermal conductivity was determined by requiring a match of the measured and calculated in-depth temperatures (References 4-5, 4-6, and 5-1).

conduction heat flux,  $q_{\text{cond}}$   
 radiation heat flux from the wall,  $q_{\text{rad out}}$   
 pyrolysis off gas energy flux,  $q_{\text{pyrol}}$   
 char energy flux,  $q_{\text{char}}$   
 surface recession,  $s$   
 surface temperature,  $T_w$   
 pyrolysis off gas rate,  $\dot{m}_g$   
 char removal rate,  $\dot{m}_c$

Note that all these terms are a function of time through the test or firing. The solution of the energy balance, Equation (5-1), is now reduced to

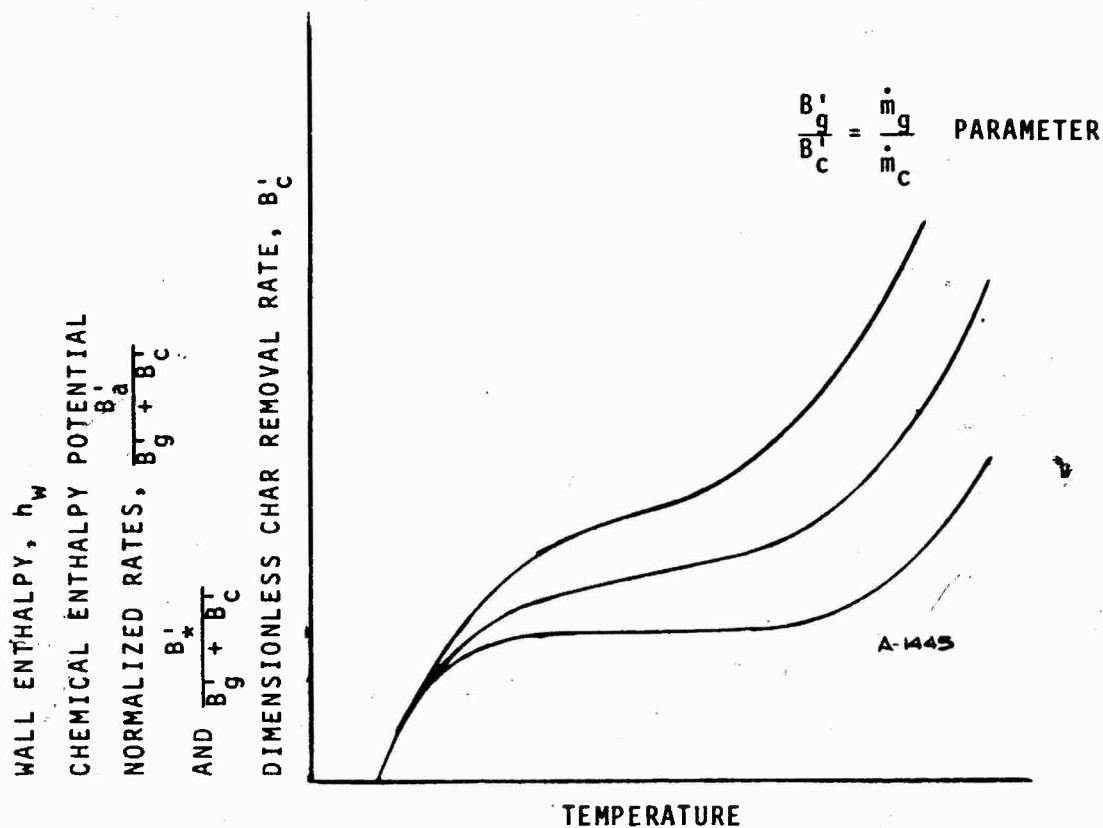
$$q_{\text{conv}} + q_{\text{rad in}} = \Sigma (\text{known } q's) + q_{\text{abl}} + q_{\text{blow}} + q_{\text{mech}} \quad (5-2)$$

The above results, together with a parametric calculation of the surface thermochemical response using the Aerotherm Chemical Equilibrium (ACE) computer program (Reference 4-3), allow the calculation of the other required terms. For the materials of interest herein, diffusion rate controlled (equilibrium) surface thermochemistry is valid and is required in the calculations. The program output provides the following information as a function of surface temperature, dimensionless off gas rate  $B'_g$ , and dimensionless char removal rate  $B'_c$ :

dimensionless gas phase ablation rate,  $B_a = (\rho v)_w / \rho u C_M$   
 dimensionless condensed phase removal rate,  $B_* = \dot{m}_* / \rho u C_M$   
 wall enthalpy,  $h_w$   
 recovery enthalpy,  $h_r$   
 chemical enthalpy potential,  $\Sigma (Z_{ie} - Z_{iw}) h_i^{T_w}$   
 transport properties, specifically Lewis number,  $Le$ , where

$$C_M / C_H = Le^{2/3}$$

Plots of this output in the form shown below allow the calculation of the remaining flux terms.



The energy flux due to convection of the ablation products from the surface is given by

$$q_{abl} = (\rho v)_w h_w = (\dot{m}_g + \dot{m}_c) \frac{B_a'}{B_g' + B_c'} h_w \quad (5-3)$$

where  $\dot{m}_g$  and  $\dot{m}_c$  are available from the conduction solution and the other two terms are available from the surface thermochemistry solution (see the above plot). The energy flux due to mechanical removal, if appropriate, is given by

$$q_{mech} = m_* h_* = (\dot{m}_g + \dot{m}_c) \frac{B_*'}{B_g' + B_c'} h_w \quad (5-4)$$

where the terms are available as above, except that the condensed phase enthalpy is a function of the surface temperature only.

The calculation of the convective heat flux decrement due to blowing requires the definition of the heat and mass transfer coefficients. The dimensionless char removal rate  $B_c'$  is first determined from a plot of the form above. The mass transfer coefficient is then calculated from the defining relation between  $\dot{m}_c$  and  $B_c'$

$$\rho u C_M = \dot{m}_C / B'_C \quad (5-5)$$

and the heat transfer coefficient calculated from Colburn's analogy

$$\rho u C_H = \rho u C_M Le^{-2/3} \quad (5-6)$$

The blowing reduction flux is given by

$$q_{\text{blow}} = \left(1 - \frac{\zeta}{e^\zeta - 1}\right) q_{\text{conv}} = \left(1 - \frac{\zeta}{e^\zeta - 1}\right) \left[ \rho u C_{H_O} (h_r - h_w) + \rho u C_{M_O} \sum_i (z_{ie} - z_{iw}) h_i^T \right] \quad (5-7)$$

where  $\zeta = 2\lambda(\rho v)_w / \rho u C_{M_O}$ . Note, however, that  $\rho u C_{H_O}$  and  $\rho u C_{M_O}$  are not known, rather  $\rho u C_H = \frac{\zeta}{e^\zeta - 1} \rho u C_{H_O}$  and  $\rho u C_M = \frac{\zeta}{e^\zeta - 1} \rho u C_{M_O}$

only are known. Some simple algebraic manipulation, however, yields a solvable expression for  $\zeta$

$$e^\zeta - 1 = \frac{2\lambda(\rho v)_w}{\rho u C_M} = 2\lambda B'_a \quad (5-8)$$

from which  $\rho u C_{H_O}$  and  $\rho u C_{M_O}$  can be calculated and Equation (5-7) solved. Note that the chemical enthalpy term in Equation (5-7) is also determined from a plot of the form above.

With all flux terms on the right of Equation (5-1) now calculated, the total heat flux is available by the summation of these terms.

### 5.1.3 Accuracy of Total Heat Flux

The sources of error in the calculation of total heat flux by the method described in Section 5.1.2 are uncertainties in the primary temperature measurement, in the internal conduction solution, and in the surface equilibrium calculation. The severity of errors introduced due to the mathematical modeling of physical events is difficult to assess. Based on past experience with the analytical technique utilized in the heat flux analysis, however, the accuracy of calculated results can be approximated. Sources of uncertainty in the temperature measurements, the conduction solution, and the thermochemical model are discussed below.

The overall uncertainties in the measured in-depth temperatures were presented in Section 4.4. Their estimated values at high temperature are  $-75^{\circ}\text{R}$  and  $+15^{\circ}\text{R}$  for carbon phenolic and  $-125^{\circ}\text{R}$  and  $+150^{\circ}\text{R}$  for silica phenolic. These potential errors, of course, propagate through the subsequent data reduction procedures.

The accuracy of the internal conduction solution is dependent upon the material response model employed, the thermophysical and degradation properties input, the experimental in-depth temperature response, and the sensitivity of the iterative procedure. Experience has shown that, for the materials utilized in this program, the response model and material properties give accurate results. Also, the iterative procedure is quite sensitive to the input values of surface recession and surface temperature. Therefore, the final values of the  $q_{\text{cond}}$ ,  $q_{\text{char}}$ ,  $q_{\text{pyro}}$ ,  $q_{\text{rad out}}$ ,  $s$ , and  $T_w$  histories are expected to be within the accuracy limitations of the in-depth temperature determinations on which the iteration is based.

The sensitivity of the conduction solution to the in-depth temperature uncertainties was studied by parametrically varying the surface temperature and surface recession rates about the values calculated in the NASA/Aerojet 260-SL-3 nozzle prediction presented in Reference 4-6. Figure 5-1 presents a graphical display of some important results of the parametric study at 30 seconds through the firing. It defines the dependence of the predicted in-depth temperature profile on a  $\pm 200^{\circ}\text{R}$  variation of surface temperature. Conversely, the effect of in-depth thermal response uncertainties on surface temperature accuracy can be evaluated for a given surface location uncertainty. Note that the range of uncertainty is represented by the shaded region. Also, the uncertainty values chosen for the analysis were extreme and are more illustrative than real. It is apparent that the uncertainty in the surface location and in-depth temperature has a strong effect on the surface temperature. For the combined extremes considered,  $\pm 0.025$  inch and  $\pm 200^{\circ}\text{R}$ , the surface temperature is within  $\pm 400^{\circ}\text{R}$  of the true value in the case considered. More realistic uncertainty values (Section 4.4 and above) yield approximate surface temperature

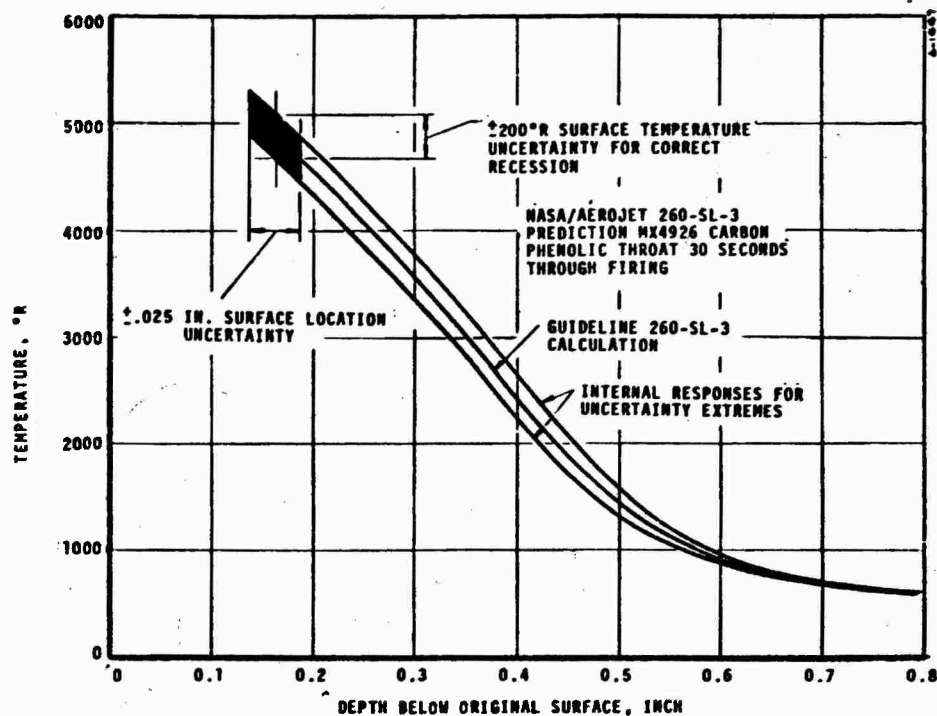


FIGURE 5-1 EFFECT OF MEASUREMENT UNCERTAINTIES ON THE DETERMINED SURFACE TEMPERATURE

uncertainties of  $-125^{\circ}\text{R}$  and  $+25^{\circ}\text{R}$  for carbon phenolic and  $-200^{\circ}\text{R}$  and  $+75^{\circ}\text{R}$  for silica phenolic in the char motor nozzle.

The parametric calculations of the 260-SL-3 nozzle response were also utilized to assess the effects of conduction solution uncertainties on the calculated total heat flux. For each CMA conduction solution the total heat flux was calculated so that the effects of surface temperature or recession errors could be evaluated. The variation of surface recession had only a slight effect on the various heat flux terms; however, the total heat flux was quite sensitive to the variation of surface temperature. Figure 5-2 quantitatively relates surface temperature uncertainty to a corresponding uncertainty in total heat flux. The sensitivity is primarily due to the dominance of the radiation and conduction heat flux terms (both strongly dependent on surface temperature) in the surface energy balance. A  $\pm 4$  percent ( $\pm 200^{\circ}\text{R}$ ) uncertainty in surface temperature represents a  $-13$  percent and  $+18$  percent uncertainty in total incident heat flux. If the results of Figure 5-2 are applied to the more accurate uncertainties of the previous paragraph, the resultant error band in total heat flux is  $-8$  percent and  $+2$  percent for carbon phenolic and  $-15$  percent and  $+8$  percent for silica phenolic. Note that the results for silica phenolic are estimates since Figure 5-2 is strictly valid only for carbon phenolic response.



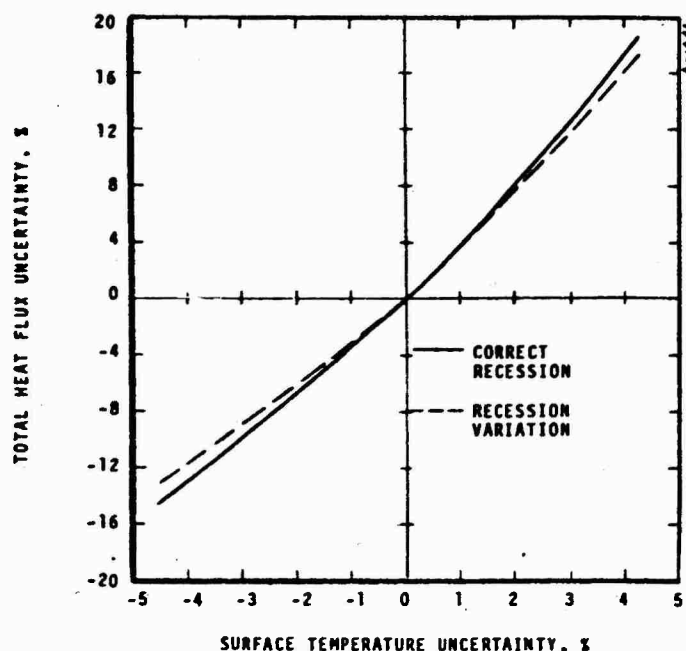


FIGURE 5-2 SENSITIVITY OF TOTAL HEAT FLUX TO SURFACE TEMPERATURE UNCERTAINTY

The above uncertainties assume that the heat flux terms based on the surface thermochemical response ( $q_{abl}$ ,  $q_{blow}$ ,  $q_{mech}$ ) are completely accurate. Realistically this is not the case, and account must be taken of their contribution to the error in total heat flux. These terms are small, however (e.g. see the table of Section 5.1.2), and therefore the impact of any errors in their values on the total heat flux is also small.

Summarizing the various sources of error, the overall accuracy of the determined total heat flux is estimated in the table below.

<u>Carbon Phenolic</u>	<u>Silica Phenolic</u>
-11 percent	-20 percent
+ 5 percent	+13 percent

The error analysis was done on a conservative analytical basis and, therefore, these values are felt to be outside extremes; the actual accuracy is probably better than indicated.

## 5.2 RADIATIVE HEAT FLUX SYSTEM

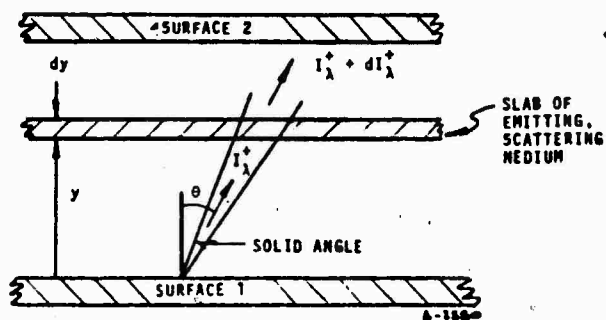
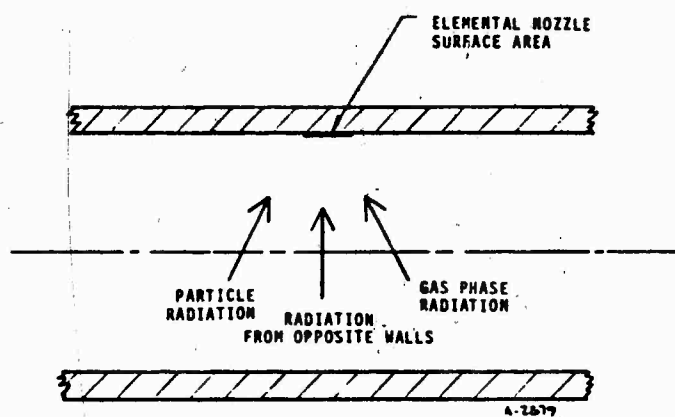
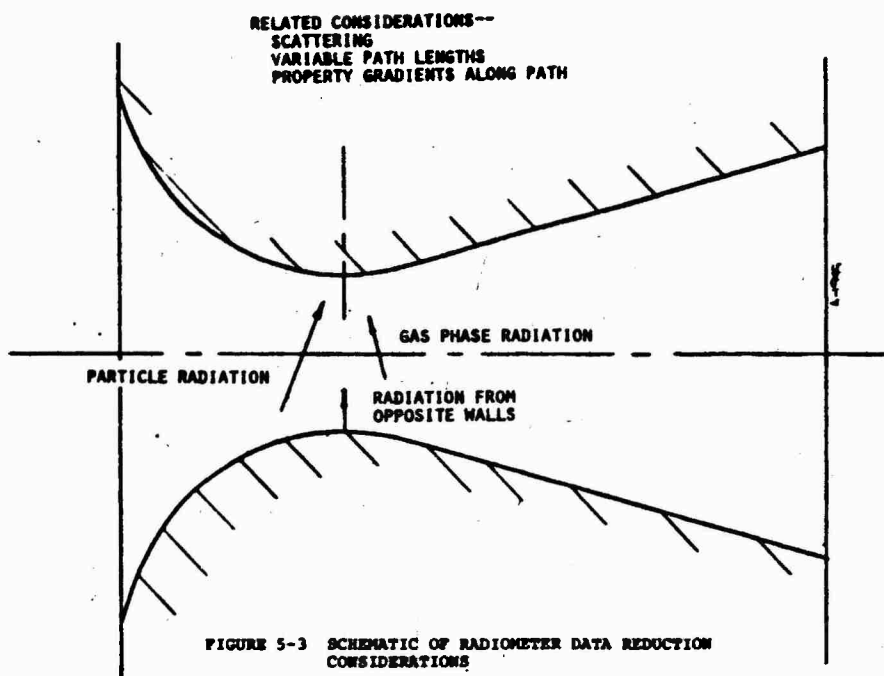
The data reduction procedure requires the conversion of the emf output from the sensor to a total hemispherical radiative heat flux. For this conversion to be meaningful, one must understand the simplifying assumptions which are made, and these are discussed in Section 5.2.1. The accuracy of the measured radiative heat flux is discussed in Section 5.2.2.

### 5.2.1 Definition of Radiative Heat Flux

The factors considered in selecting a narrow view angle radiometer to measure the total radiative heat flux to the nozzle surface were defined in Section 3.2. The topic to be considered here is the assumptions which were made to relate the output from the narrow view angle radiometer to a total hemispherical radiative heat flux.

The total radiative flux to an elemental area on the nozzle surface is a complicated function of the absorbing and scattering characteristics of the particle laden combustion products. It is complicated further by the geometry of the internal flow contour (Figure 5-3). Even though the cross sectional area of the nozzle throat and exit cone is axisymmetric, a surface elemental area has a field of view which varies in a complicated manner with the axial location. Since the basic features of the governing radiative transport equation are more easily understood by considering a simplified geometrical model, the model considered here is represented by two planar parallel slabs separated by an absorbing, scattering media. The slabs simulate the nozzle surface, and the media is representative of the particle laden combustion products for a solid propellant. A schematic of this simplified model is shown in Figure 5-4. The physical model for developing the governing radiative transport equation is shown in Figure 5-5. Note that the temperature of the media is assumed to be only a function of  $y$  and that the total intensity of radiation,  $I_\lambda(y, \theta)$ , is a result of the contributions in the positive  $y$  direction,  $I_\lambda^+(y, \theta)$ , and in the negative  $y$  direction,  $I_\lambda^-(y, \theta)$ . If the elemental surface area is on surface 2, the total intensity of radiation is given by  $I_\lambda^+(y, \theta)$ . If one assumes that the media is stationary and that the particle scattering is isotropic and coherent, then the governing radiative transport equation is (Reference 5-2)

$$I_\lambda^+(\tau_{0\lambda}, \mu) = I^+(0, \mu) e^{-\tau_\lambda/\mu} + \frac{1}{\pi} \int_0^{\tau_{0\lambda}} \frac{1}{\beta_\lambda} \left[ \kappa_\lambda e_{b\lambda}(t) + \frac{\gamma_\lambda}{4} G_\lambda(t) \right] e^{-(\tau_{0\lambda}-t)/\mu} \frac{dt}{\mu} \quad (5-8)$$



where

$e_{b\lambda}$  - Planck's monochromatic blackbody emissive power

$G_\lambda$  - scattering function

$\kappa_\lambda$  - absorption coefficient

$\gamma_\lambda$  - scattering coefficient

$\beta_\lambda$  - extinction coefficient

$\lambda$  - wavelength

$\mu$  -  $\cos\theta$

$\tau_{o\lambda}$  - optical depth

The first term in Equation (5-8) represents the energy emitted by surface 1 which is incident on surface 2. Note that the energy leaving surface 1 has been attenuated due to the absorption and scattering of the medium. The integral term in Equation (5-8) represents the effect of the emitting and scattering medium. The variables  $e_{b\lambda}$ ,  $G_\lambda$ ,  $\beta_\lambda$ , and  $\tau_{o\lambda}$  are given by

$$e_{b\lambda} = \frac{C_1}{n^2 \lambda^5 \left( e^{\frac{C_2}{n\lambda T}} - 1 \right)} \quad (5-9)$$

where

$C_1, C_2$  - radiative constants

$n$  - index of refraction

$T$  - temperature

$$G_\lambda = 2\pi \int_0^\pi I_\lambda(y, \theta') \sin\theta' d\theta' \quad (5-10)$$

$$\beta_\lambda = \kappa_\lambda + \gamma_\lambda \quad (5-11)$$

$$\tau_{o\lambda} = \int_0^L \beta_\lambda dy \quad (5-12)$$

Because the intensity of radiation is under the integral sign in Equation (5-10), Equation (5-8) is difficult to solve.

The total flux absorbed by the sensor of the narrow view angle radiometer is obtained by integrating Equation (5-8) with respect to the appropriate angle and with respect to wavelength. This is represented by

$$\dot{q}_r = \int_{\lambda=0}^{\infty} \int_0^{w_l} \epsilon_{\lambda}' \tau_{\lambda}' I_{\lambda}(\tau_{o\lambda}, \mu) \cos \theta d\omega d\lambda \quad (5-13)$$

where

- $w$  - solid angle
- $w_l$  - the integration limit on the solid angle
- $\epsilon_{\lambda}'$  - emissivity of sensor coating
- $\tau_{\lambda}'$  - transmissivity of sapphire lens

When the narrow view angle radiometer is exposed to the calibration source, the radiation flux absorbed by the sensor,  $\dot{q}_{rc}$ , is given by

$$\dot{q}_{rc} = \int_{\lambda=0}^{\infty} \epsilon_{\lambda}' \tau_{\lambda}' I_{b\lambda} \int_0^{w_l} \cos \theta d\omega d\lambda \quad (5-14)$$

Since the total hemispherical radiative flux from a blackbody source is given by

$$\dot{q}_{rcb} = \pi \int_{\lambda=0}^{\infty} I_{b\lambda} d\lambda \quad (5-15)$$

then, if one assumes that  $\epsilon_{\lambda}'$  and  $\tau_{\lambda}'$  are independent of wavelength Equations (5-14) and (5-15) can be combined to give

$$\frac{\dot{q}_{rc}}{\dot{q}_{r_{cb}}} = \frac{\epsilon' \tau' \int_0^{w_l} \cos \theta dw}{\pi} \quad (5-16)$$

Note that the ratio of the integral term to  $\pi$  is the view factor, that the sensor has of the radiation source.

During the calibration of the narrow view angle radiometer, an emf is measured, and this emf is related to a total hemispherical radiative heat flux which is measured using a calibrated standard. As a first approximation, this calibration procedure has the effect of measuring  $\dot{q}_{rc}$ , which is then related to the total blackbody hemispherical flux,  $\dot{q}_{r_{cb}}$ , using Equation (5-16).

In the data reduction procedure, the total hemispherical radiative flux is reported. However, this flux can be related to a particular radiation source only if certain restrictive assumptions are made. For example, if one assumes that 1) the radiation emitted by the particle laden combustion products is negligible, 2) the scattering coefficient for these products is zero, and 3) the opposite wall emits as a constant temperature gray body, then the reported total hemispherical heat flux is a true indication of the radiative heat flux from the opposite wall. Another set of assumptions which isolate the radiation source are 1) the scattering coefficient for the combustion products is zero, 2) the radiation intensity is independent of direction, and 3) the particle laden combustion products are optically thick. These latter set of assumptions are more realistic for calculating the radiative flux from the combustion products of a solid rocket motor, and, when used, the total heat flux emitted by the slab of combustion products,  $\dot{q}_{r_G}$ , is

$$\dot{q}_{r_G} = \int_{\lambda=0}^{\infty} 2 \int_0^{\tau_{0\lambda}} e_{b\lambda} E_2(\tau_{0\lambda} - t) dt \quad (5-17)$$

where  $E_2(t)$  is an exponential integral function. If the monochromatic form of this heat flux is set equal to

$$\dot{q}_{r_{G\lambda}} = \epsilon_{G\lambda} e_{b\lambda} \quad (5-18)$$

where  $\epsilon_{G\lambda}$  is a hemispherical monochromatic emittance. Then, assuming a constant temperature, Equations (5-17) and (5-18) can be combined to give

$$\epsilon_{G\lambda} = 1 - 2E_3(\kappa_\lambda L) \quad (5-19)$$

For an optically thick medium, the exponential integral in Equation (5-19) is zero which results in the emittance being equal to one. In this case, the combustion products radiate as a blackbody. For finite values of the monochromatic emittance which are independent of wavelength, the combustion products radiate as a gray body. In either case, the measured radiative heat flux is a true indication of the amount of radiation being emitted by the combustion products (within the assumption of a constant temperature).

Since a detailed partitioning of the measured total hemispherical radiative flux into components from the various radiation sources in a solid propellant environment is beyond the scope of the present study, the data reduction procedure is simply a conversion of the measured emf output from the narrow view angle radiometer to a total hemispherical radiative flux. This conversion is performed using the calibration supplied by the manufacturer. As discussed above, this is strictly valid only for the two sets of limiting assumptions presented above - essentially either a transparent stream or an opaque stream.

#### 5.2.2 Accuracy of Radiative Heat Flux

Based on the assumptions that the combustion products viewed by the radiometer 1) are an optically thick radiation source which is at constant temperature and 2) have an emissivity which is independent of wavelength, then the accuracy of the hemispherical radiation heat flux is identical to that given in Table 4-5 (page 4-51) for the heat flux absorbed by the sensor. The accuracy of the radiometer system stated in this table was +2.5/-3 percent.

#### REFERENCES

- 5-1. Baker, D. L., Wool, M. R., and Schaefer, J. W.: A Dynamic Technique for Determining the Thermal Conductivity of Charring Materials. Paper presented at Eighth Conference on Thermal Conductivity.
- 5-2. Sparrow, E. M. and Cess, R. D.: Radiation Heat Transfer. Brooks/Cole Publishing Co., August 1967 (Second Printing).



## SECTION 6

### TEST EVALUATION PROGRAM

The total heat flux and narrow view angle radiometer measurement systems were evaluated under laboratory test conditions typical of a rocket nozzle application in the Phase II test program. The purpose of this program was to demonstrate the measurement systems prior to subjecting them to the char motor firings at AFRPL. The Phase II test program is described in Section 6.1. The results of this program are presented in Section 6.2 for the total heat flux system and in Section 6.3 for the radiometer system.

#### 6.1 PHASE II TEST EVALUATION PROGRAM

The objectives of the Phase II test evaluation program were to verify the measurement system design and fabrication technique and to verify the data reduction procedure and firmly define the total heat flux accuracy. The tests were performed under laboratory conditions typical of a solid rocket nozzle and for which the total heat flux and other important variables which are calculated in the measurement system data reduction procedure are known.

The Aerotherm arc plasma generator (APG), Figure 6-1, was used to provide the solid propellant exhaust simulation, and a two-dimensional nozzle test section, Figure 6-2, was used as the rocket nozzle. In the APG, energy is added electrically to the test gas by a continuous arc discharge. Two test gases were used in this test program; both closely duplicate the specific heat of typical aluminized solid propellants but one is chemically inert (Mixture 5) and the other is chemically reactive (Mixture 4). In Mixture 4, the oxidation potential of typical solid propellants is duplicated (Reference 4-7). The chemical compositions of these test gases are presented in the table below and further background on their selection is presented in References 4-5 through 4-7. For Mixture 5, no surface recession occurs for MX 4926 carbon phenolic; this allows the evaluation of the measurements system for the simpler case of no surface recession and the identification of any basic problems that might have otherwise been obscured. For Mixture 4, the material response closely duplicates that in an actual nozzle. This provides the complete evaluation of the measurement system at conditions typical of its application.

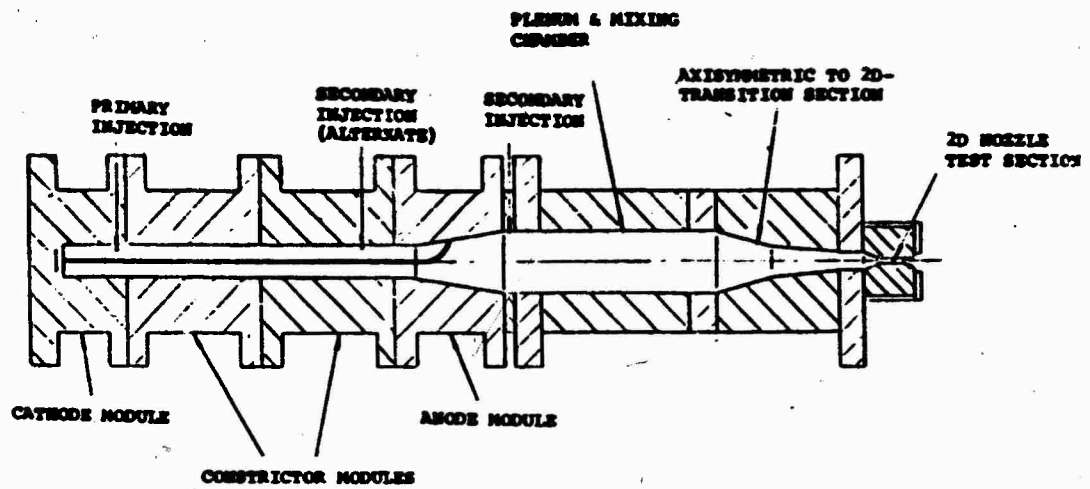


FIGURE 6-1 AEROTHERM CONSTRICTOR ARC, ROCKET SIMULATOR CONFIGURATION

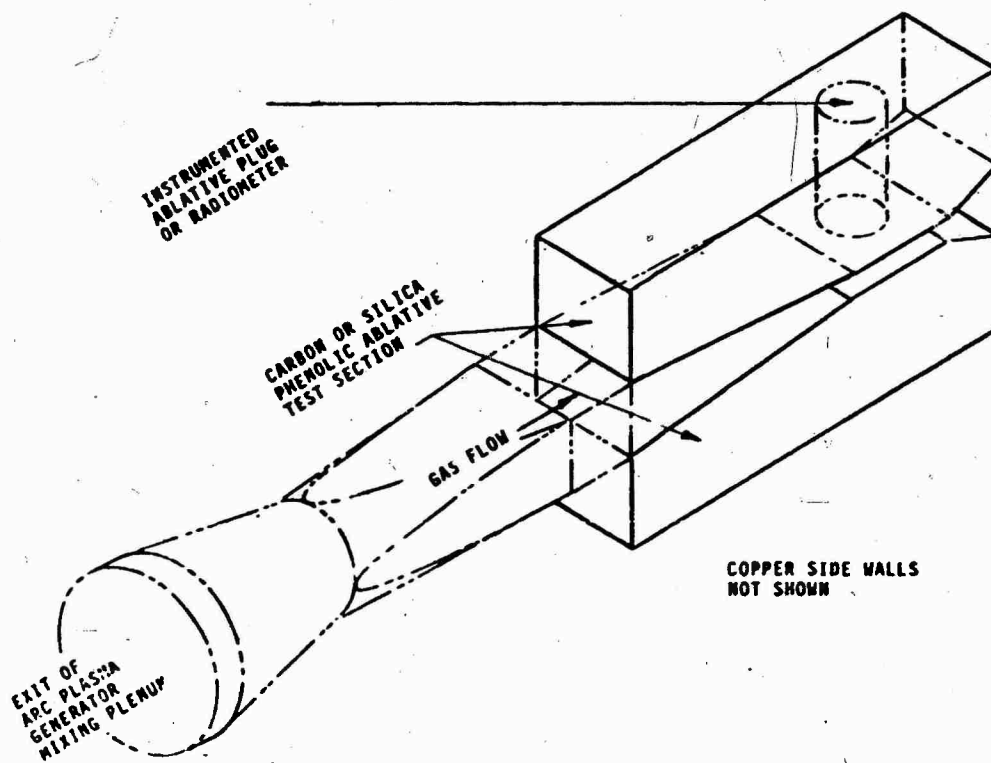


FIGURE 6-2 TWO-DIMENSIONAL NOZZLE TEST CONFIGURATION

A-1568

# ELEMENTAL MASS FRACTIONS

	<u>Mixture 4</u>	<u>Mixture 5</u>
Helium	0.228	0.224
Nitrogen	0.619	0.776
Oxygen	0.153	--

In addition to providing a test section which has a relatively constant heat flux, the two-dimensional nozzle eliminates the effect of surface curvature in the evaluation of the thermocouple plug. Since these plugs will be used in nozzle which have a local radius which is large compared to the radius of the plug, the two-dimensional nozzle provides a better geometrical simulation than an axisymmetric nozzle with the same throat area. The test sections were fabricated by rocket nozzle techniques to insure that the fabrication process was not a variable. The measurement system thermocouple plug or radiometer was located at the throat in all the evaluation tests since the test conditions can be more accurately defined at this location. The layup angle in all test sections was 60°, equal to or close to that for the measurement system locations in the char motor nozzle. The test section opposite the measurement system test section was the same material as the measurement system test section or was water-cooled copper. In the former case the radiation flux to the measurement system ( $q_{rad}$  in) was finite and in the latter case it was zero. This provided another boundary condition variable which allowed the identification of any basic problems which might have otherwise been obscured. The plug design, fabrication technique, and installation procedure used in these tests were identical to that used in the char motor except for necessary changes in plug length and thermocouple locations. These items are discussed in more detail in Sections 6.2 and 6.3.

The nominal test matrix for the Phase II test evaluation program is presented in Table 6-1. All of the test variables discussed above were included in the test matrix and two sets of duplicate tests were included to check repeatability of results. Note that since surface recession would be expected to occur for silica phenolic in both the inert and reactive environments, only the more complete simulation case, Mixture 4, was considered for this material. In addition to the tests indicated in the table, calibration tests were performed at each test condition to measure the cold wall heat flux at the nozzle throat. For those tests, the material test section was replaced by a water-cooled calorimeter test section for measurement of convective flux.

The chamber conditions achieved during the APG tests together with the material ablative performance are summarized in Table 6-2. By comparing the results of Tests 1317 and 1318 which used carbon phenolic test sections and Tests 1320 and 1321 which used silica phenolic test sections, one notes that approximately identical

TABLE 6-1  
NOMINAL PHASE II TEST MATRIX

Test	Measurement System Type	Material	Layout Angle	Chemical Environment	Total Temperature (°R)	Chamber Pressure (psia)	Cold Wall Convective Heat Flux (Btu/ft²sec)	Radiative Heat Flux to Wall (Btu/ft²sec)
1	Total	NH4926 Carbon Phenolic	60°	Mixture 4 (reactive)	6000	100	1000	200
2								
3								0
4				Mixture 5 (inert)				200
5		NH2600-96 Silica Phenolic		Mixture 4 (reactive)	5000		900	90
6								
7								
8	Radiation	NH4926 Carbon Phenolic			6000		1000	200
9								0

TABLE 6-2  
SUMMARY OF TEST CONDITIONS AND TEST RESULTS

Test No.	Measurement System	Instrument Model Material	Opposite Wall Material	Gas Mixture	Nominal Enthalpy (Btu/lb)	Maximum Pressure (psia)	Average Wall Temp (°R)	Surface Recession (mils)	Average Recession Rate (mils/sec)	Test Time (sec)
1317	Total	NH4926	NH4926	4	3900	119	4500	41.0	0.002	46.4
1318				4	3950	120	4450	41.5	0.006	46.0
1319				9	3300	150	4450	-17.0	--	46.7
1320		NH2600-96	NH2600-96	4	3400	132	4100	50.0	3.47	16.7
1321				4	3250	120	4250	70.0	3.19	24.4
1322			Cold		3050	120	3950	70.0	1.41	49.6
1323		NH4926			2150	115	4250	44.8	0.959	46.1
1324	Radiometer		NH4926		3900	131	4500	--	--	46.0
1325					4000	120	4400	--	--	47.3

chamber conditions produced identical material ablative performance, thus indicating repeatability of performance. Also, one notes that negative material recession was obtained for Test 1319, and since the environment was chemically inert, this negative recession was due to char swell. The radiometer was exposed to the APG environment in Tests 1324 and 1325. Originally, these tests were supposed to duplicate the nominal test conditions shown by Tests 8 and 9 in Table 6-1. However, the radiometer output for Test 1324 was lost due to a malfunction of the instrumentation recording equipment. Since radiometer results from a test with a hot carbon cloth phenolic opposite wall would be of more value than results for a cold copper opposite wall, the test conditions for Test 1325 were altered to repeat those of Test 1324. The cold opposite wall test was not conducted.

The thermocouple and emf data from the total and radiative heat flux systems are presented in Sections 6.2 and 6.3, respectively. These sections present the reduced data and an evaluation of the measurement systems.

## 6.2 TOTAL HEAT FLUX SYSTEM

The total heat flux system was evaluated in seven APG tests. The design and installation of the sensor for these tests is described in Section 6.2.1. The test results, including both the measured data and the reduced data using the data reduction techniques described in Section 5, are presented in Section 6.2.2

### 6.2.1 Design and Installation

The thermocoupled plug design employed in the test evaluation program was shown in Figure 4-2, and the installation in the two-dimensional test section was shown schematically in Figure 6-2. The thermocouples were installed at the nominal depth below the surface of 0.050, 0.125, 0.200, 0.300, and 0.400 inches, and the thermocouple plug was 0.800 inches long, excluding the strain relief pins. Since the test section had a one-inch depth at the nozzle throat, this left a 0.20 inch cavity at the backside of the plug. This cavity, which contained the strain relief pins and the thermocouple lead wire connections, was potted after installing the plug in the test section. As shown in Figure 6-2, the instrumented test section formed one half of the APG nozzle, and a dummy model, usually fabricated from the same material, formed the other half.

After installing the instrumented test section in the APG nozzle, the thermocouple lead wires were connected to the measuring circuit as described in Section 5. In addition, an optical pyrometer was focused on the throat of the instrumented test section. This pyrometer measured the brightness surface temperature at a

wavelength of 0.8 microns. This temperature was converted to a true surface temperature using the material emissivity.

#### 6.2.2 Test Results

The recorded data from the Phase II tests of the total heat flux sensors which are pertinent to the measurement of this flux include thermocouple and pyrometer data and pre- and post-test model geometrical measurements. In addition, sufficient parameters affecting the performance of the APG are monitored so that the properties of the high temperature gases can be defined. The gas properties of importance include enthalpy and pressure, and these have been reported in Table 6-2 of Section 6.1. Also, reported in this table is the total surface recession and the average surface recession rate for each test. In the following paragraphs, an example of the in-depth thermocouple data from a heat flux sensor is presented. This is followed by a presentation of the comparison between the calculated surface temperature (calculated using the in-depth thermocouple and surface recession data) and the measured temperatures (defined by the optical pyrometer). Finally, the total heat flux obtained from the data reduction procedure is presented for each of the tests, and this heat flux is converted to a convective heat transfer coefficient. The intermediate data reduction steps are described qualitatively. These steps have been described quantitatively in Section 5 and are described further in Section 7 by using a heat flux sensor in the char motor firing as an example.

Figure 6-3 presents the measured in-depth temperatures as a function of test time for Test 1318 and the surface temperature\* calculated using the in-depth thermocouple data and the measured surface recession. As described in Section 5.1.2, the surface temperature is determined by an iterative calculation using the CMA computer program. The predicted in-depth temperatures for the final iteration on the surface recession rate and surface temperature are also presented in Figure 6-3. Note in this figure that the nominal thermocouple depths are presented. However, the actual depths used in the analysis were defined using X-ray photographs.

The determined surface temperature for the carbon phenolic tests are compared with those measured using an optical pyrometer in Figures 6-4 through 6-6. Similar results are presented in

---

\*The surface temperature calculated using the in-depth thermocouple data is referred to as the determined surface temperature.

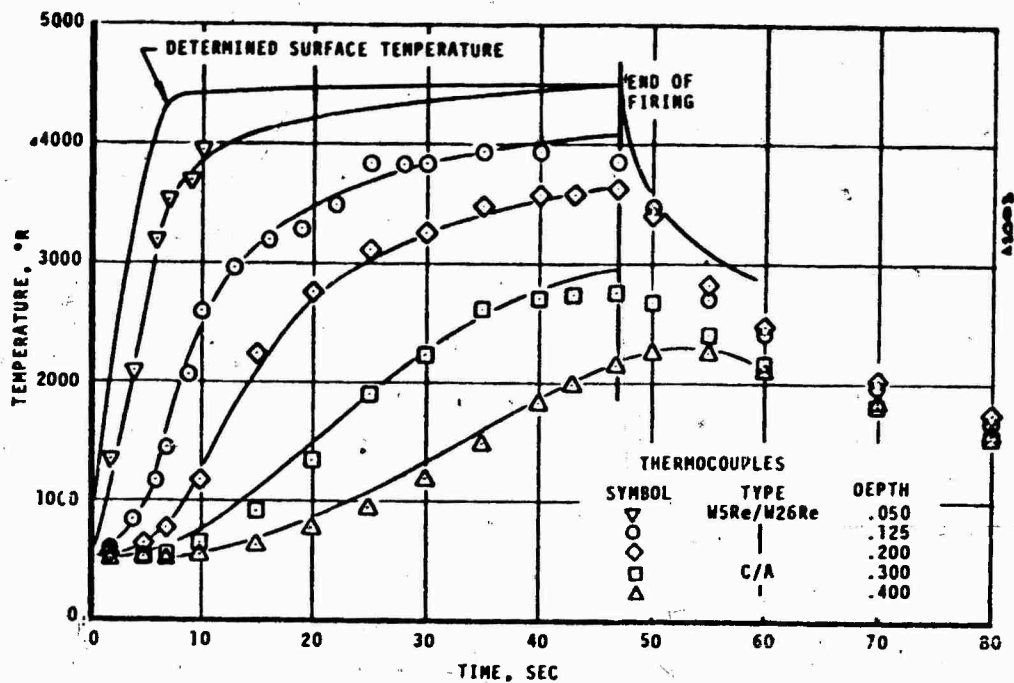


FIGURE 6-3 MEASURED THERMAL RESPONSE OF AN MX 4926 CARBON PHENOLIC ABLATIVE PLUG, TEST 1318

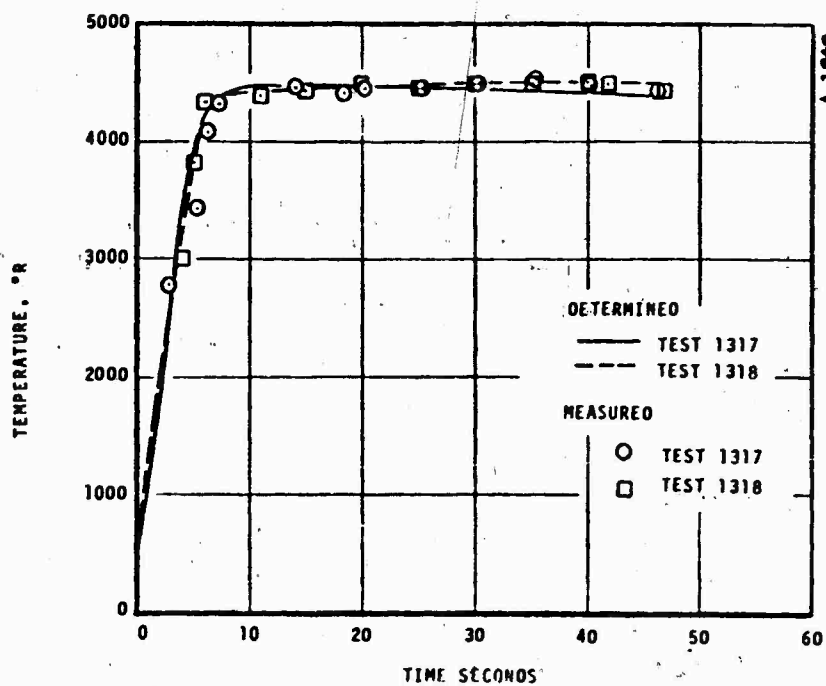


FIGURE 6-4 COMPARISON BETWEEN MEASURED AND DETERMINED SURFACE TEMPERATURE

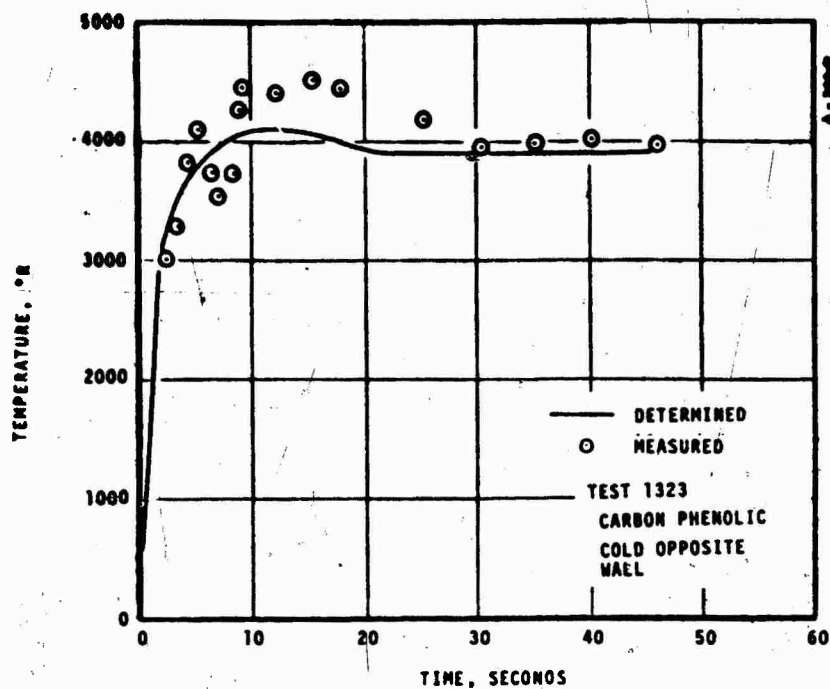


FIGURE 6-5 COMPARISON BETWEEN MEASURED AND DETERMINED SURFACE TEMPERATURE

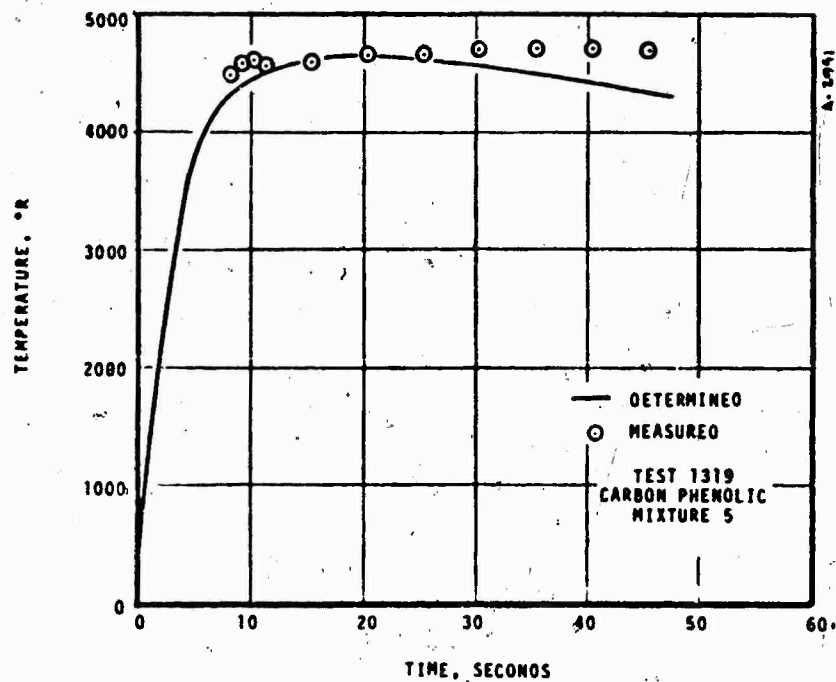


FIGURE 6-6 COMPARISON BETWEEN MEASURED AND DETERMINED SURFACE TEMPERATURE



Figures 6-7 and 6-8 for the silica phenolic tests. These figures illustrate the good agreement obtained between the determined and measured surface temperatures.

The final iterated values of the determined surface temperatures and the surface recession rates together with the in-depth pyrolysis gas generation rate (defined by the CMA program) form the basis for calculating the total heat flux. The ACE computer program generates the thermochemical information used in the data reduction procedure. Because the optical depth of the gases at the nozzle throat is very small, the gases do not have to be considered in the radiation model, and, thus, the radiative heat flux to the sensor surface is only that being emitted by the opposing wall. Therefore, the convective heat flux is easily obtained from the total heat flux. For the heat flux sensor tests in the Phase II program, both the measured total and convective fluxes are presented in Figures 6-9 through 6-11. The main item to note in these figures is that the measured heat fluxes for carbon cloth phenolic in Tests 1317 and 1318 are essentially identical. Since the arc operating characteristics for these tests were approximately identical, these measured results demonstrate the repeatability of the measurement system. In general, this same conclusion is demonstrated in Tests 1320 and 1321 for the silica cloth phenolic. However, the measured results for these latter tests show more variance than for the carbon cloth phenolic tests. Since the measurement system accuracy for silica cloth phenolic is less than for carbon cloth phenolic (Section 4), this larger variance is to be expected.

The convective heat fluxes shown in Figures 6-9 through 6-11 were converted to a convective heat transfer coefficient by dividing the difference between the free stream and wall enthalpies. These convective heat transfer coefficients are shown in Figures 6-12 and 6-13 as a function of test time. Also shown in these figures is the predicted variation of the convective heat transfer coefficient based on the 0.8 power of the pressure ratio. Note that both the predicted and measured convective heat transfer coefficients were assumed identical at the instant the measured value was a maximum. One notes from these comparisons that both the measured and predicted coefficients decrease with test duration. However, the measured values decrease more rapidly.

### 6.3 RADIATIVE HEAT FLUX SYSTEM

The radiative heat flux system was evaluated in two APG tests. A brief description of the design and installation of this system

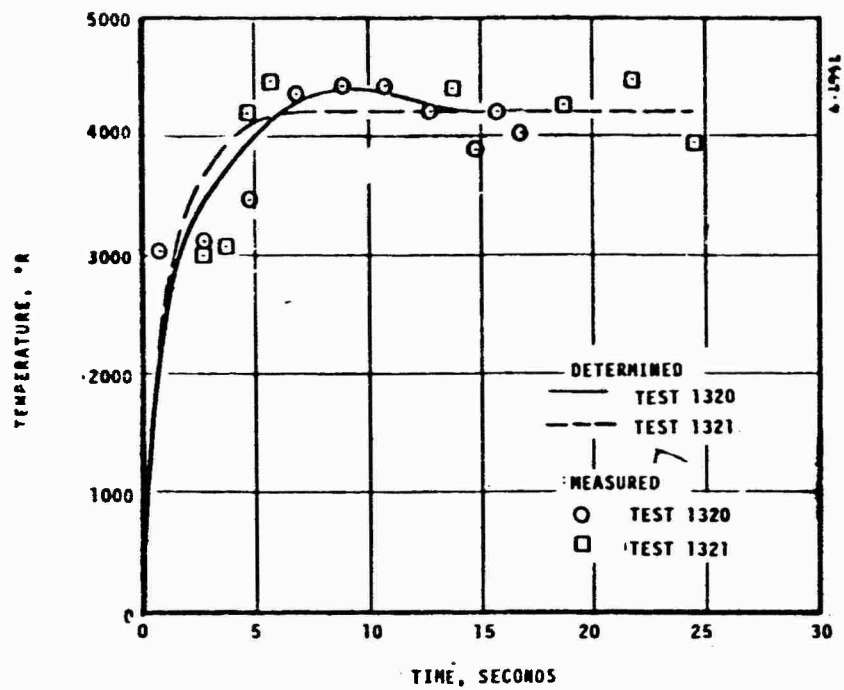


FIGURE 6-7 COMPARISON BETWEEN MEASURED AND DETERMINED SURFACE TEMPERATURE

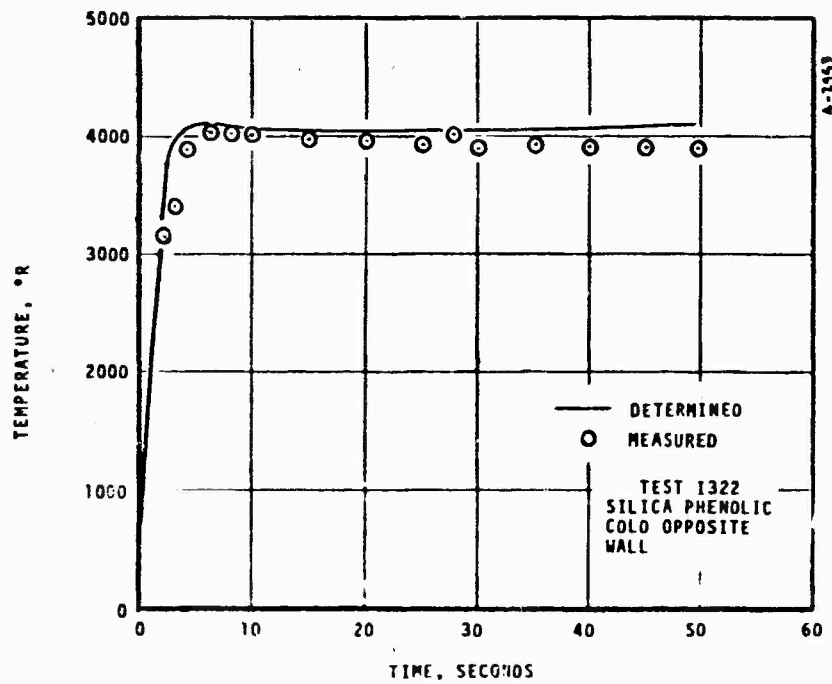


FIGURE 6-8 COMPARISON BETWEEN MEASURED AND DETERMINED SURFACE TEMPERATURE

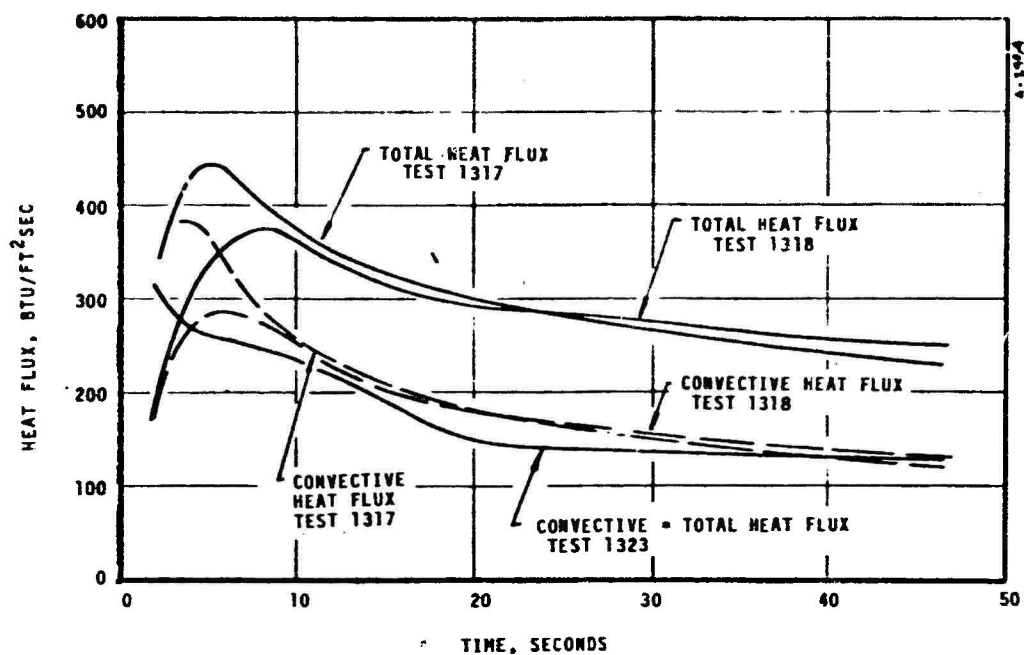


FIGURE 6-9 MEASURED TOTAL AND CONVECTIVE HEAT FLUXES

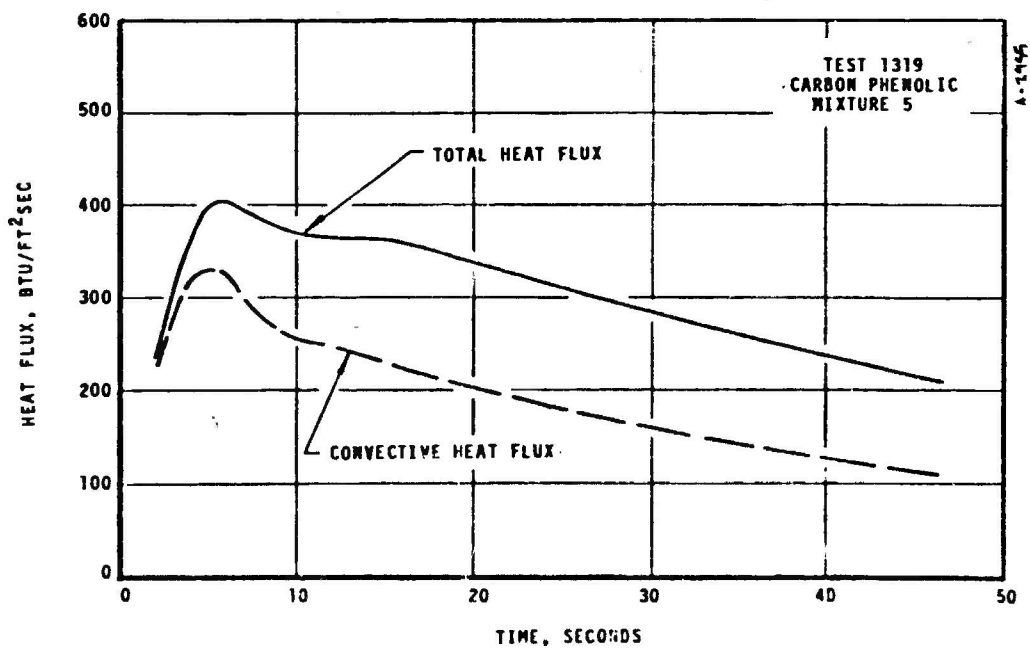


FIGURE 6-10 MEASURED TOTAL AND CONVECTIVE HEAT FLUXES

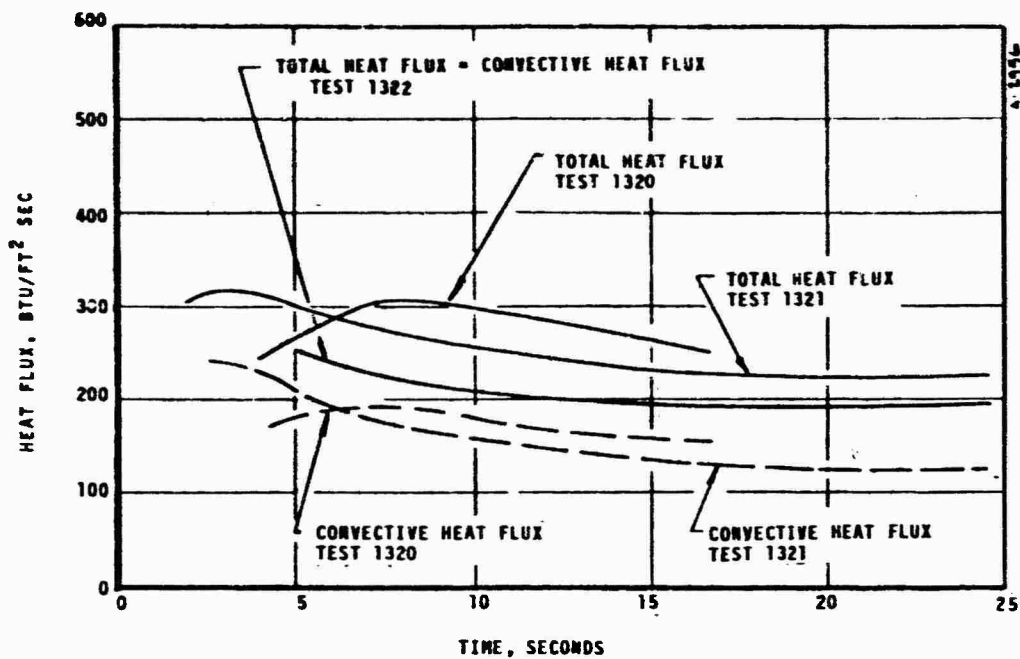


FIGURE 6-11 MEASURED TOTAL AND CONVECTIVE HEAT FLUXES

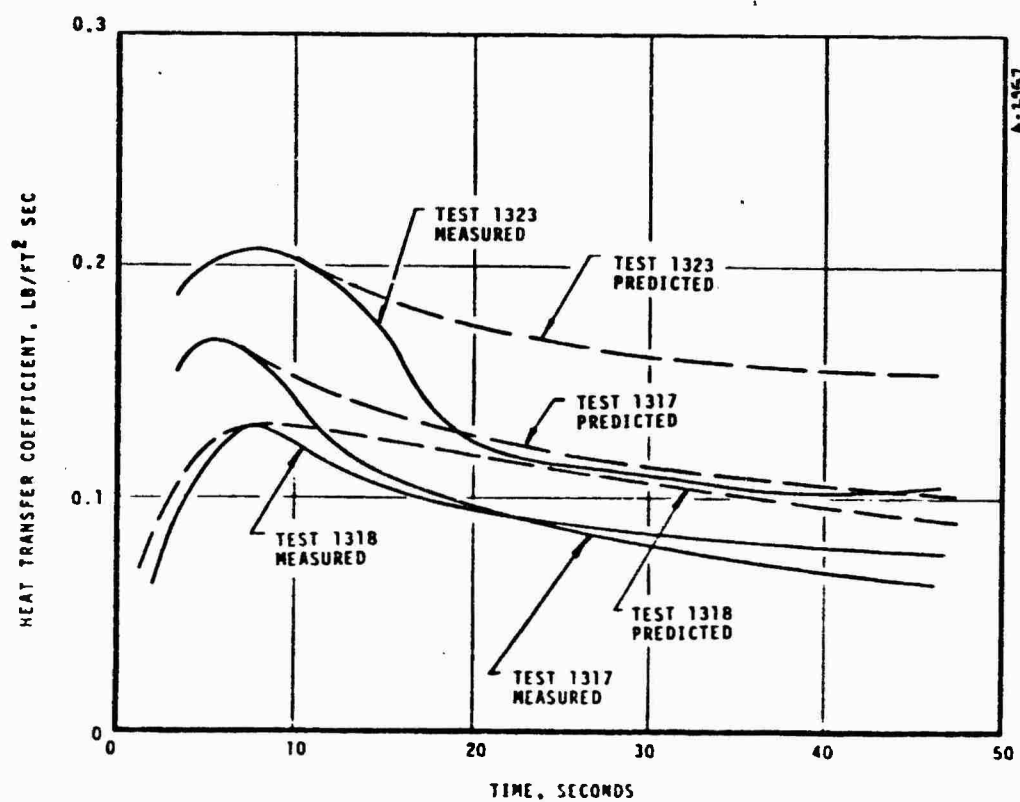


FIGURE 6-12 COMPARISON BETWEEN MEASURED AND PREDICTED CONVECTIVE HEAT TRANSFER COEFFICIENTS

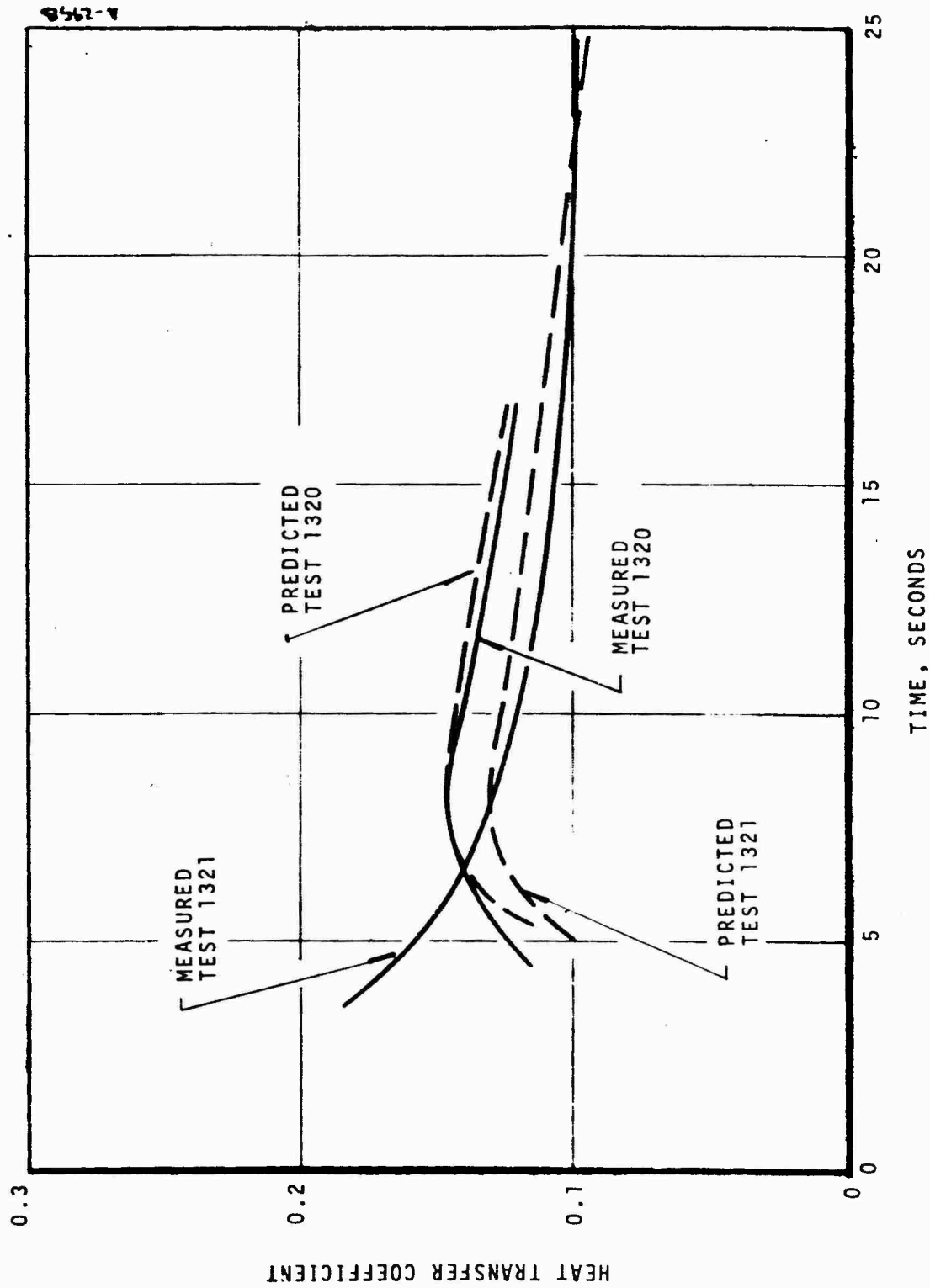


FIGURE 6-13 COMPARISON BETWEEN MEASURED AND PREDICTED CONVECTIVE HEAT TRANSFER COEFFICIENTS

is presented in Section 6.3.1. The test results from these tests are presented in Section 6.3.2.

#### 6.3.1 Design and Installation

The narrow view angle radiometer used for the APG tests was identical to the one described in Section 4. This radiometer was installed in a carbon cloth phenolic test section similar to that used for the heat flux sensor. However, the depth of the test section had to be increased in order to prevent overheating of the aperture of the radiometer. The modified test section is shown in Figure 6-14. Note that the maximum depth is 1.65 inches which means the aperture of the radiometer is 0.45 inches below the initial surface of the test section. The flange and threaded section of the radiometer were bonded to the test section. Note that the threads on the radiometer and the groove in the test section insure an effective seal of the possible gas path. After installing the instrumented test section in the APG, the thermocouple and sensor lead wires were connected to a recording circuit similar to the one described in Section 4. In addition, the purge line was connected to a 1200 psia nitrogen source. (The flow system for this purge system was similar to that shown in Figure 7-4 for the first char motor firing.) The sonic orifice in the flow system was sized to give a purge flow rate of 0.007 lbs/sec. With this flow rate, the predicted cavity temperature using the method outlined in Section 4 would be identical to that predicted for a 0.01 lb/sec purge flow rate in the char motor firings.

The anticipated test conditions for the two APG tests have been presented previously in Table 6-1 (page 6-4). As explained earlier, a malfunction of the recording equipment resulted in the requirement that both tests be run with the opposing test section being carbon cloth phenolic. The arc operating characteristics for these tests are summarized in Table 6-2 (page 6-4).

#### 6.3.2 Test Results

The primary test data from the narrow view angle radiometer are the measured emf across the constantan sensor which is related to total hemispherical radiative heat fluxes. The results of this measurement are shown in Figure 6-15 where they are compared with calculated values based on the predicted surface temperature of the opposing test section. The maximum variation between the measured and calculated radiative heat flux is approximately 20 percent which occurs approximately half way through the test. However, this variation is considerably less than 20 percent during the majority of the test and is negligible during the initial transient. Also,

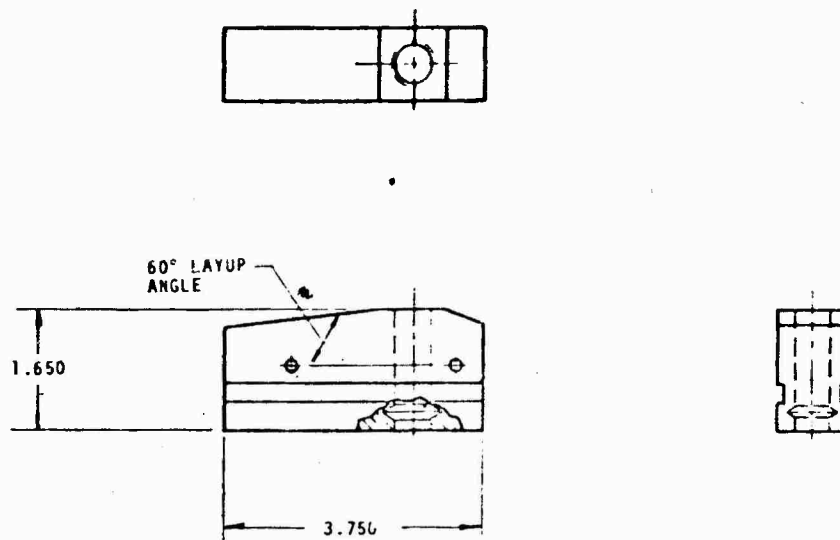


FIGURE 6-14 TEST CONFIGURATION FOR APG RADIATIVE TESTS

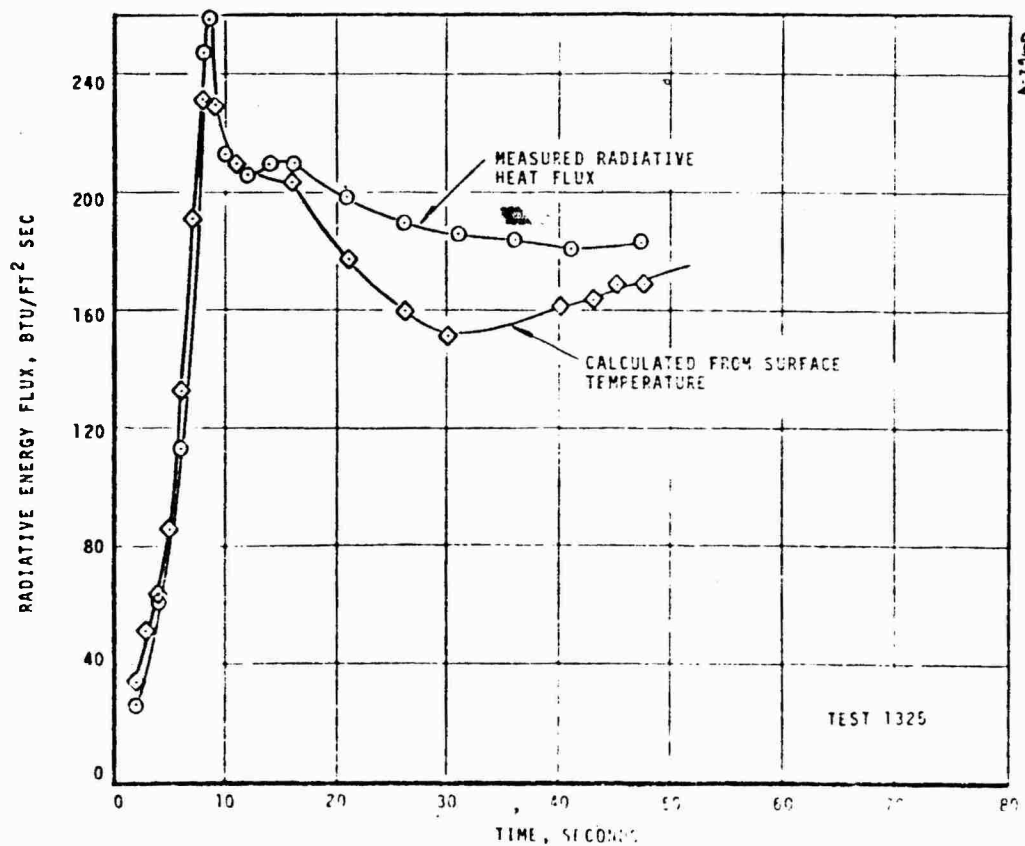


FIGURE 6-15 COMPARISON BETWEEN MEASURED AND PREDICTED RADIATION HEAT FLUX (TEST 1325)

this discrepancy is more likely due to an inaccuracy in the temperature indicated by the pyrometer than an inaccuracy in the radiometer output.

During both tests, the gas purge system functioned perfectly and did not affect the operation of the radiometer. In addition, visual post-test observations showed that the sapphire lens was clear and that the copper housing and aperture did not experience any significant heating.



## SECTION 7

### CHAR MOTOR TESTS

The total and radiative heat flux measurement systems were evaluated through two nozzle test firings which were performed on the AFRPL 40-inch char motor. The nozzle designs and firing conditions were selected to test these systems under conditions typical of their application in rocket nozzle firings. An uncured propellant, APG 112D, which has a flame temperature of 7010°R at 1000 psia was used in these firings.

The first nozzle which was fired on August 13, 1969 contained four total heat flux ablative plugs and one radiation sensor. Three of the ablative plugs were constructed of MX 4926 carbon phenolic which formed the throat approach and the nozzle throat region while the other was constructed of MX 2600-96 silica phenolic which formed the nozzle exit cone. Apparent failure of the radiometer purge flow supply resulted in only minimal radiometer data. The total and effective firing durations were 54 and 48 seconds, respectively, with the chamber pressure for the 2.30 inch diameter nozzle reaching a peak of 1080 psia at 5 seconds into the firing. An AFRPL test report was published (Reference 7-1).

The second nozzle which was fired on February 6, 1970 contained two MX 4926 carbon phenolic total heat flux measurement systems and two radiometers. One radiometer was identical to that used in the first firing while the other was identical to a radiometer scheduled for a firing under Contract F04611-69-C-0065. A molybdenum transient slug calorimeter, designed by Atlantic Research Corporation was also included in the nozzle but only qualitative information was obtained from this device. All other measurement systems performed as expected. Total and effective firing durations were 58 and 46 seconds, respectively, with the chamber pressure for the 2.40 inch diameter nozzle reaching a maximum of 930 psia at 11 seconds into the firing.

Detailed descriptions of the designs, fabrication technique and firing test conditions are presented in Section 7.1. The overall ablative and structural responses of the two nozzles are described in Section 7.2. The response of the total heat flux measurement systems is discussed in Section 7.3. Finally the measured response of the radiative heat flux measurement systems are described in Section 7.4.

## 7.1 CHAR MOTOR NOZZLES

Two ablative throat char motor nozzles were designed and fabricated under this contract. These nozzles were designed to incorporate the heat flux measurement systems described in Section 4 at a minimum risk to the nozzle structural integrity. In addition the nozzle components were designed to simplify their assembly into the steel shell in order to minimize the risk of damaging the heat flux measurement systems. The nozzle designs, the nozzle component fabrication, and the assembly of the nozzle components, including the heat flux measurement systems, are described in Section 7.1.1. The environmental conditions achieved in each of the char motor firings are described in Section 7.1.2.

### 7.1.1 Nozzle Design, Fabrication, and Assembly

The ablative throat nozzle designs for the two 40-inch char motor firings are shown in Figures 7-1 and 7-2. The internal nozzle contour for both of these nozzles was similar, with the only difference being that the second nozzle had a throat diameter of 2.40 inches while the first had a throat diameter of 2.30 inches. The same nozzle structural steel shell was used for both motor firings, but it was reworked after the first firing to accommodate additional heat flux measurement systems.

For both nozzle designs, the throat approach component was fabricated from MX 4926 carbon cloth phenolic oriented at a  $90^\circ$  layup angle with respect to the nozzle centerline. This material was chosen because it would minimize the surface recession in this region and, thus, provide a relatively smooth entrance to the nozzle throat region. The  $90^\circ$  orientation was selected in order to minimize fabrication costs. This orientation did result in the laminates being parallel to the surface at the entrance to the throat approach. However, this was not considered to be a problem because of the relatively low convective heat flux in this region. The maximum diameter of this component was dictated by the inner bore diameter of the flange on the aft closure of the char motor. The throat entrance was bonded to the steel shell and the nozzle throat assembly. Epon 913 adhesive was used.

The nozzle throat ablative component was also fabricated from MX 4926 carbon cloth phenolic but at a layup angle of  $60^\circ$ . This material was chosen because it was a well characterized material and, thus, met the requirement for the total heat flux measurement system. The layup angle was chosen to coincide with that typically used in nozzle ablative throats. The exit cone for the first nozzle was MX 2600-96 silica cloth phenolic ( $A/A_* \geq 3.0$ ) (Figure 7-1). This provided an evaluation of the total heat flux system for a typical



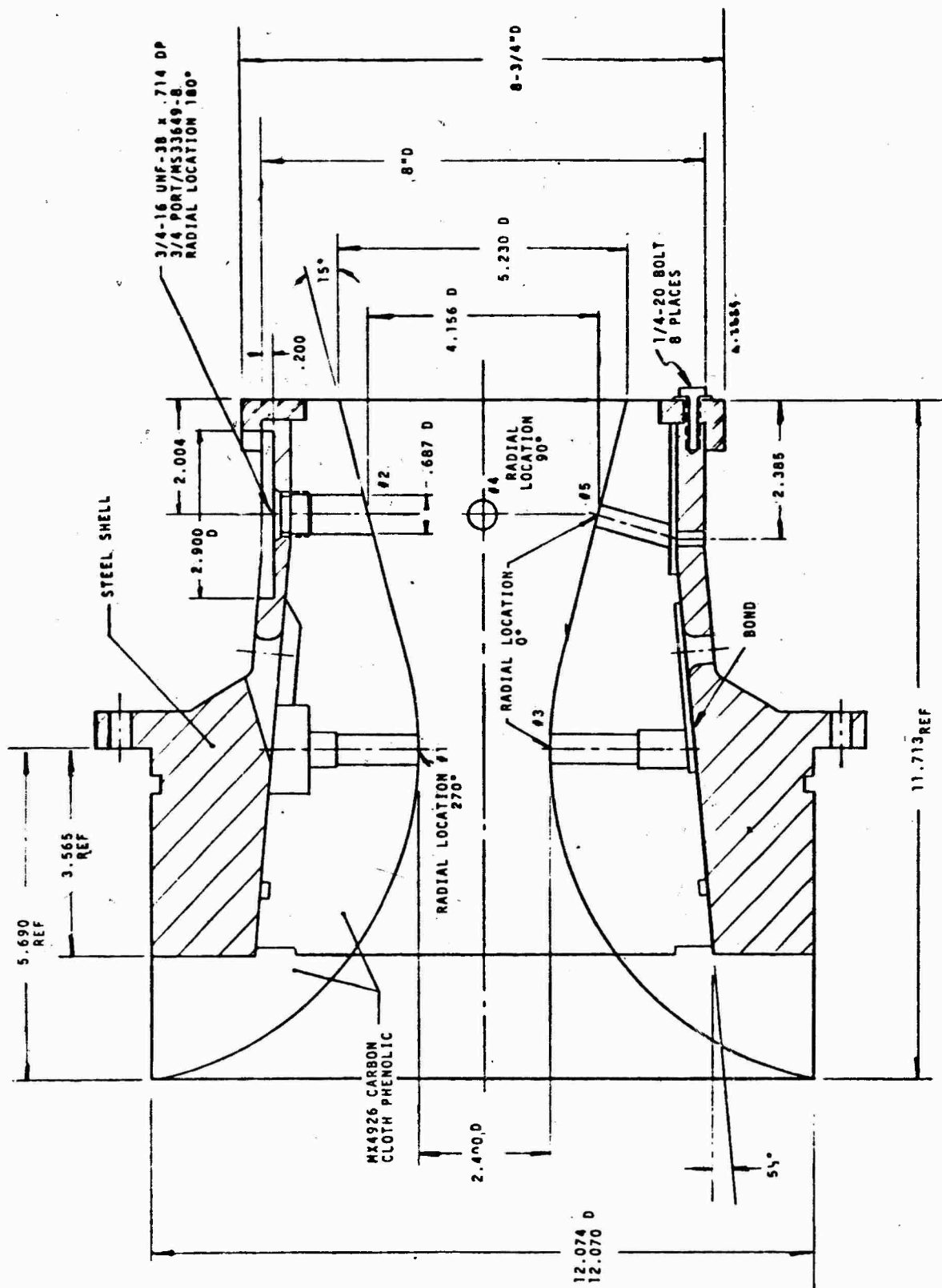


FIGURE 7-2 NOZZLE DESIGN FOR SECOND CHAR MOTOR FIRING

exit cone material. For simplicity, carbon phenolic was used throughout for the second nozzle (Figure 7-2). Also, the additional instrumentation required a homogeneous material at  $A/A^* = 3.0$ .

The nozzle throat diameter was chosen so that the maximum anticipated chamber pressure history was 740 psia. The predicted chamber pressure history based on the nozzle throat thermal predictions described in Section 4 is presented in Figure 7-3. The highly regressive pressure trace is due to the high throat surface recession associated with the ablative throat. A considerably higher than anticipated maximum chamber pressure was achieved in the first nozzle firing because of an increase in the propellant burning surface area due to the erosion of the insulation liner in previous motor firings and because of a higher than assumed propellant burning rate. As a result, the throat diameter for the second nozzle was increased to 2.40 inches.

The backside of the nozzle throat had a  $5-1/2^\circ$  taper which insured retention. In addition, the backside of the throat was bonded to the steel shell with Epon 913. This bondline had two purposes: to provide a seal between the steel shell and the ablative component and to carry the shear load at the interface. Note also that O-rings were used to seal any possible gas paths. This redundancy was employed because of the difficulty in assuring that the bond would be a 100 percent effective gas seal. The MX 2600-96 silica cloth phenolic exit cone of the first nozzle was fabricated at a layup angle of  $60^\circ$ . The thickness of the silica phenolic was defined based on the thermal predictions presented in Section 4. This part was bonded to the carbon cloth phenolic throat and the steel shell using Epon 913.

For the first nozzle (Figure 7-1), three total heat flux sensors were located in the nozzle throat region corresponding to area ratios of -2.0, 1.0, and 2.0. In addition, a narrow view angle radiometer was located at the nozzle throat plane. A fourth total flux sensor was located in the exit cone at an area ratio of 4.0. As shown in Figure 7-2, the instrumentation for the second nozzle was located at the throat and at an area ratio of 3.0. Each location included a total heat flux sensor and a narrow view angle radiometer. Wherever possible, the measurements were separated radially by  $90^\circ$ . This was done primarily to prevent any flow perturbations generated at one measurement location from interfering with the measurement system at another location.

With the exception of the narrow view angle radiometer in the exit cone of the second nozzle, all the measurement systems were bonded to the ablative component in which they were installed. This

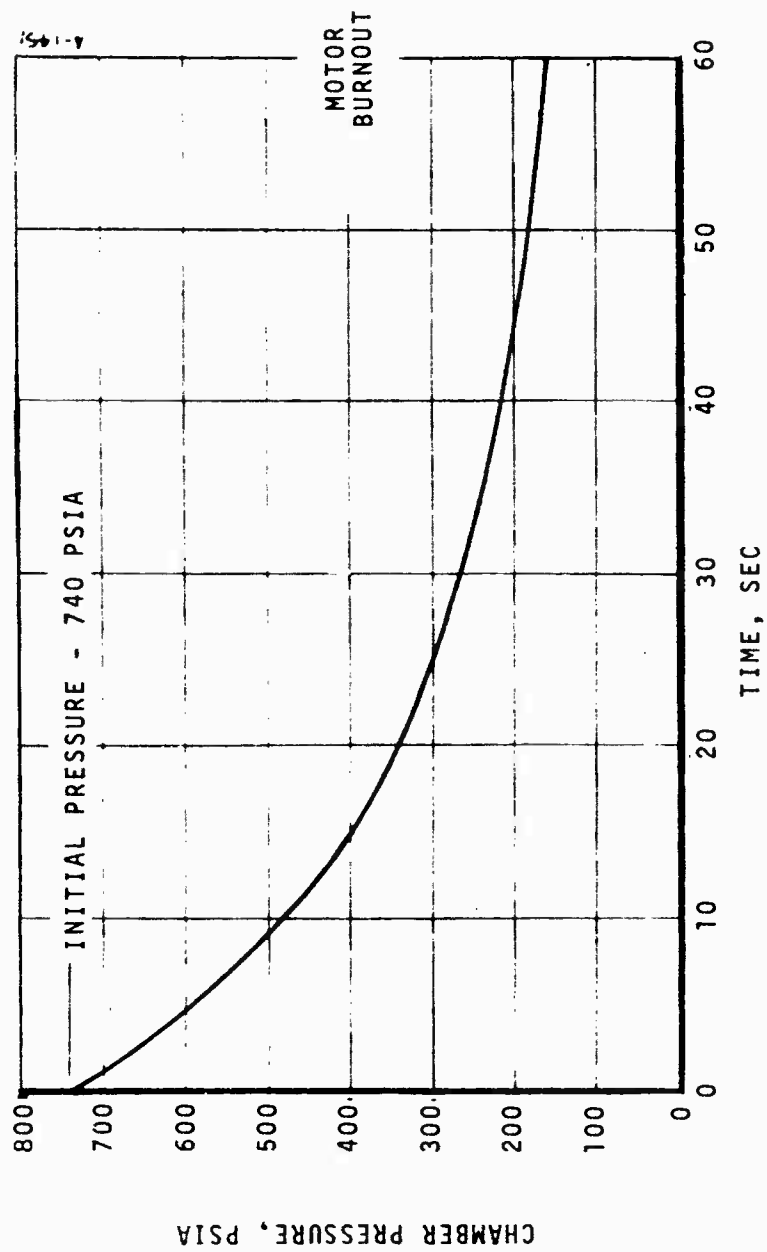


FIGURE 7-3 CHAR MOTOR CHAMBER PRESSURE HISTORY FOR  
MX4926 NOZZLE THROAT MATERIAL (INITIAL  
THROAT DIA = 2.30 IN.)

was also true of the molybdenum slug calorimeter located at an area ratio of 3.0 in the second nozzle. The narrow view angle radiometer located in the exit cone was retained by threads, and an O-ring was used to provide the seal.

As shown in Figures 7-1 and 7-2, slots were machined in the ablative components. In most locations, these slots contained either thermocouple lead wires from the total heat flux sensors or leads and gas purge line from the narrow view angle radiometer. (In the exit cone, the slot was required only in the assembly of the nozzle.)

The structural shell was fabricated from 1022 steel. A conservative approach was taken in the design of this shell due to the numerous cutouts required for the instrumentation. The size and location of the bolt holes for mounting the nozzle to the motor case were dictated by the location of the mating holes on the flange of the aft closure. As shown in Figure 7-1, the steel shell had a flange at the exit which was an integral part of the shell. However, in order to remove the ablative components after the first firing, this flange had to be machined off. For the second firing, this flange was bolted on as shown in Figure 7-2.

The fabrication of the instrumentation systems was described in Section 4 and was performed by Aerotherm for the total heat flux sensors and by Heat Technology Laboratory for the narrow view angle radiometers. Haveg-Reinhold fabricated the steel and ablative components. After the ablative components were fabricated, they were bonded together and then the final machining was performed. This assembly was shipped to Aerotherm for the installation of the instrumentation systems. Since the cylindrical barrel of the total heat flux sensors was intentionally made longer than the mating hole, the sensors were machined flush with the surface after they had been bonded in place and after the protuberance had been carefully measured. This measurement was required in order to accurately define the distance of the in-depth thermocouples from the nozzle surface. After assembly of the instrumentation, the ablative component was returned to Haveg-Reinhold where it was bonded into the steel shell. Aerotherm personnel assisted in this final assembly and bonding operation. After curing the bond, the nozzle assembly was shipped to AFRPL where it was installed on the 40-inch char motor.

The necessary thermocouple lead wire and gas purge line hookups were made after installing the nozzle assembly on the motor. A schematic of the gas purge system is shown in Figure 7-4 for the first nozzle

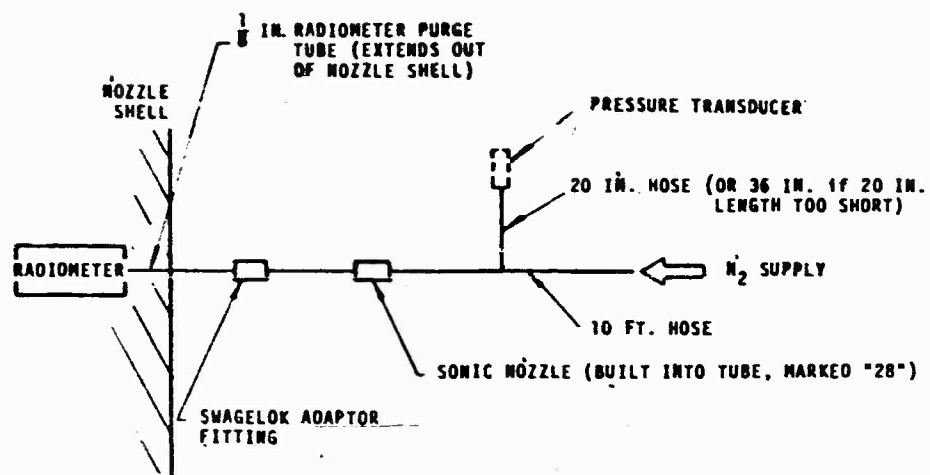


FIGURE 7-4 NITROGEN GAS PURGE SYSTEM FOR THE FIRST CHAR MOTOR FIRING

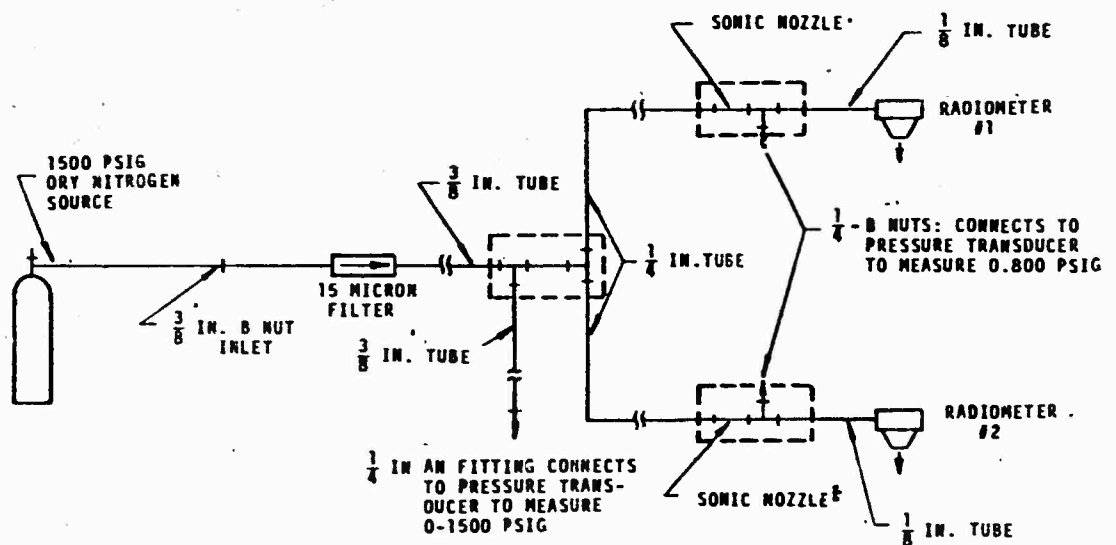


FIGURE 7-5 NITROGEN GAS PURGE SYSTEM FOR THE SECOND CHAR MOTOR FIRING



firing and in Figure 7-5 for the second nozzle firing. Both systems contained a high pressure nitrogen source, and the flow of the nitrogen gas to the radiometers was controlled by one or more sonic orifices in the line. The flow system lines for the first firing consisted of high pressure flexible tubing. However, because of the line failure caused by radiant heating from the high temperature exhaust, these lines were changed to stainless steel tubing for the second firing. In addition, a 15 micron filter was installed in the line for the second firing to insure that particles would not plug the sonic orifices. Also, note that pressure transducers were located both upstream and downstream of the sonic orifices for the second firing.

#### 7.1.2 Char Motor Firing Conditions

The propellant description and firing conditions for the two char motor firings are presented in this section and define the environmental conditions to which the heat flux measurement systems were exposed. The uncured propellant, APG 112D, produced by Atlantic Research Corporation was employed in both test firings. The elemental composition of this propellant is given in Table 7-1. Under the assumptions of chemical equilibrium, the thermodynamic state of this elemental composition is dependent on the system pressure and temperature. For a flame temperature of 7020°R and a chamber pressure of 1000 pisa, the molecular composition of the combustion products is given in Table 7-2.

The chamber pressure versus time traces are shown in Figure 7-6. Two pressure transducers were used for each firing; each agreed within 3 percent of the curves shown in Figure 7-6 for the entire duration of the respective firings. The approximately five seconds prior to pressure rise in the second firing was due to a delay in ignition. However, since the initial throat diameter was slightly larger in the second firing, peak pressure was lower and, after the start-up transients, the pressure response for the two firings were essentially identical. Pertinent chamber pressure information from the two char motor firings are compared with the anticipated values in Table 7-3. This table also presents propellant ballistic and nozzle throat geometric information.

#### 7.2 THERMAL AND ABLATION NOZZLE RESPONSE

The ablation and thermal responses of the MX 4926 carbon phenolic and MX 2600-96 silica phenolic nozzle parts to the conditions presented in Section 7.1.2 are described in this section. Qualitative descriptions of post-test nozzle appearances and overall response trends are presented and then measured ablation results are reported. In general the response of the nozzles was

TABLE 7-1  
ELEMENTAL COMPOSITION OF APG 112D PROPELLANT

Element	Atomic Weight	Relative Composition (gram-atoms/gram of propellant)
Hydrogen	1.008	0.032219
Carbon	12.011	0.005649
Nitrogen	14.008	0.005366
Oxygen	16.000	0.022486
Sodium	22.991	Trace
Aluminum <sup>a</sup>	26.980	0.010130
Sulphur	32.066	Trace
Chlorine	35.457	0.005396

<sup>a</sup> 27.3 percent aluminum mass fraction.

TABLE 7-2  
MOLECULAR COMPOSITION OF APG 112D AT ANTICIPATED CHAMBER CONDITIONS <sup>a</sup>

Chemical Species	Mole Fraction <sup>b</sup>
<u>Primary Species</u>	
H <sub>2</sub>	0.3285
CO	0.1820
Al <sub>2</sub> O <sub>3</sub> <sup>c</sup>	0.1393
H <sub>2</sub>	0.1076
HCl	0.0933
H	0.0924
H <sub>2</sub>	0.0890
<u>Other Species</u>	
AlCl	0.0291
AlCl <sub>2</sub>	0.0201
NO	0.0179
Cl	0.0174
CO <sub>2</sub>	0.0071
Al	0.0038
AlNO <sub>2</sub>	0.0029
O	0.0028
NO	0.0016
AlO	0.0015
Al <sub>2</sub> O	0.0013
Others	0.0030

<sup>a</sup> T<sub>0</sub> = 7020°R, P<sub>0</sub> = 1000 Psia

<sup>b</sup> Mole fraction defined as: moles of species per gas phase mole

<sup>c</sup> Condensed phase (liquid): mass condensed/mass gas = 0.735;  
Also system molecular weight = 33.5 grams/gas phase mole

TABLE 7-3  
SUMMARY OF CHAM MOTOR OPERATING CONDITIONS

	Anticipated	1st Firing	2nd Firing
Peak Chamber Pressure, psia	740	1080	940
Chamber Pressure at Tailoff, psia	160	310	310
Burn Time, seconds	60	46	45
Burn Rate Exponent	0.625	0.670	0.703
Initial Throat Diameter, inches	2.30	2.30	2.40
Chamber Temperature, °R <sup>a</sup>	7020	--	--

<sup>a</sup> Temperature at 1000 psia

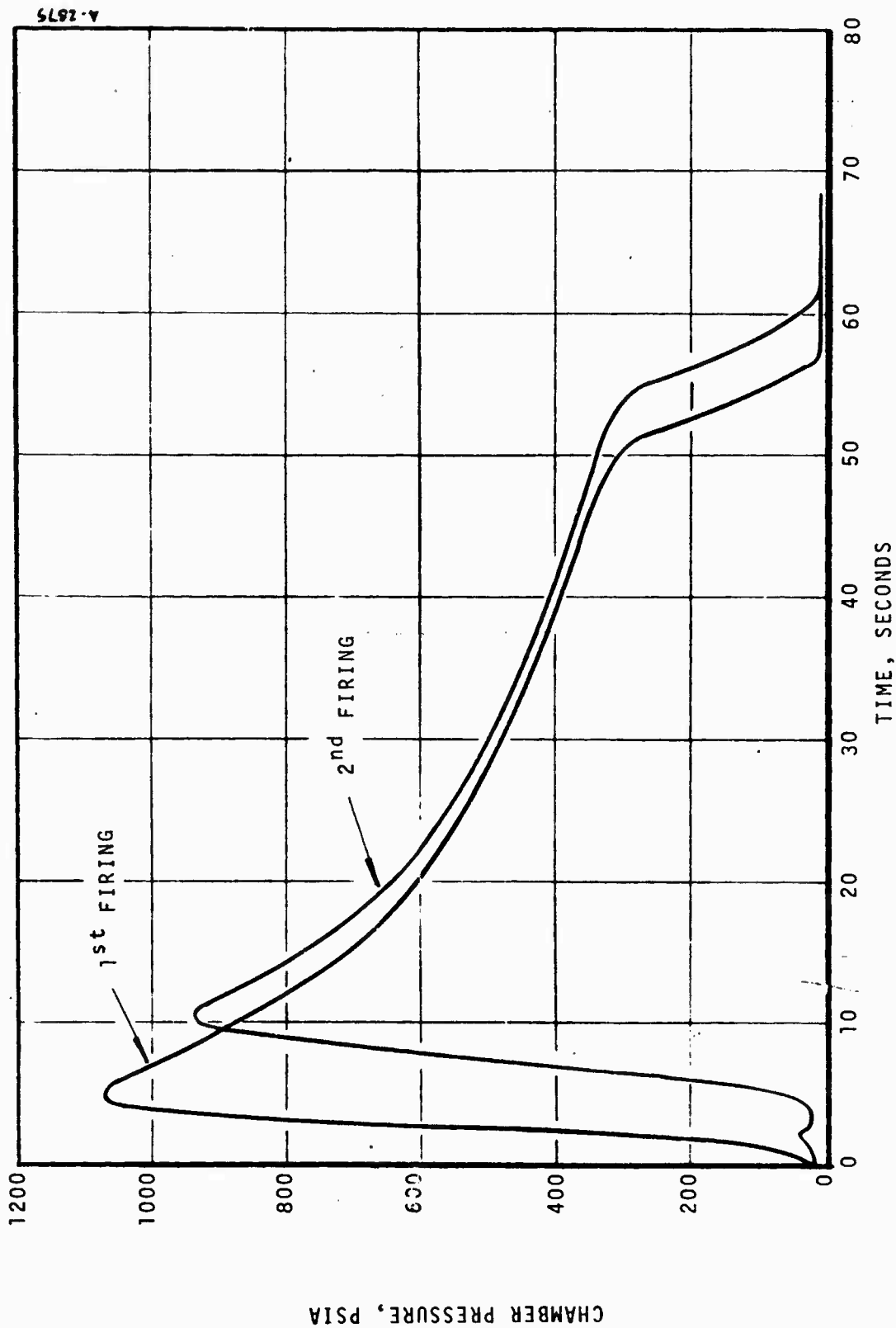


FIGURE 7-6 MEASURED CHAMBER PRESSURE HISTORIES FOR THE TWO CHAR MOTOR FIRINGS

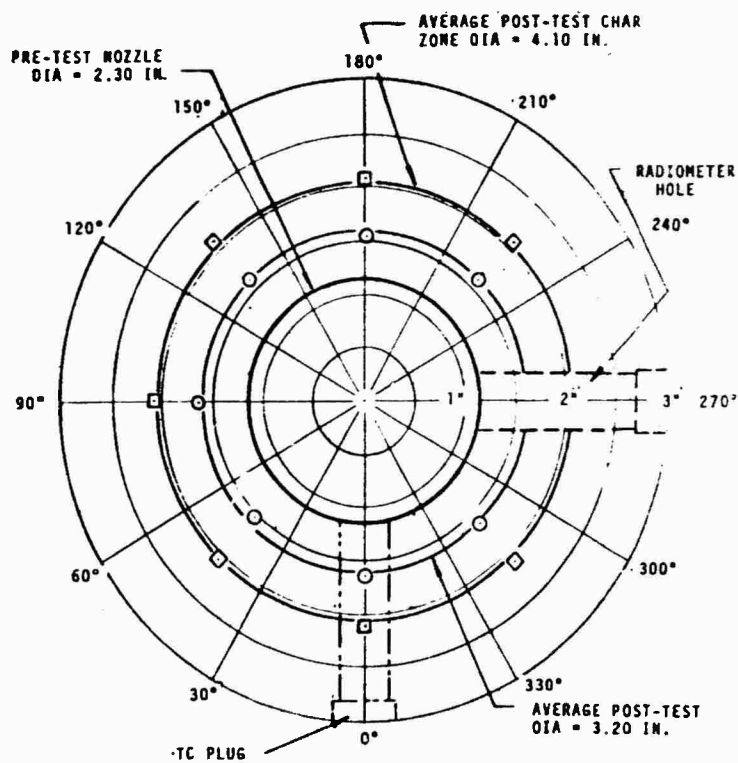
consistent with the pre-test calculation considering that the peak chamber pressures were higher than anticipated due to the problem discussed in Section 7.1.1.

The primary purpose of the firings was to establish convective and radiative heat fluxes sufficient to test the two measurement concepts. This was certainly satisfied. The surface recession and in-depth decomposition of the MX 4926 carbon phenolic and the MX 2600-96 silica phenolic components represented the type of ablative response which the two measurement systems would encounter in typical solid rocket motor applications. Moreover, since the char motor chamber conditions achieved during each firing were quite similar, a valuable indication of the repeatability of the measurements was provided.

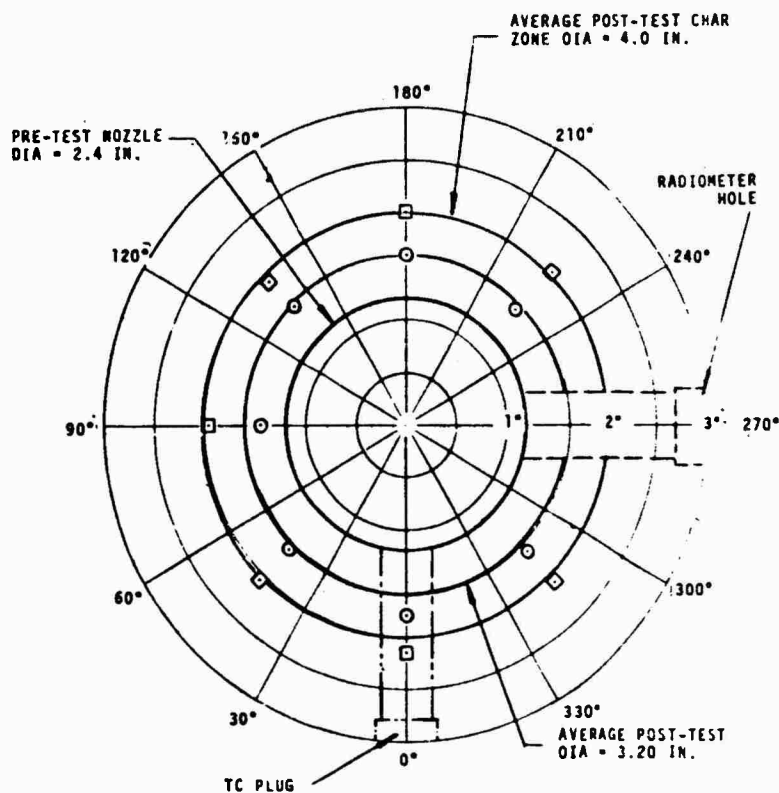
The presence of the numerous sensors embedded at various locations in the ablative nozzles appeared to have only trivial effects on the overall nozzle ablation response. The most serious deviation occurred downstream of the holes provided for the narrow view radiometers. At these locations the flow contour discontinuity resulted in a local gouge in the ablative material. This effect was most significant at the throat of the first nozzle for which the radiometer nitrogen purge gas supply system had failed. Other small local asymmetries occurred in the two nozzles, but these did not appear to be related in any way to the locations of the total or radiative heat flux measurement systems. It was apparent that the presence of the imbedded instrumentations did not impair the performance of the rocket nozzle.

The net surface recession at the throats of the two nozzles was slightly higher than anticipated, consistent with the higher chamber pressures. The throat surface recession and char depth and their asymmetry are shown in Figures 7-7a and 7-7b for the respective firings. The figures show measured post-test surface and char depth radii at seven angular locations. Also shown are the pre-test diameter and post-test average surface and char depth diameters. These figures show that the maximum asymmetry in surface recession is generally less than 10 percent of the respective average diameter.

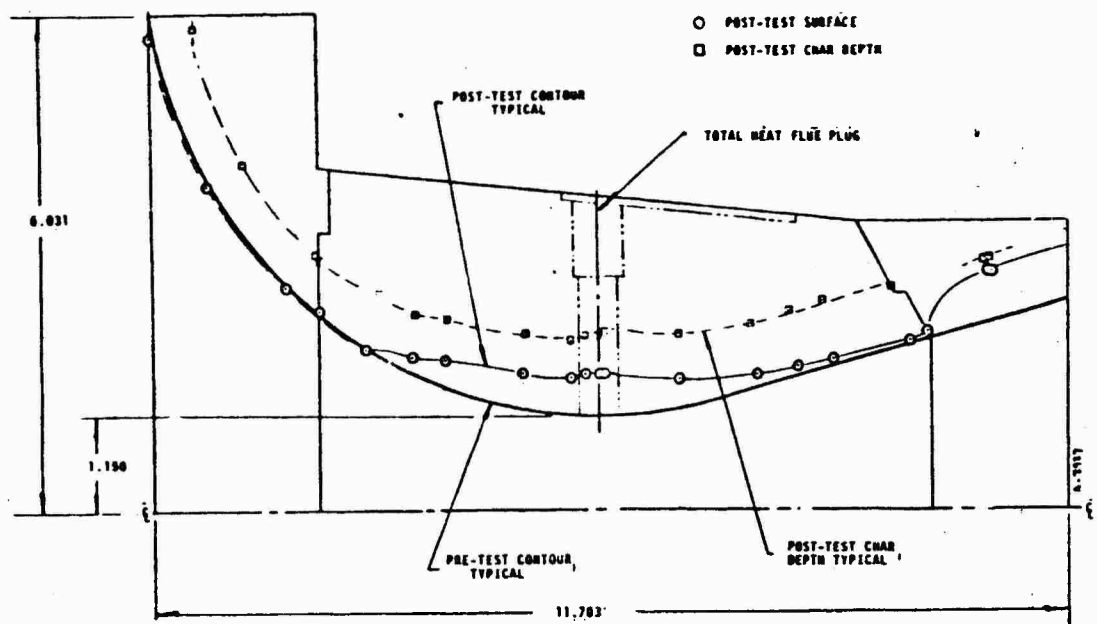
Measurements of recession and char depth at various nozzle locations are shown in Figures 7-8 and 7-9. Of particular note in these figures is the discontinuous change in recession which occurred about three inches upstream of the throat in both nozzle firings. The abrupt onset of ablation is apparently due to a flow field anomaly and not a material problem. Candidate explanations include transition from laminar to turbulent flow, a separation/re-attachment shock, and an unusual sonic region shock pattern. The actual explanation has not been defined and was beyond the scope of this program. A summary of the ablation response shown in Figures 7-8 and 7-9 is given in Table 7-4.



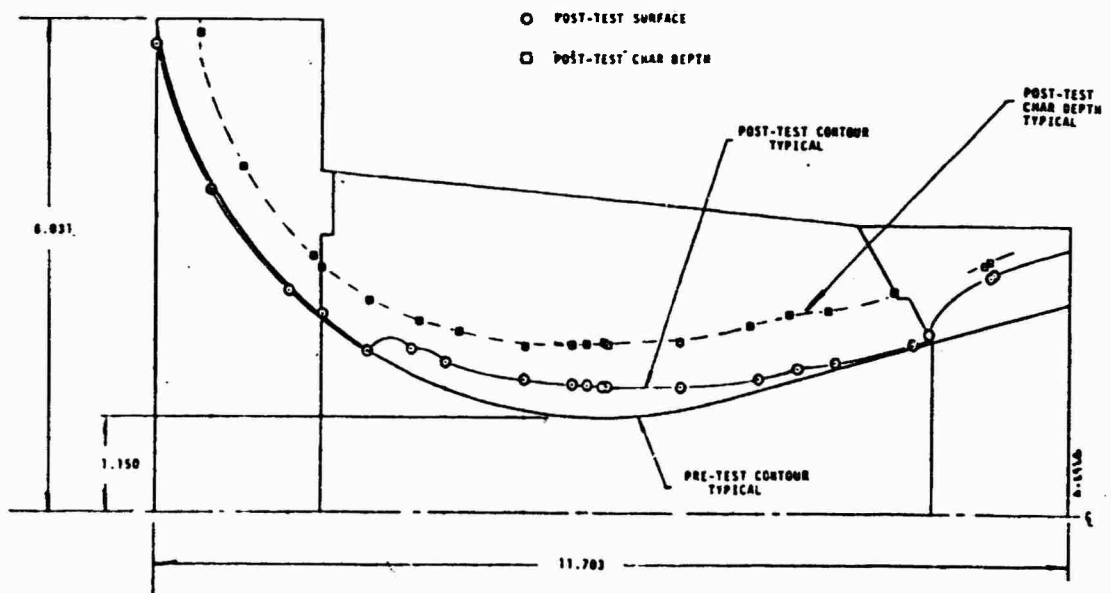
a) 1st CHAR MOTOR NOZZLE TEST FIRING  
FIGURE 7-7 THROAT ABLATION RESPONSE MEASUREMENTS



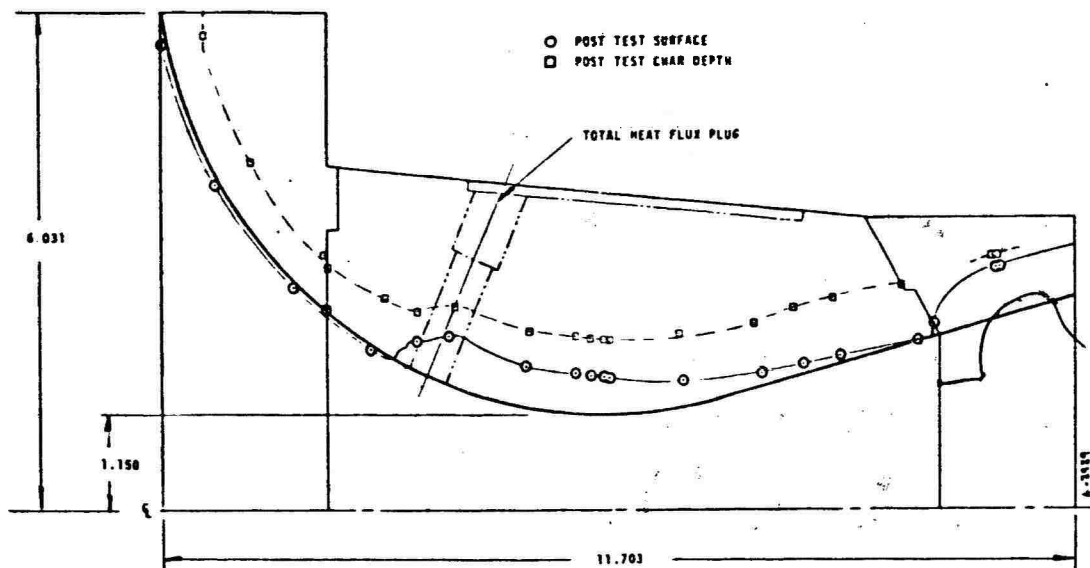
b) 2nd CHAR MOTOR NOZZLE TEST FIRING  
FIGURE 7-7 CONCLUDED



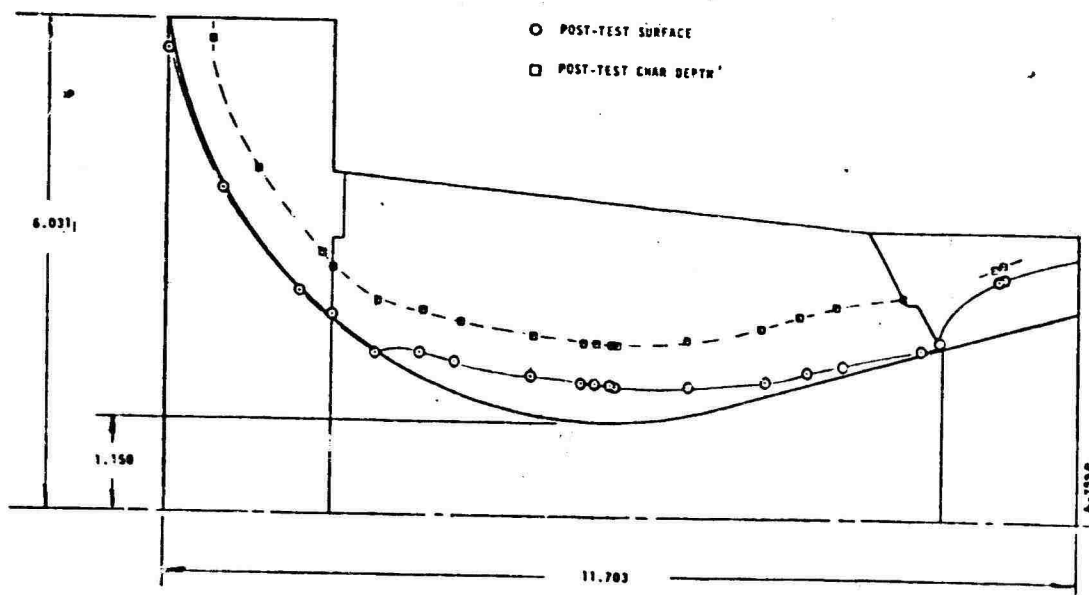
a) 0° SECTION VIEW  
FIGURE 7-8 PRE- AND POST-TEST CHAR MOTOR NOZZLE SURFACE CONTOURS  
AND CHAR DEPTH CONTOUR, FIRST FIRING



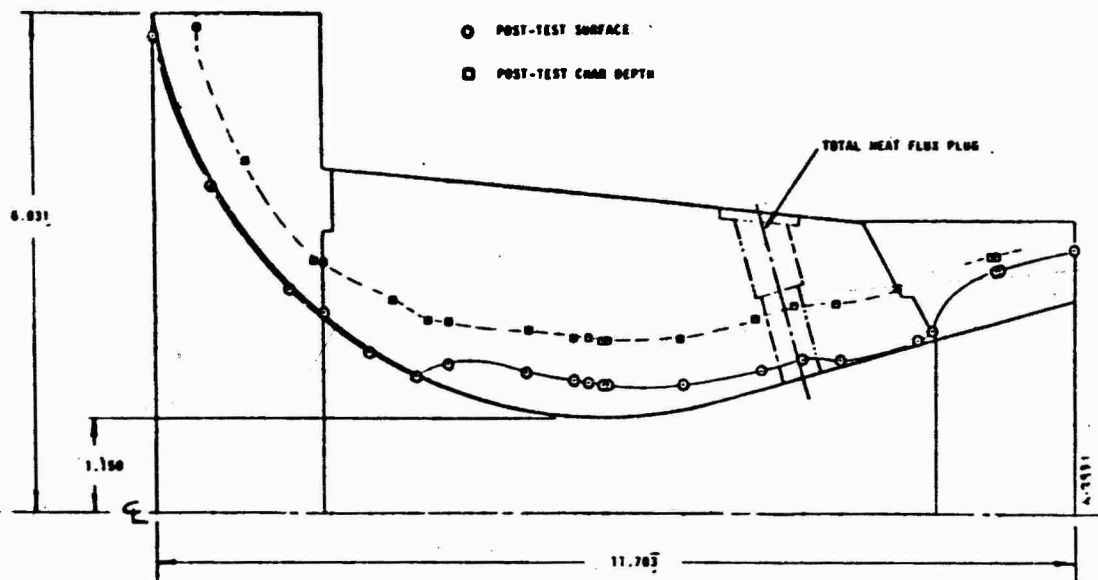
b) 45° SECTION VIEW  
FIGURE 7-8 CONTINUED



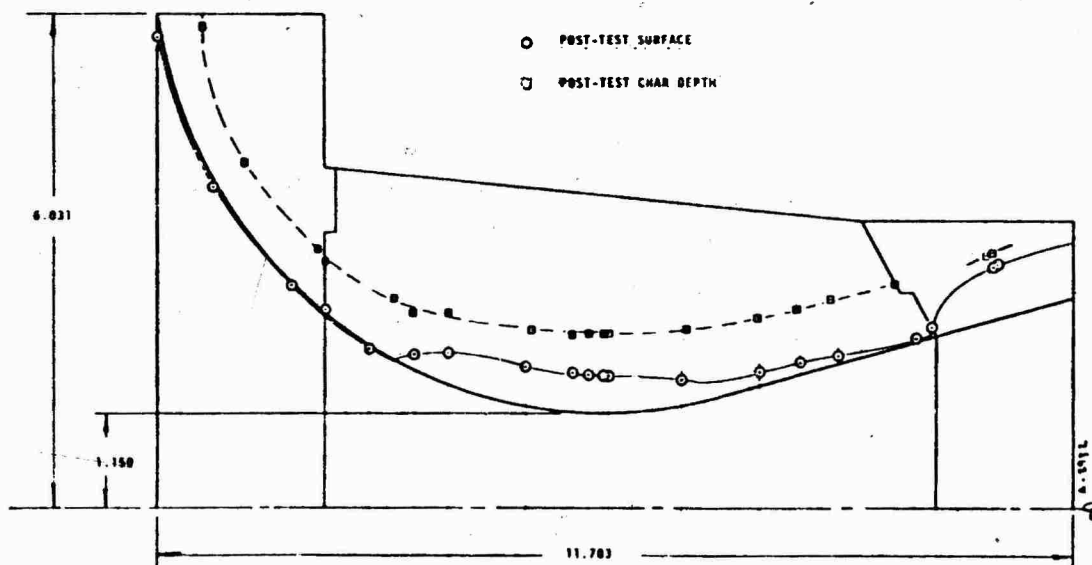
a) 90° SECTION VIEW  
 FIGURE 7-8 CONTINUED



b) 135° SECTION VIEW  
 FIGURE 7-8 CONTINUED

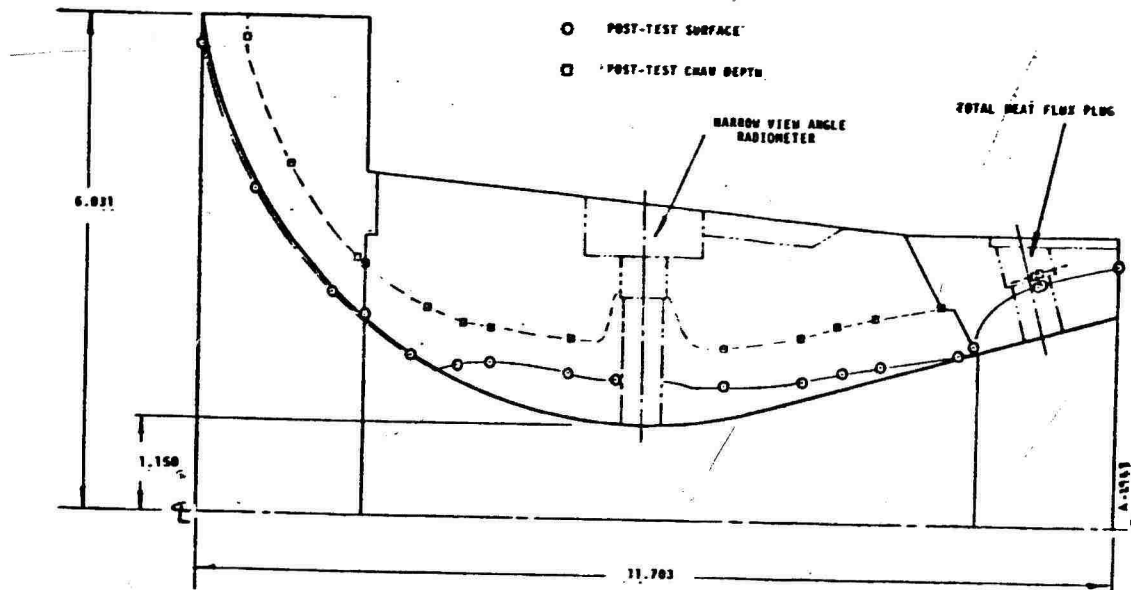


a) 180° SECTION VIEW  
 FIGURE 7-6 CONTINUED



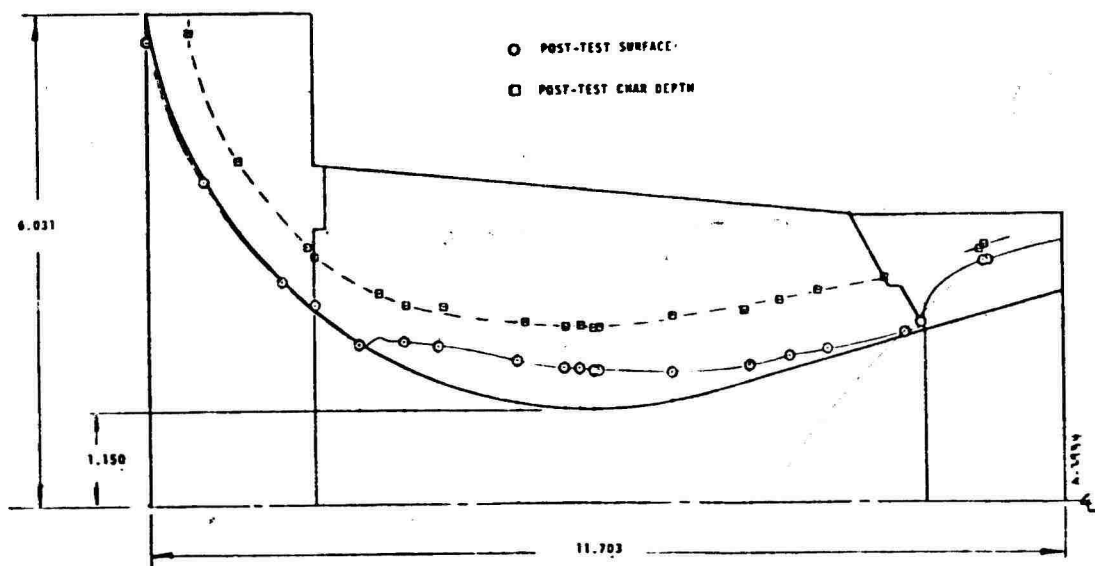
b) 225° SECTION VIEW  
 FIGURE 7-6 CONTINUED





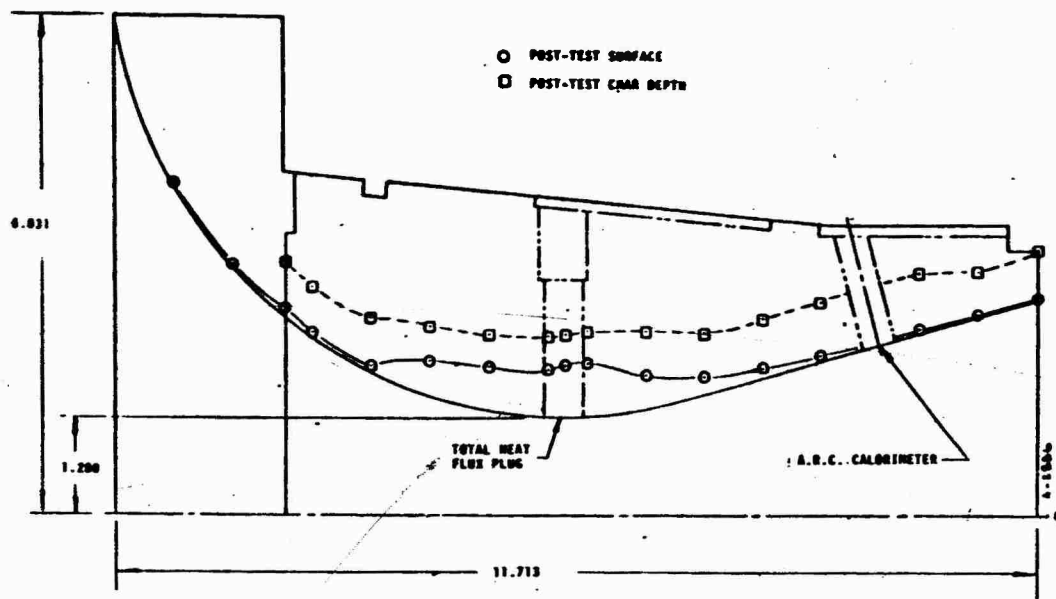
9) 270° SECTION VIEW

FIGURE 7-8 CONTINUED



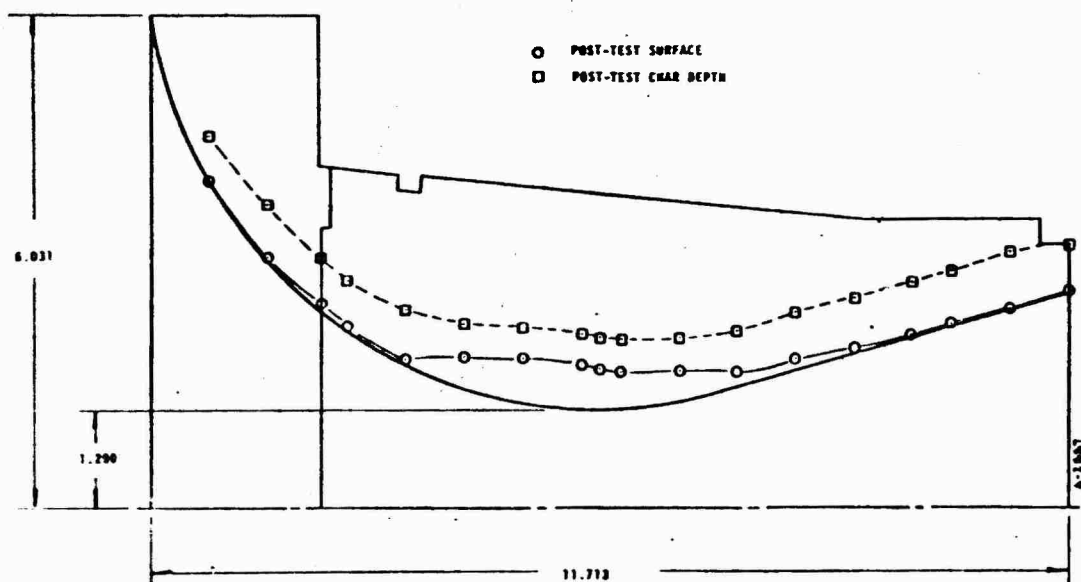
10) 315° SECTION VIEW

FIGURE 7-8 CONCLUDED



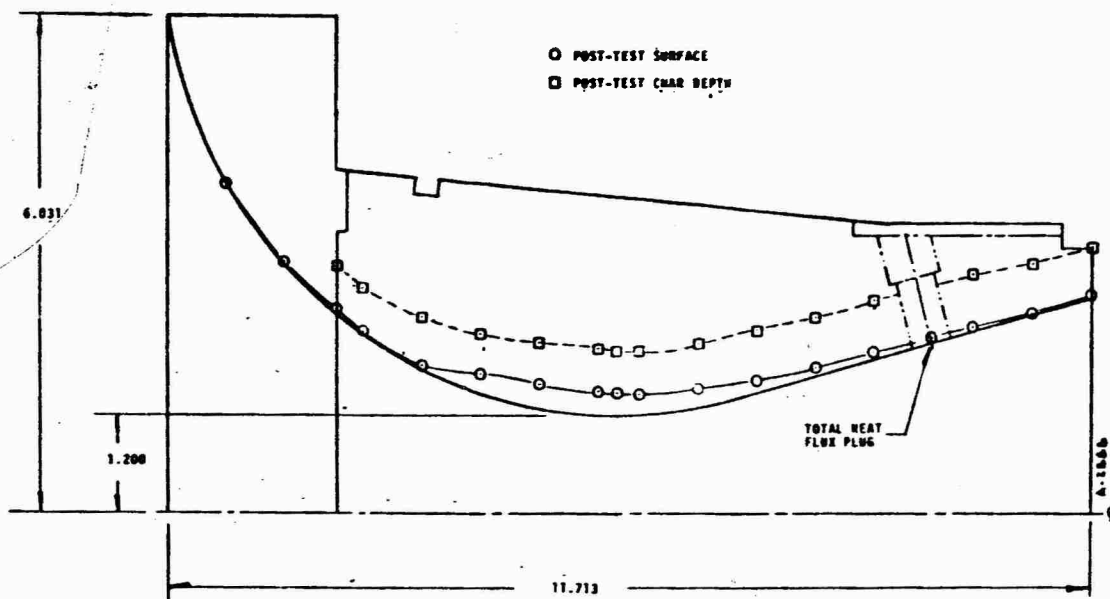
a) 0° Section View

FIGURE 7-9 PRE- AND POST-TEST CHAR MOTOR NOZZLE SURFACE CONTOURS AND CHAR DEPTH CONTOUR, SECOND FIRING

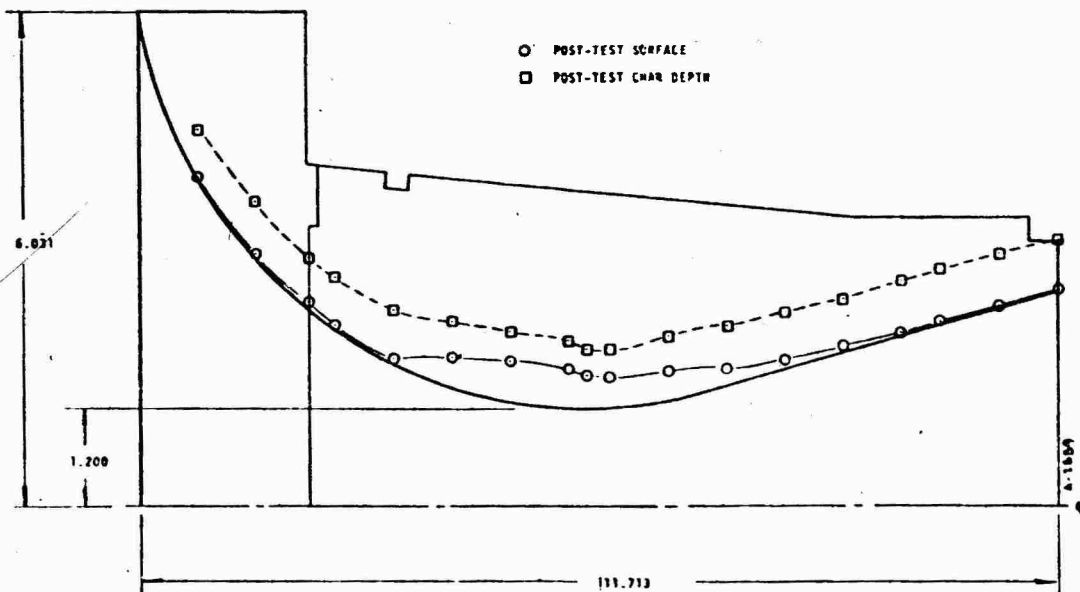


b) 45° SECTION VIEW

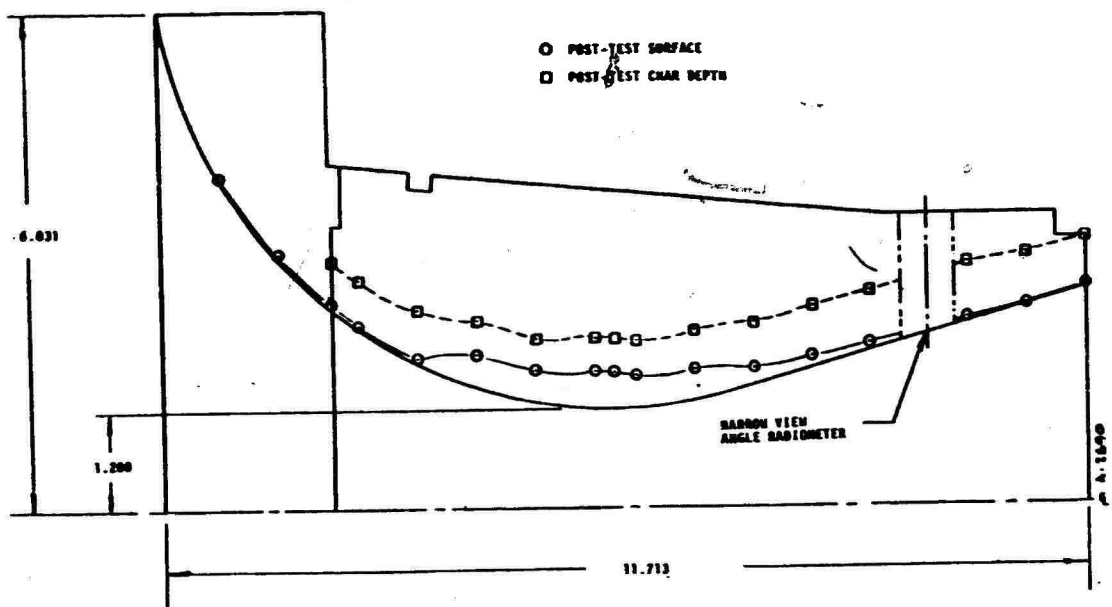
FIGURE 7-9 CONTINUED



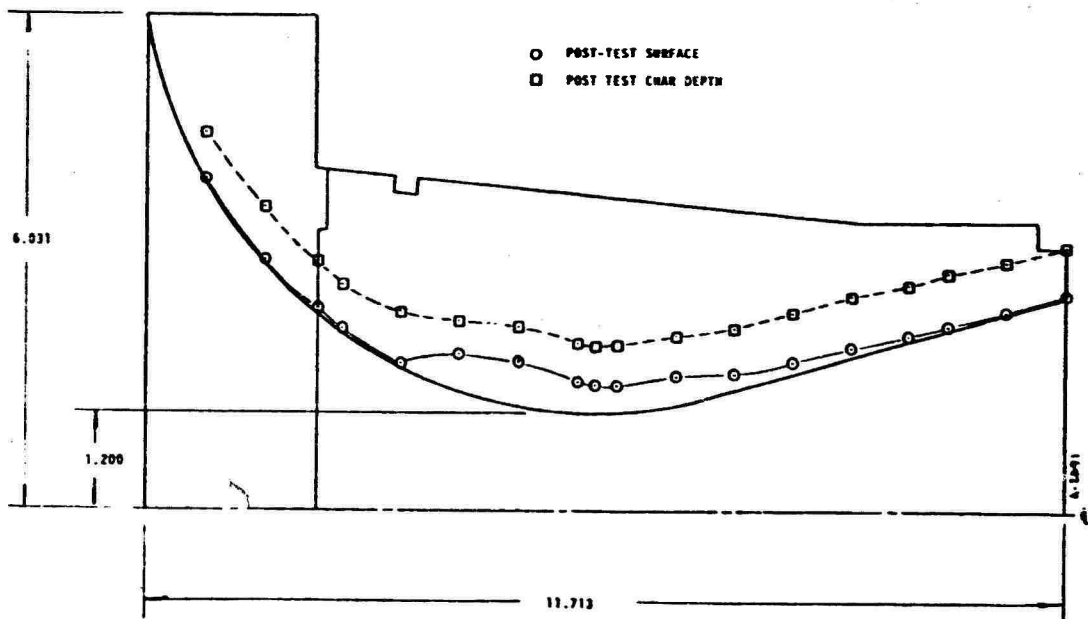
c) 90° SECTION VIEW  
Figure 7-9. Continued



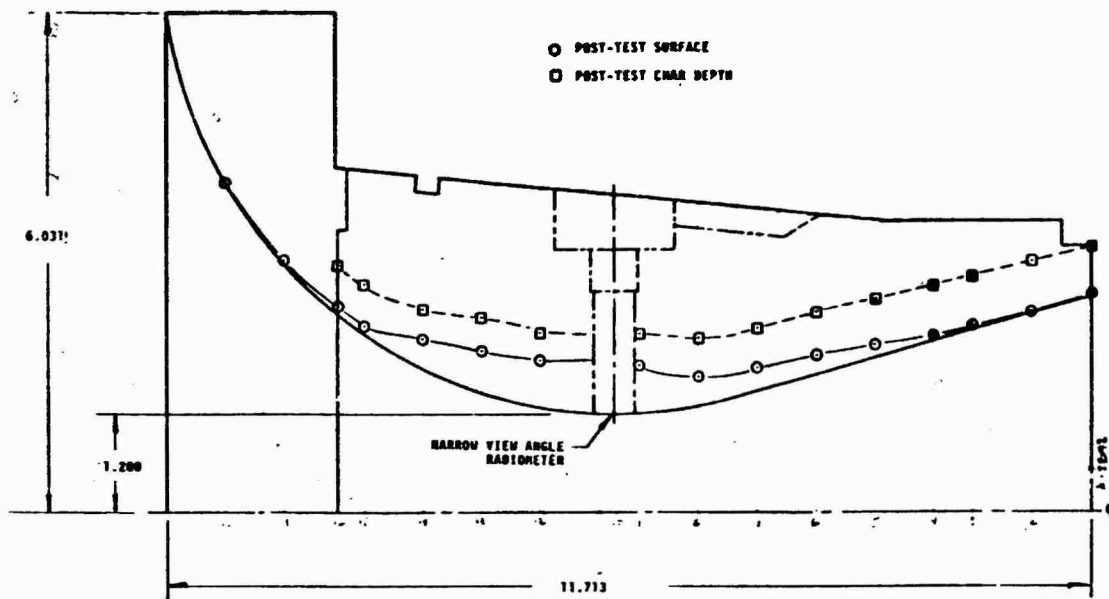
d) 135° SECTION VIEW  
Figure 7-9. Continued



e) 180° SECTION VIEW  
Figure 7-9. Continued

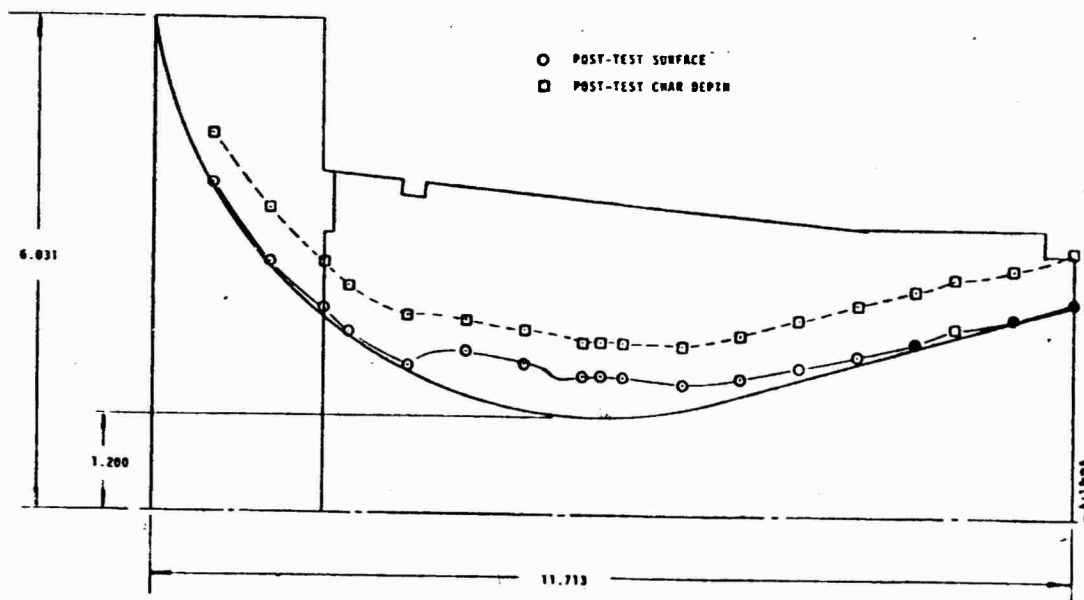


f) 225° SECTION VIEW  
Figure 7-9. Continued



g) 270° SECTION VIEW

Figure 7-9. Continued



h) 315° SECTION VIEW

Figure 7-9. Concluded

TABLE 7-4

## SUMMARY OF CHAR MOTOR NOZZLE ABLATION RESPONSE MEASUREMENTS

## 1st Firing Results

Location <sup>a</sup> (inches)	Area Ratio <sup>b</sup>	Recession <sup>c</sup> (inches)	Char Thickness <sup>d</sup> (inches)	Char Depth <sup>e</sup> (inches)
0.	-27.88	-0.383	0.571	0.188
0.71	-12.36	-0.166	0.513	0.347
1.71	- 5.64	-0.099	0.574	0.475
Bond	- 4.19	0.067	0.577	0.644
2.71	- 2.88	0.000	0.617	0.617
3.21	- 2.01	0.276	0.480	0.756
3.71	- 1.63	0.424	0.447	0.871
4.71	- 1.11	0.499	0.454	0.953
5.33	Throat	0.479	0.473	0.952
5.52		0.464	0.488	0.952
5.71		0.449	0.494	0.943
5.76		0.447	0.501	0.948
6.71	1.14	0.364	0.551	0.915
7.71	1.65	0.196	0.620	0.816
8.24	1.96	0.178	0.656	0.834
8.71	2.31	0.122	0.686	0.808
9.71	3.07	0.053	0.691	0.744
Bond	3.29	0.110		
10.71	3.93	0.643	0.143	0.786
10.75	4.16	0.590	0.156	0.746

<sup>a</sup> Downstream of the nozzle entrance plane.<sup>b</sup> Negative area ratio is subsonic entrance region.<sup>c</sup> Negative recession is due to delamination of the MX 4926 in the throat entrance component during cooldown.<sup>d</sup> Relative to post-test surface.<sup>e</sup> Depth below original surface.

## 2nd Firing Results

Location <sup>a</sup> (inches)	Area Ratio <sup>b</sup>	Recession <sup>c</sup> (inches)	Char Thickness <sup>c</sup> (inches)	Char Depth <sup>d</sup> (inches)
0.	-11.40	0.044	0.566	0.610
0.750	- 6.30	0.024	0.640	0.664
1.412	- 4.05	0.074	0.541	0.615
1.750	- 3.25	0.040	0.543	0.583
2.500	- 2.09	0.089	0.570	0.659
3.250	- 1.46	0.410	0.415	0.825
4.000	- 1.73	0.482	0.388	0.870
4.750	Throat	0.445	0.407	0.852
4.972		0.422	0.407	0.829
5.250		0.430	0.412	0.842
6.000	1.13	0.358	0.471	0.829
6.750	1.45	0.227	0.532	0.759
7.500	1.88	0.174	0.580	0.754
8.250	2.36	0.107	0.613	0.720
8.996	2.93	0.057	0.623	0.680
9.500	3.33	0.080	0.639	0.719
10.250	3.96	0.025	0.631	0.656
11.000	4.75	0.013	0.620	0.633

<sup>a</sup> Downstream of the nozzle entrance plane.<sup>b</sup> Negative area ratio is subsonic entrance region.<sup>c</sup> Relative to post-test surface.<sup>d</sup> Depth below original surface.

### 7.3 TOTAL HEAT FLUX MEASUREMENT SYSTEM

The operation of the six total heat flux measurement systems tested in the two rocket nozzle firings is described in this section. A brief summary of the installation and fabrication details of the sensors which are significant to the data reduction procedure is discussed in Section 7.3.1. The response of each sensor is then presented in Section 7.3.2, and the results of the data reduction are reported in Section 7.3.3.

#### 7.3.1 System Design and Installation

The basic design of the total heat flux measurement system has been described in Section 4. Specific details about the particular sensors utilized in the two char motor firings of this program are reported in Table 7-5.

For the first nozzle firing the various sensor locations were selected so that the total heat flux measurement systems would be exposed to a wide range of convective and radiative boundary conditions. In addition the effects of material type and reinforcement tape layup angle on measurement system operation could be examined since the layup angle (referenced to the nozzle contour tangent) varied with area ratio. The orientation of each sensor was shown as a part of the overall nozzle response diagrams (Figures 7-8 and 7-9). As was mentioned previously, the angular location of each sensor was selected to minimize the possibility of disturbances in the local flow resulting from upstream sensors. Based on the post-fire appearance of the nozzles, this precautionary measure was probably not necessary since only small local disturbances could be attributed to the sensors.

The total heat flux measurement plugs utilized in the second char motor firing were positioned to confirm results of the first firing and obtain data for an additional nozzle location. Since results of the first firing were satisfactory, the basic sensor design was not altered for the second firing. The slight changes in thermocouple depths shown in Table 7-5 between the nozzle firings (and between each sensor plug) resulted from machining tolerances allowed during sensor fabrication.

The fabrication and installation techniques employed to position each sensor plug in the two ablative nozzles were as described in Sections 4.1, 4.2, and 7.1. In the assembly of the steel shell and ablative liner, special care was taken to insure that the lead wires remained in their respective slots in the ablative liner and were

TABLE 7-5  
DETAILS OF TOTAL HEAT FLUX MEASUREMENT SYSTEM DESIGNS

Ablative Material	Layup <sup>a</sup> Angle (degrees)	Area Ratio	Angular Location <sup>b</sup> (degrees)	Thermocouples <sup>d</sup> Type / Depth (inches)			
<u>First Nozzle Firing</u>							
MX 4926 Carbon Phenolic	36	-2.	90	W-Re/0.151	W-Re/0.275	W-Re/0.423	W-Re/0.626
	60	1	0	W-Re/0.129	W-Re/0.255	W-Re/0.407	W-Re/0.605
	75	2	180	W-Re/0.124	W-Re/0.259	W-Re/0.402	W-Re/0.603
MX 2600-96 Silica Phenolic	—	4	270	W-RE/0.105	W-RE/0.208	W-Re/0.311	W-Re/0.475
<u>Second Nozzle Firing</u>							
MX 4926	60	1.	0	W-Re/0.109	W-Re/0.238	W-Re/0.386	W-Re/0.584
	75	3.	90	W-Re/0.117	W-Re/0.241	W-Re/0.343	W-Re/0.536
							CR-AL/0.828
							CR-AL/0.804
							CR-AL/0.807
							CR-AL/0.609
							CR-AL/0.780
							CR-AL/0.692

<sup>a</sup> Layup angle is reference to a tangent at the plug surface.

<sup>b</sup> Relative to throat plug location.

<sup>c</sup> W-Re: tungsten 5 percent rhenium - tungsten 26 percent rhenium thermocouple.

CR-AL: Chromel-Alumel thermocouple.

<sup>d</sup> Depths below prefire surface.



properly aligned and fed through the holes in the steel shell as it was slipped on to the liner. Even though the installation process was successful and the same process was used for both nozzles, some thermocouple circuits were lost during this installation for the second nozzle. These included three thermocouple circuits going to the total heat flux sensor at an  $A/A^* = 3.0$  and the circuit to the Atlantic Research Corporation (ARC) calorimeter. These failures were detected by continuity checks of the circuits. The continuity checks were made continually through the fabrication and installation process. If these checks had revealed a significant number of circuit failures, the sensor would have been replaced. However, any repair of the sensor was impossible after assembly of the ablative part in the steel shell.

#### 7.3.2 Sensor Response

The response of the total heat flux sensors was consistent with the requirements for effective measurement of the heat flux boundary conditions. One of the primary uncertainties in the expected response of the sensors was the degree to which flow discontinuities would be generated during the ablation of the heat flux sensors. The design was directed towards minimizing such disturbances, and the post-firing appearances of the sensor locations indicated that this design requirement was satisfied. Photographs of five of the six plug locations are given in Figure 7-10. The other location was not photographed because the photographer could not find the sensor/nozzle interface. The most significant deviation from ideal performance occurred at the throat location of the first nozzle firing where slight gouging occurred at the thermocouple lead wire slots on the side of the sensors (Figure 7-10). This gouging caused premature failure of the thermocouples as ablation occurred. None of the other sensors including the one at the throat of the second nozzle exhibited such significant gouging.

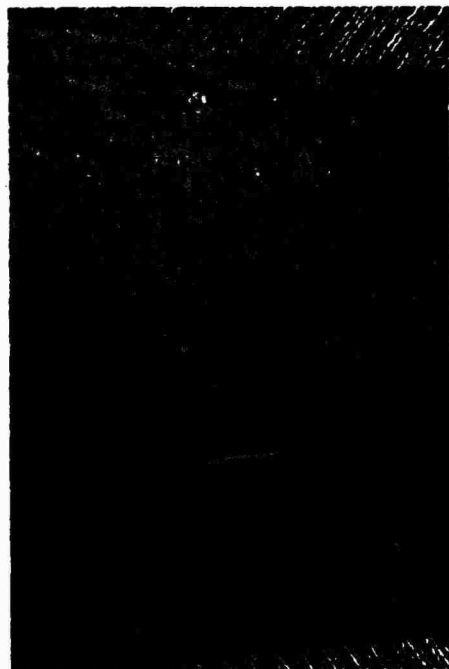
As discussed earlier in the descriptions of the measurement system concept, all information about surface heat flux boundary conditions are derived from the subsurface thermocouple measurements. Moreover, since the evaluation of the surface events from these measurements are extremely sensitive to experimental error, the data recording system and the thermocouple calibrations must be accurate. In the test firings, the AFRPL digital data recording system recorded thermocouple millivolt output continuously and it was sampled approximately every 10 milliseconds in the data reduction process. Standard NBS calibration curves were utilized for the Chromel-Alumel thermocouples. This standard was checked against manufacturers specifications for the particular wire lot used for the total heat flux



A/A\* = -2.0 (SUBSONIC)



THROAT



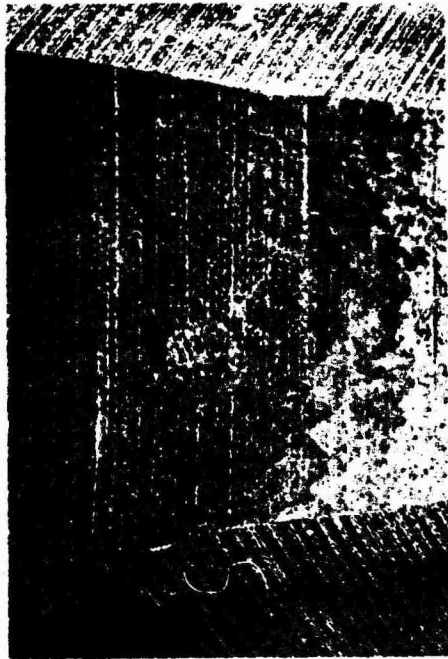
A/A\* = 2.0 (SUPERSONIC)

a) FIRST CHAR MOTOR TEST FIRING

FIGURE 7-10 PHOTOGRAPHS OF NOZZLE SURFACES SHOWING ABLATIVE PLUG SENSORS



THROAT



$A/A^* = 3.0$  (SUPERSONIC)

b) SECOND CHAR MOTOR TEST FIRING

FIGURE 7-10, CONCLUDED

sensor and was found to be accurate. For the tungsten-5 percent rhenium/tungsten-26 percent rhenium thermocouples (W5Re/W26Re), no NBS standard is available. Manufacturer's specifications, available to 4200°F, were curve-fit and utilized to reduce the data. A different wire lot was used for each char motor nozzle; hence two calibration curves were required. For temperatures from 4200°F to 5400°F, data of Reference 4-12 were curve-fit. The calibration equations utilized to reduce the measured thermocouple millivolt outputs are summarized in Table 7-6.

The reduced thermocouple data are presented in Figure 7-11. Also shown are thermal response predictions to be described in Section 7.3.3. Some anomalies are apparent from Figure 7-11. The most significant is the shift in the rate of temperature increase which occurred for practically all thermocouples at 3000°R. An error in a calibration equation was suspected so the millivolt output was plotted for the A/A\* = 2.0 sensor of the first firing. This is presented as Figure 7-12 and shows the same trend. Therefore, either the trend is real or some unexpected calibration shift or electrical grounding of the circuit occurred to compromise the accuracy of measurements above 3000°R. Despite these anomalies, the accuracy of the heat fluxes evaluated from the overall system response was not significantly impaired because sufficient data are available at temperatures below 3000°R.

The anomalous responses of the three deepest thermocouples of the throat sensor in the first nozzle (Figure 7-11) are believed to be a result of the gouging in the thermocouple lead slots described above. Sufficient data were, however, obtained in this case to provide a basis for extrapolating heat flux to the end of the firing. In conclusion, although a few anomalies in the thermocouple data did occur, enough redundancy was provided in the measurement system concept and design to allow the partial definition of heat flux histories for all of the locations where a sensor was placed.

### 7.3.3 Total Heat Flux System Evaluation

In the previous section the response of the total heat flux sensors was described and the temperature history measurements were presented. The evaluation of the total heat fluxes from the firing condition information and sensor output is presented in this section. The basic data reduction technique was described previously in Section 5. Specific details about the data reduction for the ablative materials tested in the two char motor firings are presented in the following paragraphs. In addition the analysis is concluded with a comparison of predicted heat flux to the measured values and a discussion of measurement system performance.

TABLE 7-6

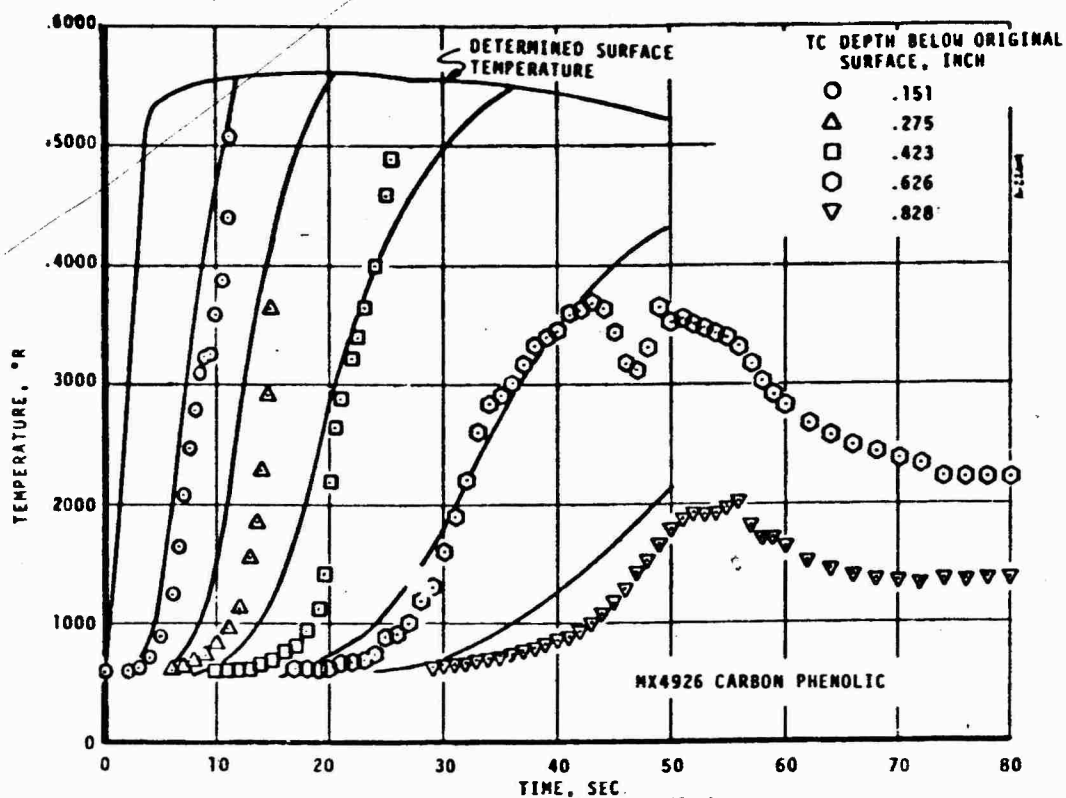
THERMOCOUPLE CALIBRATION CURVE-FIT CONSTANTS<sup>a</sup>

Thermocouple Type	Temperature Range (°R)	XI (mv)	XO (mv)	YO (°F)	DOY (°F)	DIY (°F)	D2Y (°F)	D3Y (°F)	D4Y (°F)
Chromel-Alumel	500-1240	3.376	0.180	40.0	148.52	0.82	0.57	-5.50	10.90
	1240-2940	7.496	17.060	780.0	316.92	3.64	9.13	-3.92	7.25
	492-1460	1.000	0.000	32.0	127.48	-4.56	0.	0.	0.
	1460-2460		9.304	1000.0	91.54	0.74			
	2460-2960		19.823	2000.0	99.23	3.14			
	2960-3460		24.575	2500.0	114.17	2.66			
	3460-4080		28.955	3000.0	125.43	4.74			
	4080-4460		33.580	3620.0	148.46	10.59			
	4460-4960		36.015	4000.0	185.00	25.01			
	4960-5460		38.475	4500.0	261.32	34.36			
W26Re/W5Re (1st Firing)	Above 5460		40.291	5000.0	256.59	-58.38			
	500-1660	2.276	0.062	40.0	280.29	-40.57	18.74	-3.56	-5.38
	1660-3120	2.888	11.440	1200.0	272.08	4.53	2.64	10.00	-22.05
	3120-4480	1.914	25.882	2660.0	239.42	22.88	-12.82	11.32	5.72
	4480-4660	0.189	34.450	4020.0	33.78	0.77	0.49	-0.48	0.84
	4660-4960	1.000	36.015	4000.0	185.00	25.01	0.	0.	0.
	4960-5460		38.475	4500.0	261.32	34.36			
	Above 5460		40.291	5000.0	256.59	-58.38			
	500-1660	2.276	0.062	40.0	280.29	-40.57	18.74	-3.56	-5.38
	1660-3120	2.888	11.440	1200.0	272.08	4.53	2.64	10.00	-22.05
W26Re/W5Re (2nd Firing)	3120-4480	1.914	25.882	2660.0	239.42	22.88	-12.82	11.32	5.72
	4480-4660	0.189	34.450	4020.0	33.78	0.77	0.49	-0.48	0.84
	4660-4960	1.000	36.015	4000.0	185.00	25.01	0.	0.	0.
	4960-5460		38.475	4500.0	261.32	34.36			
	Above 5460		40.291	5000.0	256.59	-58.38			
	500-1660	2.276	0.062	40.0	280.29	-40.57	18.74	-3.56	-5.38
	1660-3120	2.888	11.440	1200.0	272.08	4.53	2.64	10.00	-22.05
	3120-4480	1.914	25.882	2660.0	239.42	22.88	-12.82	11.32	5.72
	4480-4660	0.189	34.450	4020.0	33.78	0.77	0.49	-0.48	0.84
	4660-4960	1.000	36.015	4000.0	185.00	25.01	0.	0.	0.

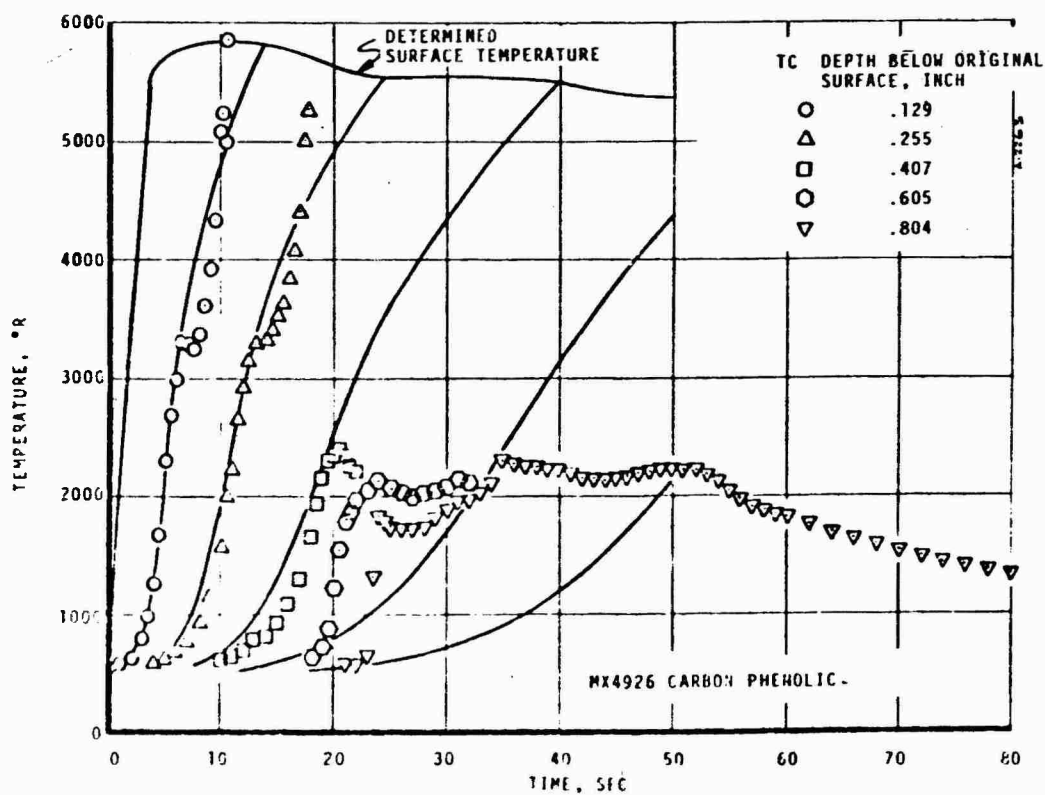
$$^a \text{Temp (°F)} = YO + DOY \times U + \frac{1}{2} \times DIY \times U + \frac{1}{6} \times D2Y \times U + \frac{1}{120} \times D4Y \times U \quad (U-1) \quad (U-2)$$

$$+ \frac{1}{24} \times D3Y \times U \quad (U-1) \quad (U-2) \quad (U-3) + \frac{1}{120} \times D4Y \times U \quad (U-1) \quad (U-2) \quad (U-3) \quad (U-4)$$

$$\text{where } U = (X(\text{mv}) - XO) / XI$$

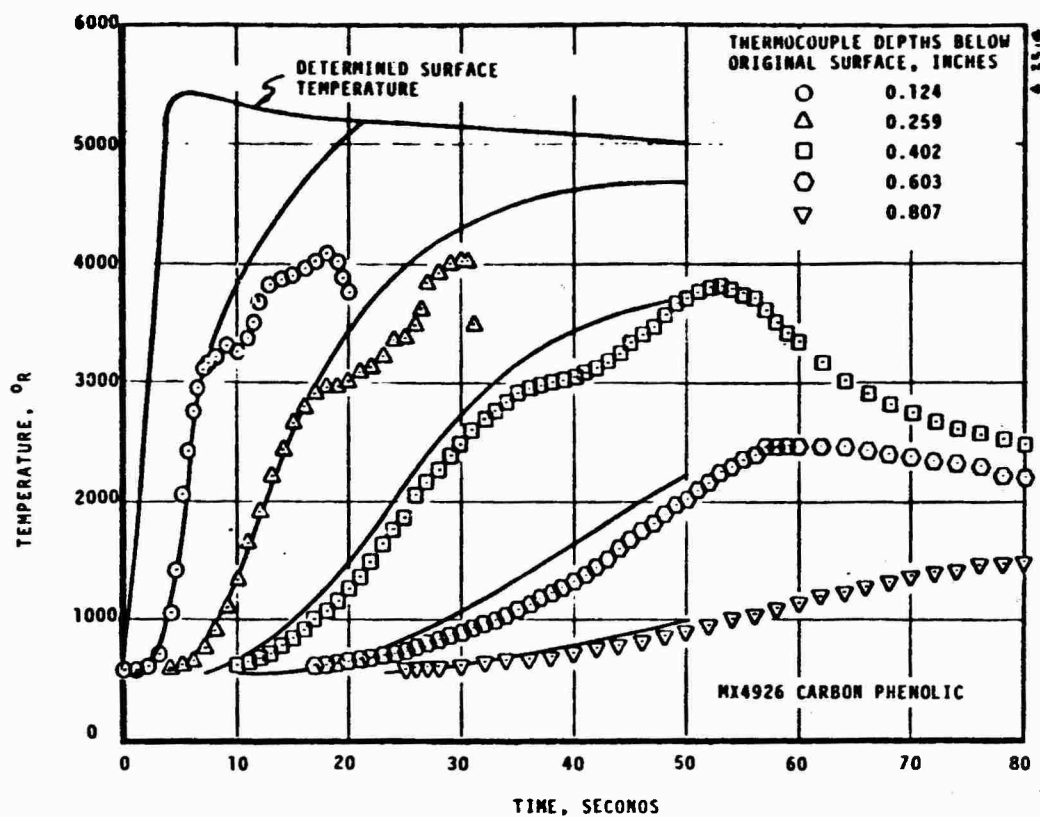


a)  $A/A^* = -2.0$  (SUBSONIC), 1st NOZZLE FIRING  
 FIGURE 7-11 MEASURED AND COMPUTED IN-DEPTH TEMPERATURE AND DETERMINED SURFACE TEMPERATURE



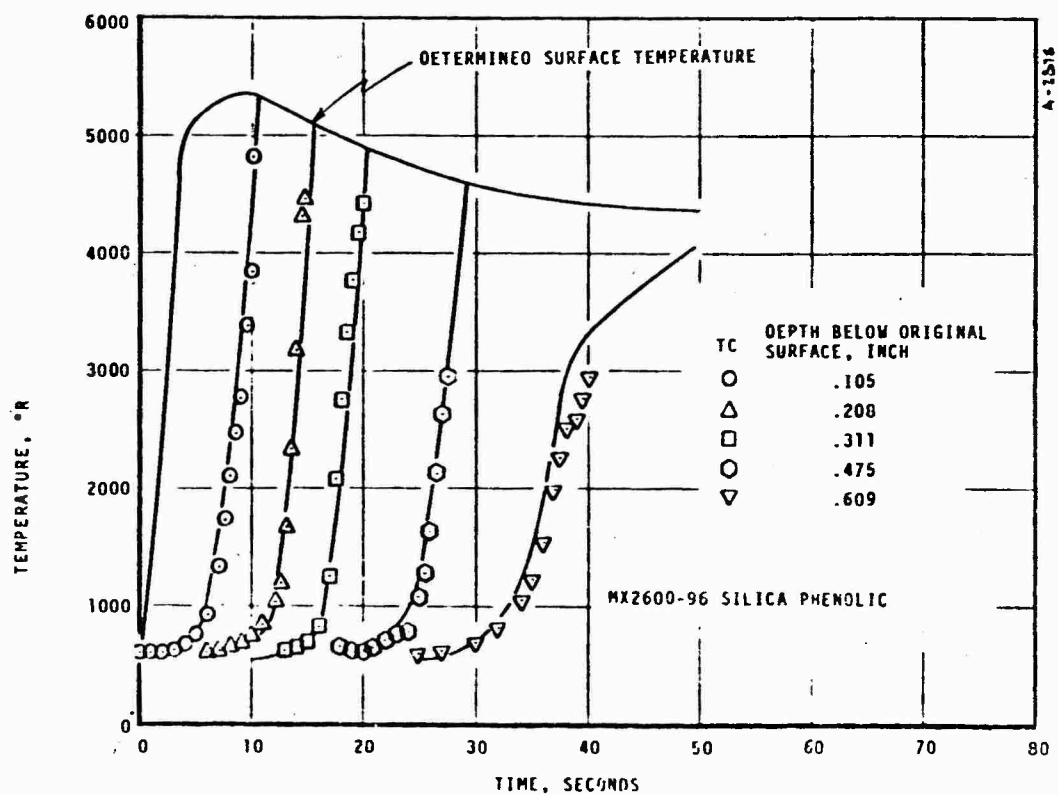
b) THROAT, 1st NOZZLE FIRING

FIGURE 7-11 CONTINUED



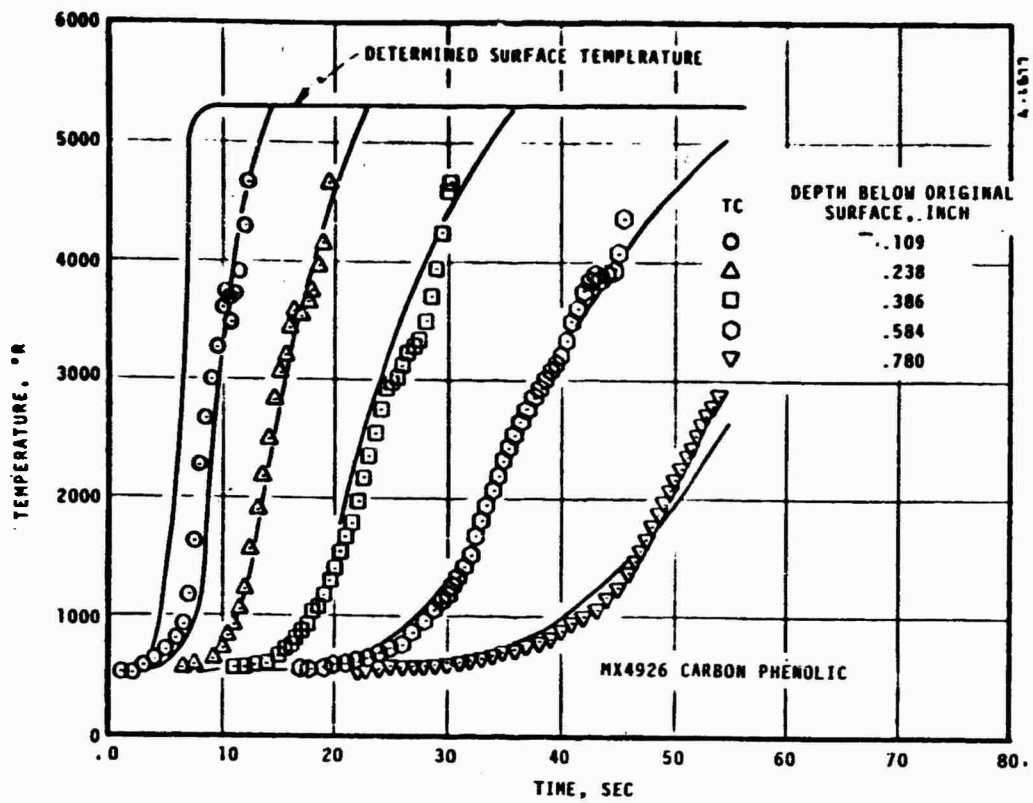
c)  $A/A^* = 2.0$  (SUPERSONIC), 1st NOZZLE FIRING

FIGURE 7-11 CONTINUED



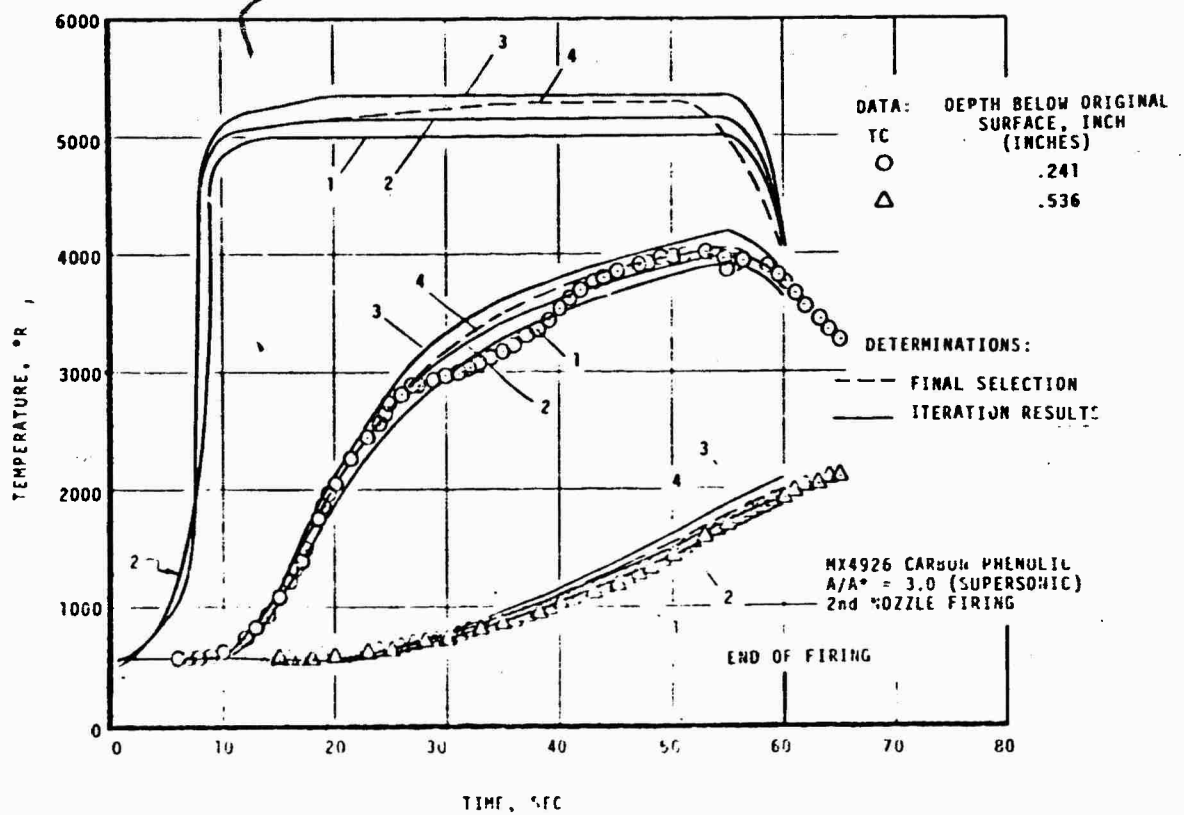
d)  $A/A^* = 4.0$  (SUPERSONIC), 1st NOZZLE FIRING

FIGURE 7-11 CONTINUED



e) THROAT, 2nd FIRING

FIGURE 7-11 CONTINUED



f) A/A\* = 3.0 (SUPERSONIC), 2nd NOZZLE FIRING

FIGURE 7-11 CONTINUED

4 164



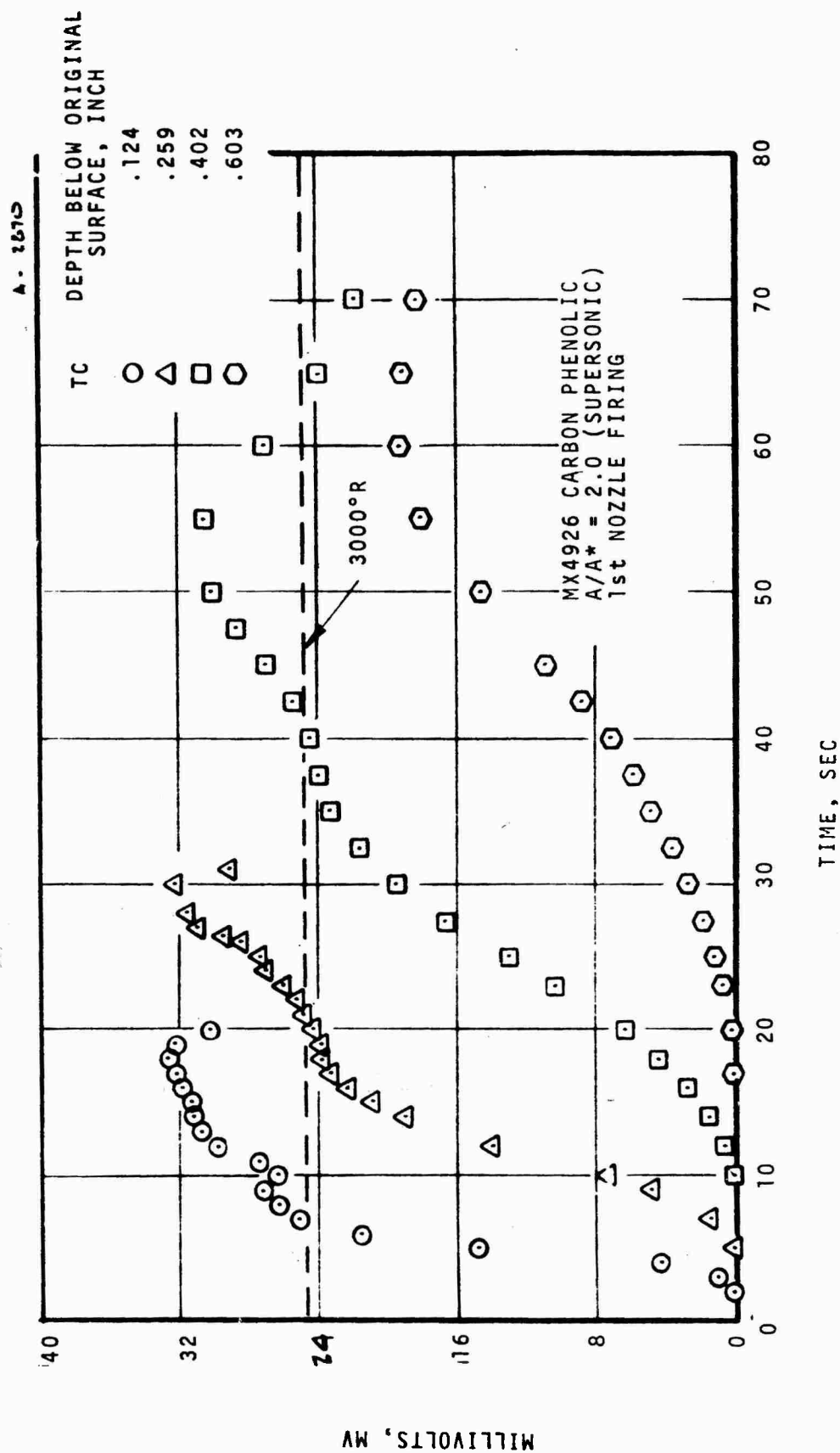


FIGURE 7-12 TYPICAL THERMOCOUPLE MILLIVOLT OUTPUTS SHOWING TEMPERATURE RISE RATE DECREASE NEAR 3000°R

The steps in the evaluation of total incident heat flux may be summarized as follows:

- Analysis of overall consistency between the temperature histories, thermocouple depths, ablative material thermophysical properties, and the one-dimensional thermal response model.
- Estimation of first guess surface temperature and recession histories.
- Iterative evaluation of surface temperature, surface recession and in-depth decomposition events.
- Consideration of char swell.
- Evaluation of surface thermochemical events from parametric surface mass balance calculations.
- Evaluation of surface total heat flux.

Discussions of the techniques employed to accomplish each of these steps are given in Sections 7.3.3.1 through 7.3.3.6. Concluding remarks are then given in Section 7.3.3.7.

#### 7.3.3.1 Verification of Heat Conduction Model and Temperature Response Data.

One advantage of calculating heat flux from multiple thermocouple temperature histories is that redundant information is available. For an ideal one-dimensional slab of ablative material being heated on one surface and insulated on all others, the surface temperature and heat flux conducted into the material can be defined from a single in-depth temperature history, provided the pertinent material thermal and chemical properties are accurately known. A well characterized ablative material used as the exposed surface material in a rocket nozzle is a good approximation of this ideal model. The measurement of temperatures at more than one in-depth location provides sufficient information to estimate how closely the measured response approaches that predicted by the ideal model. This comparison, if satisfactory, between the predicted and measured in-depth material thermal response, using the material thermal and chemical properties for MX 2600-96 and MX 4926 described in Section 4, provides the verification of the theoretical model.

For the temperature history data obtained in this program, these verifications of data consistency were performed by inputting

thermocouple locations as pseudo-surfaces and by inputting thermocouple data as pseudo-surface temperature into the Aerotherm Charring Material Ablation (CMA) computer code. The code then calculated the transient thermal response of the material below the pseudo-surface. The degree to which the measured in-depth temperatures could be predicted was an indication of the quality of the data. A typical example of the results of one of these calculations is given in Figure 7-13. Notice that since the thermocouple closest to the surface was lost during the firing, a shift in the driver was required. This shift was accomplished by impressing a large recession rate for a short time so that the surface moved to the location of the third thermocouple. At the same time the pseudo-surface temperature was decreased to the measured value of the third thermocouple. This rapid shift caused the anomaly seen in the prediction for the fourth thermocouple at 20 seconds. Despite anomalies of this type, these calculations showed that in general the thermocouple depths and corresponding temperature data obtained from the sensors were consistent with the thermal properties and heat conduction model utilized in the data reduction procedure.

#### 7.3.3.2 Estimation of Surface Response Boundary Conditions

The second step in the evaluation of the total heat flux was to estimate the surface temperature and recession responses of each ablative plug. This information is the input boundary conditions for the computation of the overall material thermal response. The recession response as a function of firing time is defined quite well from pre- and post-test diameter measurements and from the times at which thermocouples become exposed at the surface. Plots of recession versus time for each total heat flux sensor plug are shown in Figure 7-14. Since the thermocouple typically failed before reaching the surface, these points fall to the left (or above) the actual recession history. The initial estimate of the transient surface recession was based on this interpretation of thermocouple failure and on the post-test measurement. Figure 7-14b also shows the results of predictions based on equilibrium surface thermochemistry which were performed as a part of a heat flux measurement evaluation analysis.

Estimation of surface temperature histories was somewhat more difficult, especially for those plugs where surface recession rate was large. The technique used was to cross plot the transient responses against thermocouple location at several specified times and to extrapolate the resulting temperature profiles to the surface locations defined as described above. Due to the relatively high surface recession rate and the relatively high surface heat flux experienced by several of the plugs in these nozzle test firings, the profiles were so steep that only two or three of the thermocouples could be used in establishing this profile. Moreover, the anomalies

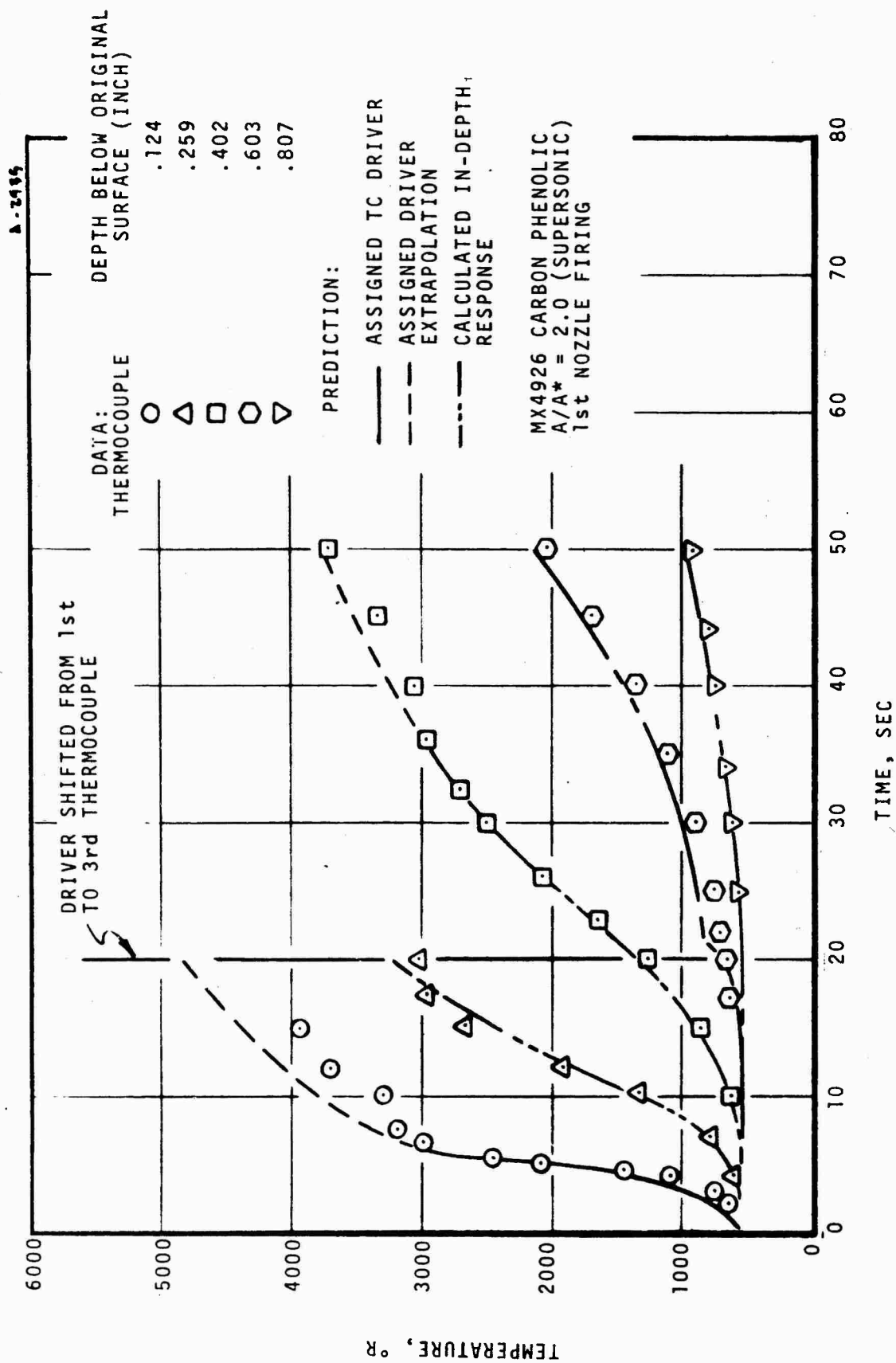
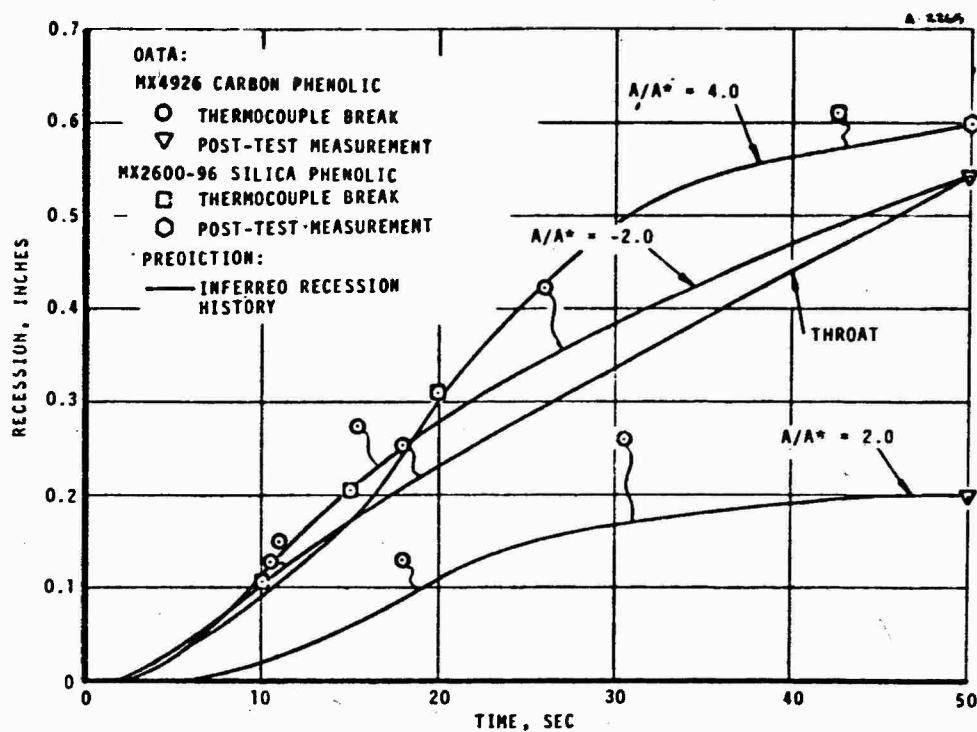
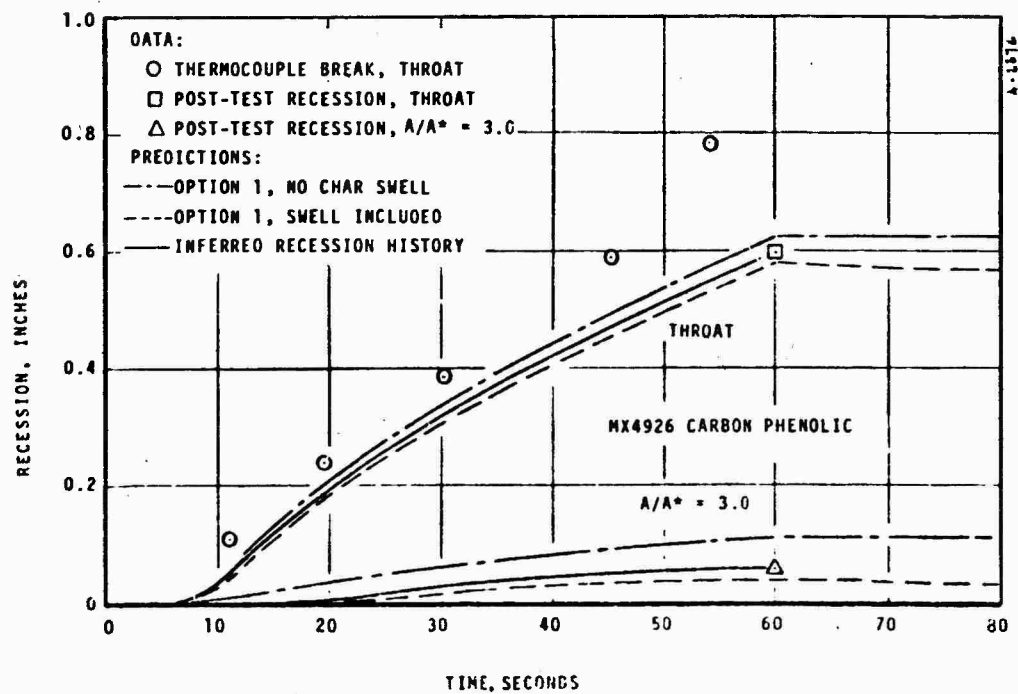


FIGURE 7-13 ASSIGNMENT OF THERMOCOUPLE MEASUREMENTS TO VERIFY THE TEMPERATURE DATA AND THE IN-DEPTH HEAT CONDUCTION MODEL



a) 1st CHAP MOTOR NOZZLE TEST FIRING

FIGURE 7-14 SURFACE RECESSION HISTORIES OF TOTAL HEAT FLUX MEASUREMENT SYSTEMS



b) 2nd CHAP MOTOR NOZZLE TEST FIRING

FIGURE 7-14 CONTINUED

observed above 3000°R certainly compromise this technique. An example of the application of this technique is shown in Figure 7-15. The definition of the shapes of the temperature profiles are assisted by the profiles computed during the data verification procedure. These calculations, along with the data points available, provided sufficient information to estimate the surface temperature histories for the initial input to the iterative thermal response evaluation procedure.

A tradeoff exists between the accuracy of the first guess surface temperature and the first guess recession. If recession is high, many thermocouples will be broken providing numerous data points for recession history estimation. If recession is low, the thermocouples will provide numerous temperature profile data points, and the accuracy of the estimated surface temperature will be improved. Finally, since these are only first guesses for the subsequent iterative evaluation procedure, uncertainties in these estimates do not significantly affect the accuracy of the final heat flux measurement. They only increase the difficulty of converging rapidly to the answer.

#### 7.3.3.3 Iterative Evaluation of Surface and In-Depth Responses

Once the first guesses for the ablative plug surface boundary conditions have been defined, iterative solutions and adjustments of the input values of surface recession and surface temperature are performed. For these calculations the CMA computer code is utilized in the mode where the heated surface response (surface recession rate and temperature) are input directly. The code computes the overall heat conduction and thermal decomposition response of the material, including predictions of thermocouple measurements. Iteration on surface boundary condition input is continued until the overall transient response of the material is predicted as closely as desired.

For each of the total heat flux measurement systems tested in the two char motor firings, an average of four iterations was performed. Figure 7-11f (page 7-32) presented typical iterative values of surface temperature and compared the computed in-depth response to thermocouple data. For this sensor only two thermocouple circuits remained after nozzle fabrication, but the resulting surface temperature was still well defined. More thermocouples, as were available for all of the other sensors, decrease the importance of errors in thermocouple depths or in thermocouple data readings because such anomalies would be apparent or averaged out. The final surface temperature histories and the corresponding in-depth thermocouple response predictions for all sensors are compared to the measured thermocouple data in Figures 7-11a through 7-11f.

In addition to defining the surface response of the ablative plug, the iterative evaluation of in-depth response defines several

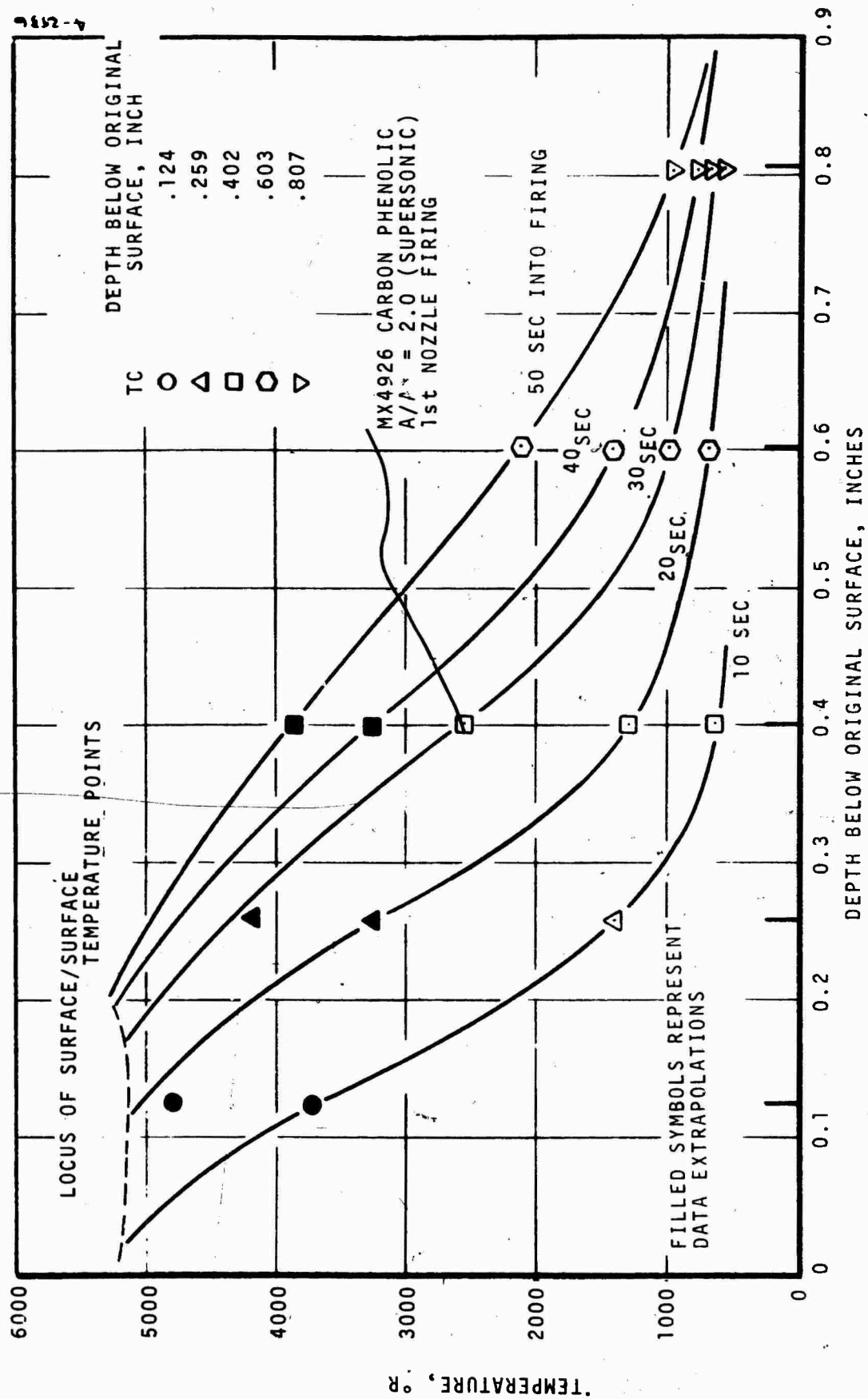


FIGURE 7-15 TEMPERATURE PROFILES UTILIZED TO ESTIMATE FIRST GUESS SURFACE TEMPERATURE HISTORY

of the ablation and heat transfer results required in the final summation of surface heat fluxes. These quantities have been described in Section 5. Some of the representative values of the variables for the six ablative sensors tested in this program are given in Table 7-7. For each plug, data are given four times during the respective firings.

#### 7.3.3.4 Char Swell Considerations

The energy flux terms associated with chemical reactions at an ablating surface are strongly dependent on the rate of surface mass removal and hence on the surface recession rate. The surface recession history determined by the technique described in the previous sections accounts for two surface movement effects:

- Surface regression due to chemical reactions
- Surface advancement due to char swelling

These response mechanisms are illustrated in Figure 7-16. The actual surface movement defined in Section 7.3.3.3 is less than that due to thermochemical attack by the net amount of char swell. That is,

$$S_m = S_{tc} - S_{swell} \quad (7-1)$$

where

$S_m$  = measured surface recession (Section 7.3.3.3)

$S_{tc}$  = net thermochemical regression

$S_{swell}$  = net surface movement due to swell

This swelling has been found to occur in MX 4926 carbon phenolic but not in MX 2600-96 silica phenolic. The causes of the phenomenon are discussed in Reference 4-6. In that study it was found that the amount of char swell was proportional to the char thickness and that the proportionality constant for the carbon phenolic is 0.135. That is,

$$S_{swell} = 0.135 \tau_c \quad (7-2a)$$

where  $\tau_c$  is the char thickness. Based on the reasonable assumption that the proportionality factor is constant with time, Equation



TABLE 7-7  
RESULTS OF IN-DEPTH RESPONSE SOLUTIONS

Sensor Material	Sensor Location <sup>a</sup>	Time (sec)	T <sub>w</sub> (°R)	m <sub>c</sub> (lb/ft <sup>2</sup> sec)	m <sub>g</sub> (lb/ft <sup>2</sup> sec)	q <sub>rad</sub> (Btu/ft <sup>2</sup> sec)	q <sub>cond</sub> (Btu/ft <sup>2</sup> sec)	q <sub>char</sub> (Btu/ft <sup>2</sup> sec)	q <sub>gas</sub> (Btu/ft <sup>2</sup> sec)	m <sub>b</sub> c <sub>swell</sub> (lb/ft <sup>2</sup> sec)	q <sub>char</sub> (Btu/ft <sup>2</sup> sec)
MX 4926	-2.0/1st	10	5560	0.146	0.045	387	666	346	221	0.007	17
		20	5600	0.062	0.032	398	462	149	163	0.004	10
		30	5550	0.056	0.025	384	352	133	122	0.003	7
		50	5220	0.043	0.018	301	233	95	81	0.001	2
		10	5850	0.088	0.041	478	621	222	222	0.007	18
	Throat/1st	20	5660	0.061	0.029	415	426	148	150	0.004	11
		30	5550	0.061	0.025	384	362	144	125	0.003	7
		50	5380	0.061	0.021	340	303	139	100	0.001	2
		10	5350	0.058	0.032	332	419	132	149	0.010	22
		20	5200	0.044	0.024	296	311	97	107	0.006	13
MX 2600-96	4.0/1st	30	5150	0.023	0.019	284	243	49	84	0.004	9
		50	5000	0.001	0.015	253	152	1	61	0.001	3
		10	5350	0.149	0.025	332	495	-449	123	0	0
		20	4900	0.165	0.030	234	528	-535	124	0	0
		30	4590	0.101	0.021	180	334	-343	75	0	0
	Throat/1st	50	4350	0.015	0.006	145	90	-54	20	0	0
		12	5300	0.101	0.043	319	591	226	197	0.006	13
		20	5000	0.083	0.032	234	453	186	149	0.004	9
		30	5000	0.065	0.027	234	376	146	122	0.003	8
		50	5000	0.053	0.021	234	294	120	97	0.003	6
MX 4926	3.0/2nd	12	5307	0.021	0.025	321	355	46	115	0.011	24
		20	5353	0.016	0.021	332	267	36	99	0.008	17
		30	5371	0.014	0.017	337	220	31	78	0.006	15
		50	5383	0.009	0.014	340	172	14	61	0.004	10
		50	5383	0.009	0.014	340	172	14	61	0.004	10

<sup>a</sup>Nozzle Area Ratio/Char Motor Test Firing

<sup>b</sup>See Section 7.3.3.4

<sup>c</sup>q<sub>char,swell</sub> = q<sub>char</sub> × m<sub>c,swell</sub> / m<sub>c</sub>

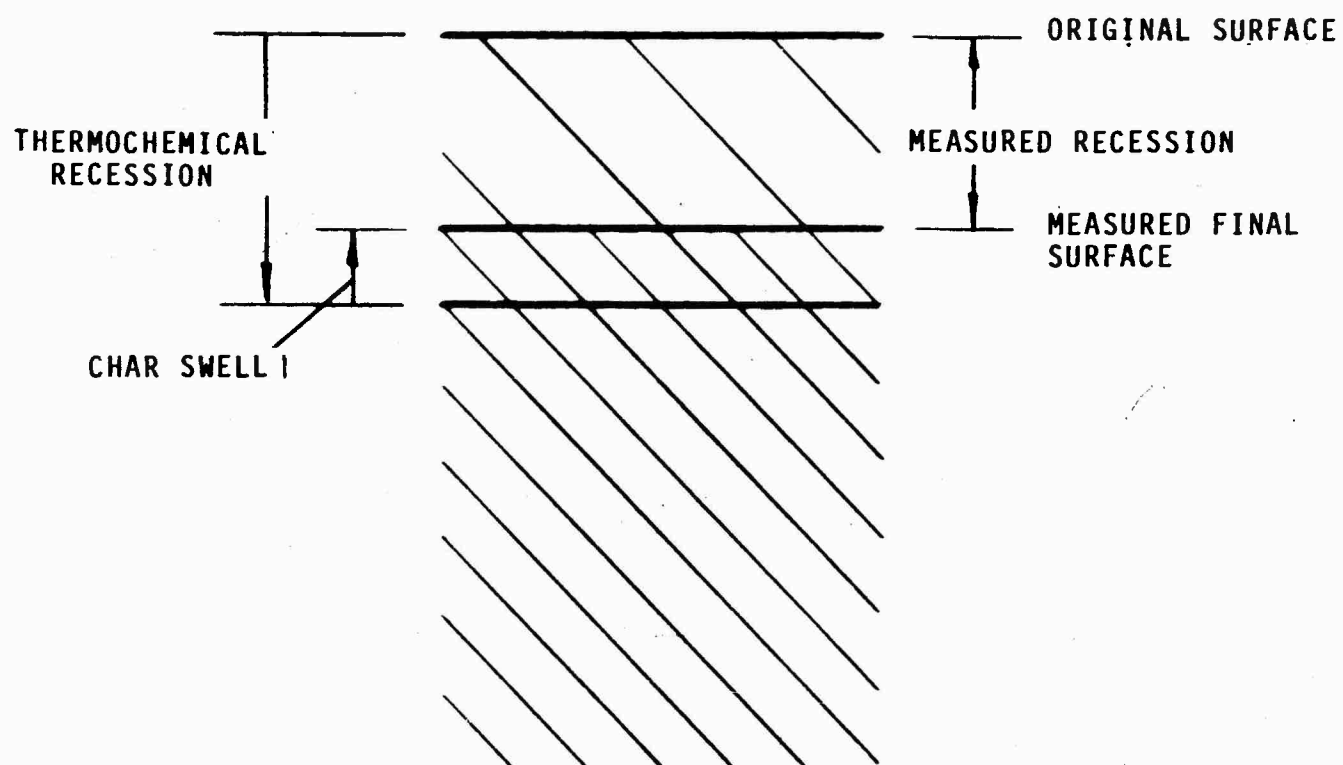


FIGURE 7-16 SCHEMATIC OF MATERIAL SURFACE RECESSION MECHANISMS

A-2961

(7-2a) says that the rate of surface movement due to char swell is proportional to the rate of char thickness increase. That is

$$\dot{s}_{\text{swell}} = 0.135 \dot{t}_c \quad (7-2b)$$

where the dot superscripts indicate derivatives with respect to time (rates).

To account for this swelling in the evaluation of chemically related energy flux terms, a mass rate term has been defined as follows

$$\dot{m}_{c\text{swell}} = \rho_c \dot{s}_{\text{swell}} \quad (7-3)$$

where  $\rho_c$  is the char density before swelling. This mass rate has been added to the mass rate defined by the technique of Section 7.3.3.3 to obtain the total effective thermochemical mass ablation rate. Values obtained from Equation (7-3) are reported in Table 7-7. In addition, the heat flux associated with this ablation rate is given.

#### 7.3.3.5 Surface Thermochemical Response Evaluation

The procedure described in Section 5 was followed for the evaluation of the quantities associated with the surface chemical events. The assumption that the surface erosion of the plug is controlled by heterogeneous equilibrium chemistry which is incorporated in this procedure has been substantiated by the results presented in Section 7.2.3.2. Moreover, since mechanical removal of surface char did not appear to be a significant recession mechanism in either the MX 4926 carbon phenolic plugs or the MX 2600-96 silica phenolic plug, the required evaluation was straightforward. This fact was somewhat surprising because usually the silica in the MX 2600-96 forms a liquid layer. In this case, however, the surface temperature was apparently high enough that an  $\text{SiO}_2$  melt did not form but rather the silica decomposed into gaseous  $\text{SiO}$  and  $\text{O}_2$ . This was confirmed by the higher than expected recession rate.

As explained in Section 5, the independent variables for defining chemically related heat flux are obtained from the in-depth thermal response evaluation and from the rocket motor firing conditions. These variables are:

ratio of  $B'_g$  to  $B'_c$

$$B'_g/B'_c = \dot{m}_g/\dot{m}_c$$

surface temperature

$$T_w$$

Local static pressure

$$P_e$$

propellant and material compositions

Typical plots of the several dependent variables needed for the total heat flux evaluation are presented in Figures 7-17 through 7-20 as a function of the independent variables. A summary of the figures and the variables obtained from the figures is given below.

Figure Number	Independent Variable	Interpolation Variable	Dependent Variable(s)
7-17	$\dot{m}_c/\dot{m}_g = B'_c/B'_g$	$T_w$	$B'_g, \rho_e U_e C_M$
7-18	$T_w$	$B'_g$	$h_w$
7-19	$T_w$	$B'_g$	$Z_{iw}^* h_i^{T_w}$
7-20	$T_w$	--	$K_{ie} h_i^{T_w}$
7-20	$T_w$	--	$K_{ie}^* h_i^{T_w}$

Surface thermochemistry maps of the type shown in Figures 7-17 through 7-20 were generated for at least two static pressures at each ablative plug location. The results for intermediate pressure were obtained by interpolation. The results for four times during the respective firings are presented in Table 7-8 for each ablative plug. Some other properties of the propellant/surface interaction which were required to obtain the values of  $q_{abl}$  and  $q_{blow}$  are also shown in Table 7-8.

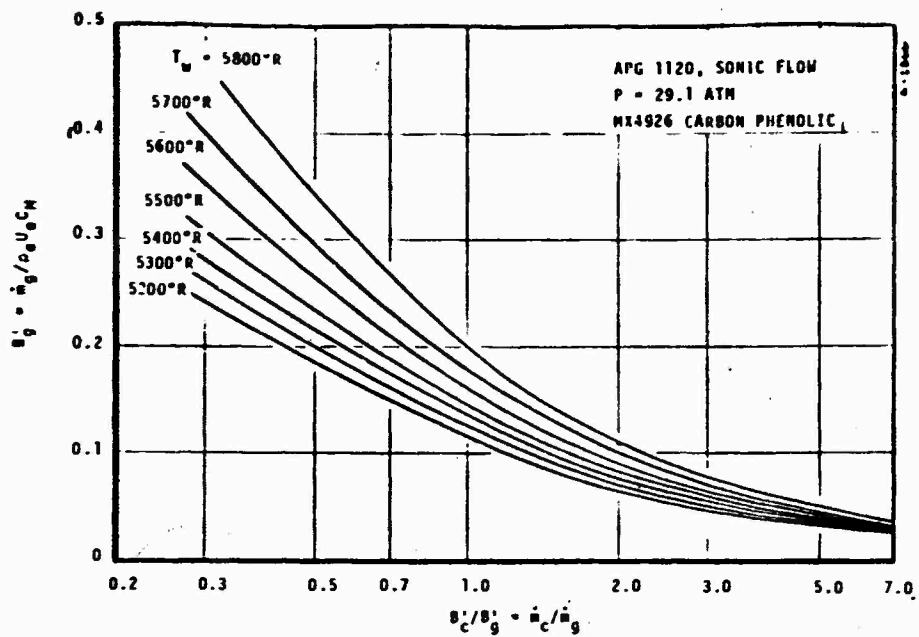


FIGURE 7-17 EVALUATION OF  $B'_g$  FROM  $T_w$  AND  $\dot{m}_c/\dot{m}_g$

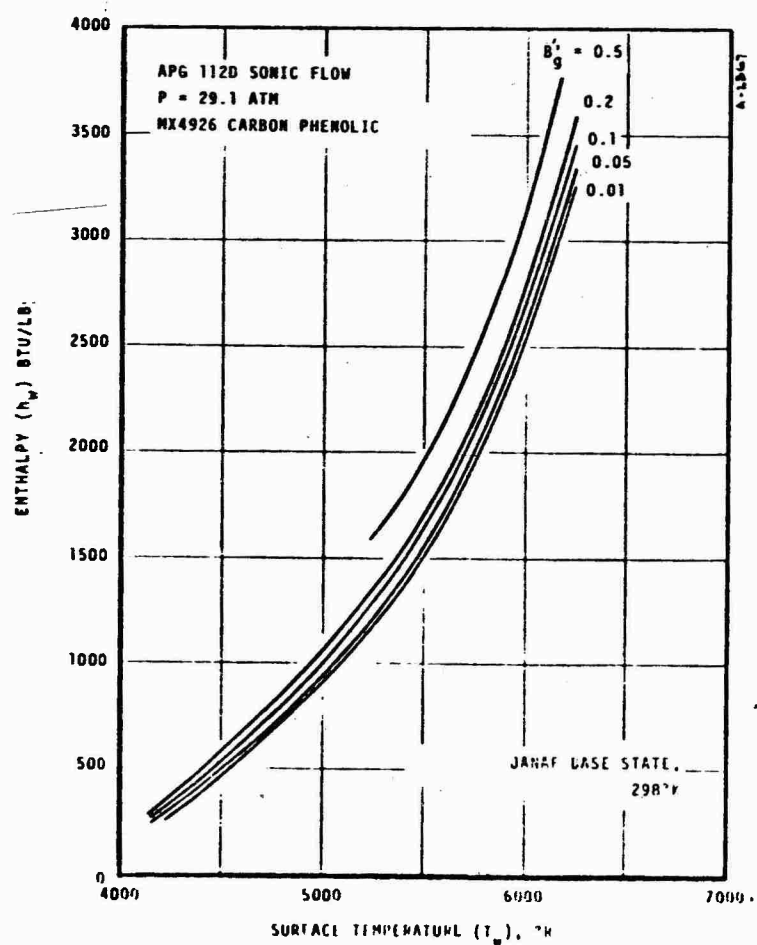


FIGURE 7-18 EVALUATION OF  $h_w$  FROM  $T_w$  AND  $B'_g$

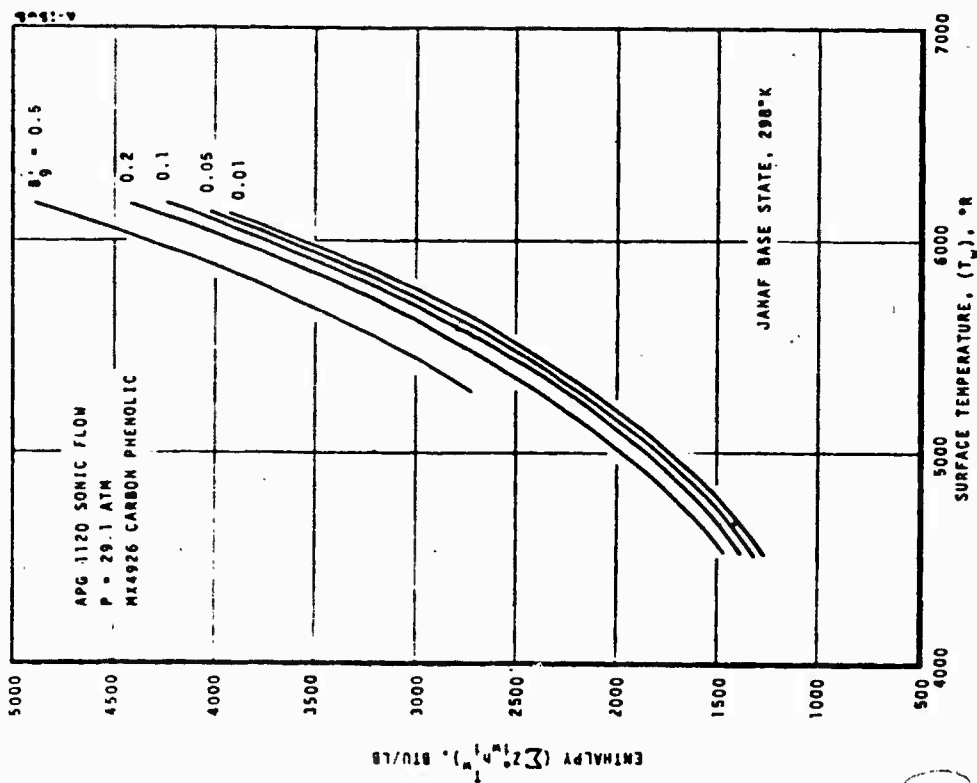


FIGURE 7-19 EVALUATION OF  $\sum z_i h_i$  FROM  $T_w$  AND  $\beta_g$

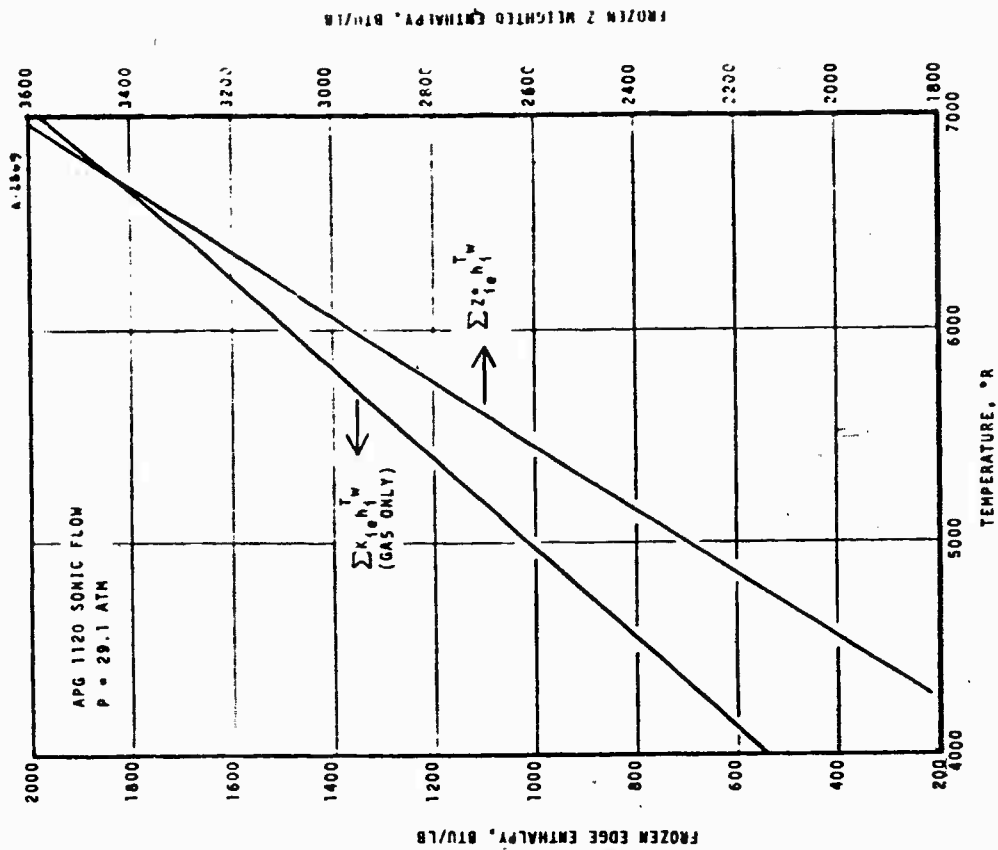


FIGURE 7-20 EVALUATION OF  $\sum z_i h_i$  AND  $\sum z_i h_i^w$  FROM  $T_w$

TABLE 7-8  
SUMMARY OF SURFACE CHEMICAL RESPONSE RESULTS

Sensor Material	Sensor Location <sup>a</sup>	Time (sec)	T <sub>w</sub> (°R)	$\dot{m}_c / \dot{m}_g$	B' g	$\rho_e U_c C_M^c$ (lb/ft <sup>2</sup> sec)	C <sub>H</sub> /C <sub>H<sub>0</sub></sub>	Enthalpy d Potential (Btu/lb)	q <sub>blow</sub> (Btu/ft <sup>2</sup> sec)	$\dot{m}_t$ (lb/ft <sup>2</sup> sec)	q <sub>abl</sub> (Btu/ft <sup>2</sup> sec)
MX 4926	-2.0/1st	10	5560	3.42	0.055	1.16	0.938	782	60	0.197	308
		20	5600	2.04	0.091	0.51	0.929	667	26	0.099	172
		30	5550	2.39	0.076	0.46	0.935	726	24	0.084	140
		50	5220	2.45	0.058	0.44	1.011	1291	32	0.062	74
	Throat/1st	10	5850	2.32	0.102	0.40	0.915	210	11	0.136	308
		20	5660	2.20	0.089	0.33	0.928	494	18	0.094	183
		30	5550	2.52	0.073	0.35	0.936	630	21	0.089	153
		50	5380	2.89	0.055	0.39	0.942	900	31	0.083	126
	2.0/1st	10	5350	2.10	0.066	0.48	0.945	630	25	0.100	158
		20	5200	2.10	0.037	0.42	0.933	845	25	0.074	101
		30	5150	1.39	0.085	0.23	0.945	964	18	0.046	60
		50	5000	0.14	0.314	0.05	0.906	1021	1	0.017	21
MX 2600-96	4.0/1st	10	5350	5.90	0.365	0.07	0.624	1007	60	0.174	218
		20	4900	5.46	0.192	0.16	0.759	1417	101	0.196	163
		30	4590	4.81	0.164	0.13	0.800	1683	77	0.122	74
		50	4390	2.51	0.168	0.04	0.867	1690	13	0.021	10
MX 4926	Throat/2nd	12	5300	2.47	0.059	0.73	0.928	1035	83	0.150	203
		20		2.67	0.058	0.56	0.945	1038	49	0.119	166
		30		2.56	0.058	0.46	0.946	1056	40	0.095	130
		50		2.63	0.053	0.40	0.949	1060	33	0.077	100
	3.0/2nd	12	5307	1.26	0.105	0.24	0.937	1079	25	0.057	89
		20	5353	1.10	0.123	0.17	0.932	988	18	0.045	75
		30	5371	1.20	0.118	0.14	0.933	948	14	0.037	64
		50	5383	1.00	0.135	0.10	0.932	915	10	0.028	48

<sup>a</sup> Area ratio/char motor firing.

<sup>b</sup>  $\dot{m}_c/\dot{m}_g = B' C/B' g$ ,  $\dot{m}_t = \dot{m}_c + \dot{m}_g$ ; includes mass rate associated with char swell.

<sup>c</sup> Crude value estimated from surface thermochemistry calculations.

<sup>d</sup> Enthalpy Potential =  $\left( h_r - \sum K_i h_{i,e}^{T_w} \right) + \frac{C_M}{C_H} \times \left( \sum z_i h_i^{T_w} - \sum z_i h_i^{T_w} \right)$ ;  $C_M/C_H = 0.70$

#### 7.3.3.6 Evaluation of Total Heat Flux

Values of the various component heat flux terms defined in Section 5 are given in Tables 7-7 and 7-8. The total incident heat fluxes were evaluated by the surface energy balance relation given as Equation (5-1). Although Tables 7-7 and 7-8 only show representative flux values for four times during the nozzle firing, more points were calculated to provide continuous knowledge of the variations in total flux. Figure 7-21 shows these curves.

#### 7.3.3.7 Discussion of Total Heat Flux Measurements

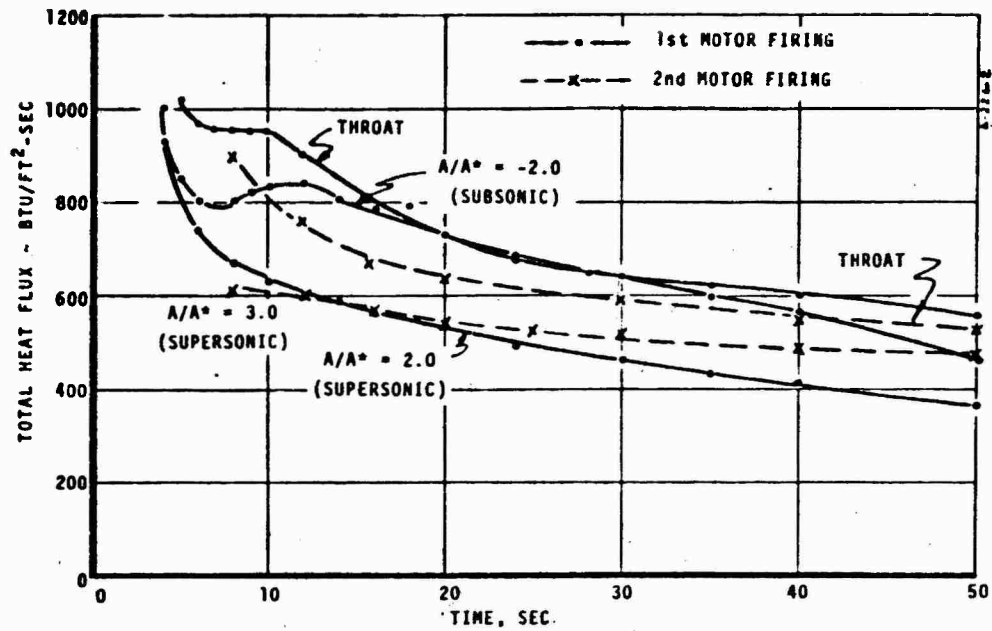
Several trends in the total heat flux measurements confirm the validity and accuracy of the measurement concept. The total incident heat flux histories for the various locations in the two char motor nozzles have been presented as Figure 7-21. The clearest and probably the most indicative trend is apparent in the responses of the MX 4926 carbon phenolic sensors shown in Figure 7-21a. All of these sensors recorded a decreasing total incident heat flux with firing time. This trend was expected since the heat transfer coefficient for turbulent flow is roughly proportional to the 0.8 power of the chamber pressure. Since a significant radiative heat flux component is part of the total incident flux, the overall drop in the total was not in general proportional to the 0.8 power pressure.

Another significant trend indicated in Figure 7-21a is the variation of total heat flux with area ratio. For the subsonic location ( $A/A^* = -2.0$ ) and the throat location, the total heat flux histories are definitely higher than those obtained at downstream supersonic locations. The inlet section is subjected to higher radiation heating and recovery enthalpies and the throat location is subjected to larger heat transfer coefficients than downstream locations. Hence this trend certainly seems reasonable.

Comparisons between results for the two char motor firings provide additional verification. At the throat location where a direct comparison was possible because firing conditions were essentially identical, the difference in total heat flux is less than 18 percent (i.e. within the expected accuracy of the system). The total heat flux measurements are repeatable and the quoted accuracies are reasonable.

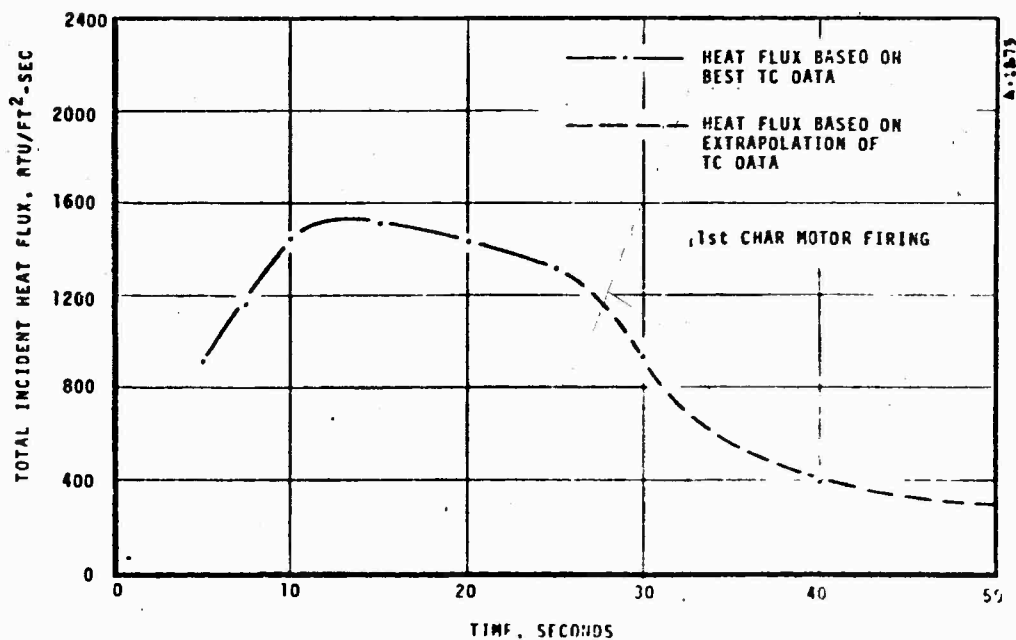
The total heat flux history shown for the  $A/A^* = 3.0$  location of the second char motor nozzle is anomalous. For this sensor, only two of the five original thermocouple circuits remained in tact after nozzle fabrication, and therefore the results are compromised. Figure 7-11f shows that the most useful data from this sensor was taken between 12 and 27 seconds of the firing. In this range the





a) MX4926 CARBON PHENOLIC TOTAL HEAT FLUX SENSORS

FIGURE 7-21 TOTAL HEAT FLUX DETERMINED FROM MEASUREMENT SYSTEM DATA



b) MX2600-96 SILICA PHENOLIC TOTAL HEAT FLUX SENSOR A/A\* = 4.0

FIGURE 7-21 CONCLUDED

reported heat flux values agree quite well in magnitude with those taken at the  $A/A^* = 2.0$  location of the first nozzle. It would be expected that these two locations have approximately the same readings since no drastic changes in boundary conditions occur between  $A/A^* = 2.0$  and  $3.0$ .

Similarly, the total heat flux determined from the response of the MX 2600-96 silica phenolic plug is less accurate for firing times greater than 20 to 25 seconds. This plug location experienced a much larger recession rate than expected and, therefore, the thermocouples became exposed and were lost early in the firing. The total heat flux history presented in Figure 7-21b shows the results of extrapolated data (past 25 seconds) as dashed lines. The total incident heat flux values determined from the silica phenolic plug are also potentially in error because the equilibrium thermochemical response of the silica phenolic is not well understood for the high surface temperatures obtained in this case. No conclusions about the relative magnitude of the silica phenolic and carbon phenolic flux results are possible since the total incident heat flux is a strong function of the significantly different surface chemical events.

In an attempt to further verify the accuracy of the total heat flux values reported for the MX 4926 carbon phenolic sensors, ablation and thermal response predictions (using the ACE and CMA computer codes) for the plug locations in the second char motor firing were performed. (The resultant surface recession predictions are included in Figure 7-14b.) For the throat location, the predicted values of total incident heat flux and incident convective heat flux are compared to measured total flux in Figure 7-22. This prediction required an assumption about the incident radiation heat flux. Based on the radiation measurements described in the following section, it was assumed that the incident radiation was the surface absorptance times the average of the black body radiation from the free stream temperature and the black body radiation from the opposite wall. This came to  $500 \text{ Btu/ft}^2\text{sec}$  and was assumed constant throughout the firing. Figure 7-22 shows that the determined and predicted heat flux values are comparable. In conclusion, it is apparent that the total incident heat flux measurement systems provide data which are self-consistent and accurate to within  $\pm 20$  percent.

#### 7.4 RADIATIVE HEAT FLUX SYSTEM

The performance of each of the three narrow view angle radiometers in the two char motor firings is described in this section. In Section 7.4.1, the details of the design and installation which are pertinent to interpreting the performance data are presented. In Section 7.4.2, the results from these radiometers are presented, and, in Section 7.4.3, the interpretation of these results is presented.

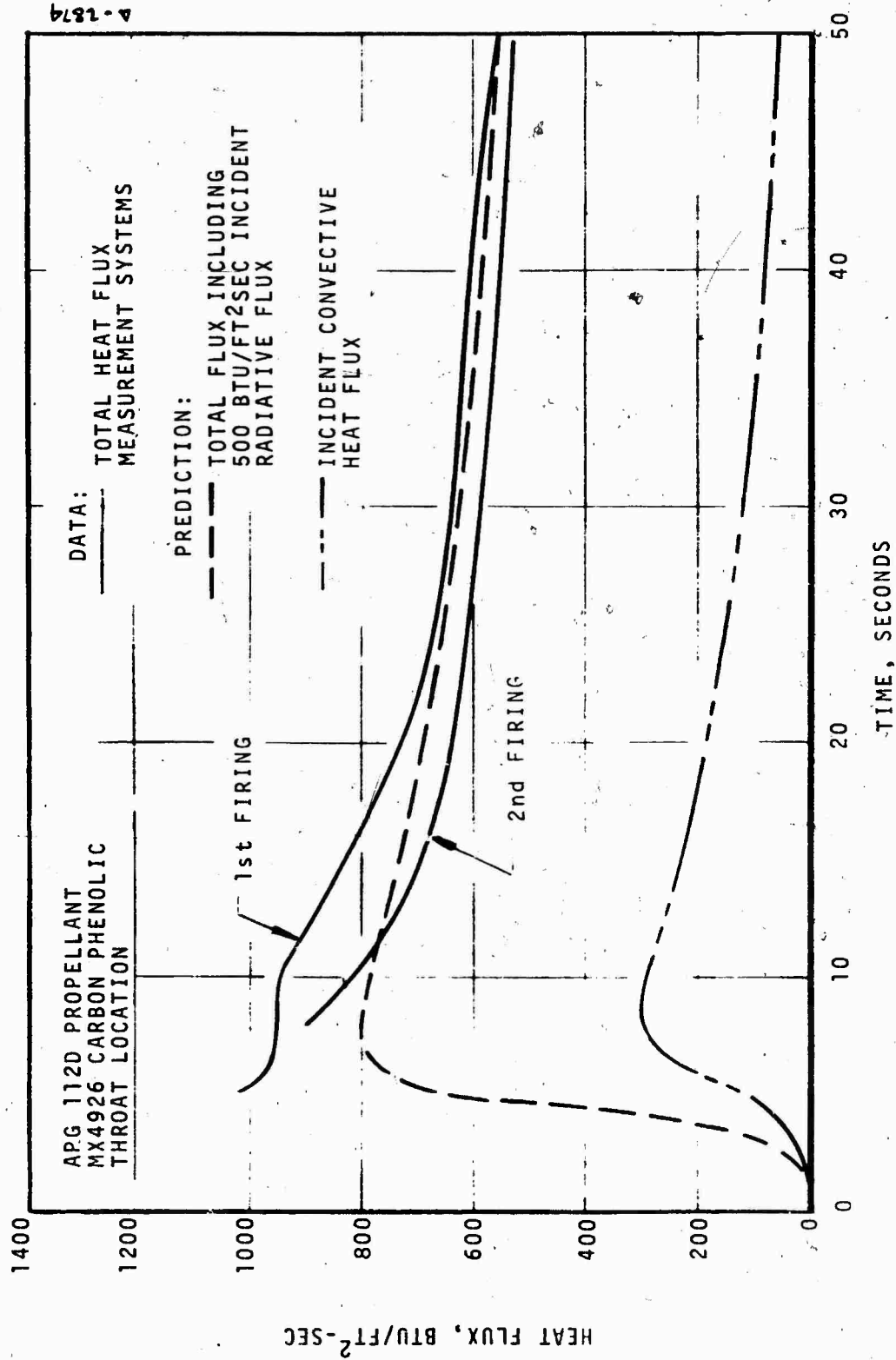


FIGURE 7-22 COMPARISON OF PREDICTED TO MEASURED TOTAL INCIDENT HEAT FLUX

#### 7.4.1 Design and Installation

A narrow view angle radiometer as defined by Figure 4-35 was installed at the throat plane for each of the char motor nozzles. For the second char motor firing, the radiometer as defined by Figure 4-36 was installed at an  $A/A^* = 3.0$ . Each of these radiometers was connected to a nitrogen gas purge flow system. In addition, the thermocouple measuring the copper sink temperature and the leads measuring the emf across the constantan sensor were connected to the recording system described in Section 4.

The gas purge plumbing system was designed for a nitrogen gas flow rate of approximately 0.01 lbs/sec for all the radiometers. The basic consideration in selecting this flow rate was that it provides an acceptable cavity temperature ( $540^\circ\text{F}$ ) as determined in the Phase II APG tests. Since no overheating of the radiometer occurred in the APG tests, this selection of purge gas flow rate for the char motor firings implies that no overheating would occur in the char motor firings. Before each test, a flow check was performed on the nitrogen purge gas system to assure that this system was operational.

#### 7.4.2 Test Results

The measured results from the narrow view angle radiometer located at the nozzle throat plane of the first char motor firing are presented in Figure 7-23. These results include the radiometer sink temperature, the radiometer millivolt output, and the gas purge supply pressure. A decrease in the required nitrogen purge gas flow apparently occurred at 3 seconds into the firing followed by a complete loss of this flow at 15 seconds. The failure at 15 seconds was due to the thermal decomposition of the supply hose caused by the high radiation flux from the exhaust plume. The explanation for the event at 3 seconds is not so clear-cut, however. Several explanations are possible as outlined below:

- The unexpected high chamber pressure resulted in a decrease in the design purge gas flow and therefore a thermal failure of the radiometer view restrictor and sapphire window (Figure 3-4). The nitrogen purge gas flow is controlled by a sonic orifice so that the variations in local static pressure (or chamber pressure) do not influence the flow rate. This requires a supply pressure slightly more than twice that of the maximum local static pressure (to also account for the pressure drop downstream of the sonic orifice). The maximum local static pressure was 620 psia which therefore indicates a nitrogen purge gas supply pressure slightly

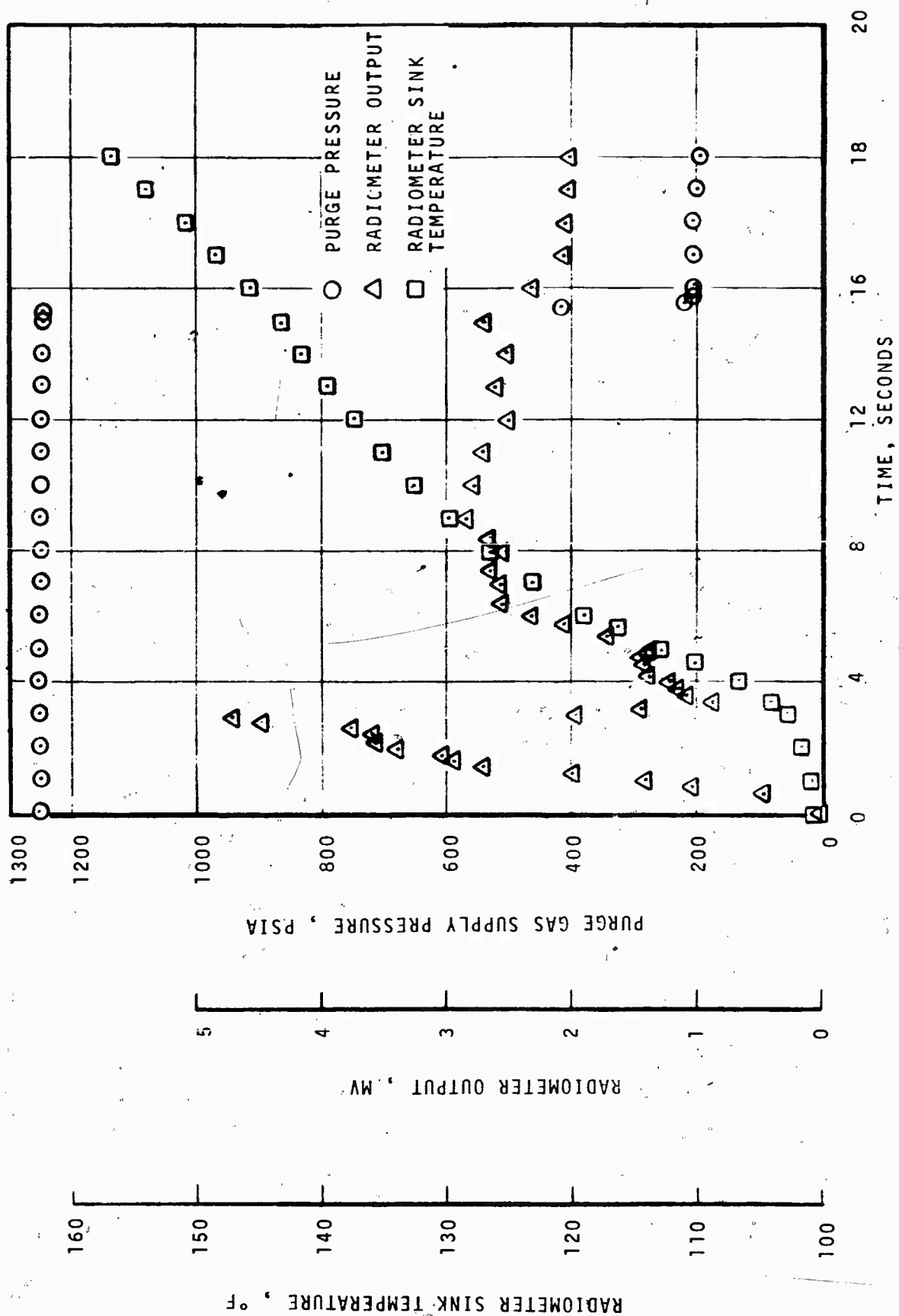


FIGURE 7-23 RADIOMETER OUTPUT AND ASSOCIATED INFORMATION FOR THE FIRST CIAR MOTOR FIRING

greater than 1240 psia is required. The actual supply pressure was 1250 psia, indicating the potential for a decrease in the purge gas flow.

- The pyrolysis products from the purge gas hose which failed 15 seconds into the firing plugged up the sonic orifice early in the test firing and thus caused radiometer failure. This hose probably started pyrolyzing very early in the firing. These pyrolysis products could have condensed on the orifice, plugging it up partially or completely. Actually, the orifice was almost completely plugged after the firing but this could also have been due to the reverse flow after hose failure.
- Dirt in the purge gas supply line plugged up the sonic orifice early in the firing and thus caused radiometer failure. The purge gas supply lines could have been dirty and some of this dirt could have been carried to the orifice and plugged it.

It is not possible to determine which of the above explanations is proper. Based on these possibilities, however, the following guidelines were established for the second char motor firing:

- The purge gas supply pressure should preferably be twice the anticipated maximum chamber pressure.
- All lines in the vicinity of the char motor should be stainless steel.
- A filter should be installed as close to the sonic orifice as practical.

The total hemispherical radiation heat flux reduced from the results shown in Figure 7-23 are shown in Figure 7-24. One notes that the magnitude of the measured radiative flux prior to the loss of the nitrogen purge was on the order expected and that the transient response of the radiometer was similar to the chamber pressure transient which was also expected.

The above mentioned recommendations were incorporated in the gas purge system for the second char motor firing, and the measured results for the two radiometers are shown in Figures 7-25 through 7-27. The hemispherical radiation heat flux obtained from the data reduction procedure is presented in Figure 7-28. The only suspicious data from these results are the measured emf output from the radiometer located at the nozzle throat plane. One notes from Figure 7-27 that the initial emf output from both radiometers have the same trend

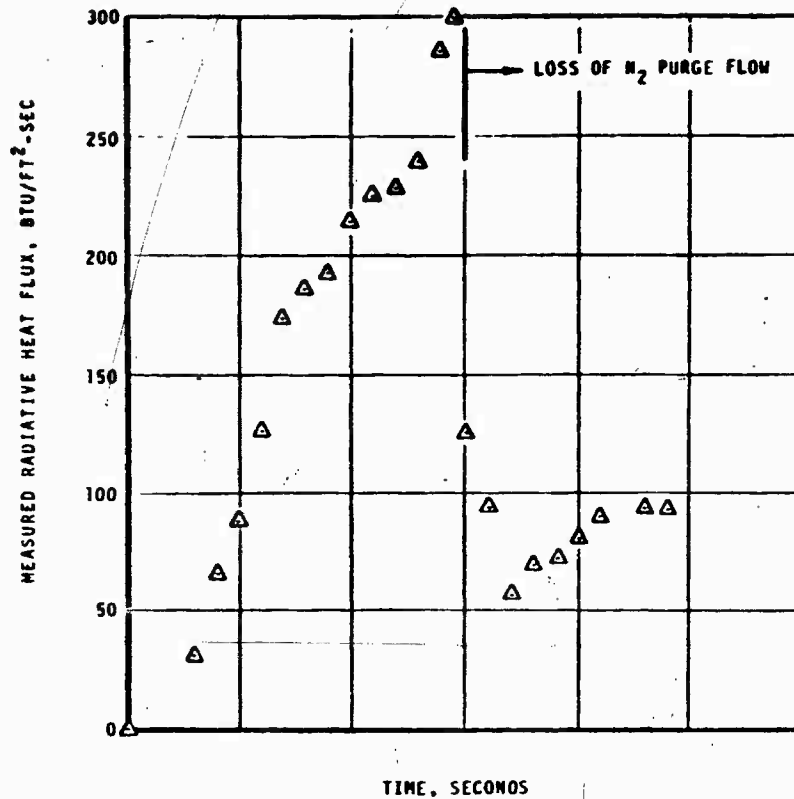


FIGURE 7-24 MEASURED RADIATIVE HEAT FLUX AT THE NOZZLE THROAT FOR THE FIRST CHAR MOTOR FIRING

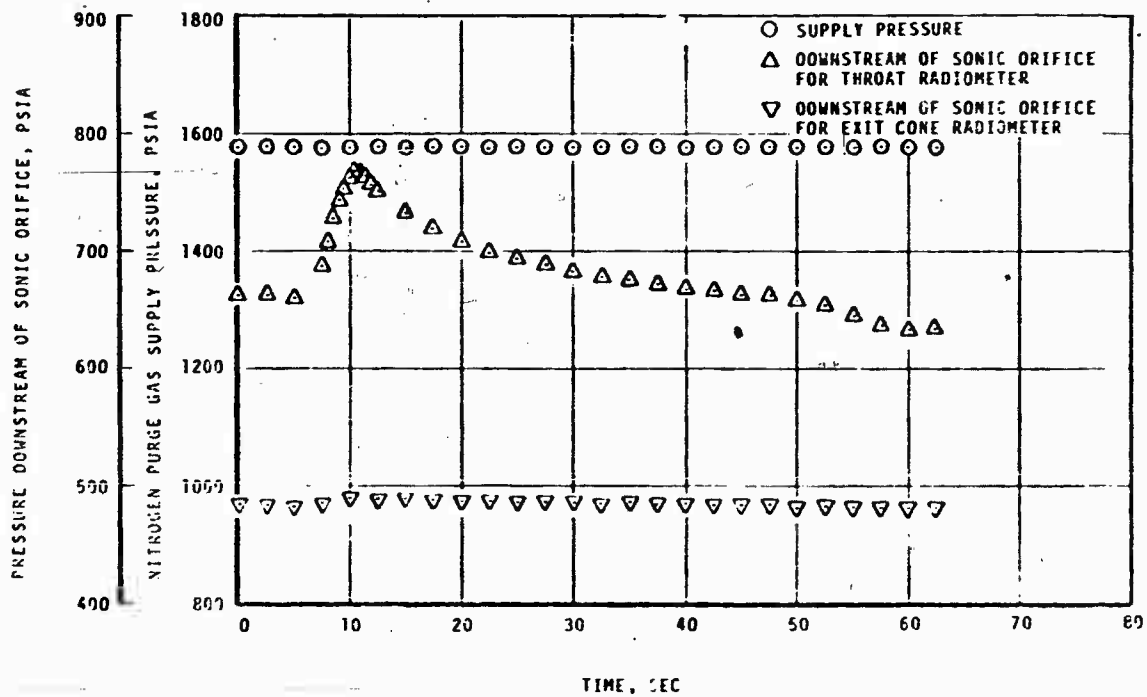


FIGURE 7-25 NITROGEN PURGE GAS SYSTEM PRESSURES FOR THE SECOND CHAR MOTOR FIRING

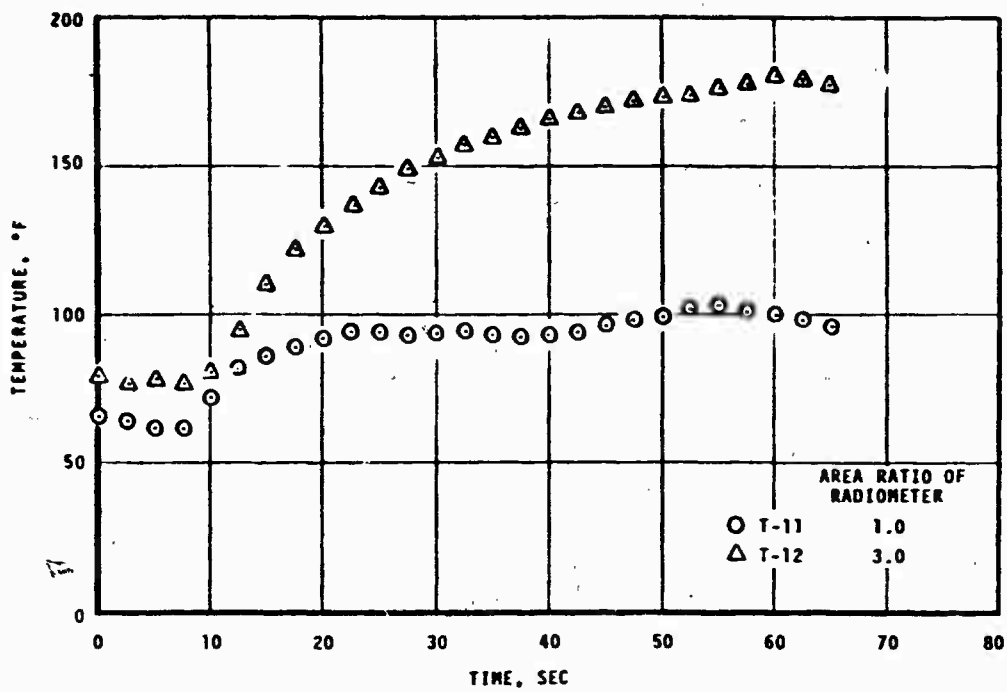


FIGURE 7-26 MEASURED COPPER HEAT SINK TEMPERATURES FOR THE SECOND CHAR MOTOR FIRING

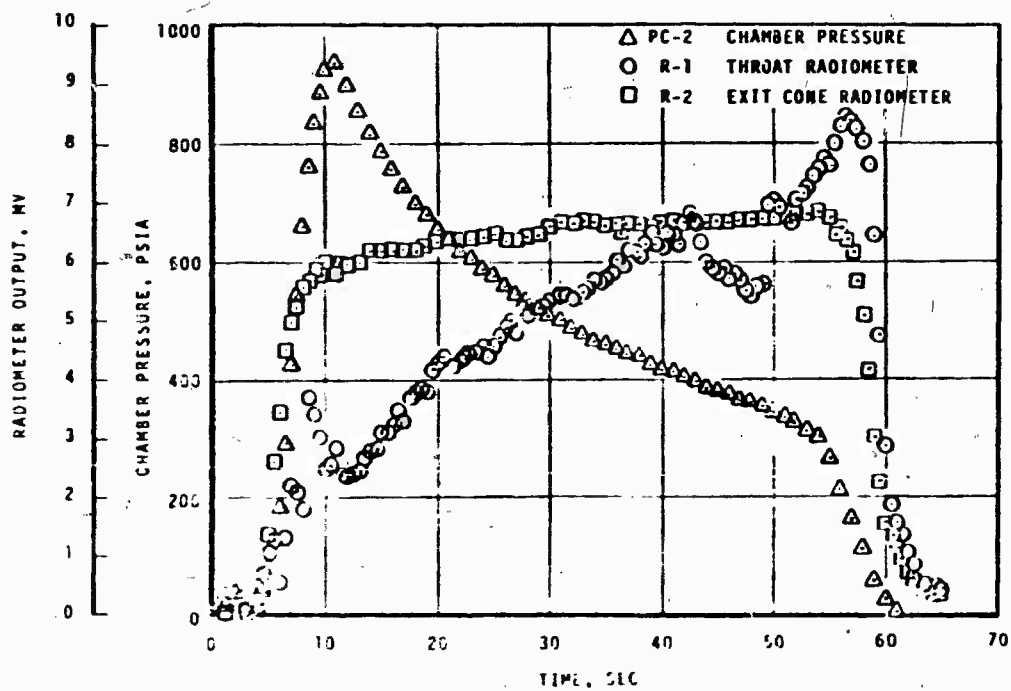


FIGURE 7-27 TRANSIENT CHAMBER PRESSURE AND NOZZLE THROAT AND EXIT CONE RADIOMETER OUTPUT FOR THE SECOND CHAR MOTOR FIRING



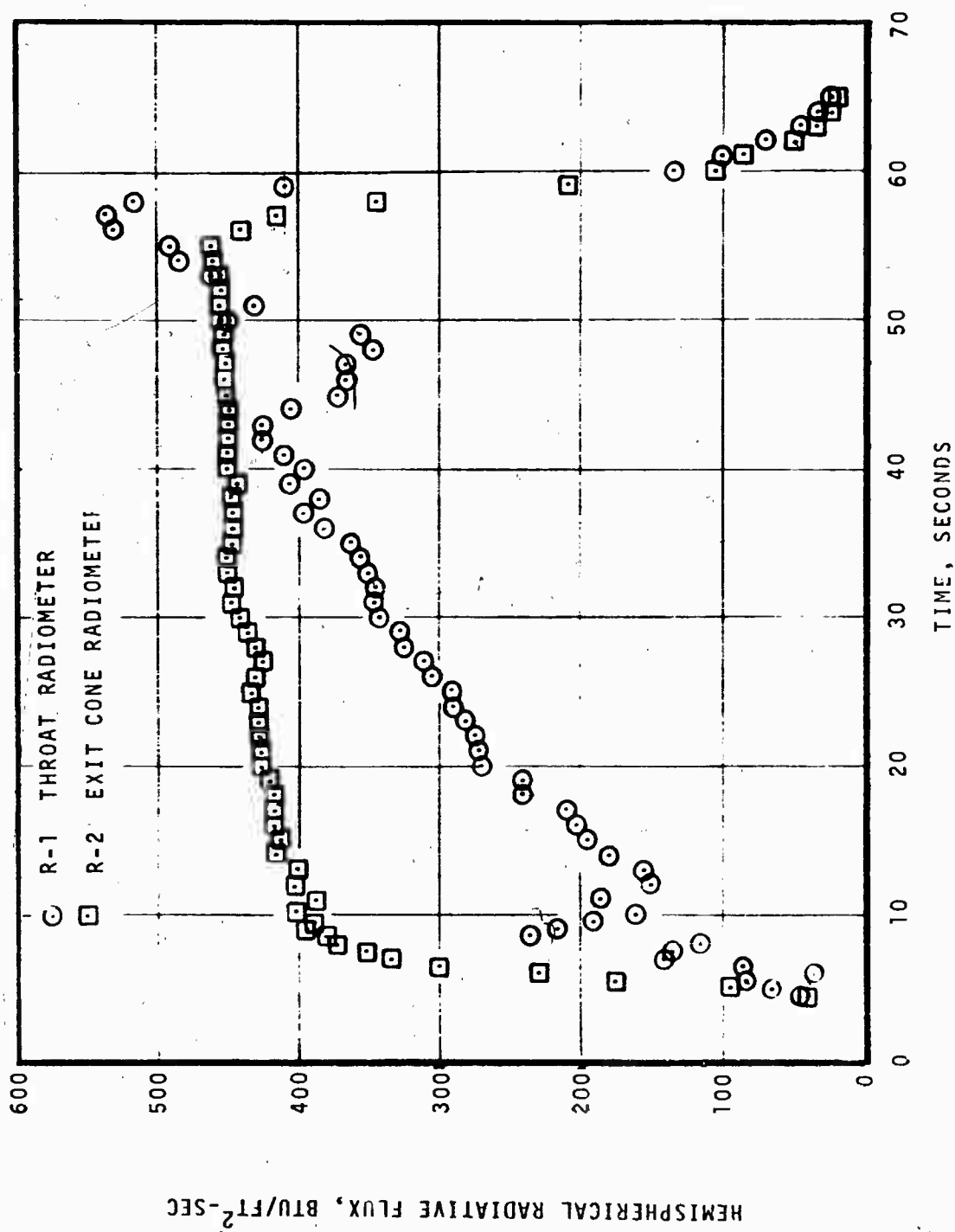


FIGURE 7-28 MEASURED HEMISPHERICAL RADIATIVE HEAT FLUX FOR THE SECOND CHAR MOTOR FIRING

as the chamber pressure. However, at approximately eight seconds through the firing, the output from the throat radiometer decreased but then started to increase again at approximately twelve seconds into the firing. The output took another dip at approximately 42 seconds but achieved its maximum value at motor burnout. Both the output from the exit cone radiometer and sink temperature and purge pressure results did not exhibit these anomalies. Before discussing possible reasons for the variations shown in the output from the throat radiometer, the following observations should be noted:

- The output from both radiometers delayed in a similar manner at motor burnout and lagged the combustion chamber pressure. This lag was expected as the temperature of the nozzle surface which is viewed by the radiometer decreases more slowly than the chamber pressure.
- Post-test observation of both radiometers showed that no effects of excessive heating were visible and that the sapphire lens was clear.
- Post-test observation of the exit cone cavity showed that it did not contain any debris. However, the side-walls of the cavity at the nozzle throat had some slag which extended to the radiometer, but, at motor burnout, this slag was not restricting the aperture or the view of the radiometer.

Based on the above observations, one possible explanation for the variations shown by the output of the nozzle throat radiometer is that during the firing either ablation products or alumina particles were falling into the cavity and adhering to the relatively cool cavity walls. However, the purge flow kept this debris from contaminating the radiometer. If the debris continued to build up on the cavity walls, it would restrict the view of the radiometer and cause the dips shown. If this debris broke off and was blown out by the purge gas, then output from the radiometer would increase. The post-test observations substantiate the validity of the maximum value measured at motor burnout. Some interpretations concerning this data point plus the output from the exit cone radiometer are presented in the next section.

#### 7.4.3 Interpretation of the Radiation Results

The validity of converting the measured radiative heat flux from a narrow view angle radiometer to a total hemispherical radiative heat flux was discussed in Section 5. In that section, it was shown that the total hemispherical radiative flux is a true measurement of the flux being emitted by the radiative source for the following situations:

- The particle laden combustion products are a non-absorbing and non-scattering media, and, thus, the radiometer views only the opposite wall.
- The particle laden combustion products form a constant temperature optically thick media which has a negligible scattering coefficient but has an absorption coefficient which is independent of wavelength. In this situation, the combustion products emit radiation as a gray body.

At the nozzle exit cone station corresponding to an  $A/A^* = 3.0$ , the emissive power of the opposite wall being viewed by the radiometer corresponds to a hemispherical radiative flux of approximately 380 Btu/ft<sup>2</sup>sec if the surface emissivity is unity. If the combustion products emit as a black body at the local static temperature, the average hemispherical radiative flux through the firing would be 540 Btu/ft<sup>2</sup>sec. The similar values at the nozzle throat are 420 Btu/ft<sup>2</sup>sec from the opposite wall and about 900 Btu/ft<sup>2</sup>sec from black body combustion products. The maximum measured values at the exit cone station and throat were 460 and 540 Btu/ft<sup>2</sup>sec, respectively, which fall between the extremes identified above. These comparisons show that the particle laden combustion products are emitting a significant amount of energy in the form of radiation. However, these comparisons do not reveal whether the radiative flux absorbed by the sensor is primarily from the opposite wall with a small contribution from the particle laden combustion products (low effective emissivity) or primarily from the particle laden combustion products alone (high effective emissivity). An attempt to define which is the valid possibility is made in the following paragraphs.

To determine the relative significance of the radiation from the particle laden combustion products, one must account for the contributions from both the gases and the alumina particles. Preliminary calculations showed the radiation from the gas was negligible. However, these calculations showed that the radiation from the particles was significant. These calculations are summarized below.

The first step in predicting the radiation from the particles was to define the optical depth which is given by

$$\tau_{o\lambda} = \int_0^D \beta_{\lambda} dy \quad (7-4)$$

Using the procedure outlined in Reference 7-2, the extinction coefficient can be defined by

$$\beta_{\lambda} = N_p \sigma_t \quad (7-5)$$

where  $N_p$  - particle density  
 $\sigma_t$  - extinction cross-section

Substituting Equation (7-5) into Equation (7-4) gives

$$\tau_o = \sigma_t \int_0^D N_p dy \quad (7-6)$$

The particle density can be defined from the aluminum loading and by assuming the mean particle radius is given by the relationship (Reference 7-2)

$$r_{pm} = 0.862 (\ln P_c - 4.17) \quad (7-7)$$

where  $r_{pm}$  - mean particle radius in microns  
 $P_c$  - combustion chamber pressure  
in psia

The extinction cross-section,  $\sigma_t$ , can be calculated using Mie theory (Ref. 7-2) provided the real and imaginary parts of the alumina index of refraction are known. The calculation of these cross-sections for the particular particle concentrations in the char motor firing was beyond the scope of this program. However, for the preliminary calculations presented here, these cross-sections can be estimated from the information presented in Reference 7-2. In this reference, it was shown that the extinction efficiency factor which is defined by

$$Q_t = \frac{\sigma_t}{\pi r_{pm}^2} \quad (7-8)$$

is approximately equal to two if the ratio  $2\pi r_{pm}/\lambda$  is also greater than two. Since this condition is satisfied, the extinction cross-section was approximated from Equation (7-8) by using Equation (7-7) to calculate the mean particle density and by assuming an extinction efficiency factor of two. The results of this calculation including the effects of nozzle surface recession and chamber pressure decay are tabulated below in Table 7-9. Also shown in the table is the blackbody emissive power based on the local static temperature of the combustion products.

TABLE 7-9  
OPTICAL DEPTH AND BLACKBODY EMISSIVE POWER

Chamber Pressure (psia)	Area Ratio of Radiometer <sup>a</sup>		Optical Depth		Blackbody Emissive Power (Btu/ft <sup>2</sup> sec)	
	Nozzle Throat	Exit Cone	Nozzle Throat	Exit Cone	Nozzle Throat	Exit Cone
940	1.00	2.76	21.4	6.92	951	495
806	1.00	2.51	20.0	6.86	924	510
300	1.00	1.50	16.5	8.85	805	585

<sup>a</sup>Changing area ratio for the exit cone location due to surface recession that occurred at the throat.

Referring to Equation (5-8), the radiation from the opposite wall is attenuated by the factor  $e^{-\tau/\mu}$ . If  $\mu = 1$  (a good approximation for a narrow view angle radiometer), the values for the optical depth in Table 7-9 indicate that the radiometer does not see the opposite wall and that the measured radiation is due to the alumina particles. This conclusion was further substantiated by solving for the emissivity of a one-dimensional slab of scattering and emitting particles. This emissivity is given by (Reference 7-2)

$$\epsilon(\tau) = 2M \left[ e^{-K'\tau} (K' + M) + e^{-K'\tau} (K' - M) - 2K' \right] / D \quad (7-9)$$

where

$$D = (K' + M)^2 e^{K'\tau} - (K' - M)^2 e^{-K'\tau}$$

$$K' = \left\{ M \left[ 2(1-M) B + M \right] \right\}^{1/2}$$

$$M = \frac{\sigma_a}{\sigma_a + \sigma_s}$$

$\sigma_a, \sigma_s$  - absorption and scattering  
cross-sections

B - fraction of radiation  
scattered backward

This equation was solved for various values of B and M which would bound the conditions of the test firing, and the results are shown in Figure 7-29. For the previously mentioned values of the optical depth, the emissivity is approximately constant for a fixed value of B and M. The similarity in the exit cone of the variations in the measured hemispherical radiative flux and in the predicted black-body emissive power substantiated the conclusion that the emissivity of the combustion products is approximately constant for this variation in the optical depth. In addition, the range of emissivity in Figure 7-29 is consistent with the measured results. To be more definitive requires an extensive analysis to evaluate B and M and, as previously mentioned, this is beyond the scope of the present contract.

In summary, the radiometer at the  $A/A^* = 3.0$  location apparently provided a valid indication of the total radiative heat flux throughout the test firing. This radiation was from the particle stream with an effective emissivity near unity. The radiometer at the throat location apparently indicated a significantly lower than actual radiative flux during all but the early and later parts of the test firing. Apparently an unexplained partial restriction of the radiometer view occurred.

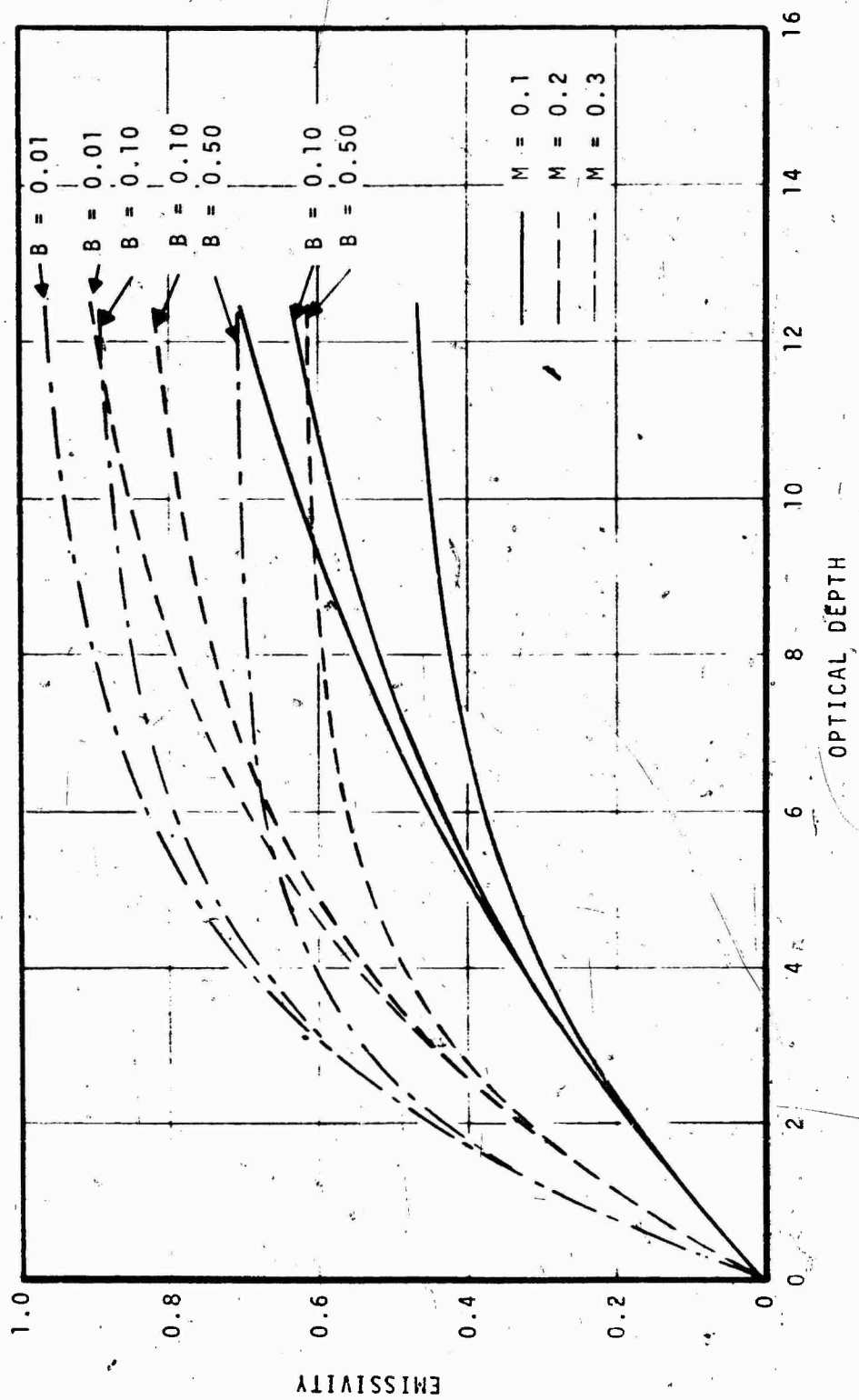


FIGURE 7-29 EMISSIVITY OF A ONE-DIMENSIONAL SLAB OF SCATTERING AND EMITTING PARTICLES

#### REFERENCES

- 7-1 Ellison, J. R. and Binder, H. I.: Evaluation of a Heat Flux Measurement System. AFRPL-TR-69-238, November 1969.
- 7-2 Rochelle, W. C.: Review of Thermal Radiation from Liquid and Solid Propellant Rocket Exhausts. NASA TM X-53579, February 20, 1967.



## SECTION 8

### CONCLUSIONS AND RECOMMENDATIONS

Total heat flux and radiative heat flux measurement systems for use in ablative solid rocket nozzles were developed and demonstrated. The total flux system is a thermocouple instrumented plug of the same material and layup angle as the material in which it is installed. The radiative heat flux system is a narrow view angle, Gardon-type radiometer. The final evaluation and demonstration tests were two nozzle firings performed on the AFRPL 40-inch char motor. The conclusions and recommendations related to the development and demonstration of these systems are as follows:

- Total heat flux measurement system provides a repeatable and accurate measurement of total heat flux
- Radiative heat flux measurement system provides an accurate measurement of total radiative heat flux provided the assumption of a uniform, grey-body source is satisfied
- These systems have been designed for use in a wide range of materials and firing conditions, including high chamber pressure
- The only limitation to the total heat flux system is that the material be well characterized in terms of thermal and ablative properties
- The only limitation for the radiative heat flux system is that the installation design does not result in a large thermal load to the radiometer body
- The reason for an apparent partial obstruction of the radiometer cavity at the throat of the second nozzle should be investigated and any necessary corrective action defined
- A radiative heat flux measurement system which measures total (hemispherical) radiation heat flux directly should be developed.

UNCLASSIFIED

Security Classification

DOCUMENT CONTROL DATA - R & D		
(Security classification of title, body of abstract and indexing annotation must be entered when the overall report is classified)		
1. ORIGINATING ACTIVITY (Corporate author) Aerotherm Corporation Mountain View, California 94040		2a. REPORT SECURITY CLASSIFICATION UNCLASSIFIED
		2b. GROUP
3. REPORT TITLE Development of Total and Radiative Heat Flux Measurement Systems for Rocket Nozzle Applications		
4. DESCRIPTIVE NOTES (Type of report and inclusive dates) Final Technical Report		
5. AUTHOR(S) (First name, middle initial, last name) Duane L. Baker Mitchell R. Wool John W. Schaefer		
6. REPORT DATE August 1970	7. TOTAL NO. OF PAGES	7b. NO. OF REFS
8a. CONTRACT OR GRANT NO. F04611-68-C-0086	8a. ORIGINATOR'S REPORT NUMBER(S) Aerotherm Final Report No. 70-11	
b. PROJECT NO.		
c.	9b. OTHER REPORT NO(S) (Any other numbers that may be assigned this report) AFRPL-TR-70-82	
d.		
10. DISTRIBUTION STATEMENT This document is subject to special export controls and each transmittal to foreign governments or foreign nationals may be made only with prior approval of AFRPL (RPOR-STINFO), Edwards, California 93523.		
11. SUPPLEMENTARY NOTES		12. SPONSORING MILITARY ACTIVITY Air Force Rocket Propulsion Laboratory Air Force Systems Command United States Air Force, Edwards, Calif
13. ABSTRACT Total heat flux and radiative heat flux measurement systems were developed for use in ablative solid rocket nozzles. The total heat flux system is a thermocouple instrumented plug of the same material and layup angle as the ablative part in which it is installed. The total heat flux through a firing is determined from an analysis of the measured in-depth temperature histories. The radiative heat flux system is a narrow view angle, Gardon-type radiometer installed in a cavity below the surface of the ablative part. The total radiative heat flux through a firing is determined from a calibration curve relating millivolt output and total radiative flux of a uniform calibration source. The ablative materials considered under the program were MX4926 carbon cloth phenolic and MX2600-96 silica cloth phenolic. Detailed accuracy, design, fabrication, and installation studies were performed to define the system configurations. A preliminary evaluation program was performed in which the measurement systems were installed in two-dimensional nozzles and successfully tested in simulated rocket environments using an arc plasma generator. Final systems evaluation and demonstration was performed through two nozzle firings on the AFRPL 40-inch char motor. A total of six total flux systems and three radiation flux systems were tested in these firings. A high flame temperature aluminized propellant, APC 112D, was used and peak pressures in both firings were approximately 1000 psia with firing durations of approximately 60 seconds. Successful performance of the two measurement systems was demonstrated.		

DD FORM 1473

REPLACES DD FORM 1473, 1 JAN 64, WHICH IS OBSOLETE FOR ARMY USE.

UNCLASSIFIED

Security Classification

14	KEY WORDS	LINK A		LINK B		LINK C	
		ROLE	WT	ROLE	WT	ROLE	WT
	Convective Heat Flux Radiative Heat Flux Total Heat Flux Thermocouples Radiometers Heat Flux Instrumentation Rocket Nozzles Ablative Material Response						